UNIVERSITY OF SOUTHAMPTON

DYNAMICS OF NEAR-SHORE VORTICES

Luca R. Centurioni

Submitted for the degree of Doctor of Philosophy

September 2000

School of Ocean and Earth Sciences

Abstract

This work addresses two problems: 1) the dispersion induced by a cloud of vortices near a straight coast-line when the bottom is flat and the coastal boundary is a vertical plane or when the bottom is a planar slope; 2) the dynamics of vortices moving over a planar sloping bottom.

Vortices near a vertical boundary are studied by the well-known method of images. For a plane sloping bottom we describe and develop a model, first introduced by Peregrine (1996) that uses a sector of a vortex ring to model a vortex in a wedge of fluid, where the wedge is formed by the water surface and by the planar sloping bottom. Numerical simulations using these free-slip analytical models are used to investigate the dispersion of vorticity and of a passive tracer induced by clouds of vortices. The results of the two models are compared. The dispersion of vortices and particles is mainly affected by the formation of vortex dipoles. The shoreline sets a preferential direction for the dispersion process and the dispersion normal to the shoreline is generally smaller, or bounded when the vortices forming the dipole have different absolute circulation. The dispersion of particles is generally smaller than the dispersion of vortices.

In the second part of this work the analytical model of Peregrine (1996) for vortices moving over a planar slope at an angle α with the horizontal is tested against a set of laboratory experiments. Experiments were made by studying the dynamics of a vortex dipole moving towards a planar sloping beach. We measured the minimum distance from the shoreline reached by the vortices and their along-shore speed. The parameter ranges examined were $3°\leq\alpha\leq45°$, and $1\cdot10^3\leq R_e\leq6\cdot10^3$ (where R_e is the Reynold's number of the vortices). We find a good agreement between the predictions and the observations when $R_e >\sim 1500$.

Acknowledgments

I am deeply indebted to professor Steve Thorpe. Working with him has been a great learning experience. His supervision has been invaluable and without him this work would have not been possible. Very special thanks also for reading the whole manuscript and pointing me towards a more canonical use of the English language. Dr Gregory Lane-Serff introduced me to the world of the experimental fluid mechanics and to the PIV technique. The laboratory experiment work hinges on his support. I am also grateful to him for commenting on chapter 4. Dr. David Smeed helped me with the spin-down problem (eq. 2A.11). I am grateful to Dr. Adonis Velegrakis for showing me figure 1.1. Special thanks to Dr. Jerome Smith for allowing me to use some of his unpublished data.

Mr. Ray Collins built the vortex generator and made the laboratory experiments possible. Dr. Andreas Thurnherr helped me to relieve my frustration while trying to produce some figures by showing me the solution.

This research work was pleasantly interrupted by my participation to a WHOI cruise. I should first thank Dr. Harry Bryden for arranging my participation and for providing some financial support. Dr. Kurt Polzin, Dr. Raymond Schmitt and Dr. John Toole are gratefully acknowledged for let me joining their field experiments and for their warm hospitality. Thanks also to professor Michael Collins for providing some funding for my travel.

I am also grateful to the James Rennell Division at SOC for letting me use their computing facilities. Dr. Sheldon Bacon, Dr. John Gould and Dr. Brian King are gratefully acknowledged for allowing the time necessary to complete this dissertation.

I don't know how to express in word my gratitude to my parents for their total support and to Cristina, for sharing her life with me.

Thank you to all my friends, especially Adonis, Andreas, Bruno, Carla, Gigi, Marino, Massimo, Mickis, Tony and Virginie.

Partial financial support for this research was provided by the School of Ocean and Earth Science, University of Southampton.

Contents

Chapter1: Introduction and review 1

1.1 Introduction 1

1.2 Objectives 3

1.3 Vortices in the surf-zone 4

1.3.1 Inverse cascade and instabilities 4

1.3.2 Rip currents 5

1.4 Point vortices and vortex rings 9

1.4.1 Point vortices 9

b. Presence of boundaries: the method of images 11

c. Point vortices and turbulence 13

1.4.2 Vortex rings 14

1.5 Vortex/boundary and vortex/vortex interactions 16

a. Vortex/boundary interactions 16

b. Vortex/vortex interactions 20

Chapter 2: Theory 25

2.1 Introduction 25

2.2 The point vortex model 26

2.2.1 Background 26

2.2.2 Vortices in a semi-infinite plane 32

a. Point vortex interacting with a straight boundary 32

b. Vortex dipole interacting with a straight boundary 33

c. Group of point vortices interacting with a straight boundary 36

2.3 The vortex ring model 37

2.3.1 Background 37

2.3.2 The case of two counter-rotating equal vortex rings 46

2.3.3 Curved line vortices in a bounded three-dimensional domain 51

2.4 Spin-down of an isolated vortex on a flat bottom 53

2.5 Summary 58

Chapter 3: Numerical experiments 59

3.1 Introduction 59

3.2 Implementation of the 2-D numerical model 62
3.2.1 Program "point" 62
3.2.2 Test of the program and tuning 68
a. Single vortex near the boundary 68
b. Two vortices near the boundary 69
c. Estimate of the error using the Hamiltonian 70
3.3 Implementation of the 3-D numerical model 72
3.3.1 Program "smoke" 72
b. Integration of the velocity field 74
c. Boundary conditions 74
d. Other features 74
e. Input and output 77
3.3.2 Test of the program and tuning 77
a. Single vortex ring 77
b. Ring pair 78
c. Estimate of the error using the kinetic energy 78
3.4 Preliminary experiments 80
3.4.1 Dispersion of vorticity and particles far from the wall - I. The case of equal vortices 81
a. Experiment set-up 81
b. Results from the 2-D model 81
c. Results from the 3-D model 81
d. Discussion : dispersion of the vortices 88
e. Discussion: dispersion of the tracer 91
3.4.2 Dispersion of vorticity and particles far from the wall - II. The case of vortices with equal absolute strength and opposite sign. 94
a. Experiment set-up 94
b. 2-D model. Results 96
c. 3-D model. Results 97
d. Discussion 97
3.4.3 Summary of the results from the preliminary experiments 108
3.5 Dispersion of vortices and mass near the wall-Case 1. Vortices and particles sharing the same surface 110
3.5.1 Experimental set-up 110
3.5.2 Analysis tools and results 113
a. Animation of the output 113
b. Dispersion of vortices and particles 114
c. Statistical analysis: comparison between dispersions from the same model 114

d. Statistical analysis: comparison between the 2-D and the 3-D models ___ 119
3.5.3 Discussion 120
a. Dispersion of vortices and particles parallel and normal to the shore 120
b. Comparison between 2-D and 3-D models 124
3.5.4 Conclusions 124

3.6 Dispersion of vortices and mass near the wall-Case 1. Vortices and particles starting in different areas 126
3.6.1 Experiment set-up 126
3.6.2 Results 128
3.6.3 Discussion 128
a. Dispersion of vortices and particles parallel and normal to the shore 128
b. Comparison between 2-D and 3-D models 129
3.6.4 Final remarks 130

3.7 Conclusions 130

3.8 Summary 132

Chapter 4: Physical experiments 134

4.1 Introduction 134
4.1.1 Background and motivations 134
4.1.2 Objectives 136
4.1.3 Structure of the chapter 137

4.2 The apparatus 137
4.2.1 The vortex generator 137
4.2.2 The tank 143
4.2.3 Recording system, flow visualisation techniques and data acquisition ___ 143
a. Recording system 143
b. Flow visualisation and data acquisition. Method 1: dye 144
c. Flow visualisation and data acquisition. Method 2: particles 144

4.3 The experiments 148
4.3.1 Plan of the experiments 148
4.3.2 Summary of observations 151

4.4 Data processing 163
4.4.1 PIV: velocity and vorticity field 165
4.4.2 Dipole's path: experiments with fluorescine 168
4.4.3 Dipole's path: experiments with particles (PIV) 169
4.4.4 Speed of the vortices 176
4.4.5 Strength of the vortices: experiments with fluorescine 176

4.4.6 Strength of the vortices: experiments with particles 180
4.4.7 Area and "radius" of the vortices 183

4.5 Data analysis 183
4.5.1 Minimum distance from the shoreline (R_f) 183
4.5.2 Speed of the vortices in the direction parallel to the shoreline 190
4.5.3 Time evolution of the radius of the vortices 193
4.5.4 Time evolution of the strength of the vortices 198

4.6 The vertical wall case 198
4.6.1 Final distance from the shore-line 201
4.6.2 Speed of the vortices along the shoreline. 201

4.7 Discussion 204

Chapter 5: Comparison with theory 209

5.1 Objectives and structure of the chapter 209
5.1.1 Objectives 209

5.2 Distance of the vortices from the shoreline: the prediction of the inviscid vortex ring model (model 1) 209
5.2.1 Introduction 209
5.2.2 Comparison with theory 212

5.3 Distance of the vortices from the shoreline: the prediction of the model with dissipation (model 2) 217

5.4 Speed of the vortices parallel to the shoreline during their along-shore motion. Comparison with theory 224
5.4.1 Introduction 224
5.4.2 Comparison with vortex ring and Norbury theory 227

5.6 Conclusion 228

Chapter 6: Conclusions 237

6.1 Dispersion 237

6.2 Comparison of theory and observations 238

6.3 Applications and related observations 238

6.4 Directions for further research 239

Appendix 2A 240

2A.1 Boundary layer velocities, volume flux into the bottom boundary layer and vertical velocity 240

2A.2 Vorticity equation. 241

2A.3 Radius of the vortex 243

Appendix 3A ***246***

3A.1 2-D model. Input-output structure 246

3A.2 Dispersion of a group of sign-like vortices far from the boundary 248

3A.3 Plots of dispersion 251

3A.4 Significance tests 260

3A.4.1 2-D model. Comparison between dispersions from the same model 261

3A.4.2 3-D model. Comparison between dispersions from the same model 262

3A.4.3 Comparison between the two models 263

3A.4.3 Comparison between the two models: plots 265

References ***274***

List of figures

1.1 Aerial photograph of river outlet with vortex dipoles..... 2
1.2 Along-shore flow instabilities..... 6
1.3 Aerial photograph of rip currents..... 7
1.4 Stirring action of two point vortices..... 12
1.5 Eruption of the boundary layer..... 18
1.6 Collision of 2-D dipole with wall..... 19
1.7 Point vortex on step-like topography..... 21
1.8 Interacting 2-D dipoles..... 23
1.9 2-D turbulent wake with dipoles..... 24

2.1 Point vortex velocity field..... 27
2.2 Rankine's vortex characteristics..... 31
2.3 Point vortex interacting with rectilinear border (image).... 32
2.4 Stream function of point vortex dipole..... 33
2.5 Dipole interacting with rectilinear boundary (images)..... 34
2.6 Tilted dipole interacting with rectilinear boundary (images) 35
2.7 Curved line vortex geometry..... 38
2.8 Circular vortex ring geometry..... 39
2.9 Stream function of circular vortex ring..... 41
2.10 Circular vortex ring in cylindrical co-ordinates..... 43
2.11 Model of a vortex in a wedge of fluid..... 52
2.12 Array of vortices in a wedge of fluid..... 54

3.1 Array of vortices near a shoreline..... 59
3.2 Illustration of Heun's method..... 64
3.3 Stream function of 20 vortices far from a wall..... 65
3.4 Time evolution of the stream function of 20 vortices..... 65
3.5 Description of the method of the images..... 66
3.6 Collision of a vortex with the boundary..... 68
3.7 Initial condition for numerical experiments..... 70

3.8 Stream function of a vortex ring..... 75
3.9 Conservation of volume of a vortex ring..... 76
3.10 2-D model. Dispersion of vortices..... 82
3.11 2-D model. Dispersion of particles..... 83
3.12 2-D model. Eddy dispersion coefficient for vortices..... 84
3.13 3-D model. Dispersion of vortices..... 85
3.14 3-D model. Dispersion of particles..... 86
3.15 3 D model. Eddy dispersion coefficient for vortices..... 87
3.16 Stream function of 20 vortices..... 89
3.17 2-D model. Dispersion of vortices..... 92
3.18 2-D model. Dispersion of particles..... 93
3.19 2-D model. Dispersion of particles..... 95
3.20 2-D & 3-D model. Dispersion of vortices..... 98
3.21 2-D & 3-D model. Dispersion of vortices..... 99
3.22 2-D & 3-D model. Dispersion of particles..... 100
3.23 2-D & 3-D model. Eddy dispersion coefficients..... 101
3.24 Typical initial condition for numerical experiments..... 102
3.25 Model evolution. Example 1..... 103
3.26 Model evolution. Example 2..... 104
3.27 Model evolution. Example 3..... 106
3.27 Model evolution. Example 4..... 107
3.29 Sketch of dispersion of sign-like vortices..... 109
3.30 Sketch of dispersion of vortices of opposite sign..... 109
3.31 Typical initial condition for numerical experiments..... 111
3.32 Dipole-like cluster of vortices..... 115
3.33 Initial situation and evolution of 10 vortices. Situation I..... 116
3.34 Initial situation and evolution of 10 vortices. Situation I..... 117
3.35 Initial situation and evolution of 15 vortices. Situation II..... 118
3.36 2-D model. Dispersion of vortices and particles. Set 1..... 252
3.37 3-D model. Dispersion of vortices and particles. Set 1..... 253
3.38 2-D model. Dispersion of vortices and particles. Set 2..... 254
3.39 3-D model. Dispersion of vortices and particles. Set 2..... 255

3.40 2-D model. Dispersion of vortices and particles. Set 3..... 256
3.41 3-D model. Dispersion of vortices and particles. Set 3..... 257
3.42 Comparison between the two models. Disp. of vort. Set 1. 266
3.43 Comparison between the two models. Disp. of part. Set 1. 267
3.44 Comparison between the two models. Disp. of vort. Set 2. 268
3.45 Comparison between the two models. Disp. of part. Set 2. 269
3.46 Comparison between the two models. Disp. of vort. Set 3. 270
3.47 Comparison between the two models. Disp. of part. Set 3. 271
3.48 Typical initial condition for numerical experiments..... 127
3.49 2-D model. Dispersion of vortices and particles. 20 vor.... 258
3.50 3-D model. Dispersion of vortices and particles. 20 vor.... 259
3.51 Comparison between the two models. Disp. of 20 vort..... 273
3.52 Comparison between the two models. Disp. of 1800 part. 273

4.1 Working principle of the vortex generator..... 136
4.2 Generation of vortices..... 139
4.3 Schematic of vortex generator..... 141
4.4 Vortex generator..... 141
4.5 Schematic of experimental tank..... 141
4.6 Image of a dipole (fluorescine)..... 145
4.7 Grid of reference..... 146
4.8 Image of a dipole (particles)..... 149
4.9 Path of a dipole (exp. 2)..... 155
4.10 Velocity and vorticity fields (exp. 17)..... 166
4.11 Velocity and vorticity fields (exp. 25)..... 167
4.12 Path followed by the centre of vorticity..... 171
4.13 Paths of the vortices (exp. 17 and exp. 25)..... 172
4.14 Processing of the vorticity field (exp. 16)..... 174
4.15 Path followed by the vortices (exp. 27)..... 175
4.16 Path and velocity of the vortices (exp. 3)..... 177
4.17 Path and velocity of the vortices (exp. 16)..... 178
4.18 Path and velocity of the vortices (exp. 27)..... 179

4.19 Time series of circulation (exp. 16, exp. 19, exp. 25)..... 182
4.20 Time series of radius (exp. 16, exp. 19, exp. 25)..... 184
4.21 Sketch of the final distance of the vortices from shoreline.... 185
4.22 Plot of minimum distance from the shoreline..... 188
4.23 Along-shore velocity of the vortices..... 192
4.24 Time series of radius (exp. 16, exp. 19, exp. 25)..... 196
4.25 Comparison of predicted/observed radius..... 197
4.26 Dissipation ratio..... 200
4.27 Path and radius of the vortices (exp. 15 a)..... 203

5.1 Sketch of a pair of vortex rings..... 211
5.2 Numerical solution of equation 5.2 214
5.3 Final dist. Comparison of observation with theory (eq. 5.2).. 216
5.4 Final dist. Comparison of observation with theory (eq. 5.10) 221
5.5 Final dist. Comp. of obs. with theories (eq. 5.2 and eq. 5.10)223
5.6 Range of Reynolds numbers..... 225
5.7 Speed of the vortices (90^{th} percentile)..... 230
5.8 Speed of the vortices (95^{th} percentile)..... 232
5.9 Speed of the vortices (99^{th} percentile)..... 234
5.10 Dissipation of strength vs R_e 236
5.11 Comparison observ./theory vs R_e..... 236

List of plates

1	Flow evolution, exp.1	152
2	Flow evolution, exp.4	153
3	Flow evolution, exp.5	154
4	Flow evolution, exp.16	158
5	Flow evolution, exp.17b	159
6	Flow evolution, exp.24	160
7	Flow evolution, exp.27	161
8	Flow evolution, exp.15b	162
9	Vertical motions on flat bottom	164
10	Frontal vortex	206

List of tables

3.1 Variations of the Hamiltonian (point vort., prel. exp.)..... 71
3.2 Variations of the Hamiltonian (vort. rings, prel. exp.)..... 80
3.3 Variations of the Hamiltonian (point vort., prel. exp.)..... 96
3.4 Variations of the Hamiltonian (vort. rings, prel. exp.)..... 97
3.5 Initial conditions of main numerical experiments.....112
3.6 Variations of the Hamiltonian for main numerical exp..... 113

4.1 Slope angle/water level (fluorescine exp.).....150
4.2 Water level for vertical wall exp. (particles).....150
4.3 Slope angle/water level (particles exp.)..... 150
4.4 Initial separation and circulation (fluorescine).....181
4.5 Final distance from the shoreline (fluorescine).....186
4.6 Final distance from the shoreline (particles)..... 187
4.7 Along-shore speed (fluorescine)..... 189
4.8 Along-shore speed (particles)..... 190
4.9 Final radius (particles)..... 195
4.10 Dissipation of strength (particles)..... 199
4.11 Summary of vertical wall exp..... 202

5.1 Final dist. From shoreline. Comp. obs./theory (eq. 5.2)..... 215
5.2 Final dist. From shoreline. Comp. obs./theory (eq. 5.10)..... 220
5.3 Vortex ring speed from Norbury (1973)..... 226
5.4 Alongshore speed. Comp. observation/theory. 90th perc..... 229
5.5 Alongshore speed. Comp. observation/theory. 95th perc..... 231
5.6 Alongshore speed. Comp. observation/theory. 90th perc..... 233

3A.4.1 Significance test. Hypothesis 1..... 261
3A.4.2 Significance test. Hypothesis 2..... 261
3A.4.3 Significance test. Hypothesis 3..... 261

3A.4.4 Significance test. Hypothesis 4..... 261
3A.4.5 Significance test. Hypothesis 5..... 262
3A.4.6 Significance test. Hypothesis 6..... 262
3A.4.7 Significance test. Hypothesis 7..... 262
3A.4.8 Significance test. Hypothesis 8..... 262
3A.4.9 Significance test. Hypothesis 8..... 263
3A.4.10 Significance test. Hypothesis 10..... 263
3A.4.11 Significance test. Hypothesis 11..... 263
3A.4.12 Significance test. Hypothesis 12..... 264
3A.4.13 Significance test. Hypothesis 13..... 264

Chapter 1

Introduction and review

1.1 Introduction

Vortical structures in the ocean are ubiquitous and, for example, range from 10^5 m of Gulf-Stream rings and Meddies (e.g. Thorpe, 1998), passing through ~10^1 m for whirlpools in tidal currents (Lugt, 1983) or river outlets (fig. 1), to ~10^{-3} m of the smallest turbulent eddies[1]. In this dissertation we concentrate on vortices that are not affected by the rotation of the planet Earth and on these that are affected by neighbouring topography. Vortices in the near-shore region satisfy our requirements.

The implications of the interaction of vortices with nearby solid boundaries are not fully understood nor is the associated dispersion of vorticity and of

---

[1]The scale at which the turbulent eddies are destroyed by viscosity is called Kolmogorov length scale and is defined as $L_k=(\nu^3/\varepsilon)^{1/4}$ (e.g. Tennekes and Lumley, 1973, p. 20). ν is the kinematic viscosity (ν~10^{-6} m^2 $s^{-1}$for water, see e.g Batchelor, 1967, p. 175) and ε is rate of dissipation of turbulent kinetic energy per unit mass (see e.g. Gill, 1982, p. 76 for a definition). ε can be calculated from the diffusivity, K_p, and from N, the buoyancy frequency, with (e.g. Toole et al, 1994):

$$K_p = 0.25\varepsilon N^{-2}$$

The diffusivity is variable, and some oceanic values are: $K_p=10^{-5}$ m^2 s^{-1} over smooth abyssal plains or in the open ocean pycnocline (Polzin et al, 1997, Ledwell et al, 1993) and $K_p=10^{-2}$ m^2 s^{-1} in the Romanche fracture zone (equatorial Atlantic, Polzin et al, 1996). The average value of $K_p=10^{-4}$ m^2 s^{-1} was given by Munk (1966) from a budget estimate. Typical values of N are: $N=10^{-4}$ s^{-1} in the deep ocean and $N=10^{-2}$ s^{-1} (Thorpe, 1998) in the thermocline. Using the averaged value $K_p=10^{-4}$ m^2 s^{-1} estimated by Munk (1996) for the main thermocline and the corresponding value for N we find $\varepsilon=5$ 10^{-8} m^2 s^{-3}, which gives $L_k=5$ 10^{-3} m.

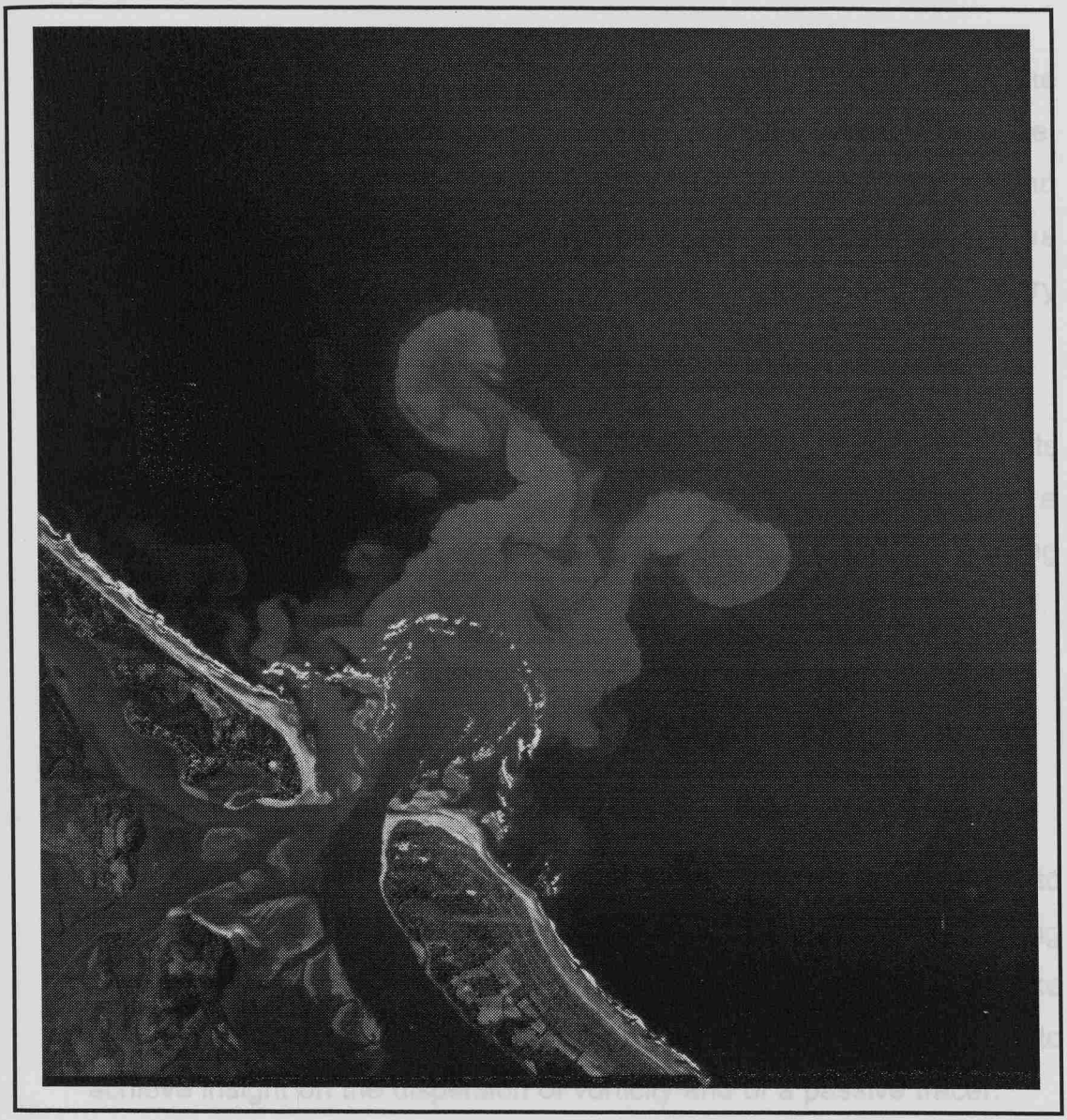

Fig. 1.1: Single vortices and vortex dipoles of different sizes at the outlet of the river Choluteca (Nicaragua) after the flooding caused by the Mitch hurricane. The load of sediments makes the vortices visible (Courtesy of U.S. Geological Survey, EROS Data Center).

passive tracers and sediments. The important role played by the boundaries was postulated for near shore environments (Peregrine, 1996), where vortical structures are sometimes observed (Smith and Largier, 1995, and Dr. J. Smith, 1998, personal communication) as well as for the deep ocean (Thorpe, 1998) where the hypothesis of boundary mixing is still the object of interesting studies (e.g. Polzin et al, 1996).

In this dissertation we concentrate mainly on: a) the dynamical effects induced by a planar sloping bottom, simulating a beach, over which a vortex is moving; b) the dispersion induced by a system of vortices moving over a plane bottom, either horizontal or sloping.

1.2 Objectives

- Improve the analytical tools needed for this research (chapter 2).
- Conduct very simple investigations, with numerical experiments, to study the fate of vorticity and of a passive tracer in a coastal sea having a flat bottom and being bounded by an infinitely long, straight, step-like coastline. The objective in this particular situation (see chapter 3) is to achieve insight on the dispersion of vorticity and of a passive tracer.
- The problem mentioned above is also investigated for a sea in which the seabed is a planar slope. The objective is to compare the results with the flat-bottom case (chapter 3).
- The last objective is to test the validity of an analytical model for vortices over a planar slope. This is done by making physical experiments (chapters 4 and 5) and comparing results with predictions.

This work, although designed for oceanographic applications, contributes to the progress of the branch of fluid mechanics dealing with vortex dynamics.

1.3 Vortices in the surf-zone

The most direct application of this work, and that which stimulated much of our investigation, is the intermediate scale of motions found in and adjacent to the surf zone on a straight beach.

1.3.1 Inverse cascade and instabilities

Surf-zone dynamics has been the subject of an impressive number of works, given perhaps its application to problem of immediate social utility, and significant progresses have been made in the last years (for reviews see e.g. Svendsen and Putrevu, 1996, Arcilla and Lemos, 1990; Battjes 1988). The surf-zone in characterised by a very large input of energy coming essentially from breaking waves: the quasi-regular motion of shoaling waves is converted in a highly disorganised, or turbulent, velocity field (Battjes, 1988). The effect of incident breaking waves is believed to set-up a circulation system made-up mainly by along-shore currents, edge waves and low-frequency waves (Peregrine, 1996).

How are vortices in the surf-zone formed? Peregrine (1996) noted that, since the horizontal length scales of near-shore flows are much bigger than the vertical scales, the flow a few hundred metres off the shoreline can be considered almost two-dimensional and results from theory of two-dimensional turbulence may be applied (if the sea bottom is not too steep). 2-D inverse energy cascade may then be invoked in order to explain the formation of large (~50 m, Dr. J. Smith, 1998, pers. comm.) and coherent vortical structures. Such an inverse cascade has been widely described by laboratory experiments. For example Boubnov et al (1994) reported an inverse energy cascade in a horizontally forced strongly linearly stratified fluid and the subsequent set-up of a large scale flow with length scale of the order of the experimental tank. Fincham et al (1996) used a

rake of flat plates to generate turbulent motion in a linearly stratified fluid. A layered pattern of flat vortices developed. The flat vortical structures forming at different levels were responsible for intense vertical shearing motions that promoted Kelvin-Helmoltz-like instability, ultimately responsible for the layered structure observed after the decay of turbulence. The authors indicate the onset of KHI as the main cause of dissipation of kinetic energy.

A second mechanism responsible for generation of coherent vortical structures in the surf zone was suggested by Bowen and Holman (1989) and by the analysis of field data of Oltman-Shay et al. (1989), who pointed out the existence of oscillatory motion with long-shore wave length of the order of 100 m and period of 100 s. These waves may be regarded as instabilities of the strongly sheared long-shore currents and therefore are called shear waves. A fairly recent review on the subject can be found in Svendsen and Putrevu (1994). The linear perturbation analysis of Bowen and Holman (1989) has demonstrated the vortical character of this wave motion; the numerical solution of the non-linear shallow water equations show that the long time evolution of instabilities is characterised by the presence of coherent vortical structures that often pair together (fig. 1.2) and move away under mutual influence (Dodd et al, 1992; Özkan-Haller et al, 1996; Allen et al. 1996; Slinn et al, 1998).

1.3.2 Rip currents

Rip currents are frequent on oceanic beaches and may be seen by occasional observers: an example is given by the picture taken by Inman (Inman et al, 1971) at Rosarita Beach, Mexico, reproduced here in fig. 1.3. A rip current is essentially a strong, $v > 0.5$ m/s (Tang et al, 1989 a), narrow jet-like flow directed offshore (e.g. Battjes, 1988, Arcilla and Lemos, 1990; Komar and Oltman-Shay, 1991; Svendsen and Putrevu, 1996 Dette et al, 1995). Rip currents are usually visible because of their load of debris and

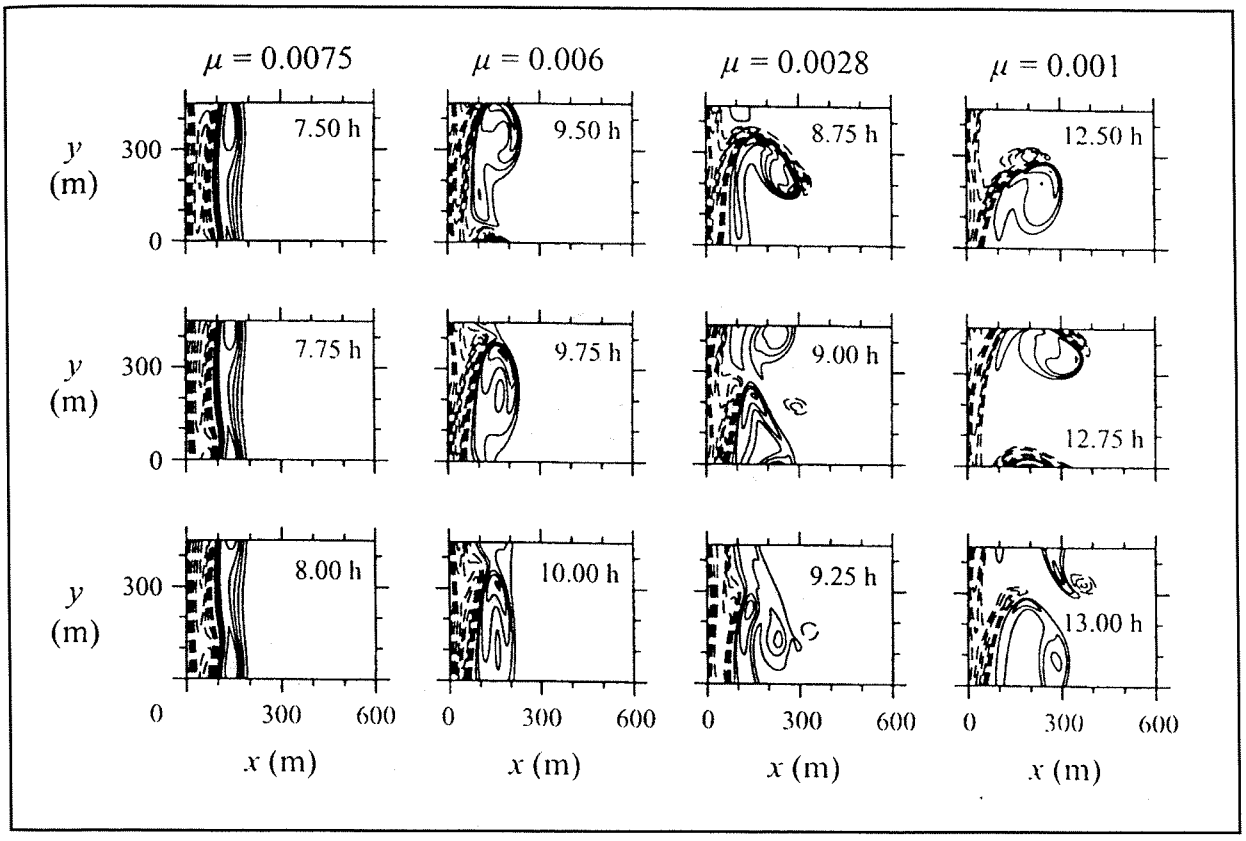

Fig. 1.2: Contour plots of the vorticity field (solid negative, dashed positive) showing instabilities of the along shore flow $V(x)=C_0x^2\exp[-(x/\alpha)^n]$. C_0 and α are chosen so that $V(90)=1$ m s^{-1}. μ is the bottom friction coefficient. $L^{(y)}$ is the along shore scale of the domain, which corresponds to a multiple of the most unstable linear mode of the basic flow V. Time is expressed in hours (rhs upper corner). As the bottom friction increases, dipolar structures form and migrate offshore (from Allen et al, 1996).

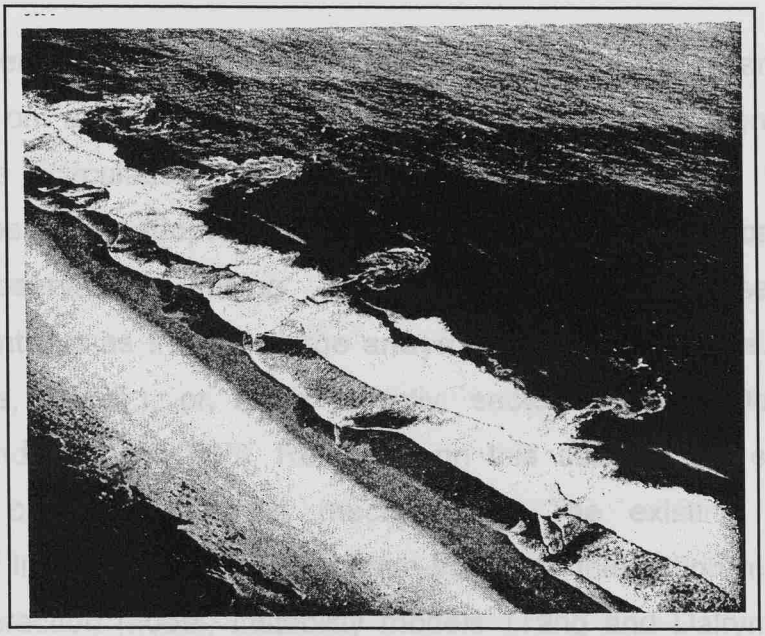

Fig. 1.3: Aerial photograph of surf-zone with evenly spaced rip-currents. The spacing between rip-currents determines the long-shore dimension of the near-shore circulation cell (from Inman et al, 1971).

sediments and because they alter the refraction pattern of incident waves. Rip currents are known to originate at the convergence point of neighbouring near-shore circulation cells (Komar and Oltman-Shay, 1991).

It is not easy to provide a comprehensive set of measurements of rip currents on a natural beach because of the non-stationarity of the nearshore circulation system (Tang and Dalrymple, 1989a): the techniques so far adopted included the use of photographically recorded visual observations (using the suspended load of sediments or fluorescent dye as tracers), large arrays of current meters (e.g. Tang and Dalrymple, 1989b,), or, more recently, sector-scanning Doppler sonar (Smith and Largier, 1995). Research on this subject has so far mainly focused on the generation mechanisms. The existing models are classified in three main groups: wave-boundary interaction models, wave-wave interaction model, instability models (Tang and Dalrymple, 1989a). Despite the large number of studies, few authors have focused their attention on the structure of the head of the rip currents, that often seems to be formed by a vortex dipole (Smith and Largier, 1995). If this would be the case, one would expect that the two vortices, under their mutual interaction would have the tendency to propagate off-shore under their mutual influence (see section 1.4.b) but the dynamics of vortex dipoles propagating over a sloping bottom is a poorly studied subject, but one to which this dissertation will contribute.

The cases described above all involve the motion and interaction of vortices over sloping topography. We shall simulate such motions with point vortices and vortex rings (in way to be described later), testing the validity of the calculations by laboratory experiments. We pave the way to the analysis by giving a brief introduction to vortices (section 1.4) and to their interaction (see section 1.5).

1.4 Point vortices and vortex rings

1.4.1 Point vortices

a. Background

A general description of the powerful concept of a line vortex can be found in many books of introductory fluid dynamics (see e.g. Lamb, 1932, Milne-Thomson, 1949, Batchelor, 1967) or specialised monographs (Saffman, 1992). If the line is straight the vortex is also called a 'point vortex' because the velocity field generated by the vortex is two-dimensional and, in any of the planes normal to the vortex line, is only a function of the strength and of the position of the vortex (see section 2.2 for more details). This very helpful idealisation has stimulated much studies with applications ranging from geophysical fluid dynamics (e.g.: Wang, 1992, Bidlot and Stern, 1994) to the physics of superfluid helium II (Donnelly, 1993, for a review).

The velocity field of a point vortex represents a weak solution of the two dimensional Euler equation because, by definition, it implies the existence of a discontinuity at the point where the vorticity is concentrated (Saffman and Baker, 1979; Aref, 1983)[2]. The Euler equation for a two-dimensional and incompressible fluid, whether the fluid is viscous or not, can be reduced, via the introduction of a stream function, to a Hamiltonian set of canonical equations and the stream function is the Hamiltonian (e.g. Aref et al, 1989). Two dimensionality and incompressibility are the only conditions required. The equations of motion for a system of point vortices in a two-dimensional domain also define a Hamiltonian system, in which

---

[2]A point vortex is defined as a vortex of infinitesimal cross-section, s, where infinite vorticity, ω, is concentrated. The order of the infinitesimal cross-section and of the infinite vorticity must be the same, so that the circulation of the vortex, defined as $\int \omega ds$, is finite (e.g. Batchelor, 1967, pp 93-95).

the number of degrees of freedom equals the number of vortices (Aref, 1983). The Hamiltonian also has the meaning of the interaction kinetic energy of the vortices (e.g. Batchelor, 1967, p. 531).

Several authors have investigated the dynamics of large groups of point vortices and, of these, two examples are reported. Murty and Sankara Rao (1970) discussed the motion of a system of ~40 point vortices, initially coincident with the vertices of a regular polygon, and inside a circular domain with rigid boundaries. After a non-dimensional time[3] $\tau>>1$ the vortices became uniformly distributed and their average separation was almost constant with time. Kuwahara and Takami (1973) used a system of discrete point vortices to model: a) the motion of a vortex tube with elliptical cross-section; b) the roll-up of a vortex sheet of finite length. To reduce what they called the 'randomisation of vortices', probably caused by the discontinuities associated with the point vortices, they used an artificial viscosity to decrease the circulation of the vortices with time.

The integrability (i.e. the possibility of calculating an analytic solution) of the motion of a system of point vortices in an unbounded domain is an important subject to which reference is required here. A discussion can be found in Aref (1983) and in Aref et al (1989). It is easy to show that the equation of motion of one or two point vortices in an unbounded domain can be integrated (e.g. Batchelor, 1967). Novikov (1975) showed that the problem of three identical point vortices in an unbounded fluid can also be integrated. This system exhibits the tendency, a feature of two-dimensional turbulence, for energy transfer towards small wave numbers, i.e. towards large spatial scales. In general the motion of three vortices in an unbounded fluid is integrable (Aref, 1983). The motion of four point vortices

---

[3]Time was made non dimensional with the ratio Γ/L, where Γ is the strength of the vortices and L is a length scale of the problem.

in an unbounded domain is in general non-integrable[4] (Novikov and Sedov, 1978; Aref and Pomphrey, 1982, Aref, 1983). If solid boundaries are present, analytical solutions may not exist even if the number of vortices is smaller than 4 (Aref, 1983). In such cases a symmetry of the system may determine its integrability (e.g. section 2.2.2.b). Aref et al (1989) point out that in some special situations, namely the motion of one point vortex in a domain enclosed by solid boundaries, which is an integrable problem, the Eulerian velocity field at any point in the domain is periodic while the displacement of a particle of fluid may show a chaotic behaviour. The problem of three equal point vortices in an unbounded fluid is also regular but the motion of an advected particle (e.g. a fourth vortex with zero circulation) is chaotic (Aref, 1983). As noted by Aref (1983) a system with 3 vortices (i.e. of order 3) is the lowest order configuration capable of exciting different scales of motion (where by scale of motion is intended the characteristic distance between the vortices).

An analytical and numerical study (Meleshko and Gurzhi, 1994) discussed the stirring properties of two and three point vortices in an unbounded domain and showed the existence of non stirred portion of the fluid imbedded in the otherwise well mixed regions. Boffetta et al (1996) considered the advection of a passive tracer in a circular domain by two point vortices. They found that the motion of the advected particles was always regular near the vortices. Like Meleshko and Gurzhi (1994), they also found 'islands' (fig.1.4) i.e. regions where the fluid is not stirred. The size of the islands was similar to the minimum separation of the vortices.

b. Presence of boundaries: the method of images

The velocity field generated by a system of point vortices in a bounded two-dimensional domain can be calculated by using the method of images. The method, also widely used in electro-magnetism, consists of extending

[4]But there are some exceptions, see e.g. section 2.2.2.b.

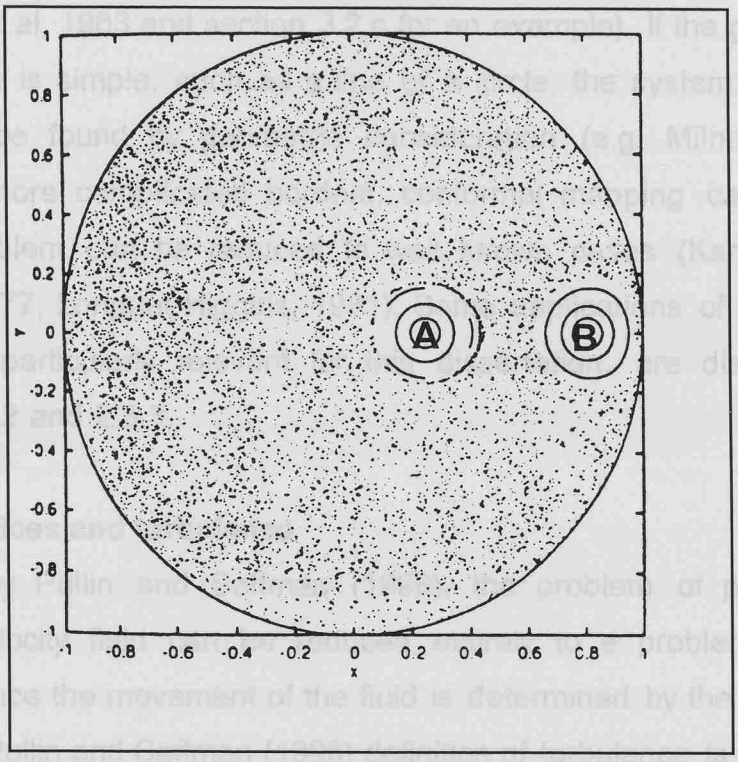

Fig. 1.4: Figure showing the stirring action of two equal point vortices, A and B, free to move in a frictionless circular domain. The dots represent the trajectory of one particle whose motion is induced by the vortices. The dots cover the area almost uniformly apart from two nearly-circular regions (islands) around the vortices. The motion there is regular, which means that the particle cannot cross the closed streamlines, which must be stationary (from Boffetta et al, 1996).

the physical domain beyond the boundaries and adding, outside of the physical domain, a distribution of vorticity that would satisfy the boundary conditions[5] if the boundaries were still present (e.g. Saffmann, 1992; Feynmann et al, 1963 and section 3.2.c for an example). If the geometry of the boundary is simple, such as a line or a circle, the system of images can easily be found by geometric consideration (e.g. Milne-Thomson, 1949). For more complicated borders, conformal mapping can be used and the problem can be reduced to well known cases (Karweit, 1975; Sheffield, 1977; Longuet-Higgins, 1981). Some applications of the method of images, particularly relevant for this dissertation, are discussed in sections 2.2.2 and 2.3.3.

c. Point vortices and turbulence

As stated by Pullin and Saffman (1998), the problem of predicting a turbulent velocity field can be reduced entirely to a problem of vortex dynamics since the movement of the fluid is determined by the distribution of vorticity. Pullin and Saffman (1998) definition of turbulence is focused on the randomness and unpredictability of the three dimensional velocity field for which solutions of the Navier-Stokes equations are not available. This statement can be applied to a two-dimensional flow (although such a view can be misleading since turbulence is generally three dimensional; Aref, 1983). On the other hand the restriction to two dimensions and the hypothesis of incompressibility allow the use of a stream function and of a particularly simple form for the vorticity equation and is of particular value when one component of the motion is suppressed, for example by boundaries (fig. 1.5) or stratification (fig. 1.6). If the fluid is also non-viscous the two dimensional Navier-Stokes equations reduce to the Euler equation, for which the kinetic energy of the system and the vorticity along the paths of fluid particles are conserved (e.g. Monin and Ozmidov, 1985;

[5]For example, the free slip boundary condition require that the component of the velocity normal to the boundary must vanish at each point of the boundary.

Batchelor, 1967). It follows that the enstrophy (one-half of the vorticity squared) must also be conserved along particle paths (Monin and Ozmidov, 1985).

Although two-dimensional turbulence is still far from being fully tractable and, following Frisch (1995), it might be regarded just as a "toy model ... easier to analyse and certainly easier to simulate and to visualise than three-dimensional turbulence", it is helpful in understanding some features of some geophysical flows. The evolution of a 2-D velocity field of an inviscid, homogeneous and incompressible fluid can be investigated by approximating the continuous distribution of vorticity with point vortices (see e.g. Milinazzo and Saffman, 1977, who study the decay of a circular vortex with this method or Siggia and Aref, 1981, who simulate a $k^{-5/3}$ inverse energy cascade with a system of point vortices). It is not clear whether the solutions obtained with those methods converge to the solution of the continuous Euler equations (Saffman and Baker, 1979) but there are some indications (Robert and Sommeria, 1991; Frisch, 1995) that a "quasi-inviscid" equilibrium theory, that prescribes the conservation of "macroscopic" vorticity and the decay of "macroscopic" enstrophy for a non-dissipative system of point vortices, might justify such an approach (the term "macroscopic" refers to the value of the quantity calculated at each point of the domain from the probability density function of all the possible realisations, or "microscopic" states, which are compatible with the energy constraint).

1.4.2 Vortex rings

A circular line vortex is called a vortex ring. There is an abundant literature on this subject, including theoretical, experimental and numerical work. Axisymmetric vortex rings have been studied extensively in the last century because of Kelvin's idea of vortex ring atoms, and more recently because

of a number of engineering and physical applications (for a review see Shariff and Leonard, 1992). For the purposes here we do not need to review this broad part of the fluid dynamics literature extensively and it will suffice to quote some of the classical results available in many fluid dynamics textbooks (e.g. Lamb, 1932; Batchelor, 1967), monographs (Saffmann, 1992) and some research papers.

A good account of the problems connected with the dynamics of a line vortex of general shape, infinitesimal cross section and non-zero circulation can be found in Batchelor (1967). If the vortex line is circular it progresses along its axis of symmetry with an infinite self-induced velocity and without deformation. The velocity field generated by a circular vortex ring is axisymmetric too and is described by a Stokes stream function (e.g. Lamb, 1932, art. 161). The speed of thin-cored rings has been investigated by several researchers over more than a century and a summary is given in chapter 10.2 of Saffman's monograph (Saffman, 1992, pp. 195-201). Fraenkel (1972) used the cross section parameter ε (i.e. a non-dimensional measure of the radius of the core, see section 2.3.1, formula 2.28) to derive an expansion scheme for thin cored rings with arbitrary distribution of vorticity. In particular, the case of a uniform distribution of vorticity inside the core was studied to provide a set of formulae that are thought to be valid for quite a substantial range of the parameter ε. The validity of these parametric expressions was subsequently investigated numerically and confirmed by Norbury (1973) who compared them with some asymptotic results, such as the Hill's spherical vortex, which represents the member of the family with the largest value of ε ($=2^{1/2}$).

Vortex rings have been created and studied in laboratory as shown by the beautiful images contained in Van Dyke's book (Van Dyke, 1982). Maxworthy (1974, 1977) gives a good description of experimental techniques for producing turbulent vortex rings and measuring their characteristics. A number of research works have used laboratory

experiments to address the development of turbulent motions as a result of unsteadiness of the vortex core. A review on this topic (Shariff and Leonard, 1992), suggests that the general tendency is for turbulent motions to be suppressed in the core of the vortices.

1.5 Vortex/boundary and vortex/vortex interactions

Our interest is in the effect of a vertical wall (in an ideally two-dimensional situation) and of a sloping bottom on the motion of one vortex or a group of vortices. Therefore we describe what is known of vortex/boundary and vortex/vortex interactions, but restricting the search to the topics that are of immediate concern and relevance.

a. Vortex/boundary interactions

A review on vortex interaction with walls can be found in Doligaski et al (1994). For our purposes this work covers the topic of two-dimensional vortex interactions. The motion of a two dimensional vortex in the presence of a vertical boundary can be described with the method of images (see also section 1.4.1.b). A point vortex of strength Γ and at a distance b from a rectilinear boundary will move parallel to it at speed $\Gamma/4\pi b$ (Saffman, 1992, p.119). The behaviour of 2-D vortices interacting with a straight boundary was investigated experimentally by Barker and Crow (1977). In their experiments a vortex dipole was generated in a non-rotating tank. The path of the dipole was directed at a right angle towards a wall. The trajectories of the vortices were found to differ from the theoretical predictions of the potential theory. The vortices were found to remain at a larger distance from the vertical boundary and to move away from it driven by secondary vortices (but this explanation is not given by the authors of the paper). The loss of circulation of the dipole was found to be about 20 %.

If a two-dimensional viscous vortex interacts with a straight boundary a secondary counter-rotating vortex develops in the boundary layer near the wall because of an adverse pressure gradient maintained by the main vortex. The final stage of this process is an eruption of the boundary layer in the form of a tiny filament that culminates with the formation of another vortex far from the boundary. The strength of the secondary vortex is comparable with the circulation of the main one and the two vortices interact in an almost inviscid manner. This problem was investigated by Peridier et al (1991 a) in the limit of infinite Reynolds number (fig. 1.5). For finite Reynolds numbers, the time for the onset of the breakdown is less than for the previous case and decreases with the Reynolds number (Peridier et al, 1991 b).

The collision of a two-dimensional dipole with a vertical wall in a linearly stratified salt solution was studied by van Heijst and Flor (1989 a, b). As the dipole approached the boundary the vortices moved apart and along the wall. Secondary vortices generated at the boundary interacted with the two main vortices to form two unbalanced dipoles that followed a curved trajectory in the direction of the original path of incidence. The two secondary vortices then paired together and moved away from the wall while the original dipolar structure was reassembled and headed again towards the wall for a new collision (fig. 1.6). Jimenez and Orlandi, 1993, studied numerically the evolution of a vortex layer near a free-slip wall: they observed the break-up of the layer in coherent vortices propagating along the wall. The case in which a vortex dipole interacts with a free surface, which bears some similarity with a head-on collision with a vertical wall, was investigated, among the others, by Barker and Crow (1977) with physical experiments, with numerical techniques by Telste (1989) and by Yu and Tryggvason (1990) for inviscid fluid and by Ohring and Lugt (1991) in the viscous case, and analitically by Tyvand (1991). The problem of a dipole rising obliquely in a non viscous fluid has been studied by Lugt and

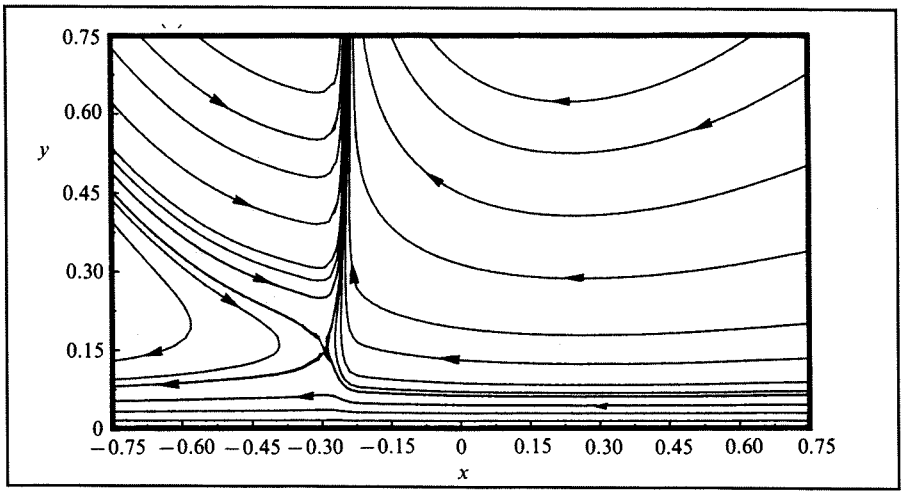

Fig. 1.5: Instantaneous streamlines pattern erupting from a highly sheared boundary layer induced by a two dimensional vortex near an infinite planar wall (coincident with the x-axis). This mechanism is probably responsible for the generation of secondary vortices as the main flow interact with the boundary (from Peridier et al, 1991 a).

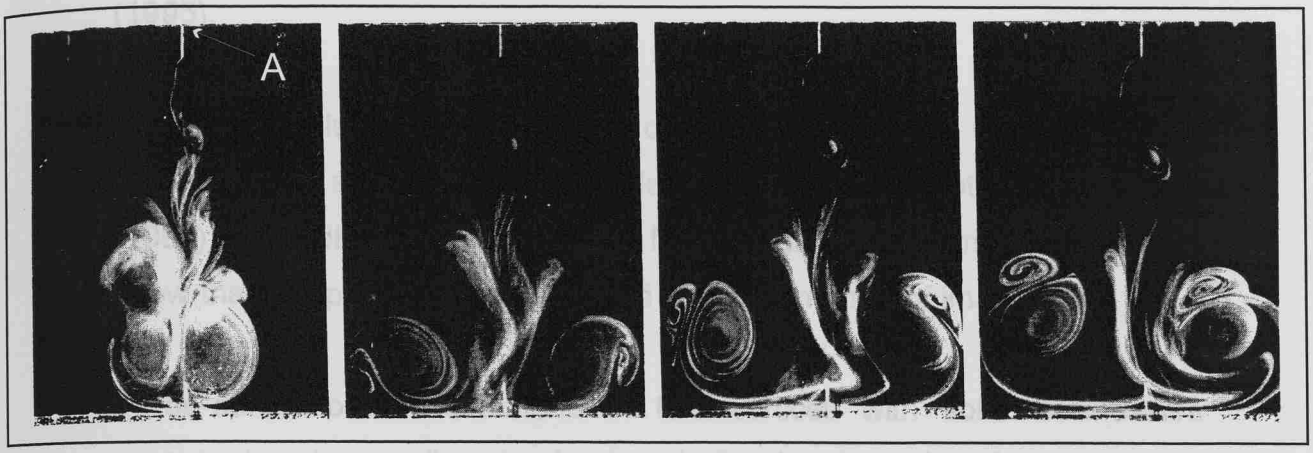

Fig. 1.6: Sequence of plan-view photographs showing the evolution of a dipole colliding against a solid wall (at the bottom of each picture). The vortices were two dimensional and were obtained by injecting dyed fluid in a linearly stratified fluid from location A. The density of the injected water was matching the density of the fluid at the level of injection. The formation and the driving effect of the secondary vortices can clearly be seen (from Van Heijst and Flor, 1989).

Ohring (1992). A brief review on this topic can also be found in Thorpe (1995).

A particular solution of the problem of a vortex interacting with a step-like topography in a otherwise unbounded fluid has been obtained by Wang (1992) and Bidlot and Stern (1994) for the point vortex limit. The authors show that this problem can be solved with the method of images (fig. 1.7).

Three-dimensional interactions of line vortices with solid boundaries represents a less well understood part of vortex dynamics. Apparently, the situation of a line vortex intersecting an infinite boundary at angles different from 90° has been investigated on very few occasions. We will address this problem again in section 2.3.3. Affes et al (1993) studied the interactions of a thin cored line vortex with a cylindrical body. From the numerical solution of the equations of motion they found that the vortex is subject to a three dimensional distortion and calculated the vortex self-induced velocity.

b. Vortex/vortex interactions

The mutual interaction of quasi two-dimensional vortical structures is discussed in Voropayev (1989) and van Heijst and Flor (1989 a, b). In the case of dipole/dipole collisions the main conclusion is that vortices interact in a way that preserves the total momentum and the total vorticity of the system. Dipoles can exchange their partners, appear to be very robust structures and the exchange of mass between vortices seems to be negligible (fig. 1.8). Voropayev et al (1992) also give an estimate of the radius of the dipole as a function of time, ambient stratification and characteristic parameters of the source of momentum.

Couder and Basdevant (1986) used thin liquid films (a solution made up mainly of water, soap and glycerol) to generate a von Kármán vortex street.

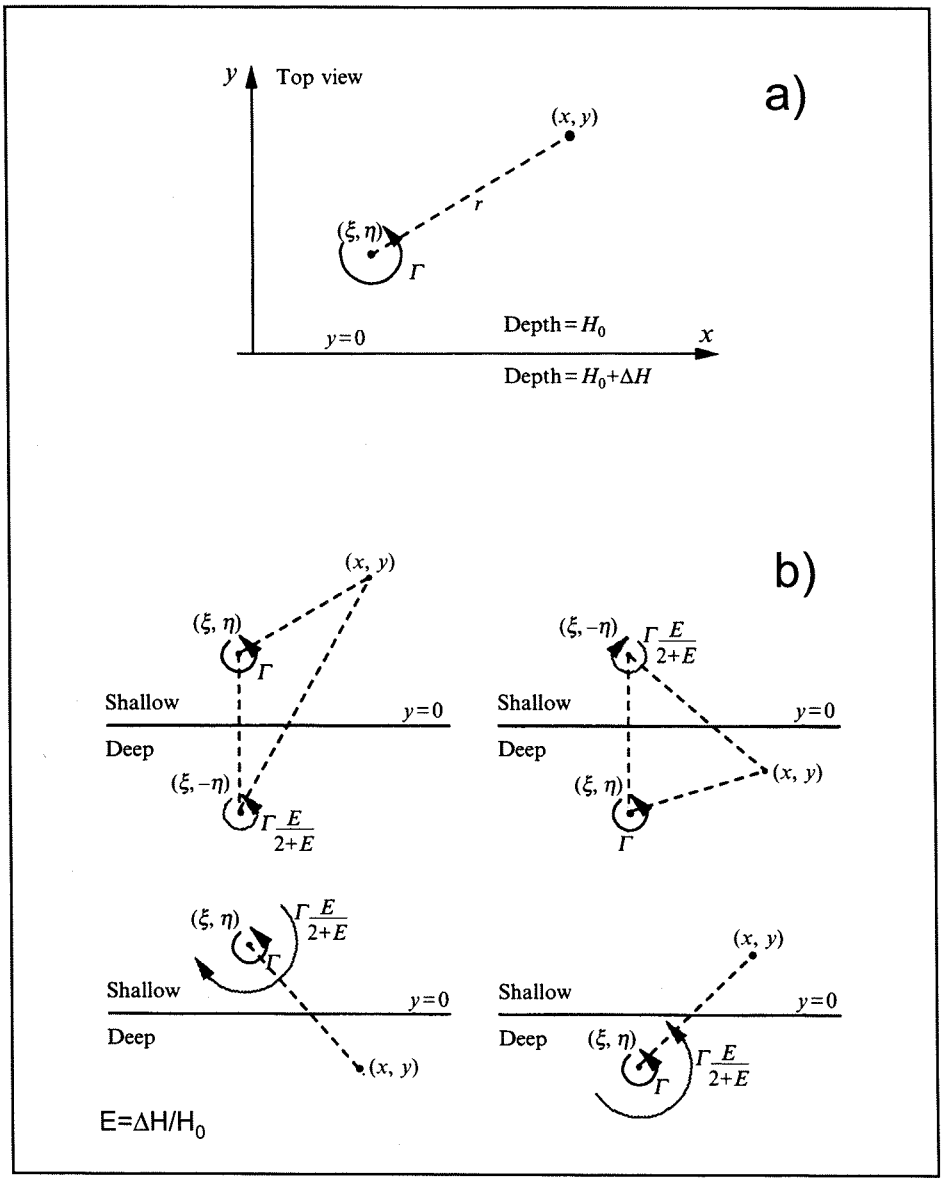

Fig. 1.7: a) A point vortex of strength Γ is located on one side of an escarpment (y=0) modelled by two regions of constant depth. b) The flow field for the escarpment problem is equivalent to a constant depth problem in which an image vortex (light arrow) is introduced to account for the step-like topography. The correction due to the presence of the escarpment ...can be viewed as a point vortex of strength Γ[E/(2+E)]sgn(y) located at (ξ,-ηsgn(η)). Four locations of the latter are possible depending on the relative position of both forcing and the point of interest as shown above (From Bidlot et al, 1994).

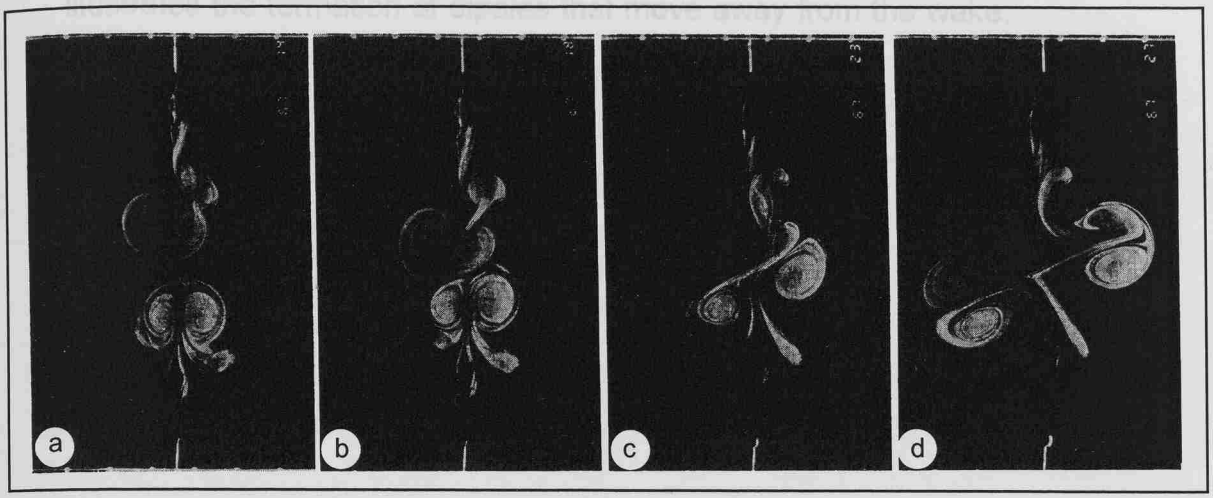

Fig. 1.8: Head-on collision of nearly two-dimensional and almost equal vortex dipoles. Note that an exchange of partners is taking place (from Van Heijst and Flor, 1989).

Their set of photographs (one of these is reproduced here in fig. 1.9) nicely illustrates the formation of dipoles that move away from the wake.

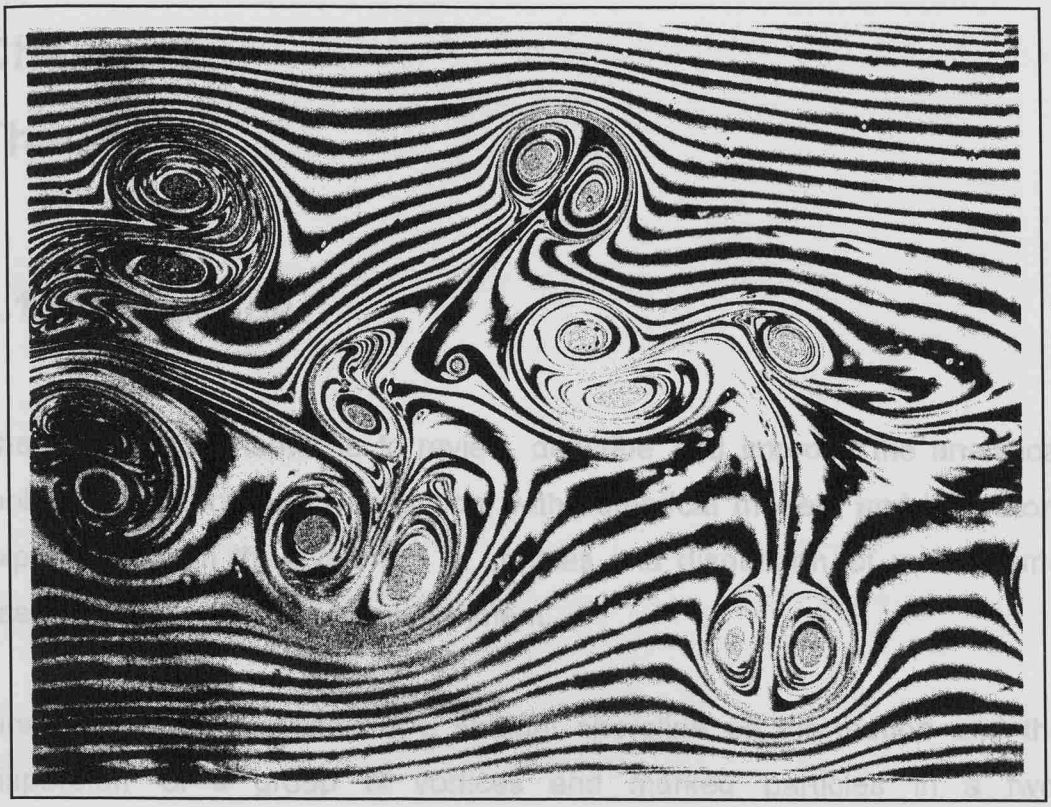

Fig. 1.9: Vortex dipoles formed in a turbulent wake. The flow is two-dimensional (thin film of soap Glycerol and water). From Couder and Basdevant, 1986.

Chapter 2

Theory

2.1 Introduction

The aim of this chapter is to review, describe and improve the analytical tools we need for our investigation, with numerical models and laboratory experiments, on the dynamics of vortices and dispersion of vorticity and passive tracers in a shore environment.

Firstly, we study the effect of a straight shoreline on the motion and the dispersion of a group of vortices and marked particles in a two-dimensional situation, i.e. with a flat free-slip bottom. The related numerical experiments, which are presented in chapter 3, will use modified point vortices and, therefore, some details of the dynamics of a cloud of point vortices and the resulting advection of passive particles are given in section 2.2.1. The already known implications resulting from the presence of an infinite straight boundary are reported in section 2.2.2.

The second situation, in which the vortices are moving over a planar slope, requires an extension to three dimensions. The motion of vortices and marked particles is studied in chapter 3 with a model that uses circular vortex rings. Vortex rings are therefore introduced in section 2.3.1 and the numerical model is described in section 2.3.3.

The spin-down problem for an isolated vortex on a flat bottom is reviewed in section 2.4.

This chapter forms the basis for the discussion of our physical experiments (chapters 4 and 5) that aim at describing the dynamics of vortices interacting with a planar sloping bottom.

2.2 The point vortex model

2.2.1 Background

A line vortex is usually defined as a curve, in the three-dimensional space, on which a singular distribution of infinite vorticity is concentrated: the flux of the vorticity (called strength), calculated for any surface that intersects the line vortex only once, is finite. The velocity field induced by the vortex at any point in the space not coincident with the line can be calculated with the Biot-Savart law (e.g. Lamb, 1932, Batchelor, 1967).

When the line is straight the situation is remarkably simple: if we refer to a Cartesian frame of reference, (x,y,z), and we suppose that the vortex is parallel to the z-axis, the resulting velocity field is two dimensional and equal in all the planes z=const. (figure 2.1).

Since the velocity field is two-dimensional it is common practice to call straight-line vortices 'point vortices' (see e.g. Saffman, 1992). Figure 2.1 shows that the streamlines associated with point vortices are circular with the common centre coincident with the position of the vortex. The speed of the fluid is proportional to 1/l, where l is the distance from the vortex. It follows that a three-dimensional system of parallel line vortices is equivalent to a two-dimensional system of point vortices because the total velocity field has no components along the direction of orientation of the lines and the vortices will therefore remain parallel to each other throughout the evolution of the system.

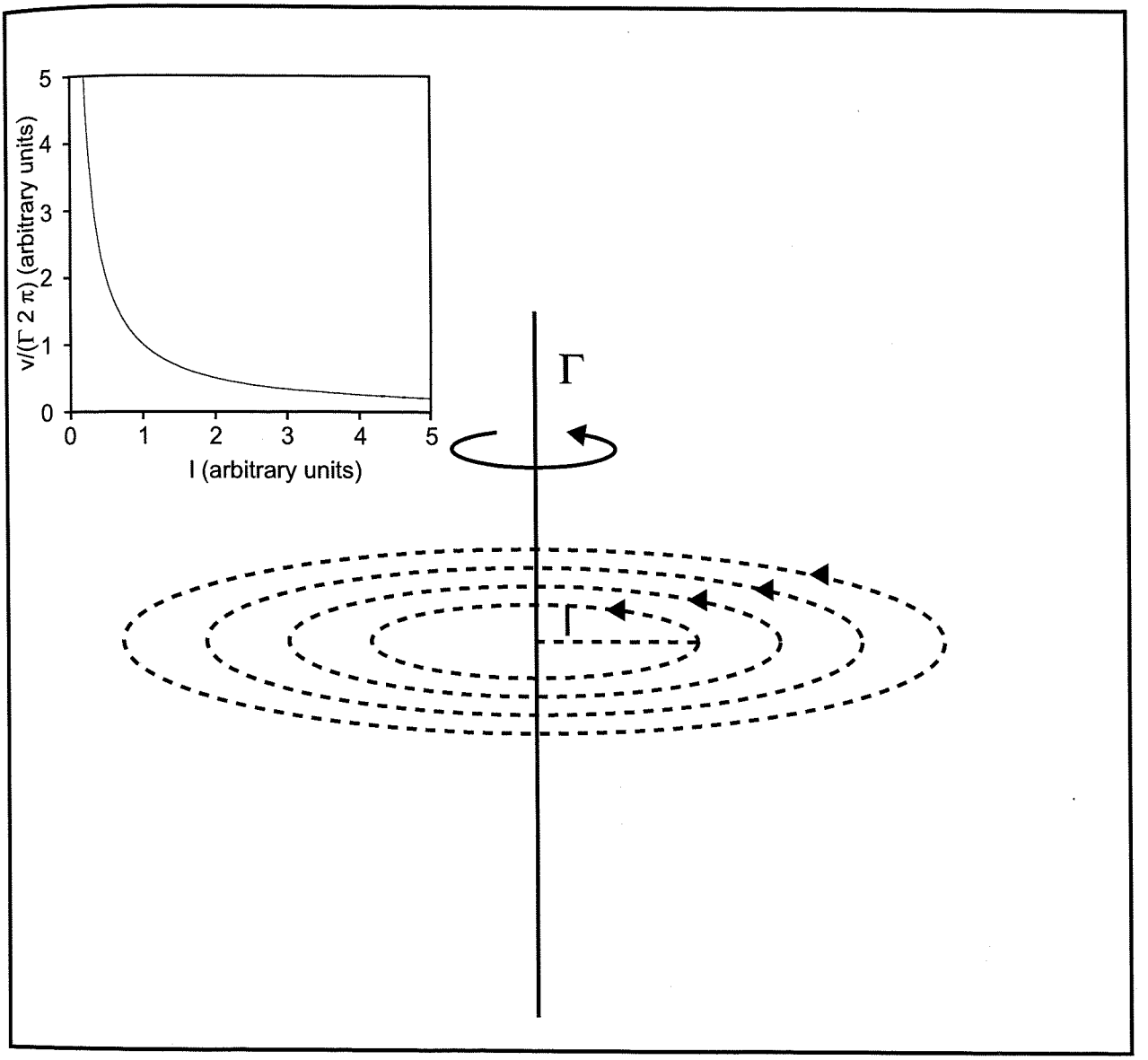

Fig 2.1: The velocity field generated by a straight line vortex of strength Γ is two dimensional and is contained in a plane perpendicular to the vortex line. In any of these planes, the velocity at a distance l from the vortex is given by: $v=\Gamma/(2\pi l)$ (see plot in the upper left corner) and is tangent to the dashed lines.

The velocity field at the point (x,y) induced by a group of n vortices with centre co-ordinates at (x_i,y_i), i=1,...,n, can be described with the stream function

$$\psi(x,y) = -\frac{1}{4\pi}\sum_{i=1}^{n}\Gamma_i \log\left[(x-x_i)^2+(y-y_i)^2\right], \qquad (2.1)$$

where Γ_i is the strength of the i^{th} vortex (see e.g. Batchelor, 1967, p. 530); the presence of the logarithm in equation 2.1 requires that the conditions $x\neq x_i$ and $y\neq y_i$ (i=1,...,n) are satisfied. The total velocity field is the superposition of the velocities induced by each vortex. The velocity at the position (x,y) is obtained by differentiating 2.1 (Batchelor, 1967, p. 530),

$$u = \frac{\partial\psi}{\partial y} \quad \text{and} \quad v = -\frac{\partial\psi}{\partial x}, \qquad (2.2)$$

e.g., explicitly, from 2.1,

$$u = -\frac{1}{2\pi}\sum_{i=1}^{n}\Gamma_i\frac{(y-y_i)}{l_i^2}, \qquad (2.3\ a)$$

$$v = \frac{1}{2\pi}\sum_{i=1}^{n}\Gamma_i\frac{(x-x_i)}{l_i^2}, \qquad (2.3\ b)$$

where

$$l_i = \sqrt{(x-x_i)^2+(y-y_i)^2}. \qquad (2.4)$$

Here l_i is the distance between the i^{th} vortex and the point (x,y). The velocity of the j^{th} vortex induced by all the others can still be expressed with formulae 2.3 a and b by substituting (x,y) with (x_j,y_j), the summation being

now restricted to the couple of indices that satisfy the condition $j \neq i$, meaning that the j^{th} vortex does not influence itself.

It is useful to define the following quantity, which has the same formalism of the centre of mass, using the vortex strength (Batchelor, 1967, p. 530):

$$X\sum_{i=1}^{n}\Gamma_i = \sum_{i=1}^{n}\Gamma_i x_i, \qquad Y\sum_{i=1}^{n}\Gamma_i = \sum_{i=1}^{n}\Gamma_i y_i. \tag{2.5 a,b}$$

X and Y, as defined by 2.5 a and b, have the meaning of co-ordinates of the centre of vorticity.

Another quantity, D, with the meaning of the dispersion of vorticity about its fixed centre, is defined by:

$$D^2\sum_{i=1}^{n}\Gamma_i = \sum_{i=1}^{n}\Gamma_i\left[\left(x_i - X\right)^2 + \left(y_i - Y\right)^2\right]. \tag{2.6}$$

When defined, i.e when $\sum\Gamma_i \neq 0$, X, Y and D are constant throughout the evolution of the system (Batchelor, 1967, p. 530). Another invariant of the motion, with the meaning of the interaction kinetic energy of a system of point vortices, is given by (Batchelor, 1967, p. 531):

$$W = -\frac{1}{4\pi}\sum_{i=1}^{n}\sum_{j(\neq i)=1}^{n}\Gamma_i\Gamma_j \log l_{ij}. \tag{2.7}$$

W is the part of kinetic energy that depends on the relative position of the vortices and not the total kinetic energy of the system[6]. While calculating the numerical solutions of the motion of a system of point vortices the

[6]The kinetic energy of an isolated point vortex is infinite since the velocity varies as l^{-1}, and so is the total kinetic energy of a group of vortices.

constancy of X, Y, D and W can be used to estimate the accuracy of the numerical scheme (i.e. the errors introduced by the machine round-off and by approximating the derivatives by means of finite differences).

These conservation laws have a more profound implication: the case of a group of equal point vortices interacting in an unbounded infinite plane is a bounded system in the sense that, at any time, the characteristic dimension of the cloud of vortices is of the same order as its initial value (Batchelor, 1967; Viecelli, 1993).

The stream function of n point vortices has n singularities and this leads to numerical difficulties when two or more vortices approach within an infinitesimal distance, for then their velocities tend to infinity as the distance from the centres tends to zero. This can be readily seen from the formulae 2.3 a and b. A modified stream function can be used to bypass this problem. Consider the stream function where the spatial dependence is confined to the general term $F(r_i)$:

$$\psi(x,y) = -\frac{1}{2\pi}\sum_{i=1}^{n}\Gamma_i F(r_i). \qquad (2.8)$$

Using the notation proposed by Milinazzo et al (1977) we can write:

$$F(r_i) = \begin{cases} \log\left(\frac{l_i}{r_i}\right) & l_i \geq r_i, \\ \frac{1}{2}\frac{l_i^2}{r_i^2} & l_i < r_i. \end{cases} \qquad (2.9)$$

The function 2.9 describes a Rankine's vortex, i.e a disc of fluid of radius r_i rotating as a solid body with constant angular velocity Ω; as before l_i is the distance from the centre of the vortex. We see from formula 2.9 that when $l_i > r_i$, the dependence of the velocity from r_i is the same as for a point vortex

with the same strength. Vorticity, strength and velocity of a Rankine's vortex as a function of l are shown in fig. 2.2. Note that the vorticity is constant and is twice the rotation rate.

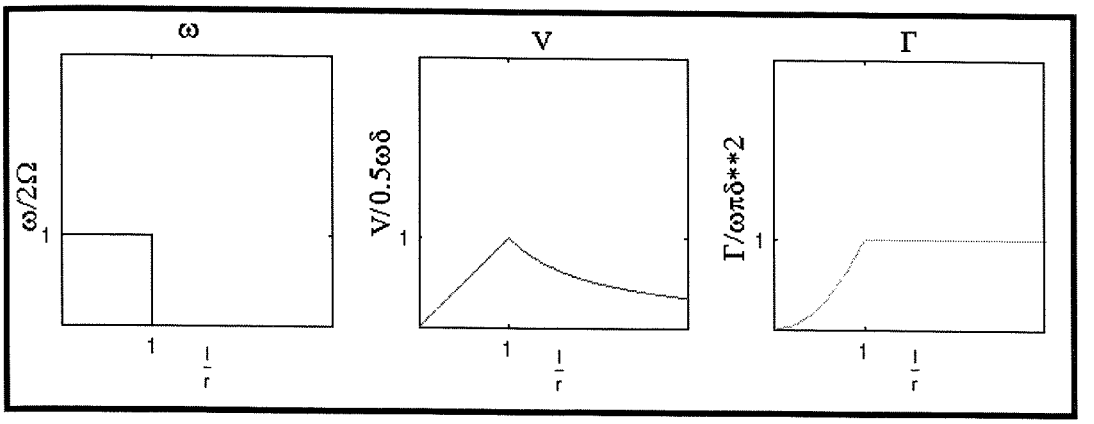

Fig. 2.2: Non-dimensional vorticity (ω), velocity (V) and strength (Γ) for a Rankine's vortex plotted versus the non-dimensional distance from the vortex centre.

Like the point vortex, a Rankine's vortex can only be regarded as an highly idealised model since, for real fluids, the velocity must go to zero within a finite distance from the vortex centre and the functional form as l^{-1} cannot apply to real vortices. Different functional forms for the stream function were used by other investigators. For example Kuwahara et al (1973) defined:

$$F(l_i) = \frac{1}{l_i}\left(1 - e^{\left(-\frac{l_i^2}{4\nu t}\right)}\right). \qquad (2.10)$$

Here ν plays the role of an artificial viscosity with the role of damping the velocity within a short distance from the core.

The introduction of cores with finite radius leads to considerations on the fate of vortices approaching close to one another. With the model proposed above any deformation of the core of the vortex is excluded.

2.2.2 Vortices in a semi-infinite plane

a. Point vortex interacting with a straight boundary

In chapter 1 we briefly mentioned that the problem (e.g. Batchelor, 1967) of a point vortex near a straight boundary, or "wall", (figure 2.3.a) can be solved with the method of the mathematical images. To satisfy the kinematic boundary condition an image vortex of equal strength and opposite sign must be introduced at the symmetric position of the vortex with respect to the wall, which can be removed. The equivalent system is therefore a vortex dipole (i.e. a pair of vortices of opposite sign, see fig. 2.3.b) that moves in the direction parallel to the wall with speed

$$v_x = \frac{\Gamma}{2\pi s}, \qquad (2.11)$$

where Γ is the vortex strength and s/2 is the distance of the vortex from the wall.

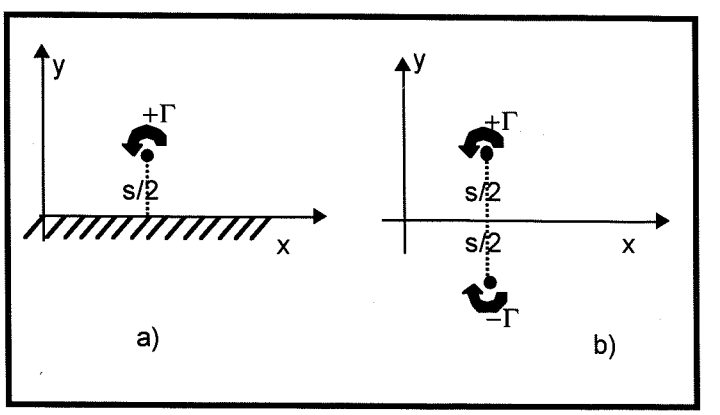

Fig 2.3: A point vortex interacting with a straight boundary (a) is equivalent to a vortex dipole (b) with the wall removed. The axis of the dipole is coincident the boundary.

The stream function of the dipole is shown in figure 2.4 (in a frame of reference coincident with the centre of the dipole and moving with it).

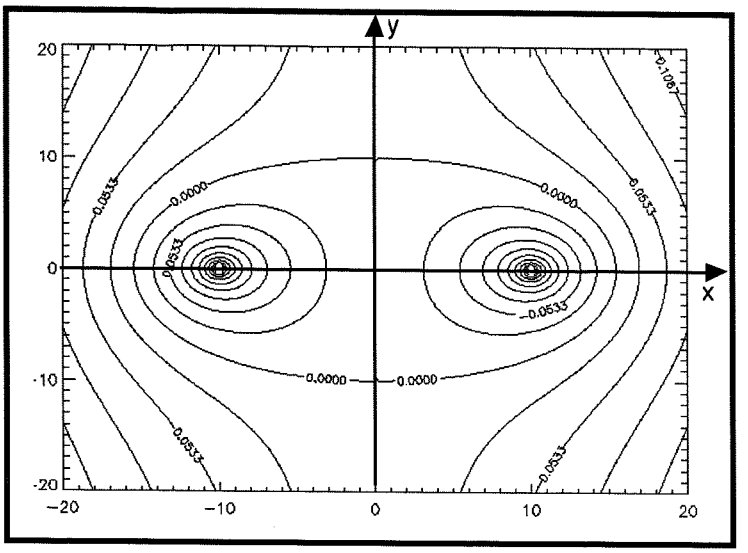

Fig. 2.4: Stream function of a vortex dipole. The positive vortex is now on the lhs. A rigid boundary can be introduced at the y-axis without modifying the flow. The oval bounded by the zero streamline is called recirculation cell. The frame of reference is moving with the dipole.

The oval bounded by the zero stream-line is usually called recirculation cell because the fluid contained inside is rotating around the two vortices and moving with them without escaping from this region. This is an important mechanism of transport, as we shall see in chapter 3.

b. Vortex dipole interacting with a straight boundary

An analytic solution of the equation of the path followed by a vortex dipole, when the line passing through the two vortices is parallel to the wall (fig. 2.5.a) can be found in Lamb (1932). If the mathematical images are introduced the system is equivalent to a vortex quadrupole (see previous section and fig. 2.5.b). In many text books the equation of the path is obtained by direct solution of the equation of motion (Lamb, 1932).

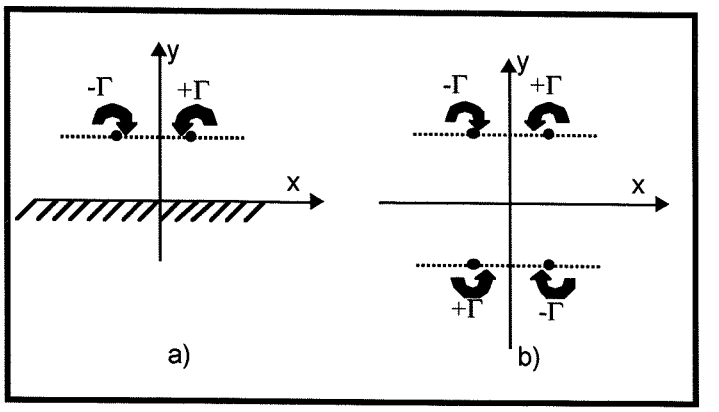

Fig. 2.5. Vortex dipole interacting with a straight boundary (a) and equivalent system (b).

An alternative way to calculate the equation of the path is to use the conservation of the interaction kinetic energy (relation 2.7) of the equivalent system. If the dipole is initially at an infinite distance from the boundary and the separation of the vortices is s, the initial total interaction kinetic energy is given by:

$$W_{tot} = \frac{1}{\pi}\Gamma^2 \log s \,. \qquad (2.12)$$

At a finite distance from the wall, relation 2.7 becomes:

$$W_{tot} = \frac{1}{\pi}\Gamma^2 \log 2x + \frac{1}{\pi}\Gamma^2 \log 2y - \frac{1}{\pi}\Gamma^2 \log 2\sqrt{x^2+y^2} \,. \qquad (2.13)$$

Because W_{tot} is constant, equating 2.12 and 2.13 we obtain:

$$4x^2y^2 = s^2(x^2+y^2). \qquad (2.14)$$

A situation in which one of the axis of the dipole is tilted with respect to the boundary is shown in figure 2.6.

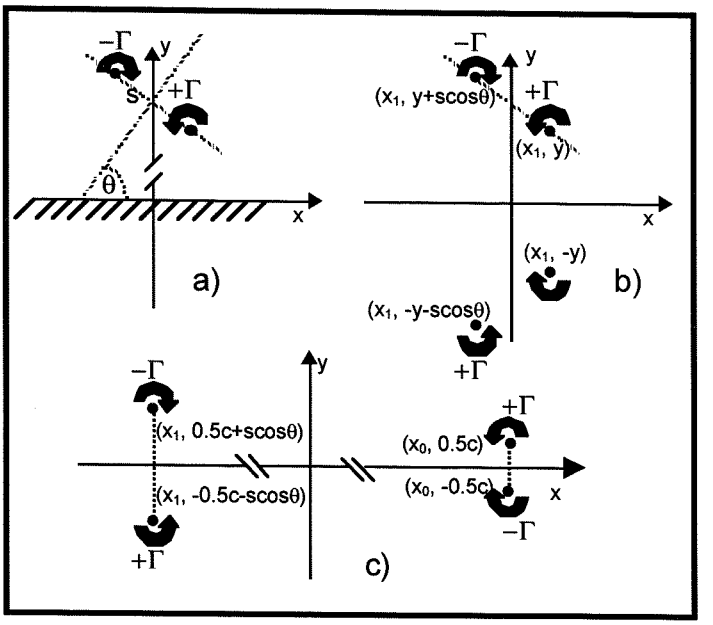

Fig. 2.6. a) Vortex dipole non-parallel to the boundary. s is the distance between the vortices. The dipole is at an infinite distance from the boundary. b) The two vortices are within a finite distance from each other and from the boundary. c) The two vortices have moved infinitely apart.

During the motion, the axis of the dipole is always tilted at the same angle θ from the boundary: because of the symmetry, the y components of the velocity of the vortices are equal and therefore the vortices maintain the original separation of s·cosθ in the y direction. When the vortices have moved apart from each other by an infinite distance in the x direction they move along the boundary (in opposite directions) only under the influence of their own mathematical images. To calculate the distance, c/2, of the positive vortex from the wall we can equate, as before, the interaction kinetic energy for the situation a) and c) in fig. 2.6, i.e.:

$$W_{tot} = \frac{1}{\pi}\Gamma^2 \log s \,, \qquad (2.15)$$

for the situation sketched in a) and

$$W_{tot} = \frac{1}{2\pi}\Gamma^2 \log c + \frac{1}{2\pi}\Gamma^2 \log\left(c + 2s\cos\theta\right), \tag{2.16}$$

for the situation in c).

Equating the two terms we obtain:

$$2\log s = \log c + \log(c + 2s\cos\theta), \tag{2.17}$$

which gives the two solutions

$$c_{1,2} = -s\cos\theta \pm s\sqrt{1+\cos^2\theta}. \tag{2.18}$$

The one with the + sign has physical meaning.

c. Group of point vortices interacting with a straight boundary

The case of a single point vortex interacting with a straight boundary can be extended for an arbitrary number of vortices, since the velocity field is given by the summation of the velocity induced by each single vortex plus its mathematical image. From heuristic geometric consideration it turns out that the evolution of a system of n vortices plus the corresponding mathematical images (i.e. with the wall removed) preserves its symmetry. Therefore, as expected, none of the real vortices can cross the border and nor can the images, and no new discontinuities are introduced in the real fluid.

We now go back to formulae 2.5 a, b and 2.6. Because of the presence of the images the sum of the strengths is zero and X,Y and D are not defined.

2.3 The vortex ring model

2.3.1 Background

If the line vortex is axisymmetric, many interesting results are available. Batchelor (1967) offers a good account of the main features for curved line vortices and Saffman (1992) gives an extensive description of the mathematics involved.

An isolated straight-line vortex (i.e. a vortex with infinitesimal cross-section and infinite vorticity) in an infinite fluid with no boundaries, has zero velocity at any point. If the vortex line is not uniformly curved it is subject to a non-uniform translation and the line changes shape. It has been shown (e.g. Saffman, 1992) that writing down the Biot-Savart law[7] using a parametric representation of the line vortex with the Frenet-Serret formulae, and taking the limits 1) for an infinitesimal portion of the line and 2) for a point infinitely close to the line, the velocity at that point, written up to order $o\left(\frac{\Gamma l}{C^2}\right)$ (where Γ is the strength of vortex, $l = \sqrt{x^2 + y^2}$ is now the shortest distance of the point from the line vortex L and C is the radius of curvature) is infinite and points in the direction of the binormal $\bar{b}$ (figure 2.7). This behaviour is governed by one of the binormal terms (Batchelor, 1967),

---

[7]The Biot-Savart law, also widely used in magnetism, in this context is a vectorial relationship to calculate the velocity $\bar{v}$ induced by a generic line vortex of strength Γ:

$$\bar{v}(\bar{x}) = \frac{\Gamma}{4\pi}\oint \frac{\bar{s} \times \left(\bar{x} - \bar{R}(\zeta)\right)}{\left|\bar{x} - \bar{R}(\zeta)\right|^3} d\zeta,$$

where the integral is calculated along the closed curved $\bar{R}(\zeta)$.

$$-\frac{\Gamma}{4\pi C}\log l. \qquad (2.19)$$

All the other terms are either bounded or cancel the singularities reciprocally.

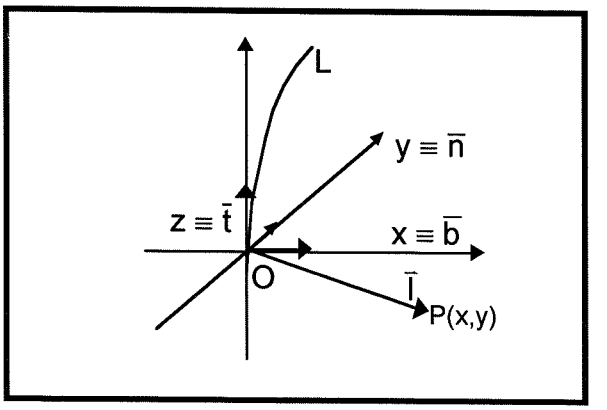

Fig. 2.7. Curved line vortex (L) and definition of the frame of reference. The line vortex is (locally) contained in the z-y plane. The self-induced motion at the origin O (induced by the vortex curvature) is in the binormal (i.e. x) direction.

Expression 2.19 therefore suggests that the effect of the variations of the (local) curvature is to deform the line vortex since it moves with infinite speed but the translation is not uniform along the vortex line. On the contrary an axisymmetric vortex ring, with constant curvature, will move along the binormal direction –i.e. along its axis of symmetry- with infinite speed and no deformation.

An axisymmetric vortex ring, sometimes called a "smoke ring", is shown in figure 2.8. The velocity field of a smoke ring is axisymmetric too and can be expressed in terms of a Stoke's stream function. Hence, if we adopt cylindrical co-ordinates (x,σ,ϕ), with $\sigma=0$ coincident with the axis of symmetry and (u,v,w) being the respective velocity components (with the condition of no swirl w=0), the formulae

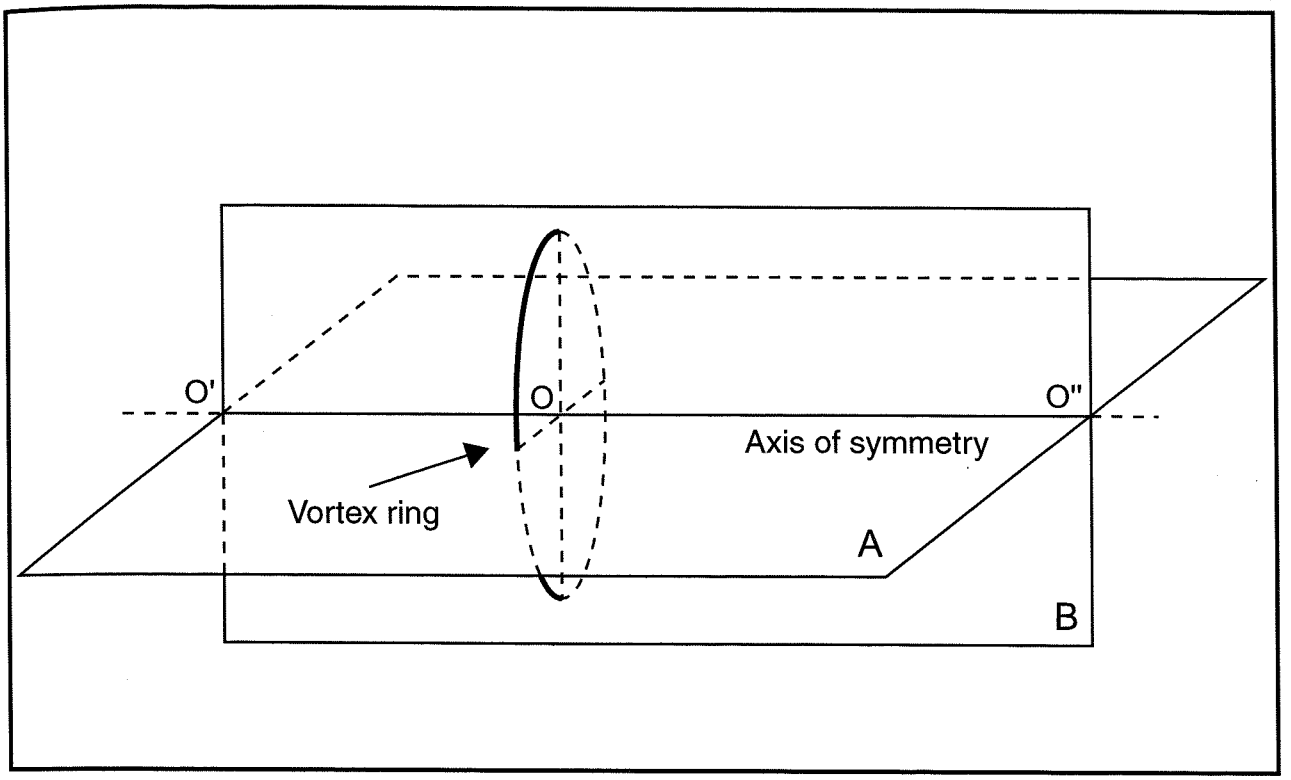

Fig. 2.8. A circular vortex ring is axisymmetric and the induced velocity field is axisymmetric too. In other words the velocity field is the same in all the planes passing from the axis of symmetry O'O" (of which A and B are an example).

$$u = \frac{1}{\sigma}\frac{\partial \psi}{\partial \sigma} \quad \text{and} \quad v = -\frac{1}{\sigma}\frac{\partial \psi}{\partial x}, \tag{2.20 a,b}$$

relate the stream-function to the velocity field (Batchelor, 1967).

The stream function can be expressed by (Lamb, 1932):

$$\psi(x,\sigma) = \frac{\Gamma}{2\pi}(l_1 + l_2)\left[K(\lambda) - E(\lambda)\right], \tag{2.21}$$

where

$$l_1 = \sqrt{(x - x_0)^2 + (\sigma - \sigma_0)^2} \tag{2.22}$$

and

$$l_2 = \sqrt{(x - x_0)^2 + (\sigma + \sigma_0)^2} \tag{2.23}$$

are respectively the minimum and the maximum distance of the point $P(x,\sigma)$ from the ring centre $C(x_0,\sigma_0)$. λ is given by

$$\lambda = \frac{l_2 - l_1}{l_2 + l_1}, \tag{2.24}$$

$d=2R=2\sigma_0$ is the diameter of the vortex ring and r_0 is the radius (at the moment infinitesimal) of the cross section of the line vortex. $K(\lambda)$ and $E(\lambda)$ are the complete elliptic integral of the first and second kind. Note that λ tends to 1 as l_1 tends to zero for when K and E are not defined. The stream function in any of the planes passing from the axis of symmetry (see fig.

2.8) is shown in figure 2.9. Figure 2.10 illustrates the geometry of the system.

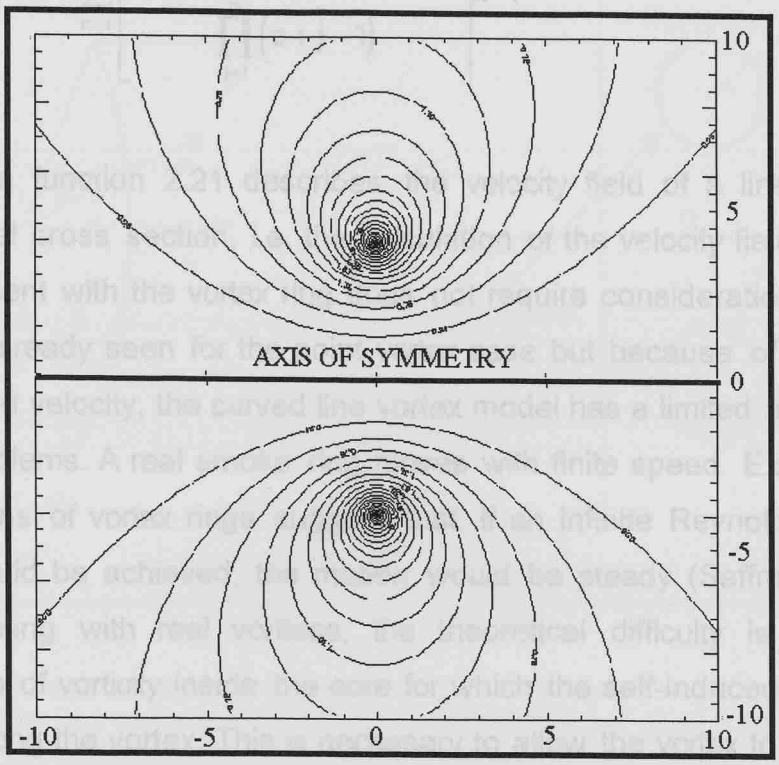

Fig. 2.9: Streamlines for a circular ring vortex in a plane of symmetry and with no background flow. The reference system is not moving with the vortex. The interval between the contour lines is constant.

The complete elliptic integrals can be evaluated with the following series:

$$K(\lambda) = \frac{\pi}{2} F\left(\frac{1}{2}, \frac{1}{2}; 1; \lambda^2\right) = \frac{\pi}{2}\left[1 + \left(\frac{1}{2}\right)^2 \lambda^2 + \left(\frac{1 \cdot 3}{2 \cdot 4}\right)^2 \lambda^4 + ...\right], \qquad (2.25)$$

$$E(\lambda) = \frac{\pi}{2} F\left(-\frac{1}{2}, \frac{1}{2}; 1; \lambda^2\right) = \frac{\pi}{2}\left[1 - \left(\frac{1}{2}\right)^2 \lambda^2 - \left(\frac{1 \cdot 3}{2 \cdot 4}\right)^2 \frac{\lambda^4}{3} + ...\right]. \qquad (2.26)$$

Here $F(a,b;c;x^2)$ is the hypergeometric function (Korn & Korn, 1961):

$$F(a,b,c,x^2) = 1 + \sum_{n=1}^{\infty} \left[\frac{\prod_{j=1}^{n}(a+j-1)\prod_{j=1}^{n}(b+j-1)}{\prod_{j=1}^{n}(c+j-1)} \right] x^{2n}. \qquad (2.27)$$

The stream function 2.21 describes the velocity field of a line vortex of infinitesimal cross section, i.e. the calculation of the velocity field at points not coincident with the vortex ring does not require consideration of cored rings, as already seen for the point vortex case but because of its infinite self-induced velocity, the curved line vortex model has a limited applicability to real problems. A real smoke ring moves with finite speed. Experimental observations of vortex rings suggest that, if an infinite Reynolds number regime could be achieved, the motion would be steady (Saffman, 1992). When dealing with real vortices, the theoretical difficulty is to find a distribution of vorticity inside the core for which the self-induced velocity is uniform along the vortex. This is necessary to allow the vortex to propagate steadily and without deformation (Batchelor, 1967). This problem has been treated for smoke rings of small cross section, for which the stream line bounding the core that contains the vorticity is approximately circular and the vorticity is uniformly distributed inside the core (see e.g. Saffman, 1992).

We consider a circular vortex ring with a thin core of finite size r and no swirl (w=0, fig. 2.10). Following Fraenkel (1972), the condition of small cross section can be expressed by the smallness of the parameter ε defined as:

$$\varepsilon = \sqrt{4A/\pi d^2}\,. \qquad (2.28)$$

A is the area of the cross section and d is the distance between the centroids, very close to the diameter of the ring for vortices with small cross

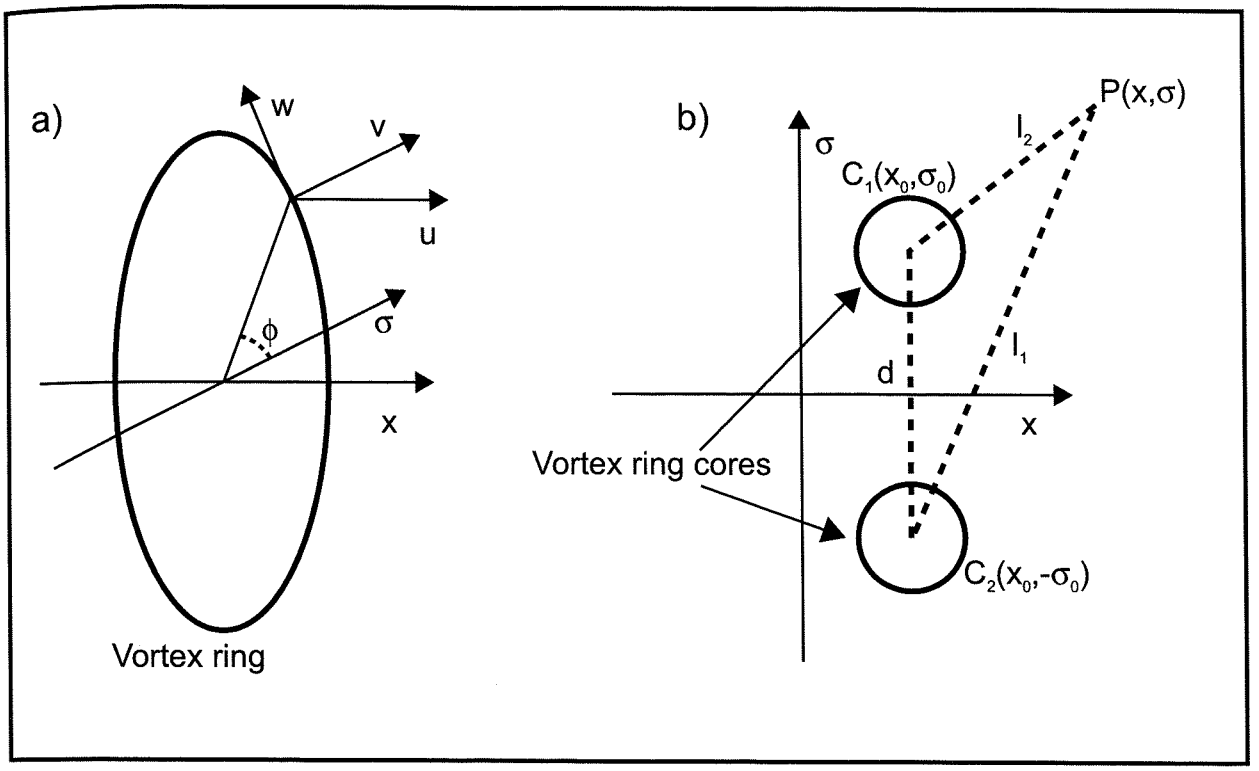

Fig. 2.10. Vortex ring in cylindrical co-ordinates (a) with the induced velocities. No swirl means w=0. Two dimensional section of a vortex ring of infinitesimal cross-section πr_0^2 (b) in a plane passing through the axis of symmetry x.

section (fig. 2.10). Formula 2.28 is the ratio between the area of the cross section of the line vortex and the area subtended by the circular ring. In the hypothesis of $\varepsilon \ll 1$, the self induced velocity of the ring corresponds to the one of the stagnation points inside the core, which exists if it is assumed that the stream function is constant on ∂A, the boundary of A (Saffman, 1992). If the condition $\varepsilon \ll 1$ is satisfied, the core of the vortex is an ellipse with axis ratio given by:

$$1+\varepsilon^2\left\{\frac{3}{8}\log\frac{8}{\varepsilon}-\frac{17}{32}\right\}, \qquad (2.29)$$

and the core can be approximated with a circumference (Saffman, 1992).

The self induced velocity of the vortex, v_c, is parallel to the axis $\sigma=0$ and is given by (e.g. Lamb, 1932; Fraenkel, 1972):

$$v_c=\frac{\Gamma}{4\pi R}\left\{\log\frac{8R}{r}-\frac{1}{4}+\left(\frac{r}{R}\right)^2\left[-\frac{3}{8}\log\frac{8R}{r}+\frac{15}{32}\right]+o\left(\left(\frac{r}{R}\right)^4\log\frac{8R}{r}\right)\right\} \qquad (2.30)$$

The presence of a finite core eliminates the logarithmic discontinuity at the vortex centre contained in the relation 2.19, the tendency at the discontinuity being now expressed as $\log(r^{-1})$; v_c increases as r decreases and eventually tends to ∞ when r tends to zero.

To complete the description we now need to give an explicit expression for the velocity field induced by a single smoke ring: this can be calculated with the stream function 2.21 and formulae 2.20 a, b:

$$u=\frac{\Gamma}{2\pi\sigma}\left[\left(\frac{\partial I_1}{\partial\sigma}+\frac{\partial I_2}{\partial\sigma}\right)\left(K(\lambda)-E(\lambda)\right)+\left(I_1+I_2\right)\left(\frac{\partial K(\lambda)}{\partial\lambda}\frac{\partial\lambda}{\partial\sigma}-\frac{\partial E(\lambda)}{\partial\lambda}\frac{\partial\lambda}{\partial\sigma}\right)\right], \qquad (2.31\ a)$$

$$v = -\frac{\Gamma}{2\pi\sigma}\left[\left(\frac{\partial I_1}{\partial x}+\frac{\partial I_2}{\partial x}\right)\left(K(\lambda)-E(\lambda)\right)+\left(I_1+I_2\right)\left(\frac{\partial K(\lambda)}{\partial \lambda}\frac{\partial \lambda}{\partial x}-\frac{\partial E(\lambda)}{\partial \lambda}\frac{\partial \lambda}{\partial x}\right)\right], \quad (2.31\ b)$$

where:

$$\frac{\partial E(\lambda)}{\partial \lambda} = \frac{E(\lambda)-K(\lambda)}{\lambda}, \quad (2.32)$$

$$\frac{\partial K(\lambda)}{\partial \lambda} = \frac{E-\lambda_1^2 K(\lambda)}{\lambda\lambda_1^2}, \quad (2.33)$$

and $\lambda_1 = \sqrt{1-\lambda^2}$. (2.34)

Finally,

$$\frac{\partial \lambda}{\partial x} = \frac{2I_1\frac{\partial I_2}{\partial x}-2I_2\frac{\partial I_1}{\partial x}}{\left(I_1+I_2\right)^2} \quad (2.35)$$

$$\frac{\partial \lambda}{\partial \sigma} = \frac{2I_1\frac{\partial I_2}{\partial \sigma}-2I_2\frac{\partial I_1}{\partial \sigma}}{\left(I_1+I_2\right)^2} \quad (2.36)$$

The calculations involved in the determination of the velocity field for a generic system of smoke rings can be quite a cumbersome exercise because it involves the use of the Biot-Savart law and the velocity field is obtained by integrating along all the line vortices; furthermore, in general, the circular symmetry is lost after the initial instant since the vortices are subject to deformation. A system of n coaxial vortex rings each with different radii and strengths is a much simpler case to study: for such a system the velocity of each vortex can be calculated by summing its self

induced velocity with the velocity induced by all the others, using expressions 2.31 a,b. The total velocity field is in this special case axisymmetric and remains so during the evolution of the array of vortices: this implies that the system of vortices will preserve too its symmetry. The velocity field at a generic point in the space non coincident with any of the line vortices is the sum of the effect of the n smoke rings, and again is calculated with formulae 2.31a and b.

Similar to the point vortex model, the velocity field inside the vortex core presents a discontinuity: from relations 2.24 and 2.34, if $I_1=0$ then $\lambda=1$ and $\lambda_1=0$; for $\lambda=1$ the complete elliptic integrals are not defined and from 2.34 we have the additional condition that λ_1 can only be positive and different from zero.

The derivatives of I_1 and I_2 are given by:

$$\frac{\partial I_1}{\partial x}=\frac{(x-x_0)}{I_1}, \qquad \frac{\partial I_1}{\partial \sigma}=\frac{(\sigma-\sigma_0)}{I_1}, \tag{2.37 a,b}$$

and

$$\frac{\partial I_2}{\partial x}=\frac{(x-x_0)}{I_2}, \qquad \frac{\partial I_2}{\partial \sigma}=\frac{(\sigma+\sigma_0)}{I_2}. \tag{2.38 a,b}$$

The conditions $I_1>0$ and $I_2>0$ must be always true.

2.3.2 The case of two counter-rotating equal vortex rings

Consider the situation in which two equal, thin-cored and co-axial vortex rings of opposite sign and radius R_i move under their reciprocal influence; this case is the three-dimensional equivalent of a point vortex dipole

interacting with a rectilinear boundary (or a vortex quadrupole see fig. 2.5 and fig. 2.9). The behaviour of the vortices is similar in the two cases (2D and 3D) with the couple moving away from the wall when the vortex on the left hand side is positive and vice versa when negative.

Suppose that the lhs vortex is negative and the initial distance between the centres of the two rings is s: we want to calculate the final radii of the rings (R_f) when they have moved infinitely apart and translate at constant speed given by formula 2.30.

As already done for the point-vortices, we can use an energy argument. The energy balance can be written as:

$$E_i+E^{12}{}_i=E_f, \tag{2.39}$$

where E_i is the initial kinetic energy of the two vortices as if the other were not present, $E^{12}{}_i$ is the initial interaction kinetic energy for the couple and E_f is total final kinetic energy of the system. The subscripts "i" and "f" refers to the initial and final situations respectively. This equation simply states that the system is conservative or, in other words, that the final kinetic energy, computed when the two vortices are sufficiently far from each other to ignore their mutual interaction, must equal the initial kinetic energy, when the two vortices interact.

The kinetic energy of a sector α of an isolated vortex ring is given by (see e.g. Saffman, 1992)

$$E_s(\Gamma,R,r)=\frac{\Gamma^2 R}{2}\left\{\log\frac{8R}{r}-\frac{7}{4}+....\right\}\left(\frac{\alpha}{2\pi}\right), \tag{2.40}$$

and therefore E_i and E_f are simply given by:

$$E_i = 2E_s(\Gamma, R_i, r_i), \tag{2.41}$$

$$E_f = 2E_s(\Gamma, R_f, r_f). \tag{2.42}$$

The initial and final radius of the core are related, using the conservation of volume, by:

$$r_f = r_i\left(\frac{R_i}{R_f}\right)^{\frac{1}{2}}. \tag{2.43}$$

The interaction kinetic energy for the vortex pair, E^{12}_i, given the symmetry of the problem and considering again only a sector α of the rings, can be calculated using the formula (e.g. Batchelor, 1967):

$$E_i^{12} = \alpha\int \omega_+\psi_- dA_+ = \alpha\int \omega_-\psi_+ dA_-, \tag{2.44}$$

where $\omega_{+(-)}$ is the vorticity of the positive (negative) vortex, $\psi_{-(+)}$ is the stream function of the negative (positive) vortex. The integral is calculated over the region containing the positive (negative) vorticity, i.e. over the core of the positive (negative) vortex.

Assuming that at the initial instant the vortices are at sufficient distance to neglect variations of ψ_- over the area of integration, which is a good approximation if s»r, the interaction kinetic energy takes the form:

$$E_i^{12} = -\frac{\alpha\Gamma^2}{2\pi}\left(s+\sqrt{s^2+4R^2}\right)\left[K(\lambda)-E(\lambda)\right], \tag{2.45}$$

where K and E are the complete elliptic integrals of the first and second kind respectively, s is the distance between the two vortices, for example measured on the common axis of symmetry, and λ has the form:

$$\lambda = \frac{\sqrt{s^2 + 4R^2} - s}{\sqrt{s^2 + 4R^2} + s}. \qquad (2.46)$$

The interaction kinetic energy tends to zero as λ tends to zero, which is equivalent to the condition for s becoming infinite. Therefore vortices that are very far apart have zero interaction kinetic energy.

The energy balance, ignoring terms of order higher than one, can then be written as:

$$R_i\left[\log\left(\frac{8R_i}{r_i}\right) - \frac{7}{4}\right] - \left(s_i + \sqrt{s_i^2 + 4R_i^2}\right)\left[K(\lambda) - E(\lambda)\right] = R_f\left[\log\left(\frac{8R_f}{r_f}\right) - \frac{7}{4}\right]. \qquad (2.47)$$

This equation relates the final radii of the rings to their initial radii and has no dependence from Γ (this statement is true if we assume that the circulation of the vortices is conserved and therefore only geometrical factors define the energy of the system).

We now show that the path followed by the centroids of the core of the vortices is independent of the strength. If we assume that the centre of the core has initial co-ordinates (x_0,σ_0) at the instant $t=t_0$ (see fig. 2.10), its position in time is given by:

$$x_0(t) = \int_{t_0}^{t} v_x d\tau, \qquad (2.48)$$

$$\sigma_0(t) = \int_{t_0}^{t} v_\sigma d\tau \qquad (2.49)$$

The x-component of the velocity of the core has two contributions: the first is the self-induced velocity of the vortex, v_{x1}, (formula 2.30) and the second is the velocity induced by the other ring, v_{x2}, (formula 2.31 a) and the two components can be written as

$$v_{x1} = \frac{\Gamma}{R} G_1(r,R), \tag{2.50}$$

$$v_{x2} = \frac{\Gamma}{R} G_2(s,R), \tag{2.51}$$

so that the total velocity of the core in the x direction is the sum of 2.50 and 2.51, i.e.:

$$v_x = \frac{\Gamma}{R} G(s,r,R), \tag{2.52}$$

with $G=G_1+G_2$. Similarly, the other component of the velocity is given, via relation 2.31 b, by:

$$v_\sigma = \frac{\Gamma}{R} F(s,R). \tag{2.53}$$

The path followed by the vortices can be calculated by solving numerically the differential equation

$$\frac{dx}{d\sigma} = \frac{v_x}{v_\sigma} = \frac{G(s,r,R)}{F(s,R)}, \tag{2.54}$$

Therefore the trajectory of the vortices is independent of Γ.

2.3.3 Curved line vortices in a bounded three-dimensional domain

We have already observed (section 2.3.1) that the self induced velocity of a singular curved line vortex is infinite and is directed along the binormal direction; if the curvature is not constant, the vortex in general will also change its shape with infinite speed (Batchelor, 1967, p. 511). If cored vortex filaments are considered, there is the possibility to circumvent the difficulties connected with the calculation of the self induced velocity of a vortex of generic shape. The first technique is called the local induction approximation and among several limitations, it requires that the condition log 1/r » 1 is satisfied, which may be hard to meet for real vortices; this approximation predicts that the self induced velocity is proportional to the inverse of the radius of curvature times the logarithm of the radius of the core, r (Saffman, 1992, p. 209). The second technique is the cut-off method for which the singularity in the Biot-Savart law is removed ad-hoc by using a cut-off parameter (Saffman, 1992, p. 212). In both cases there are no general results and few numerical experiments have been carried out. For example Dhanak et al (1981) have calculated the evolution of an elliptical vortex ring and have found that the deformations are periodic only for values of the axis ratio between 1 and 0.2 and the evidence suggest that in the other cases the vortex is subject to a break-down.

A cored line vortex that is able to propagate with a finite self-induced speed without deformations and satisfies the kinematic boundary conditions for a sloping boundary is the circular smoke-ring (see section 2.3.1).

From a mathematical point of view, the vortex-ring model can be used to simulate a vortex on a planar sloping beach (Thorpe and Centurioni, 2000, and Peregrine, 1996). Suppose that a vortex is moving on a wedge-like domain whose boundaries are a planar sloping sea-bed (forming an angle $\alpha \neq 90^{\circ}$ with the horizontal) and the surface of the water (fig. 2.11 a). If

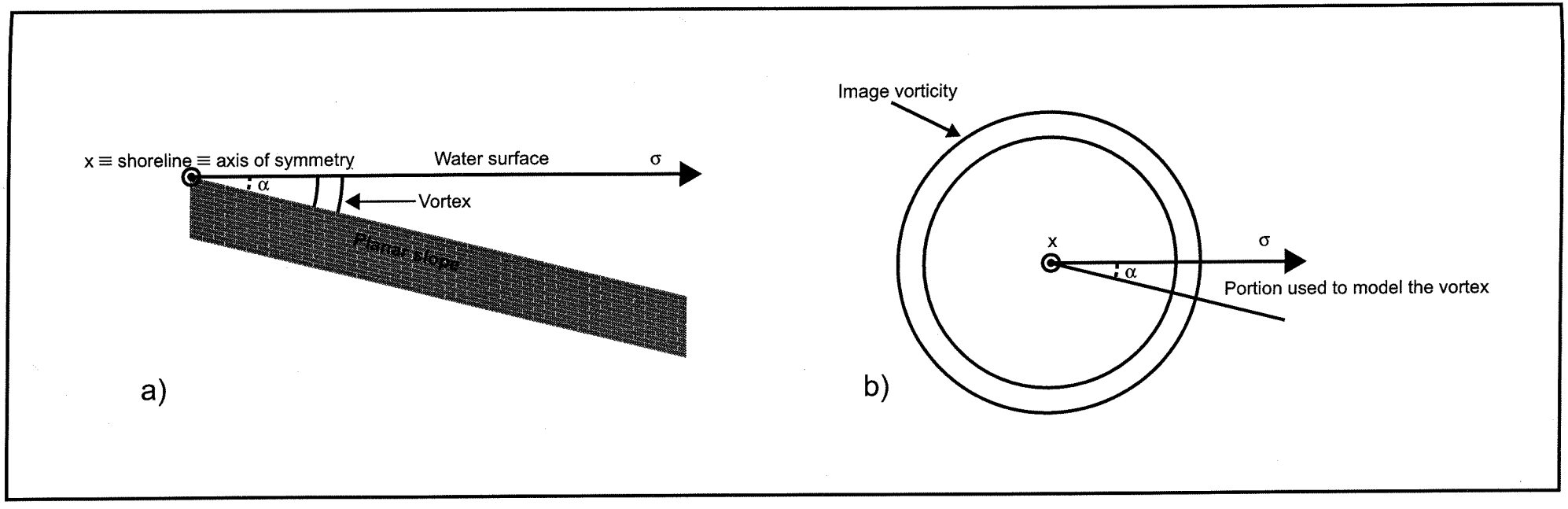

Fig. 2.11: A vortex ring is divided in two parts (right). Each part is the image of the other. The smallest sector can be used to model a vortex in a wedge-like domain (left).

a straight line vortex is introduced in this domain it will intersect at least one of the two boundaries at an angle different from 90° therefore requiring the introduction of image vorticity to satisfy the boundary conditions. One immediate consequence is that the vortex cannot remain straight. A vortex line that is able to meet both boundaries at right angles is a sector of circumference, i.e. a sector of a vortex ring. This vortex has also a constant curvature and therefore will preserve its shape. The image vorticity is in this case the part of the ring outside the wedge and it is needed to keep the vorticity field solenoidal (fig. 2.11 b). By definition this model satisfies the condition that the vortex line meet the boundaries at right angles, which is the only one required if the non-slip condition is relaxed.

A system of axisymmetric and co-axial vortex rings can therefore be thought of as a group of vortices moving over a sloping bottom (figure 2.12). The presence of the common axis of symmetry allows a simple approach to the problem: the velocity field can be computed only in an axial plane without requiring the application of the Biot-Savart law in three-dimensional space.

2.4 Spin-down of an isolated vortex on a flat bottom

Consider a vortex at $t=t_0$ with initial radius r_0, depth h, constant vorticity ω_0 and therefore circulation $\Gamma_0=\omega\pi r_0^2$. The Froude number, defined as $F_r=\Gamma^2/(ghr_0^2)$, is small, thus implying that the depression at the centre of the vortex is negligible (e.g. Thorpe and Centurioni, 2000). If the fluid is inviscid everywhere the vortex rotates with constant angular velocity $\Omega_0=\omega_0/2$. On the contrary, if a viscous boundary layer, with kinematic viscosity ν, is added, the vortex spins down. The interior of the fluid is still inviscid, i.e. there is no dissipation of energy or, alternatively, the total strength Γ_0 is conserved. The viscous boundary layer provides a mechanism to redistribute the angular momentum of the vortex (see e.g. H.P. Greenspan, 1969 pp. 30-38). We want to calculate $\omega(t)$ and $r(t)$ for $t>t_0$ in the absence of

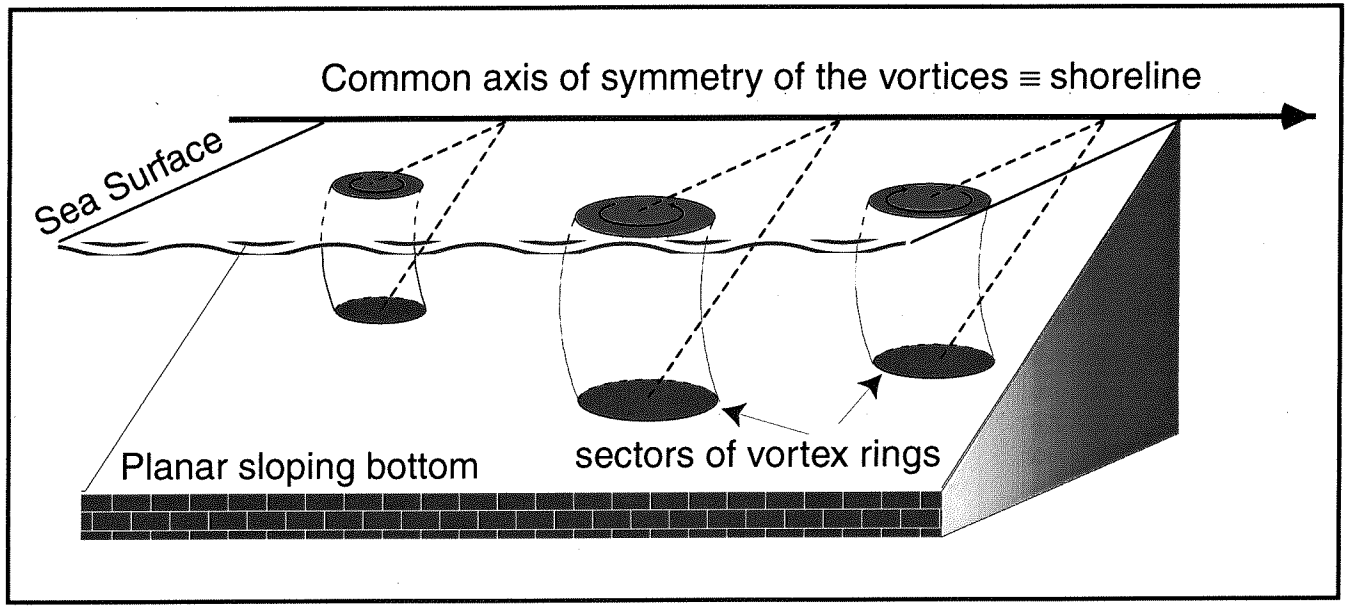

Fig. 2.12: A system of vortices in a wedge-like region of fluid, whose boundaries are a planar sloping beach and the sea surface, is modelled with an array of coaxial vortex rings. The remaining portion of the rings (not shown) are the images.

forcing. This problem has been treated by a variety of authors and it is known that the spin-down time scale is (e.g. Greenspan and Howard, 1963):

$$T = \left(\frac{h^2}{\nu \Omega_0} \right)^{\frac{1}{2}}. \qquad (2.55)$$

If we neglect the effect of the air friction at the surface, the volume of rotational flow (vortex) changes because of a radial inflow confined in the bottom boundary layer with thickness (e.g. Greenspan and Howard, 1963):

$$\delta_E = \left(\frac{2\nu}{\omega} \right)^{\frac{1}{2}}. \qquad (2.56)$$

Note that $\omega/2=\Omega_0$ is the characteristic time of the system since it is inversely proportional to the rotation period of the vortex. Formula 2.56 tells us that a boundary layer of thickness δ_E will grow in a few revolutions of the vortex. This mechanism is responsible for a decrease of vorticity and, since there is a radial inflow in the bottom boundary layer that must satisfy the conservation of volume, for an increase in the radius of the vortex. If we refer to a Cartesian co-ordinate system with the x axis tangent to vortex and with origin at a distance ρ from the centre, with the y axis directed towards the centre of the vortex and the z axis pointing upwards, the velocities in the bottom boundary layer are (e.g. Pedlosky, 1987, p189):

$$u = V(\rho)\left(1 - e^{\frac{-z}{\delta_E}} \cos\frac{z}{\delta_E} \right) \text{ and} \qquad (2.57\ a)$$

$$v = V(\rho) e^{\frac{-z}{\delta_E}} \sin\frac{z}{\delta_E}, \qquad (2.57\ b)$$

where V(ρ) is the velocity induced by the vortex at a distance ρ from its centre, i.e., with the condition of spatially constant vorticity:

$$V(\rho) = \frac{\Gamma}{2\pi\rho} = \frac{\omega\rho}{2} = \Omega\rho \qquad (2.58)$$

The maximum volume flux per unit length in the y direction is obtained at ρ=r and is;

$$T'_M = \int_0^\infty v(r,\zeta)d\zeta = \frac{V(r)\delta_E}{2}, \qquad (2.59)$$

where ζ is the vertical co-ordinate (see appendix 2A). The total volume flux inside the vortex bottom boundary layer is therefore:

$$T_M = T'_M\, 2\pi r = \pi r V(r)\delta_E \qquad (2.60)$$

For the conservation of volume, T_M must therefore be equal to the volume of fluid moving upwards that is entering the interior vortex from the bottom boundary layer, e.g.:

$$T_M = w\pi r^2, \qquad (2.61)$$

where w is the velocity of the water entering the interior of the vortex. Assuming a constant vertical gradient for w and with the condition of w=0 at the surface, we also have:

$$\frac{\partial w}{\partial z} = -\frac{T_M}{\pi h r^2} = -\frac{V(r)\delta_E}{hr}, \qquad (2.62)$$

In order to calculate ω(t) and r(t), we solve the system:

$$\begin{cases} \dfrac{\partial \omega}{\partial t} = \omega \dfrac{\partial w}{\partial z} \\ \dfrac{\partial r}{\partial t} = \dfrac{T_M}{2\pi h r} \end{cases}, \qquad (2.63)$$

with the initial conditions:

$$\omega(0)=\omega_0, \qquad (2.63\ a)$$

and

$$r(0)=r_0 . \qquad (2.63\ b)$$

The first equation of the system 2.63 is the vorticity equation. The second equation is obtained from the conservation of volume (see appendix 2A for more details). Note that since $\vec{\omega} = (0,0,\omega_z)$ is spatially constant, the non-linear viscous terms are zero and there is no dissipation of energy. Substituting 2.56, 2.58, 2.61, and 2.62 into 2.63, we obtain:

$$\begin{cases} \dfrac{\partial \omega}{\partial t} = -\dfrac{(2\nu)^{\frac{1}{2}} \omega^{\frac{3}{2}}}{2h} \\ \dfrac{\partial r}{\partial t} = \dfrac{(2\nu)^{\frac{1}{2}} r \omega^{\frac{1}{2}}}{4h} \end{cases}. \qquad (2.64)$$

The solutions are:

$$r(t) = r_0\left(1+\frac{t}{4T}\right), \qquad (2.65)$$

$$\omega(t) = \omega_0 \left(\frac{1}{1+\frac{t}{4T}} \right)^2 , \qquad (2.66)$$

where T is the spin-down time scale 2.55. If the water depth increases the growth of the radius is slower.

2.5 Summary

We have reviewed some aspects of the dynamics of a system of point vortices and of an array of co-axial vortex rings.

In section 2.2.2 we have worked out the analytical solutions of the final distance from the boundary for two point vortices moving towards a straight boundary at an angle different from 90°. In section 2.3.2 we have calculated the radius of two cored equal axisymmetric and inviscid vortex rings of opposite sign that move infinitely apart. Again the principle of the conservation of the kinetic energy was used to find the analytical solution of the problem.

Section 2.3.3 presents the idea on which much of this dissertation hinges, i.e. the possibility of using sectors of vortex rings to model a vortex on a wedge-like domain (Peregrine, 1996, Thorpe and Centurioni, 2000).

The problem of the spin-down of a vortex on a flat bottom is reviewed in section 2.4, where the analytical solutions for the time evolution of the radius and for the vorticity are calculated.

Chapter 3

Numerical experiments

3.1 Introduction

Two numerical models are used to study the effect of a straight vertical wall and of a planar and uniformly sloping bottom on the dispersion of particles of fluid and vortices in a velocity field that is entirely sustained by the latter. A schematic representation of the situation that we are modelling is illustrated in figure 3.1. We shall neglect all viscous effects.

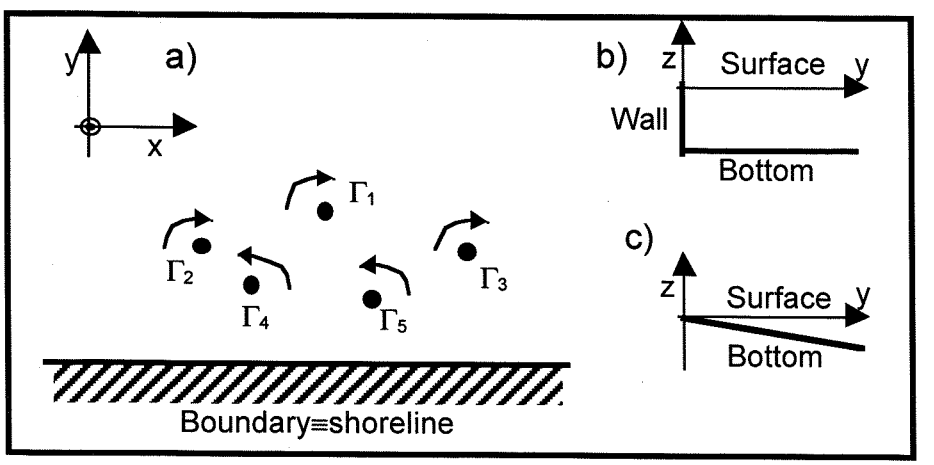

Fig. 3.1: a) A straight boundary divides the plane in two parts and simulates a shoreline. The motion of the system is studied for b) a sea with flat bottom and bounded by a vertical wall and c) a sea with a planar sloping bottom and no vertical wall. In c) the intersection between the bottom and the surface is the shoreline.

If the bottom is flat, a model that uses Rankine's vortices and their images (see section 2.2.2 c) is used. The boundary conditions are satisfied at the wall. If the bottom is a uniformly sloping plane, the interpretation in term of vortex rings is formally correct, and, as discussed in section 2.3.3, the

boundary conditions for the wedge-like equivalent system are automatically satisfied. It follows that the angle that the planar slope forms with the horizontal does not affect the dynamics of the vortices. We call the first model two-dimensional (2-D) and the second three-dimensional (3-D). The shoreline is always coincident with the x-axis.

One environment to which this model might relate, is the portion of sea near the shoreline and for vortices for which the effect associated with the rotation of the Earth is negligible. It is obvious that this situation is highly idealised: for example we do not consider the effects associated with the presence of incident and breaking waves, of along-shore currents and of near-shore circulation cells. We also ignore completely bottom friction and irregular topography. Spin-down caused by a viscous bottom boundary layer is also neglected.

The aims of the numerical experiments are:

-to compare the dispersion of the vortices with the dispersion which they produce in a passive tracer;

-to give a qualitative description and comparison of the effect of a vertical wall, in the 2-D case, and of a shore-line and of a sloping bottom, in the 3-D case, on the dispersion of vortices and particles; more precisely we want to understand whether the dispersion is in general isotropic or if it has a preferential direction;

-to compare the dispersing properties of the 2-D model with the ones of the 3-D model when the initial conditions are equal.

The dispersal properties of a system of point vortices in the presence of an infinite and straight boundary has apparently been overlooked by previous

workers (Provenzale, 1998, personal communication), this fact being perhaps a sufficient reason to undertake this study.

We are aware of the very high degree of schematisation of our model and for this reason we will not attempt to give any quantitative estimates of the eddy dispersion coefficients for vortices and particles; it also turns out that to parameterise those coefficients in terms of the characteristics dimensions of the system is not straightforward and only in very special situations some conclusions can be made from theory. Nevertheless we think that the models should give some indications of the behaviour of vortices and tracer near an infinite and straight boundary and form the basis of a zero order understanding of the problem, which will help in identifying some features important in understanding dispersion in the ocean.

We first describe in details the implementation of the 2-D numerical model, the theory for which has been already presented and discussed in section 2.2.2 c. We then present the results of two experiments made under very special condition and with the vortices at a distance from the boundary much larger than their average spacing. The purpose is to give some basics elements for the understanding of the problem of vortex/border interactions and associated dispersion in successive experiments. Those preliminary experiments also provide a good tool to evaluate the performance of the programs by comparing the results with analytical solutions. The reader who wishes to avoid the programs and preliminary tests might turn directly to sections 3.5 and 3.6 where we address the problem of vortices near the shoreline. There we first study a situation in which some vortices and some marked particles are initially sharing the same portion of fluid. Secondly, we look at the situation in which a passive tracer occupies, at the beginning of the experiments, a portion of fluid much bigger than the one occupied by the vortices. Conclusions and summary are presented in sections 3.7 and 3.8

respectively. The definitions of the dispersion of vortices and particles (formulae 3.7 and 3.8) and the related eddy dispersion coefficients, on which the discussion of this chapter hinges, are given in appendix 3A.1.

3.2 Implementation of the 2-D numerical model

3.2.1 Program "point"

To calculate the displacement and the dispersion of a system of Rankine's vortices and of marked particles, we wrote a FORTRAN program (called "point"). The main features of the model are discussed below.

a. Velocity field

The velocity field is given by the vortices, i.e. there is no background flow. The 2-D model is based on the stream function for a system of Rankine's vortices (chapter 2, relations 2.8 and 2.9). These formulae show that the motion of the fluid inside the core of radius r_i of the i^{th} vortex is the superposition of a rigid body rotation and the motion induced by the other vortices. The formulae used in the program are therefore:

$$u = \begin{cases} -\dfrac{1}{2\pi}\displaystyle\sum_{i=1}^{n}\Gamma_i\frac{(y-y_i)}{l_i^2}, & l_j \geq r_j; \\ -\dfrac{1}{2\pi}\displaystyle\sum_{i(\neq j)=1}^{n}\Gamma_i\frac{(y-y_i)}{l_i^2} - \sum_{j=1}^{n}\frac{1}{2\pi}\Gamma_j\frac{(y-y_j)}{r_j^2}, & \forall j : l_j < r_j; \end{cases} \qquad (3.1\text{ a})$$

$$v = \begin{cases} \dfrac{1}{2\pi}\displaystyle\sum_{i=1}^{n}\Gamma_i\frac{(x-x_i)}{l_i^2}, & l_j \geq r_j; \\ \dfrac{1}{2\pi}\displaystyle\sum_{i(\neq j)=1}^{n}\Gamma_i\frac{(x-x_i)}{l_i^2} - \sum_{j=1}^{n}\frac{1}{2\pi}\Gamma_j\frac{(x-x_j)}{r_j^2}, & \forall j : l_j < r_j; \end{cases} \qquad (3.1\text{ b})$$

where the notation is the same of section 2.2.1. If the velocity field is calculated at the position of the j^{th} vortex, i.e. when $r_j=0$, formulae 3.1 a and b are still used and there is no need to remove the contribution from the j^{th} vortex that in this case is zero: with these formulae all the discontinuities are eliminated from the computational domain.

b. Integration of the velocity field

The calculation of the position of vortices and particles with time is in our case equivalent to the solution of 2(n+m) equations of the kind:

$$\begin{cases} \dfrac{dx}{dt} = f(x,y,x_{v1}(t),y_{v1}(t),\ldots,x_{vn}(t),y_{vn}(t),\Gamma_1,\ldots,\Gamma_n,r_1,\ldots,r_n), \\ \gamma(t_0) = \gamma_0, \end{cases} \qquad (3.2)$$

where x and y are the Cartesian co-ordinates of a vortex or a particle, x_{vi} and y_{vi} are the co-ordinates of the centre of the vortices, t is the time, Γ_i are the strengths, r_i are the radii of the core, n is the number of vortices and m is the number of particles. The function f is the velocity given by the formulae 3.1 a, b. Note that the velocity field is evolving with time because is a function of the position of the vortices.

The position of the vortices and of the particles is computed with the Heun's method (e.g. Chapra and Canale, 1988), a brief description of which follows. Consider for example the x co-ordinate of one particle: we want to integrate the function x=x(t), indicated by γ in equation 3.2, which represents the evolution of the position of the particle with time induced by the vortices. Suppose now that the particle is at the position (x_i, y_i) at the time t_i: we know the time derivative of x(t) at the time t_i, say $f(x_i,y_i,x_{vi},y_{vi}...)$, from the relations 3.1 a and we can estimate the position $\underline{x}_{i+1}$, called predictor, at $t_{i+1}=t_i+\Delta t$, Δt being a fixed time step, from the simple Euler formula, i.e.

$$\underline{x}_{i+1} = x_i + f(x_i, y_i, \ldots, t_i)\,\Delta t. \qquad (3.3)$$

The same procedure applies to calculate the predictor of the ordinate, $\underline{y}_{i+1}$. $\underline{x}_{i+1}$ and $\underline{y}_{i+1}$ are the new co-ordinates of the particle at which a new predicted velocity, $f(\underline{x}_{i+1}, \underline{y}_{i+1}, \ldots)$, can be calculated, always from formulae 3.1 a, when all the vortices have moved to their new predicted position. This principle is illustrated in figure 3.2.

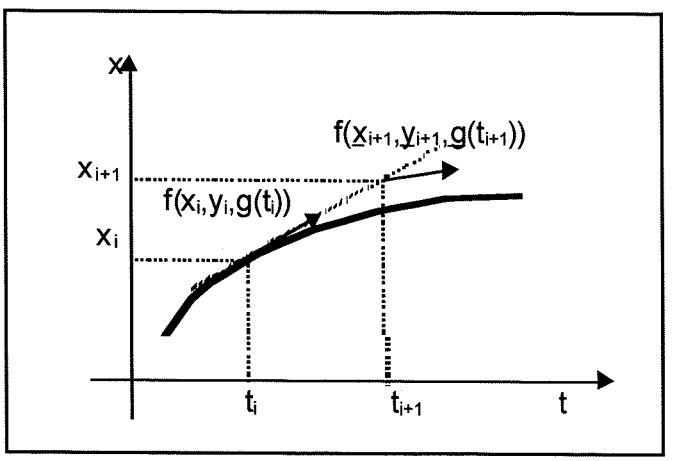

Fig. 3.2: Illustration of the Heun's method. The derivative of the unknown function x(t) is calculated at the instant t_i from which the predicted value $\underline{x}(t_{i+1})$ is also computed. The derivative of x(t) is then re-calculated for the predicted values $\underline{x}(t_{i+1})$, $\underline{y}(t_{i+1},)$, etc. The dependence from the position, radius and strength of the vortices, that is also a function of time, is indicated by the function g.

The value of the "true" position can now be calculated, using the average of the two velocities, i.e.:

$$x_{i+1} = x_i + 0.5[f(x_i, t_i) + f(\underline{x}_{i+1}, t_{i+1})]\,\Delta t. \qquad (3.4)$$

The Heun's method substantially allows a better estimate of the slope of the unknown function x(t).

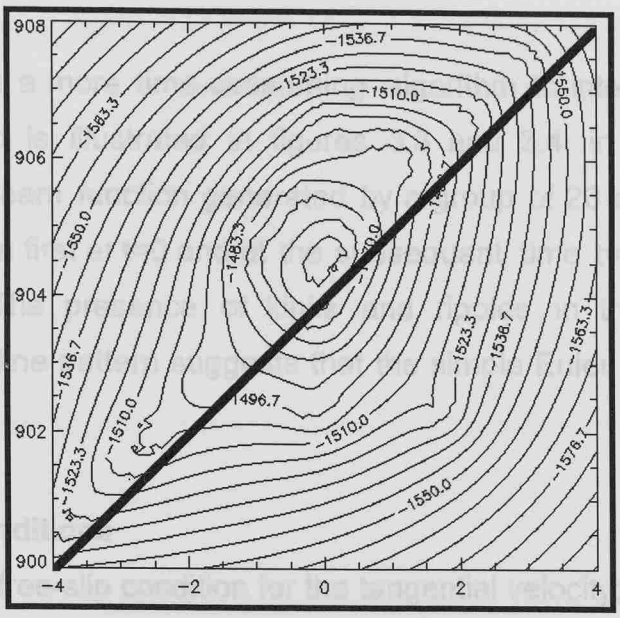

Fig 3.3: Stream-function, in a fixed frame of reference, generated by 20 Rankine's vortices, each of non-dimensional strength of 40, that are almost aligned on the diagonal indicated in the picture, at the non-dimensional time t=0. The contour lines were calculated with formulae 2.8 and 2.9 and have a spacing of 6.65 units. An infinite rectilinear boundary is coincident with the x-axis at y=0 (not shown). The co-ordinates are expressed in non dimensional units.

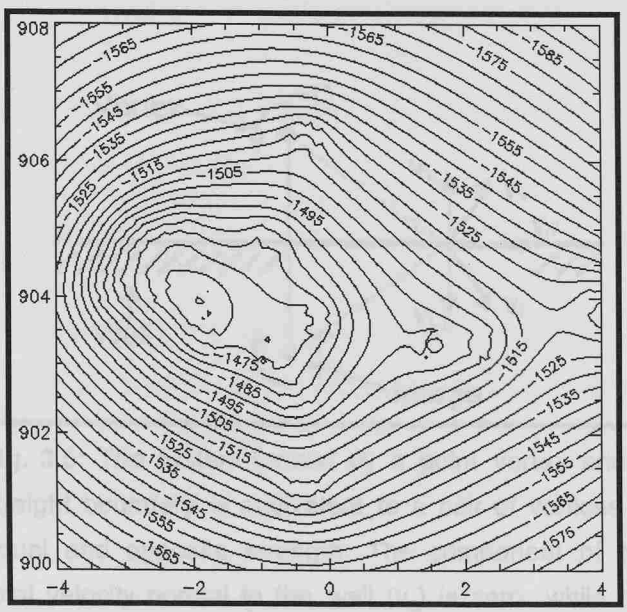

Fig 3.4: Evolution of the situation depicted in figure 3.3 at t=0.6. The contour lines have now a spacing of 5 units.

The need to use a more time-consuming algorithm to integrate accurately the velocity field is illustrated in figures 3.3 and 3.4, in which the non dimensional stream function generated by a group of 20 equal Rankine's vortices is shown first at t=0 and at the subsequent time t=0.6 (time is non dimensional). The presence of kinks and ripples in the rapidly time-evolving streamline pattern suggests that the simple Euler method may be inaccurate.

c. Boundary conditions

We used: i) the free-slip condition for the tangential velocity; ii) the condition of zero normal velocity at the rigid wall (with the wall at rest). These are satisfied with the method of the images (see section 2.2.2), i.e. if for each real vortex, we introduce another vortex of equal strength and opposite sign at the mirror position with respect to the wall (fig. 3.5).

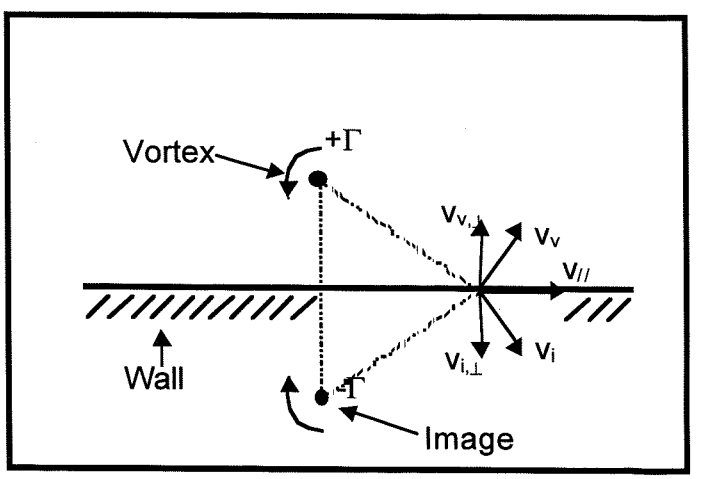

Fig. 3.5: The system formed by a point vortex and a straight boundary is equivalent to a pair of vortices of equal and opposite strength. The component of the total velocity normal to the wall ($v_\perp$) is zero, while the tangential component ($v_{//}$) is twice the velocity induced by each vortex at that point.

The program works on the equivalent system, with the wall removed and the images added in the extended domain, and calculates the path followed by each of the n real vortices, the latter being concisely represented with

$$\{\Gamma_i,\ r_i,\ (x_i,y_i)\}, \qquad i=1...n, \tag{3.5}$$

induced by the remaining n-1 real vortices and by the images, represented by

$$\{-\Gamma_i,\ r_i,\ (x_i,-y_i)\}, \qquad i=1...n. \tag{3.6}$$

Since the velocity field is symmetric with respect to the x-axis, there is no need to calculate the position of the images. Note that for the system of vortices plus images the quantities 2.5 a, b and 2.6, defining respectively the centre of strength and its dispersion are not defined. On the contrary the interaction kinetic energy of the vortices (relation 2.7) can still be calculated and, since it is also the Hamiltonian of the system, it must be constant. This quantity turns out to be very important in the choice of the time step, as discussed in section 3.2.2 c.

d. Other features

Formulae 3.1 a and b allow the vortices to pass undisturbed through each other. This does not create any computational problem since all the discontinuities of the velocity field are removed, but it is very unrealistic. In our model we impose that if two or more vortices are at a distance, d, less than a fraction, f, of the maximum radius between the two, r_{max}, a collision event is flagged and the two vortices are cancelled. A new vortex is created at the average position of the former two, with strength and radius given by averages between the ones of the two cancelled vortices. The parameter that controls the merging, f, is fixed during the execution of the program.

This procedure may appear very artificial but prevents us from including the very non-physical feature of two vortices that overlaps without merging.

A similar condition is used for those vortices that were pushed close to the boundary. This situation is treated like the collision of a vortex with its image and the algorithm used to model this situation is equal to the one just described for the vortex/vortex collision. It was therefore natural to define a stripe of width δ=(0.5fr) in which the vortex of radius r is absorbed. The width of the stripe varies with the radius of the colliding vortex. This situation is sketched in figure 3.6.

The input/output of the program is discussed in appendix 3A.1

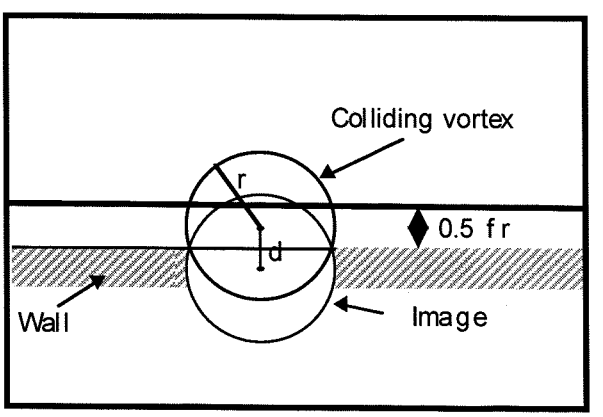

Fig 3.6: Collision of a vortex with its image. The stripe of width 0.5fr in which the vortex is absorbed, is also shown.

3.2.2 Test of the program and tuning

We now discuss some test cases in order to evaluate the errors introduced by the integration algorithm. Therefore we simulated some situations for which analytical solutions are available. We also show how the time step was chosen. All the values given below are non-dimensional.

a. Single vortex near the boundary

This is the simple situation already discussed in section 2.2.2 a (see also figure 2.3). The velocity of the vortex parallel to the wall is given by formula 2.11. The calculation of the abscissa of the position of a vortex with strength $\Gamma=2$ at a distance $d=1/(4\pi)$ from the wall after a time interval of 10 is compared with the theoretical value $x_{teo}=20$. The relative error, calculated as $\mu=|x_{teo} - x_{mod}|/x_{teo}$, where x_{mod} is the abscissa calculated with "point", was $1\cdot10^{-4}$ .The time step was $\Delta t=0.001$.

b. Two vortices near the boundary

We now go back to the two cases described in section 2.2.2 b. In the first, when the line passing through the centre of the vortices is parallel to the wall (fig. 2.5), we suppose that the vortices are initially at a distance d from each other and at an infinite distance from the boundary. We used the program "point" to calculate the distance of the two vortices from the wall when they have moved sufficiently apart that it can be assumed they move only under the effect of their images. We have taken two vortices of absolute strengths $\Gamma=100$ at an initial distance of d=50 from each other and of 1000 from the wall. The theory predicts a final distance of the vortices from the wall of d/2. If we rewrite equation 2.14 as:

$$y^2 = \left(\frac{4}{d^2} - \frac{1}{x^2}\right)^{-1}, \tag{3.9}$$

we have:

$$y \xrightarrow[x\to\pm\infty]{} \frac{d}{2}. \tag{3.10}$$

The value of d/2 calculated with our program, with a time step $\Delta t=0.01$, was 25.0000.

If the axis of the dipole is tilted of an angle θ to the wall, relation 2.18 can be used instead to calculate the value of c/2. With reference to figure 2.6, we choose $\theta=45^{\circ}$, $x_0=-x_1=25$, $y=1000$ and $\Gamma=\pm100$. With a time step $\Delta t=0.01$ we obtained, for the positive vortex $y_{\infty}=18.1897$ and for the negative vortex $y_{\infty}=68.1380$ (y_{∞} indicates that the values has been taken when the mutual influence of the real vortices is negligible if compared with the effect of the images i.e. when the abscissa of the vortices remain constant). The relative error on the ordinate of the positive vortex was $\mu=6\cdot10^{-3}$ and $\mu=2\cdot10^{-3}$ for the negative one.

c. Estimate of the error using the Hamiltonian

In section 3.2.1 c, we pointed out that the second order moment of the strengths (formula 2.6) is not defined if the sum of the strengths is zero. On the other hand the interaction kinetic energy, W (formula 2.7), can still be calculated and, since this is the Hamiltonian, it must be constant during the motion of the vortices. It is convenient to use W to choose the time step so that the variations of W are kept within fixed limits. Once a suitable time step has been set for a particular run, if the initial conditions of other experiments are similar enough, the same time step may be used. As an example, we show one experiment in which twenty vortices, each with equal strength $\Gamma=40$, are placed in a square box of size 9 x 9 (fig. 3.7).

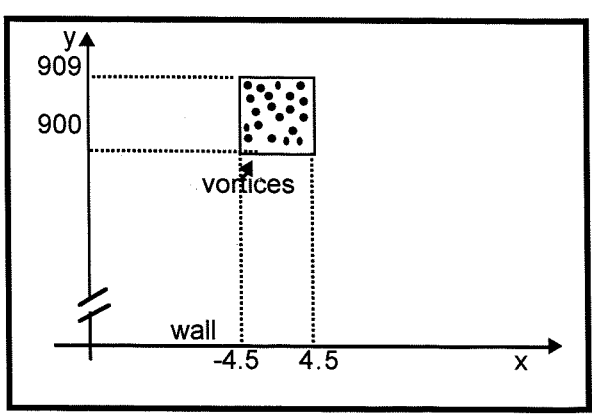

Fig 3.7: Initial position of vortices. For each experiment all the vortices are placed randomly inside a square box of size 9 x 9 (non- dimensional units). The offset of the square box relative to the wall is 900.

All the vortices have the same radius, r=0.2, and the merging parameter (see section 3.2 d) is f=0.5. We performed ten runs in which we varied randomly the initial position of the vortices inside the square box. The initial co-ordinates were calculated with a random number generator that used a uniform distribution (see appendix 3A.1). For $\Delta t=5\cdot10^{-4}$, the absolute variation, μ, of the interaction kinetic energy relative to its initial value after $1.2\cdot10^{5}$ iterations (corresponding to $t_{max}=60$), are reported in table 3.1. No merging events happened.

Run:	01	02	03	04	05	06	07	08	09	10
μ, 10^{-3}	1	1	0.02	0.03	0.01	0.03	0.05	0.03	0.02	0.02

Tab 3.1. Variations of the Hamiltonian of a system of point vortices relative to its initial value after a non-dimensional time of 60.

The use of Rankine's vortices makes the use of formula 2.7 not completely correct since the vorticity is not concentrated in one point. The parameter μ can be interpreted as a measure of how well our model reproduces the behaviour of a system of point vortices. The choice of a small radius r for the core of the vortices should be regarded more as an artifice to avoid high speeds near their centres than a physical feature.

This experiment reveals other interesting properties that will be further discussed in section 3.4.1. We assumed that since algorithm is able to integrate the trajectory of the vortices properly, it is also reliable, to the same extent, for the integration of the paths followed by the marked particles. For this reason no further checks were made. More applications of the 2-D model are described in section 3.4.

3.3 Implementation of the 3-D numerical model

The program "smoke" was designed to calculate the motion of a system of axisymmetric and co-axial vortex rings and the motion and the dispersion of a group of marked particles. It is based on formulae 2.30 and 2.31, and this represents our model for vortices moving over a planar sloping bottom (see section 2.3.3).

3.3.1 Program "smoke"

a. Velocity field

Like in the 2-D model, there is no background flow and the velocity field induced by a single vortex is described by formulae 2.31 a and b. Formulae 2.31 fail if $I_1=0$ (see also fig. 2.10 b), for then $\lambda=1$ and the elliptic integrals are not defined. The use of cored vortices is still necessary to avoid discontinuities. Similarly, if $I_1=I_2$, i.e. when the point at which we want to calculate the velocity lies on the axis $\sigma=0$ in fig. 2.10 b, the velocity cannot be calculated with the stream function 2.21; in this case $\lambda=0$ and formulae 2.32 and 2.33 are not defined. To calculate the velocity induced at a point (x,σ) by n vortex rings, the cores of which have centre co-ordinates $(x_{0,i}, \pm\sigma_{0,i})$ (see fig. 2.10 b), we use the following set of relations:

$$u=u_1+u_2+u_3, \qquad (3.11\ a)$$

$$v=v_1+v_2+v_3, \qquad (3.11\ b)$$

with:

$$\begin{cases} u_1 = \sum_{i=1}^{n} \frac{1}{\sigma} \frac{\partial \psi_i}{\partial \sigma}, & \forall i : l_{1,i} > r_i,\ l_{1,i} \neq l_{2,i}; \\ u_2 = \sum_{i=1}^{n} \frac{\Gamma_i}{2\pi} \frac{R_i^2}{\left[R_i^2 + \left(x - x_{0,i}\right)^2 \right]^{\frac{3}{2}}}, & \forall i : l_{1,i} > r_i,\ l_{1,i} = l_{2,i};, \\ u_3 = \sum_{i=1}^{n} v_{c,i}, & \forall i : l_{1,i} \leq r_i. \end{cases} \qquad (3.12\ a)$$

and

$$\begin{cases} v_1 = \sum_{i=1}^{n} -\frac{1}{\sigma} \frac{\partial \psi_i}{\partial x}, & \forall i : l_{1,i} > r_i,\ l_{1,i} \neq l_{2,i}; \\ v_2 = 0, & \forall i : l_{1,i} > r_i,\ l_{1,i} = l_{2,i}; \\ v_3 = 0. & \forall i : l_{1,j} \leq r_i, \end{cases} \qquad (3.12\ b)$$

The stream function ψ_i is given by 2.21. The expression for u_2 comes from the integration of the Biot-Savart law for this special situation[8] and $v_{c,i}$ is given by formula 2.30. We also imposed that the velocity of a particle of fluid inside the core of a vortex is the same as the self-induced velocity for that vortex [in other words the effect of the vortex on the particle is that of a pure translation with a speed equal to the speed of the vortex]. However the effect of the remaining vortices is added.

In section 2.2.1 we observed that a straight line vortex has no influence on itself. On the contrary, in section 2.3.1, we showed that a curved line vortex has a self-induced velocity. This feature is contained in formula 3.12 a via the term u_3, that also plays its role when $l_{1,i}$ =0. In this particular case the self induced velocity of the i^{th} vortex is added to all the other terms [there is

[8]The expression for u_2 is formally equivalent to the magnetic field generated by a circular loop of electric current on its axis of symmetry (e.g. Halliday & Resnick, 1981, ch. 34)

an analogy between this situation and a point vortex moving under the influence of its mirror image].

Cored rings require more care compared with the 2-D case because, while with Rankine's vortices a finite core is a device to eliminate the discontinuities, a finite core determines the self-induced velocity of the ring. Therefore the choice of the radius cannot merely be based on considerations of numerical efficiency.

b. Integration of the velocity field

We have used the same algorithm described for the 2-D case (see section 3.2.1 b).

c. Boundary conditions

This model does not require extra boundary conditions given the equivalence between an array of vortex rings and an array of vortices in a wedge-like domain (see section 2.3.3).

d. Other features

We suppose that the core of the vortex has a finite cross section that satisfies the condition $\varepsilon \ll 1$ (see section 2.3.1, formula 2.28). The vortex core is not a circumference but an ellipse (see formula 2.29), but in the limit of small cross section the circular approximation can be made (see fig. 3.8). In our model it is therefore assumed that the cross section of the ring is circular.

As with the Rankine's vortex model, we need to solve the problem of vortices approaching too closely. The case of a vortex that starts to overlap with another one is represented by the condition $d<r_1+r_2$, where d is the distance between the centres of the two vortices and r_1+r_2 is the sum of their radii. We also assume that the vortices can collide and merge (see section 3.2.1 d).

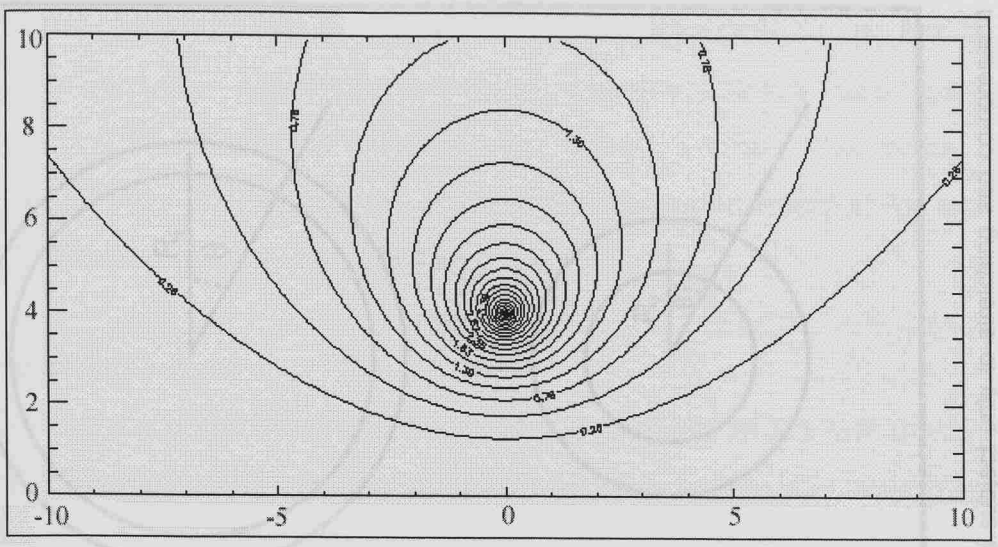

Fig 3.8: Streamlines for a circular ring vortex in a frame of reference moving with the vortex. The interval between the lines is constant. The streamlines close to the vortex centre are approximately circular.

An inviscid vortex moving across isobaths in a wedge-like region of fluid is subject to compression and stretching with consequent variation of its radius. In our model a vortex ring that changes its radius R accounts for the change cross-section of a vortex in a wedge (fig. 3.9). The conservation of volume for a torus of radius R and cross-section area of πr^2 is:

$$2\pi^2 R_i r_i^2 = 2\pi^2 R_f r_f^2, \qquad (3.13)$$

from which:

$$r_f = r_i \sqrt{\frac{Ri}{R_f}}. \qquad (3.14)$$

where the subscripts i and f refer to the initial and final situation. When a vortex approaches the axis of symmetry, as the depth h (and the radius R) decreases, the area of the cross section increases and eventually becomes infinite for vanishingly small depths. This situation violates the condition for a thin cored ring, on which the theory discussed in chapter 2

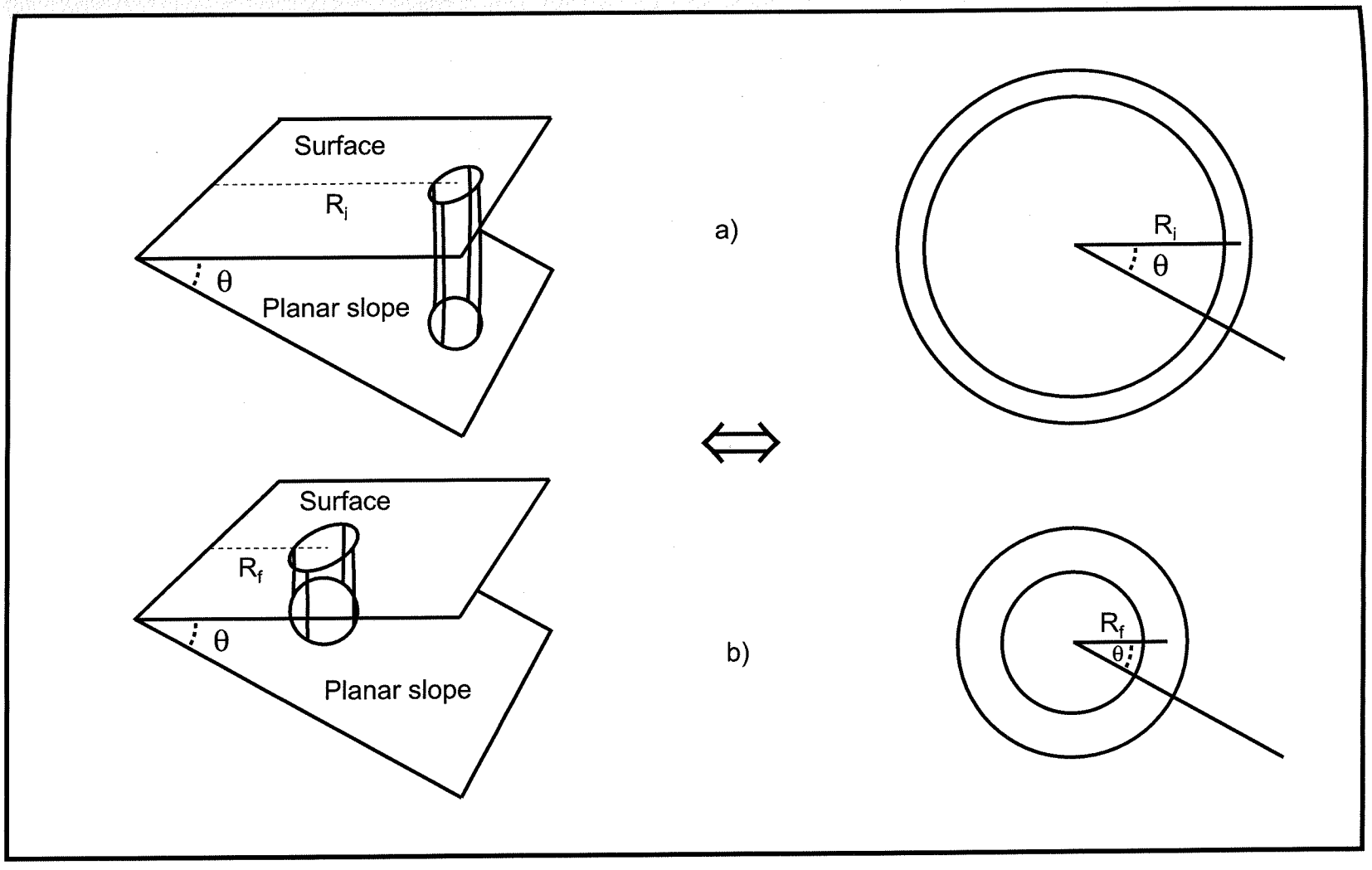

Fig 3.9: An inviscid vortex that moves from a deep region (a) to a shallow region (b) and subject only to stretching and compression conserves its volume in the same way as the equivalent vortex ring. The final size of the core can be calculated with formula 2.43 (section 2.3.2)

is based. However we considered vortices with $0 \leq \varepsilon \leq 2^{1/2}$, i.e. the family ranging (Norbury, 1973) from thin-cored rings ($\varepsilon \ll 1$) to the Hill's spherical vortex ($\varepsilon = 2^{1/2}$). When the condition $\varepsilon > 2^{1/2}$ was verified, the vortex was cancelled (this condition is the equivalent "absorption event at the wall" in the 2-D model, see section 3.2.1 d).

e. Input and output

The structure of the input and the output is identical to the one discussed for the Rankine's vortices (see appendix 3A.1)

3.3.2 Test of the program and tuning

In this section we evaluate the performance of the program "smoke" by comparing some cases for which analytical solutions are available with our numerical calculations. All the values given in the following sections are non-dimensional.

a. Single vortex ring

An isolated vortex ring, i.e. a vortex ring in absence of other vortices, background flow and boundaries, has a self-induced velocity given by formula 2.30. With the program "smoke" we calculated the position of a vortex ring with characteristics: $\Gamma=2$, $r=0.1$, $R=R_0$. R_0 is chosen so that the self-induced velocity of the ring is 0.5; this value is obtained by solving numerically the equation for R_0:

$$\pi = F(R_0) = \frac{1}{R_0}\left\{\log\frac{8R_0}{0.1} - \frac{1}{4} + \left(\frac{0.1}{R_0}\right)^2\left[-\frac{3}{8}\log\frac{8R_0}{0.1} + \frac{15}{32}\right]\right\}.$$

For $R_0=1.426219$ we found $F(R_0)-\pi = -6^{-11}$. With a time step $\Delta t=0.001$, at $t=10$ we compared the distance travelled by the vortex with the theoretical value $x_{teo}=5$. The relative error, as defined in section 3.2.2 a, is $\mu=1\cdot10^{-4}$.

b. Ring pair

This situation, analogous to the 2-D case of section 3.2.2 b, was discussed in section 2.3.2, where an analytical expression for the radius of two counter-rotating rings of equal absolute strength moving an infinite distance apart, $R_{\infty,teo}$, was given as a function of their initial separation, of the radius of the ring R and of radius of the core r (formula 2.47). The situation studied with the program "smoke" consisted of two rings with: $\Gamma=\pm 20$, $R_1=R_2=37.7$, $r_1=r_2=1$ and initial separation s=7.7. The time step was $\Delta t=0.01$. The relative error of the radius R_∞, $\mu=|(R_{\infty,teo}- R_{\infty,mod})/ R_{\infty,teo}|$, when the two vortices are at a distance from each other such that $R_{\infty,mod}$ calculated by the program "smoke" remains constant, was $\mu=2.2\cdot 10^{-4}$.

c. Estimate of the error using the kinetic energy

In section 2.3.2 we used the conservation of the interaction kinetic energy to describe some details of the motion of two counter-rotating and coaxial vortex rings with cross-section area small compared with the area of the ring. Since the rings are co-axial the axial symmetry is preserved and the formula for the kinetic energy is particularly simple. The same considerations made there apply to a system of n thin cored coaxial vortex rings. The total kinetic energy is:

$$\mathcal{E} = \sum_{i=1}^{n} \mathcal{E}_i + 2\sum_{i=1}^{n-1}\sum_{j=I+1}^{n} \mathcal{E}_{ij}, \qquad (3.15)$$

where $\mathcal{E}_j$ is the kinetic energy of an isolated ring, formula 2.40, and $\mathcal{E}_{ij}$ is the interaction kinetic energy between the vortex i and the vortex j. Assuming that the stream function of the vortex j is constant inside the core of the vortex i, the interaction kinetic energy of the vortex rings is (using formula 2.44):

$$\mathcal{E}_{ij} = \frac{\Gamma_i \Gamma_j}{2}\left(I_{1,ij} + I_{2,ij}\right)\left[K(\lambda_{ij}) - E(\lambda_{ij})\right], \qquad (3.16)$$

with

$$I_{1,ij} = \sqrt{\left(x_i - x_j\right)^2 + \left(\sigma_i - \sigma_j\right)^2}, \qquad (3.17\ a)$$

$$I_{2,ij} = \sqrt{\left(x_i - x_j\right)^2 + \left(\sigma_i + \sigma_j\right)^2}, \qquad (3.17\ b)$$

where λ_{ij} is defined by 2.24. Likewise in the 2-D case (see section 2.2.1), $\mathcal{E}$ is also the Hamiltonian (e.g. Saffman, 1992) and must remain constant. In our experiments the time step was chosen in order to keep the variation of $\mathcal{E}$ within pre-fixed limits. The complete elliptic integrals of formula 3.16 where computed with two FORTRAN double-precision library routines constructed on the Carlson's algorithm based on his formulation of the problem in terms of standard integral of the first and second kind (e.g. Press et al, 1992). This algorithm is much more robust, fast and reliable than the formulation of K(λ) and E(λ) with the hypergeometric function (section 2.3.1, formula 2.27). In table 3.2 we show the variations of $\mathcal{E}$ relative to its initial value in a series of 10 experiments similar to the ones described in section 3.2.2 c (see also fig. 3.7).

Run:	01	02	03	04	05	06	07	08	09	10
$\mathcal{N}$	4	1	2	1	2	3	3	3	2	3
μ, 10^{-2}	1	0.4	0.6	0.4	1	1	0.9	0.7	0.6	1

Tab 3.2. Variations of the Hamiltonian (μ, see section 3.2.2 c) of a system of 20 vortex rings relative to its initial value after a non-dimensional time of 20. $\mathcal{N}$ is the number of vortices that have been cancelled either after a collision with another vortex or because the condition for the Hill's spherical vortex, $\zeta>2^{1/2}$ see section 3.3.1 d, has been violated. Other initial conditions: strength $\Gamma=80$ for all vortices; initial radius of the cross section $\varepsilon=1$ for all vortices; size of the square box (see fig.3.7): 15 x 15; distance of the centre of the square box from the shoreline: 10.5; time step: $\Delta t=5\cdot10^{-4}$; number of iterations $4\cdot10^{4}$ (corresponding to a non dimensional time t=20). The initial position of the vortices was calculated with a generator of random numbers (see appendix 3A.1).

3.4 Preliminary experiments

We present some experiments for which conclusions on the dispersion of vortices and particles can be made with the help the theory of point vortices and of vortex rings. We shall consider two archetypal situations: 1) the vortices have equal positive strength (i.e. the system has a net positive vorticity); 2) the vortices have equal strength but may have opposite sign such that the net vorticity is, or nearly is, zero. In both cases the vortices are far enough from the boundary that the action of the images is negligible if compared with the mutual effect of the real vortices. We intend to:

- study some basic mechanisms responsible for the dispersion of vortices and particles and their relative importance;

- gain further confidence in the performances of the two computer programs.

The definitions of the dispersions for vortices and particles and the related eddy dispersion coefficients are given in appendix 3A.1.

3.4.1 Dispersion of vorticity and particles far from the wall - I. The case of equal vortices

a. Experiment set-up

We now discuss in more details the experiment described in section 3.2.2 c (see fig. 3.7). Before we analysed only the conservation of the Hamiltonian but nothing was said on the dispersion of vortices and particles of fluid. An additional set of 10 runs was made with the 3-D model using the same initial conditions of the 2-D experiment, (with the only difference of t_{max}=20). The initial radius of the vortex rings was r=0.2 (like the 2-D case). We also computed the displacement of 100 marked particles of fluid, initially filling the square area shown in figure 3.7 and located at the nodes of a regularly spaced grid.

b. Results from the 2-D model

The results were very similar for each of the 10 experiments, and one example is shown in figures 3.10 to 3.12. The total dispersions of vortices and particles and their x and y components are shown in figures 3.10 and 3.11. Figure 3.12. is the plot of the eddy dispersion coefficient for the vortices.

c. Results from the 3-D model

The same quantities described in the previous section were calculated with the 3-D model and the results were all very similar. A typical example is shown in figures 3.13 to 3.15.

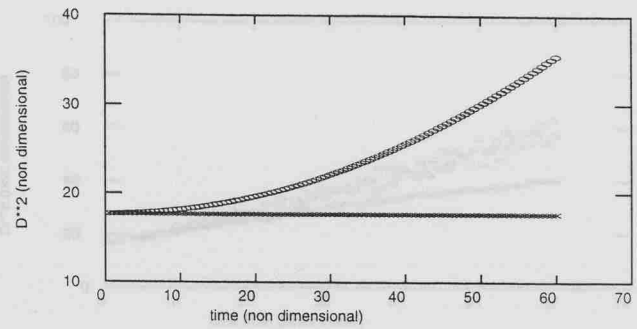

a)

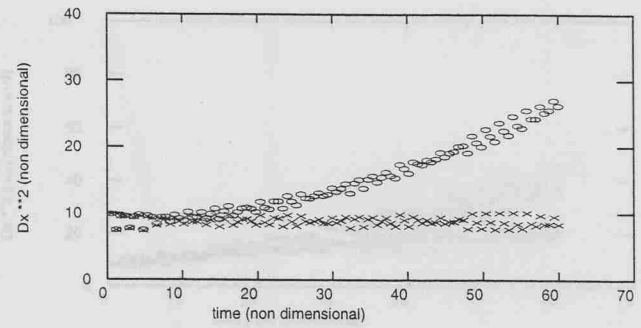

b)

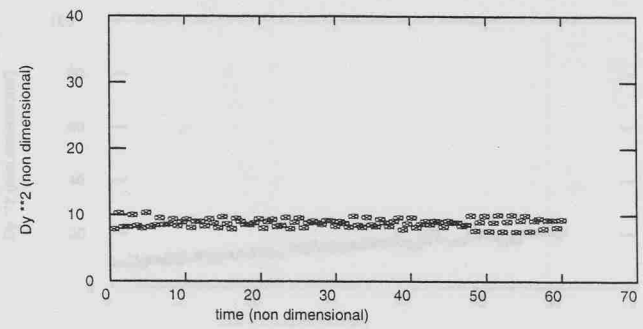

c)

Fig 3.10: 2-D model. Dispersion of vortices. See appendix 3A.1 for a definition of the dispersion. a) Plot of $D^2_{v,0}$ (o) and $D^2_{v,t}$ (x) versus time. b) Plot of $DX^2_{v,0}$ (o) and $DX^2_{v,t}$ (x) versus time. c) Plot of $DY^2_{v,0}$ (o) and $DY^2_{v,t}$ (x) versus time.

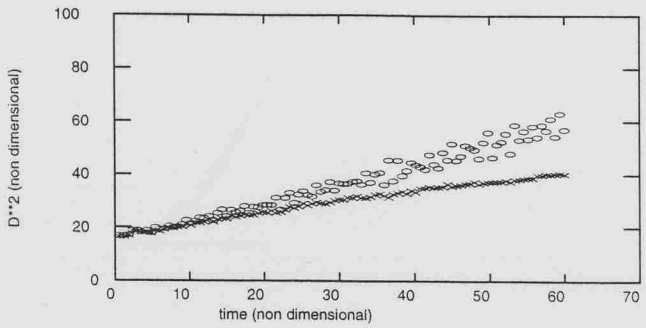

a)

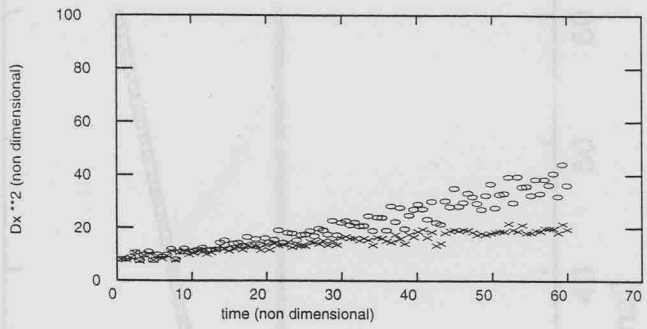

b)

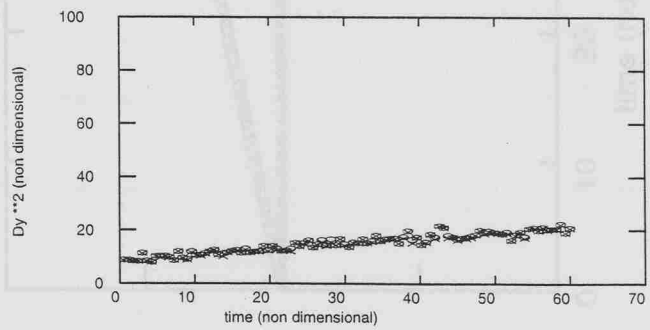

c)

Fig 3.11: 2-D model. Dispersion of particles. See appendix 3A.1 for a definition of the dispersion.a) Plot of $D^2_{m,0}$ (o) and $D^2_{m,t}$ (x) versus time. b) Plot of $DX^2_{m,0}$ (o) and $DX^2_{m,t}$ (x) versus time. c) Plot of $DY^2_{m,0}$ (o) and $DY^2_{m,t}$ (x) versus time.

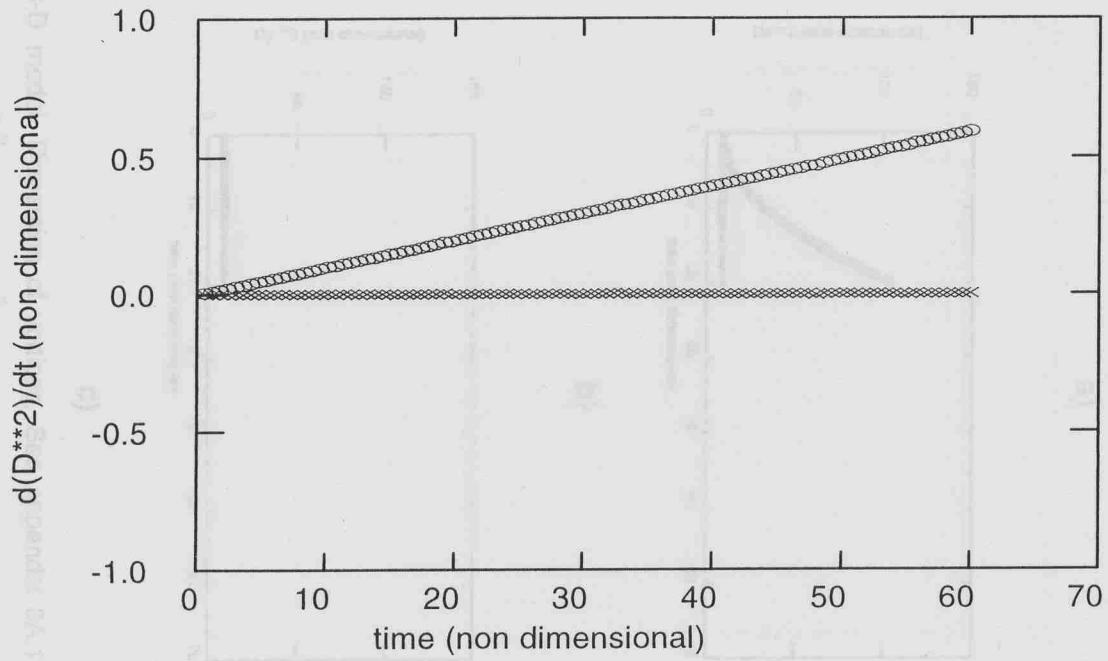

Fig 3.12: 2-D model. Plot of the rate of change of the dispersion of vortices ($k_{v,0}$ (o) and $k_{v,t}$ (x)) versus time. See appendix 3A.1 for the definition.

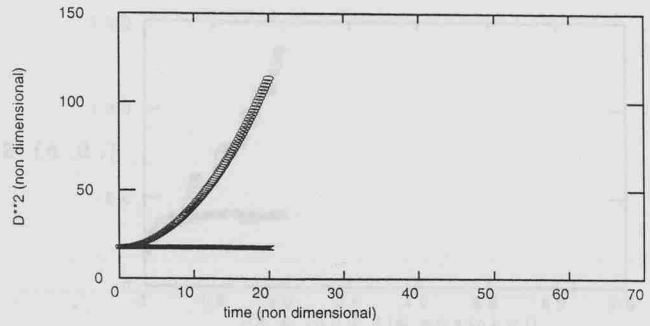

a)

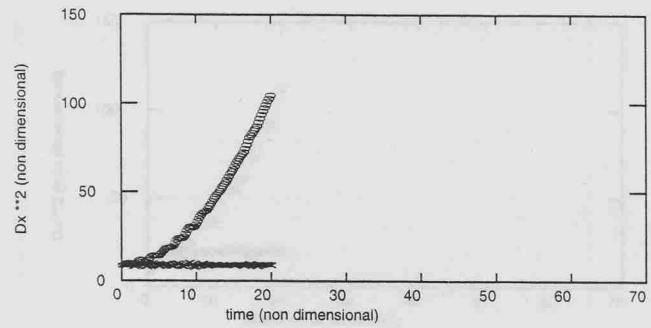

b)

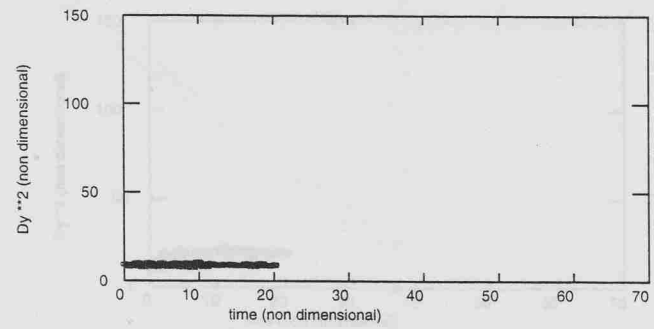

c)

Fig 3.13: 3-D model. Dispersion of vortices. See appendix 3A.1 for a definition of the dispersion. a) Plot of $D^2_{v,0}$ (o) and $D^2_{v,t}$ (x) versus time. b) Plot of $DX^2_{v,0}$ (o) and $DX^2_{v,t}$ (x) versus time. c) Plot of $DY^2_{v,0}$ (o) and $DY^2_{v,t}$ (x) versus time.

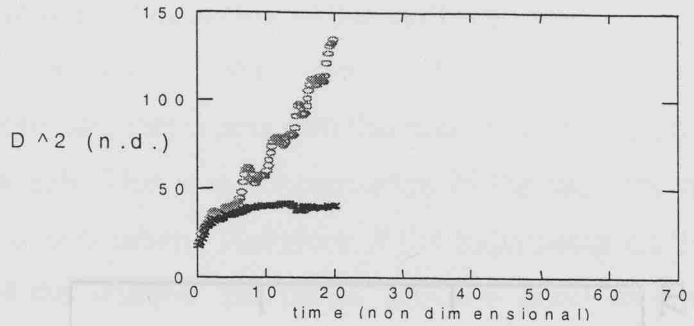

a)

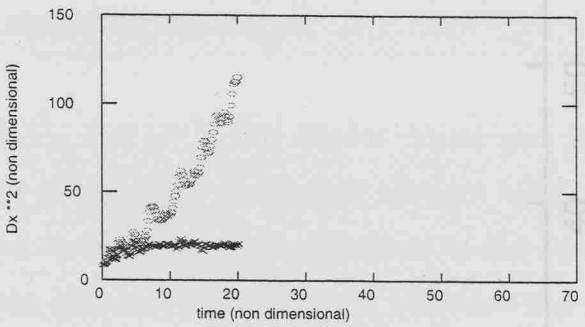

b)

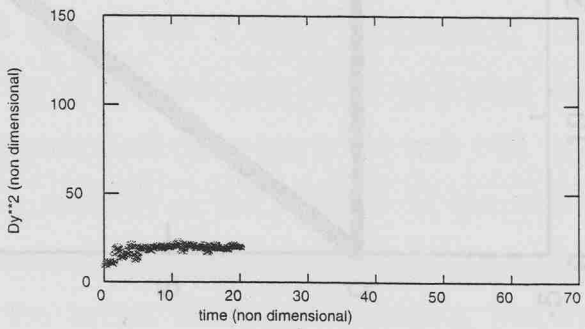

c)

Fig 3.14: 3-D model. Dispersion of particles. See appendix 3A.1 for a definition of the dispersion.a) Plot of $D^2_{m,0}$ (o) and $D^2_{m,t}$ (x) versus time. b) Plot of $DX^2_{m,0}$ (o) and $DX^2_{m,t}$ (x) versus time. c) Plot of $DY^2_{m,0}$ (o) and $DY^2_{m,t}$ (x) versus time.

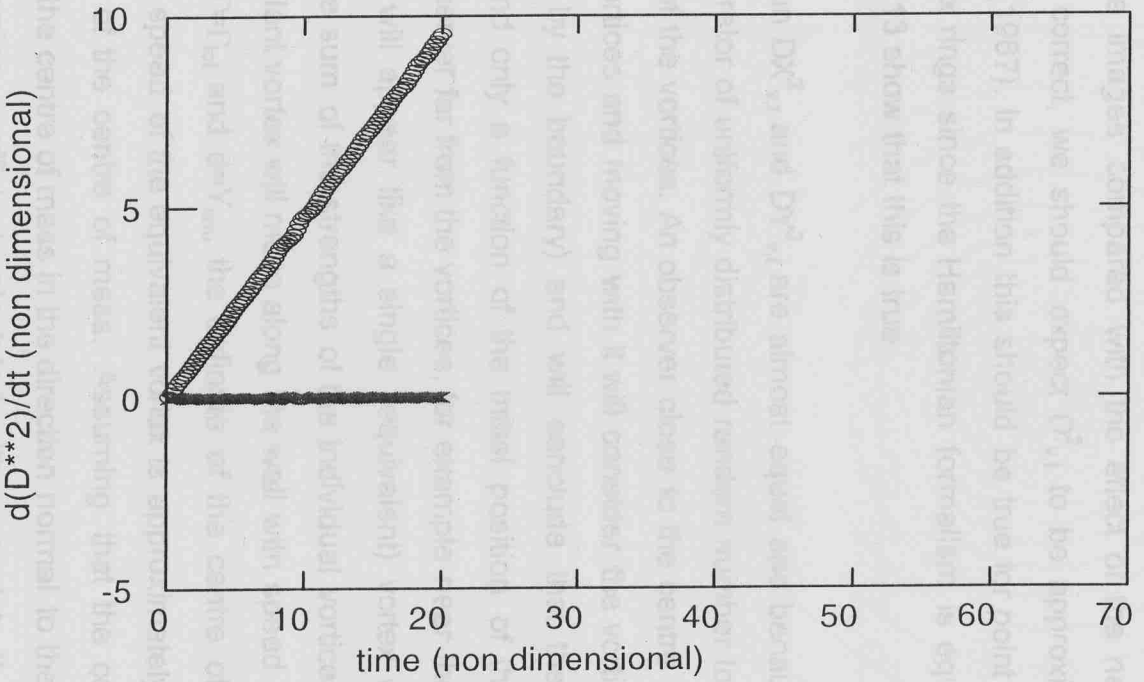

Fig 3.15: 3-D model. Plot of the rate of change of the dispersion of vortices ($k_{v,0}$ (o) and $k_{v,t}$ (x)) versus time. See appendix 3A.1 for the definition.

d. Discussion : dispersion of the vortices

$D^2_{v,t}$ (dispersion of the vortices from the instantaneous centre of circulation) calculated only with the real vortices is proportional to D^2 (formula 2.6). This is a consequence of the fact that all the vortices have the same circulation. Therefore, if the hypothesis on the smallness of the effect of the images compared with the effect of the neighbouring real vortices is correct, we should expect $D^2_{v,t}$ to be approximately constant (Batchelor, 1967). In addition this should be true for point vortices as well as for vortex rings since the Hamiltonian formalism is equivalent. Figures 3.10 and 3.13 show that this is true.

For each run $DX^2_{v,t}$ and $DY^2_{v,t}$ are almost equal and because we used the same generator of uniformly distributed random number to initiate both co-ordinates of the vortices. An observer close to the centre of vorticity of the cloud of vortices and moving with it will consider the vortices isolated (i.e. unaffected by the boundary) and will conclude that their dispersion is constant and only a function of the initial position of the vortices. To a second observer far from the vortices, for example near the wall, the group of vortices will appear like a single (equivalent) vortex with strength Γ_{tot} equal to the sum of the strengths of the individual vortices (see fig. 3.16). The equivalent vortex will move along the wall with speed given by formula 2.11 with $\Gamma=\Gamma_{tot}$ and $d=Y_{cm}$, the ordinate of the centre of mass; in other words, the speed of the equivalent vortex is approximately coincident with the speed of the centre of mass. Assuming that the component of the velocity of the centre of mass in the direction normal to the wall is zero, the eddy dispersion coefficient calculated with respect to the initial centre of mass, $k_{v,0}$, is given by (see appendix 3A, section 3A.2 for the derivation of formula 3.18):

$$k_{v,0} = 2V_x\left[X_{cm}(t) - X_{cm}(t_0)\right] = 2V_x^2(t - t_0), \qquad (3.18)$$

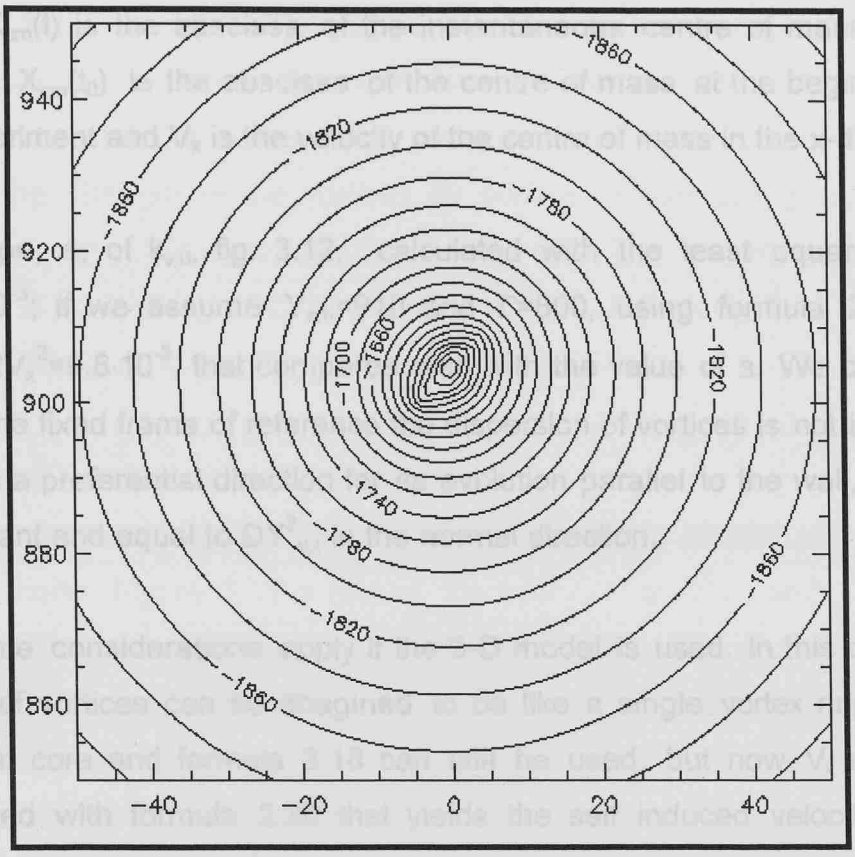

Fig 3.16: Stream-function, in a fixed frame of reference, generated by 20 Rankine's vortices, each of non-dimensional strength of 40. This picture is the plot of the same stream-function showed in figure 3.3 but now on a larger domain. The contour lines are now spaced by 20. For a distant observer the group of vortices behaves like a single vortex, the strength of which is the sum of the strengths of the single vortices.

where $X_{cm}(t)$ is the abscissa of the instantaneous centre of mass at the instant t, $X_{cm}(t_0)$ is the abscissa of the centre of mass at the beginning of the experiment and V_x is the velocity of the centre of mass in the x-direction.

The slope, s, of $k_{v,0}$, fig. 3.12, calculated with the least square fit, is $s=9.9\cdot10^{-3}$; if we assume $Y_{cm}=910$ and $\Gamma=800$, using formula 2.11 we obtain $2V_x^2=9.8\cdot10^{-3}$, that compares well with the value of s. We conclude that in the fixed frame of reference the dispersion of vortices is not isotropic and has a preferential direction for its evolution parallel to the wall, while it is constant and equal to $DY^2_{v,t}$ in the normal direction.

The same considerations apply if the 3-D model is used. In this case the cluster of vortices can be imagined to be like a single vortex ring with a turbulent core and formula 3.18 can still be used, but now V_x must be calculated with formula 2.30 that yields the self induced velocity of the equivalent ring: with $R\approx945$, $\Gamma=800$ and $r= D_{v,0}\approx4.2$, we obtained $V_x=0.488$ that compares well with the value s=0.479, where s is the slope of the curve in figure 3.15. The higher speed of the equivalent vortex in the three dimensional case is responsible for the faster growth of $D^2_{v,t}$ in figure 3.14 a and b compared with the 2-D case.

The first conclusion is that, in a situation in which the vortices are far from the boundary, uniformly distributed and all equal, the choice of the way in which the dispersion is calculated is very important. If the dispersion is calculated relative to the instantaneous centre of mass of the vortices its value is constant and equal in the directions parallel and normal to the wall. If the dispersion is calculated with reference to the initial centre of mass, the steady translation of the system of vortices along the boundary will give the impression that the dispersion of the vortices along the wall is much greater then in the normal direction.

When the vortices are not all equal $D^2_{v,t}$ is not constant but nevertheless it appears to be bounded. The amplitude of its oscillation depends on the differences of circulation amongst the vortices. We made three more experiments with the same initial conditions described above, but now varying the strength of the vortices by adding or subtracting a random fraction of their reference circulation (Γ_{ref}=40). The maximum possible variation of strength was 100%. The results are shown in fig. 3.17 and 3.18 for variations of up to ± 20%, ±60% and ±100%.

e. Discussion: dispersion of the tracer

The tracer behaves quite differently and only partially similar conclusions can be made. Figure 3.11 a shows the evolution of $D^2_{m,0}$ and $D^2_{m,t}$ with time: the first shows a faster growth if compared to the second. Figures 3.11 b and c show that $DX^2_{m,0}$ still grows faster than $DX^2_{m,t}$ while the y components of the two dispersions are almost equal: therefore the particles are isotropically dispersed in the plane if the $D^2_{m,t}$ is taken as a measure of dispersion, but the x direction, parallel to the wall, appears to be a preferential direction if $D^2_{m,0}$ is used. This is again a consequence of the translation of the centre of mass of the vortices along the wall, as already discussed for the vortices. Fig. 3.14 a, b and c show that the same conclusions can be reached for the 3-D model but now the growth rate of dispersion is much faster and appears to reach its maximum after a non dimensional time of about 10. We conclude that a system of coaxial vortex rings is, at least in this situation, a more efficient stirrer.

The dispersion of particles seems to have a maximum. This can be explained by considering that the system of real vortices and images, as seen from a distant position, can be considered like a single vortex dipole or a single vortex ring. After a sufficient long time, the particles will be

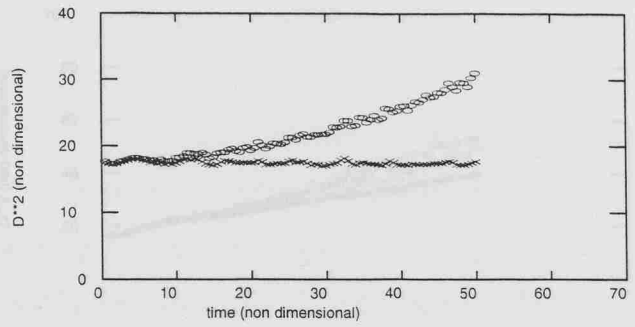

a)

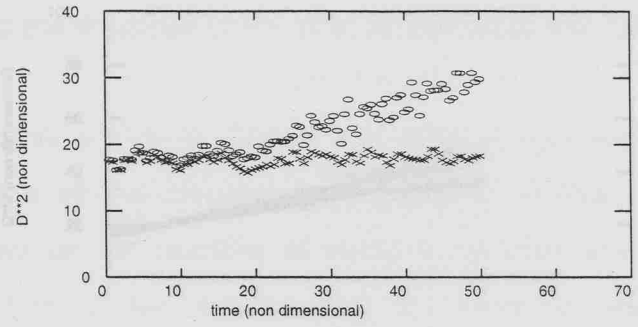

b)

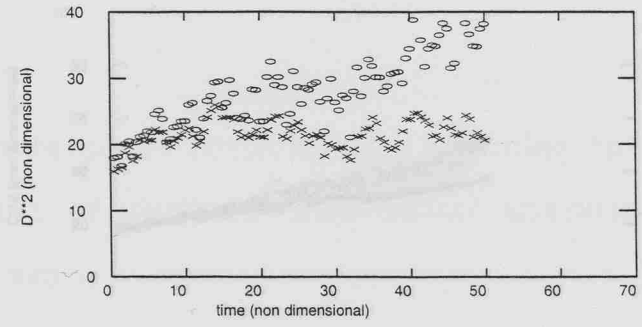

c)

Fig 3.17: 2-D model. Dispersion of vortices. See appendix 3A.1 for a definition of the dispersion. a) Plot of $D^2_{v,0}$ (o) and $D^2_{v,t}$ (x) versus time with $\Delta\Gamma_{max}/\Gamma = \pm 20\%$ b) Plot of $D^2_{v,0}$ (o) and $D^2_{v,t}$ (x) versus time with $\Delta\Gamma_{max}/\Gamma = \pm 60\%$ c) Plot of $D^2_{v,0}$ (o) and $D^2_{v,t}$ (x) versus time with $\Delta\Gamma_{max}/\Gamma = \pm 100\%$.

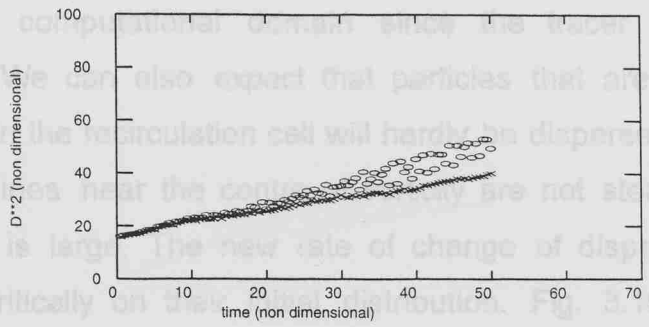

a)

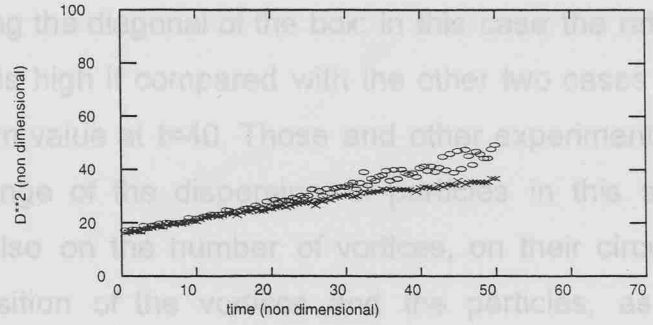

b)

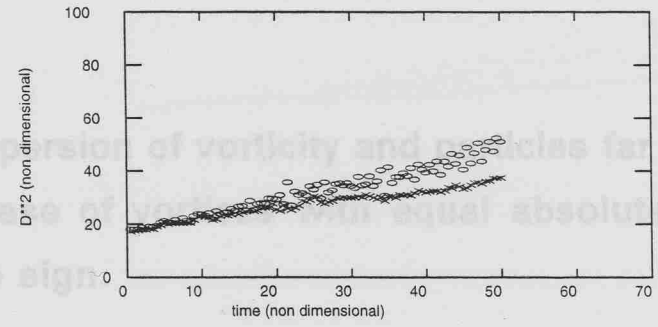

c)

Fig 3.18: 2-D model. Dispersion of particles. See appendix 3A.1 for a definition of the dispersion. a) Plot of $D^2_{m,0}$ (o) and $D^2_{m,t}$ (x) versus time with $\Delta\Gamma_{max}/\Gamma=\pm20\%$ b) Plot of $D^2_{m,0}$ (o) and $D^2_{m,t}$ (x) versus time with $\Delta\Gamma_{max}/\Gamma=\pm60\%$ c) Plot of $D^2_{m,0}$ (o) and $D^2_{m,t}$ (x) versus time with $\Delta\Gamma_{max}/\Gamma=\pm100\%$.

stirred until when they fill half of the recirculation cell[9] [but only in the real part of the computational domain since the tracer cannot cross the boundary]. We can also expect that particles that are initially uniformly distributed in the recirculation cell will hardly be dispersed. On the contrary the streamlines near the centre of vorticity are not steady and there the dispersion is large. The new rate of change of dispersion of particles depends critically on their initial distribution. Fig. 3.19 illustrates three experiments in which the size of the box containing the tracer at the initial instant (concentric with the box containing the vortices) was varied. Figure 3.19 b) refers to an initial situation in which the vortices were lying almost exactly along the diagonal of the box: in this case the rate of change of the dispersion is high if compared with the other two cases and $D^2_{m,t}$ reaches its maximum value at t=40. Those and other experiments suggest that the rate of change of the dispersion of particles in this set of experiments depends also on the number of vortices, on their circulation and on the relative position of the vortices and the particles, as well as on their distribution. Interestingly, figure 3.18 shows that $D^2_{m,t}$ and $k_{m,t}$ do not depend, for these experiments, on inequalities of circulation between the vortices.

3.4.2 Dispersion of vorticity and particles far from the wall - II. The case of vortices with equal absolute strength and opposite sign.

a. Experiment set-up

This experiment is similar to the one described in section 3.4.1 but now each vortex may have a strength of Γ=40 or of Γ=-40. Therefore the total

[9]The recirculation cell is bounded by an almost stationary streamline, in the frame of reference moving with the centre of mass of the cloud of vortices. The tracer cannot cross this border (see also section 2.2.2 a).

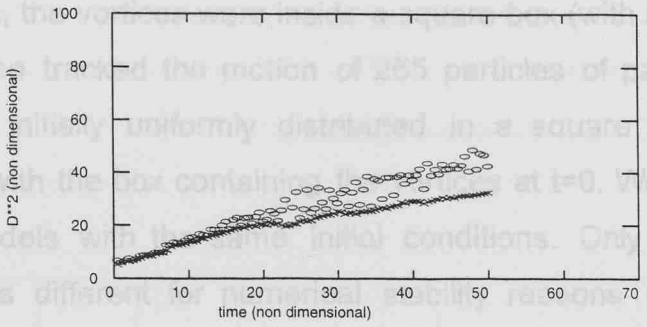

a)

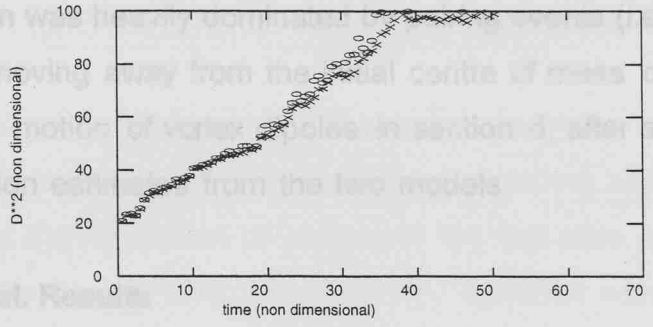

b)

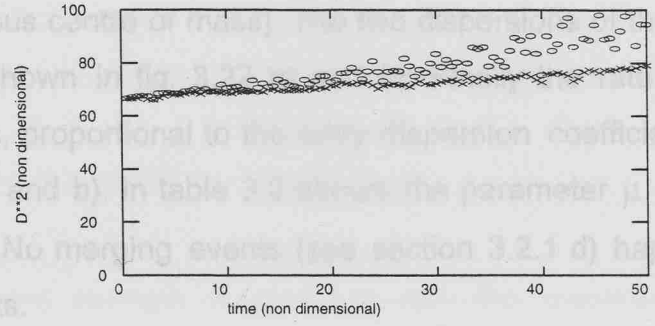

c)

Fig 3.19: 2-D model. Dispersion of particles. See appendix 3A.1 for a definition of the dispersion. Experiment with 100 particles. a) Plot of $D^2_{m,0}$ (o) and $D^2_{m,t}$ (x) versus time with box size (for particles) of 4.5 x 4.5. b) Plot of $D^2_{m,0}$ (o) and $D^2_{m,t}$ (x) versus time with box size (for particles) of 9 x 9 and vortices on the diagonal of the box. c) Plot of $D^2_{m,0}$ (o) and $D^2_{m,t}$ (x) versus time with box size (for particles) of 18 x 18.

strength is, or is nearly, zero. As before, at the beginning of the experiments, the vortices were inside a square box (with size 9 x 9, see fig. 3.7). We also tracked the motion of 255 particles of passive tracer. The tracer was initially uniformly distributed in a square box of 18 x 18, concentric with the box containing the vortices at t=0. We run the 2-D and the 3-D models with the same initial conditions. Only the radius of the vortices was different for numerical stability reasons (r=0.2 for the 2-D model and r=1.0 for the 3-D model).

Since the vortices had opposite sign and equal absolute strength this configuration was heavily dominated by pairing events (i.e. by the formation of dipoles moving away from the initial centre of mass of the system). We discuss the motion of vortex dipoles in section d, after a brief summary of the dispersion estimates from the two models.

b. 2-D model. Results

The estimates of $D^2_{v,0}$ and $D^2_{v,t}$ for similar initial conditions were very different [see fig. 3.20 a), b) and c) for plots of dispersion from the initial centre of mass and fig. 3.21 a), b), c) for plots of dispersion from the instantaneous centre of mass]. The two dispersions of the tracer, $D^2_{m,0}$ and $D^2_{m,t}$, are shown in fig. 3.22 a) and b). Finally the rate of change of the dispersions, proportional to the eddy dispersion coefficients, are shown in fig. 3.23 a) and b). In table 3.3 shows the parameter μ (see section 3.2.2 section c). No merging events (see section 3.2.1 d) happened during the experiments.

Run:	01	02	03	04	05	06	07	08	09	10
μ, 10^{-3}	3.3	0.4	1.5	0.7	7.0	2.6	7.2	3.1	5.3	1.0

Table 3.3. 2-D model. Variations of the Hamiltonian relative to the initial value (μ) after a non-dimensional time of 20. The time step (in all the experiments) was $\Delta t=5\cdot10^{-4}$.

c. 3-D model. Results

The same parameters presented in the previous section were computed with the 3-D model (see fig. 3.20 to 3.23). The relative variations of μ are given in table 3.4. No merging events (see section 3.3.1 d) happened during the experiments.

Run:	01	02	03	04	05	06	07	08	09	10
μ, 10^{-2}	1.8	0.07	0.2	0.5	0.9	0.4	0.3	0.8	0.5	0.1

Table 3.4. 3-D model. Variations of the Hamiltonian relative to the initial value (μ) after a non-dimensional time of 20. The time step (in all the experiments) was: $\Delta t=5\cdot10^{-4}$.

d. Discussion

The main difference between a 2-D system of vortices with nearly zero net total strength and one with net positive (or negative) strength (see section 3.4.1) is that the dispersion of vortices in the first case is in general a non predictable function of time: $D^2_{v,0}$ and $D^2_{v,t}$ increase with the time squared but values among experiments with similar initial conditions can be very different. From figures 3.20 a and 3.21 a it appears that the envelopes of the two dispersions are quite similar, implying that the position of the centre of vorticity varies slowly if compared with the position of the single vortices. The same observations are valid if the 3-D model is examined, (see fig. 3.20 d and 3.21 d). In both cases there are no preferential directions for the dispersion of vortices.

Since the net strength is close to zero the dispersion of vortices is dominated by the motion of pair of vortices of opposite sign (dipoles). See fig. 3.25 for the 2-D model at t=20, and fig 3.26 for the 3-D model at t=20. Figure 3.24 shows the position of the vortices and of the marked particles at the beginning of the two experiments. The dipoles were made of different vortices in the two runs but the same number of pairs formed. The dipoles of the 3-D model also travelled a bigger distance from the initial centre of mass and this explains the higher values of the dispersion of the

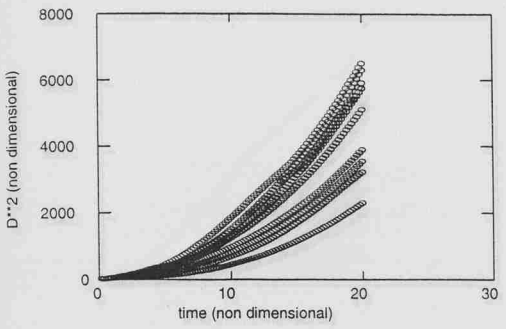

a)

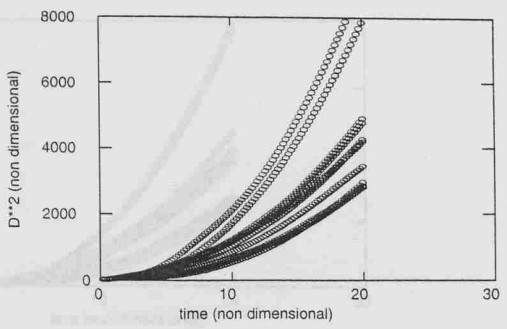

d)

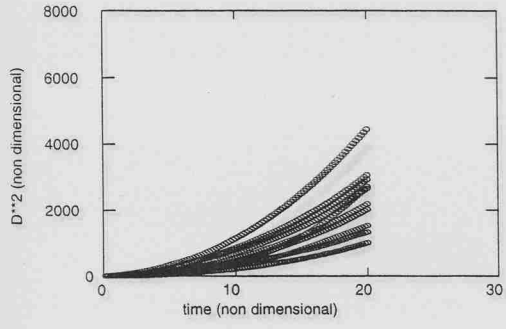

b)

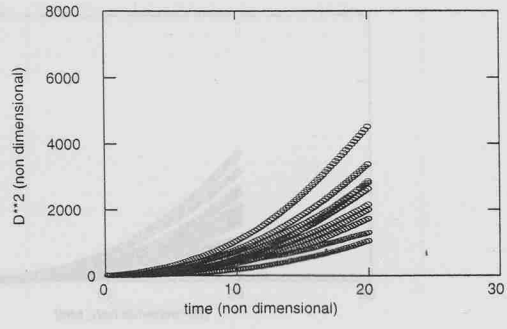

e)

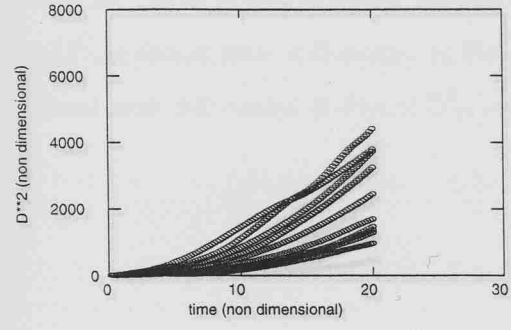

c)

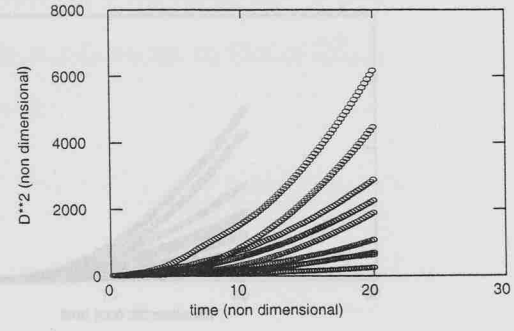

f)

Fig 3.20: Dispersion of vortices. See appendix 3A.1 for a definition of the dispersion. a) Plot of $D^2_{v,0}$ versus time: 2-D model. b) Plot of $DX^2_{v,0}$ versus time: 2-D model. c) Plot of $DY^2_{v,0}$ versus time: 2-D model. d) Plot of $D^2_{v,0}$ versus time: 3-D model. e) Plot of $DX^2_{v,0}$ versus time: 3-D model. f) Plot of $DY^2_{v,0}$ versus time: 3-D model.

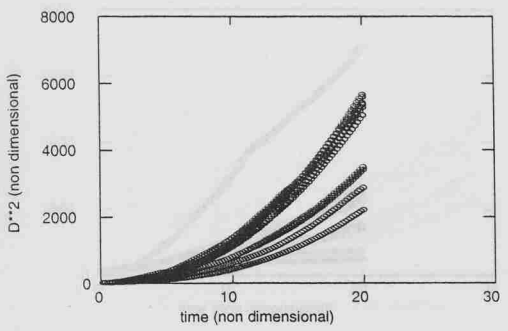

a)

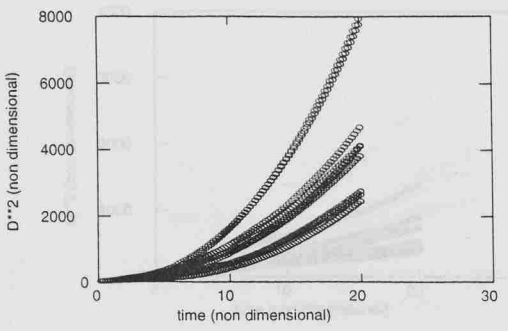

d)

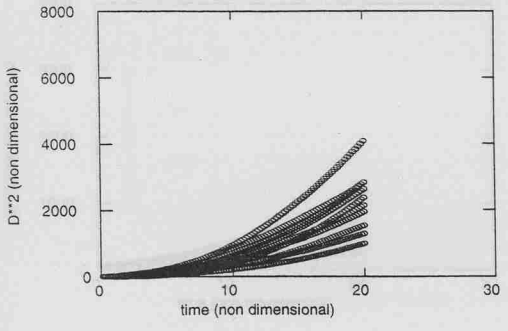

b)

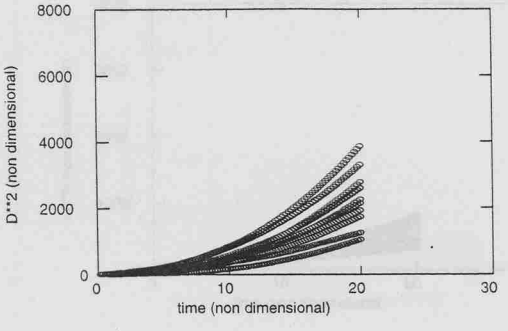

e)

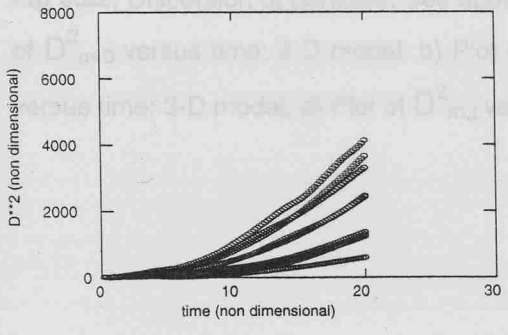

c)

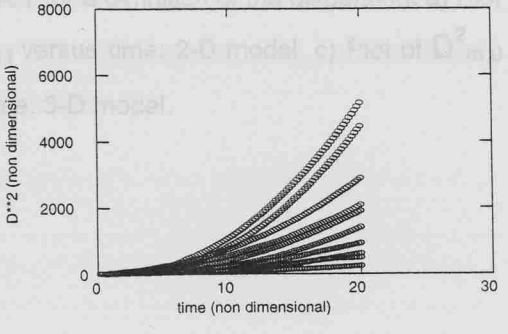

f)

Fig 3.21: Dispersion of vortices. See appendix 3A.1 for a definition of the dispersion. a) Plot of $D^2_{v,t}$ versus time: 2-D model. b) Plot of $DX^2_{v,t}$ versus time: 2-D model. c) Plot of $DY^2_{v,t}$ versus time: 2-D model. d) Plot of $D^2_{v,t}$ versus time: 3-D model. e) Plot of $DX^2_{v,t}$ versus time: 3-D model. f) Plot of $DY^2_{v,t}$ versus time: 3-D model.

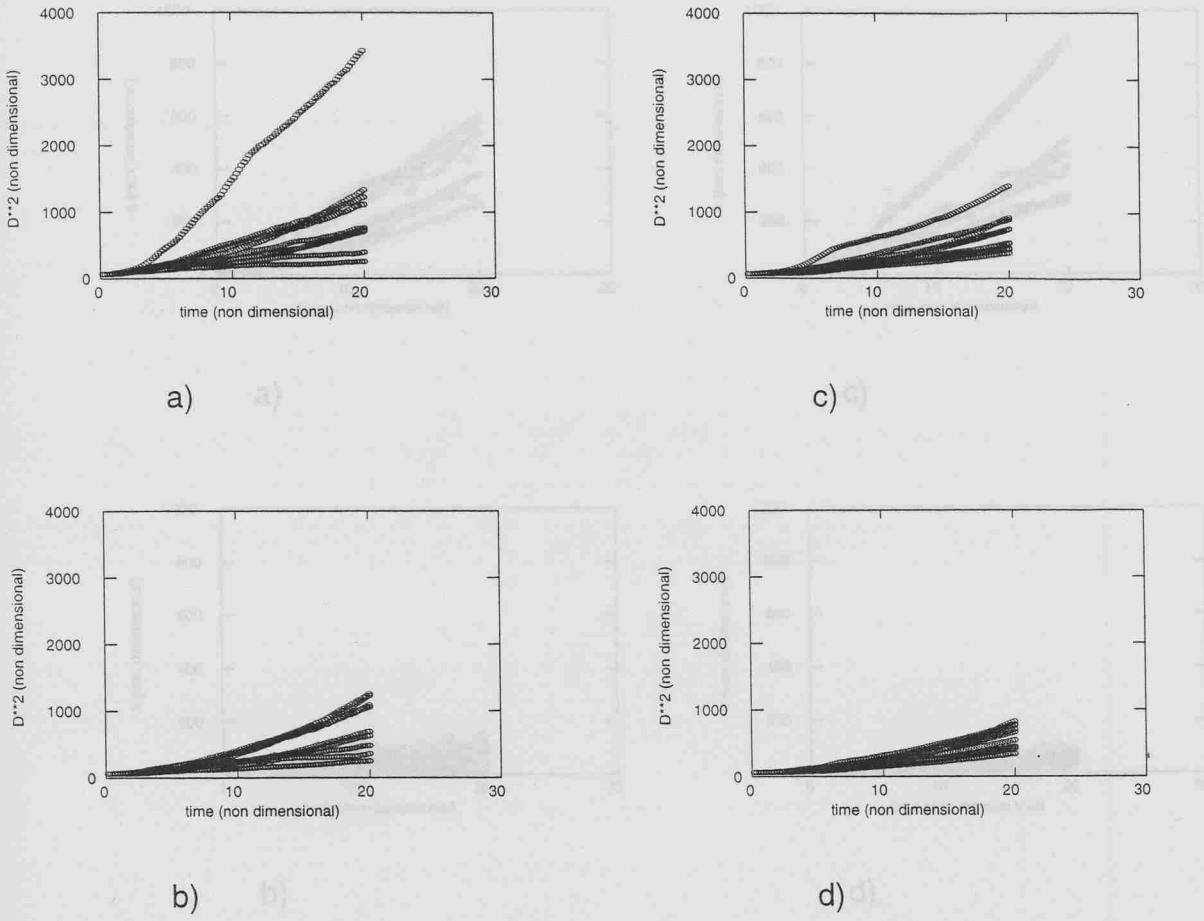

Fig 3.22: Dispersion of particles. See appendix 3A.1 for a definition of the dispersion. a) Plot of $D^2_{m,0}$ versus time: 2-D model. b) Plot of $D^2_{m,t}$ versus time: 2-D model. c) Plot of $D^2_{m,0}$ versus time: 3-D model. d) Plot of $D^2_{m,t}$ versus time: 3-D model.

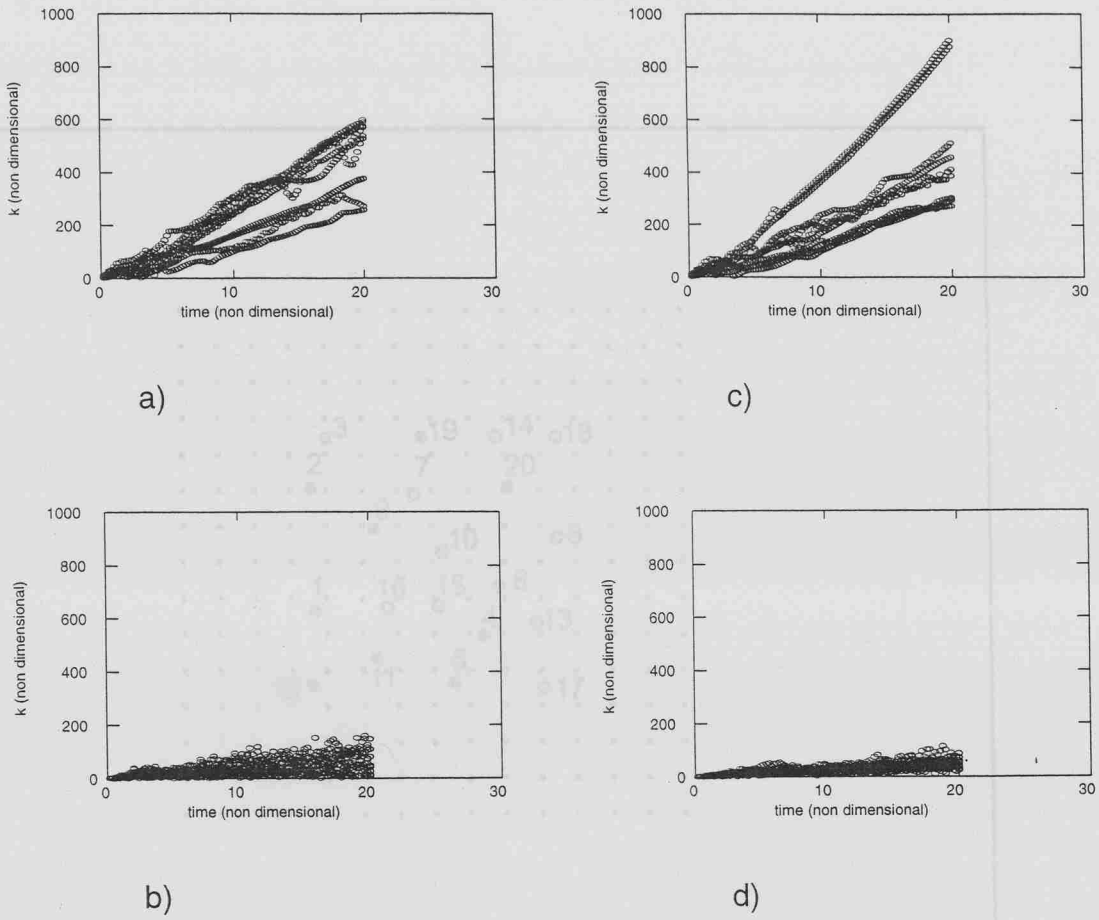

Fig 3.23: Eddy dispersion coefficients. a) Plot of $k_{v,t}$ versus time: 2-D model. b) Plot of $k_{m,t}$ versus time: 2-D model. c) Plot of $k_{v,t}$ versus time: 3-D model. d) Plot of $k_{m,t}$ versus time: 3-D model. See appendix 3A.1 for a definition of the symbols.

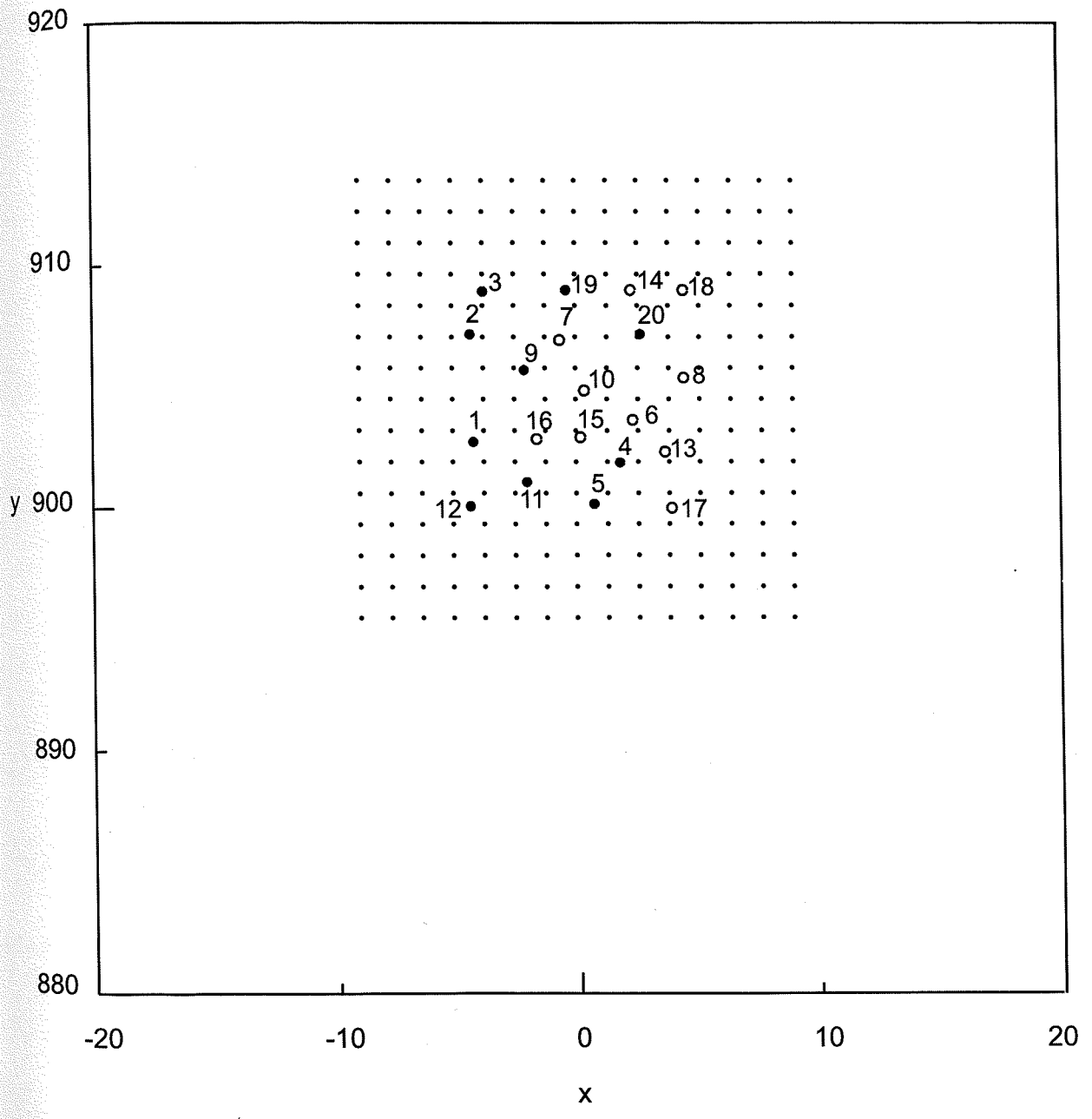

Fig 3.24: 20 Rankine's vortices (2-D model) are initially placed in a box of size 9 x 9 and 256 marked particles are contained in a concentric box of 18 x 18. The vortices have equal absolute strength, $|\Gamma|=40$, and may have opposite sign. The total circulation is zero. Vortices indicated with o are positive, and with • are negative. The smaller dots indicate the position of the tracer. A rigid infinite straight boundary is located at y=0.

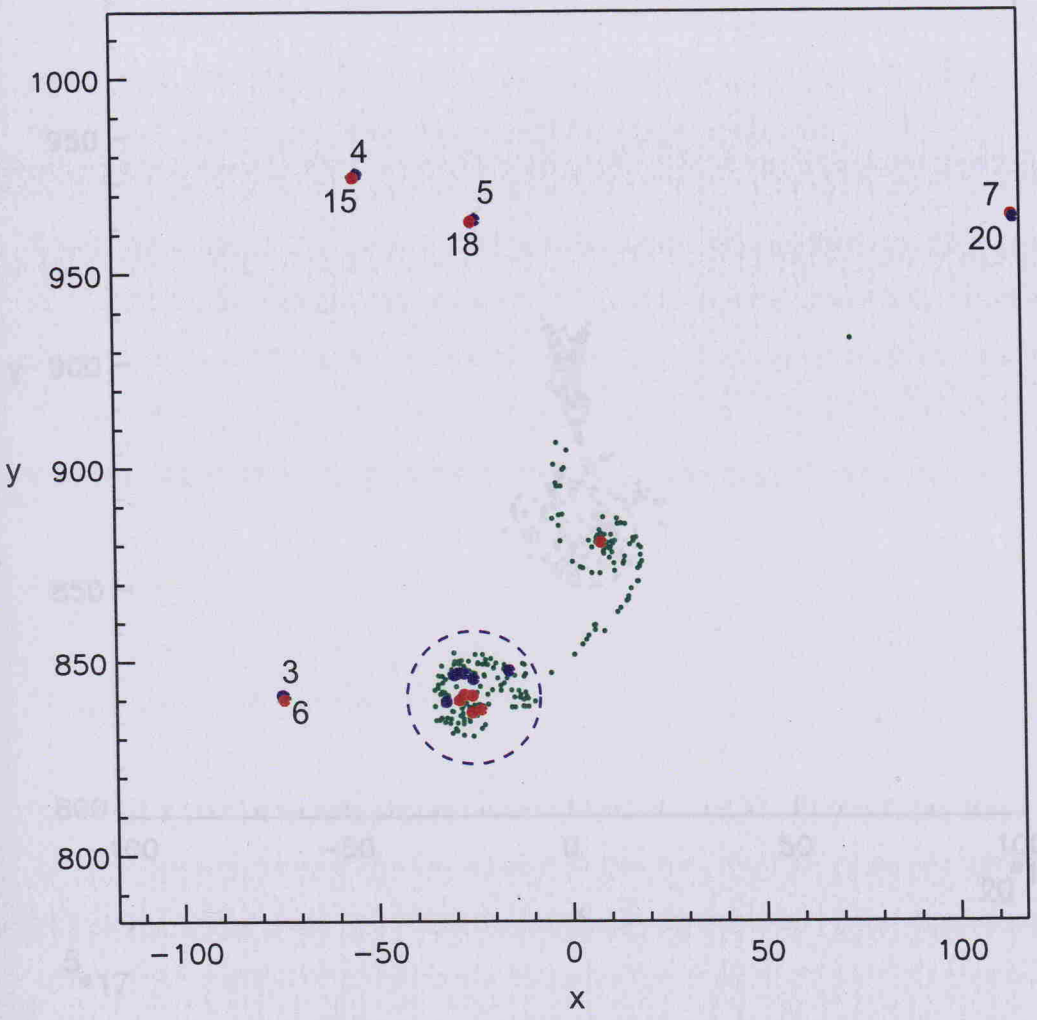

Fig 3.25: Evolution of the initial situation showed in fig. 3.24 (2-D model). Four dipoles (3&6, 4&15, 5&18 and 20&7) formed. The positive vortices are now indicated with red circles, the negative with blue circles. The size of the vortices is not to scale in order to make them more visible. The tracer position is indicated by the green dots. The distance (from the initial centre of mass) travelled by the dipoles was the biggest contribution to the dispersion of the vortices. The marked particles did not disperse as much as the vortices. The remaining vortices formed a dipole-like structure (blue dashed circle) that captured and transported most of the particles away from their initial centre of mass. This snapshot was taken at t=20 (non dimensional).

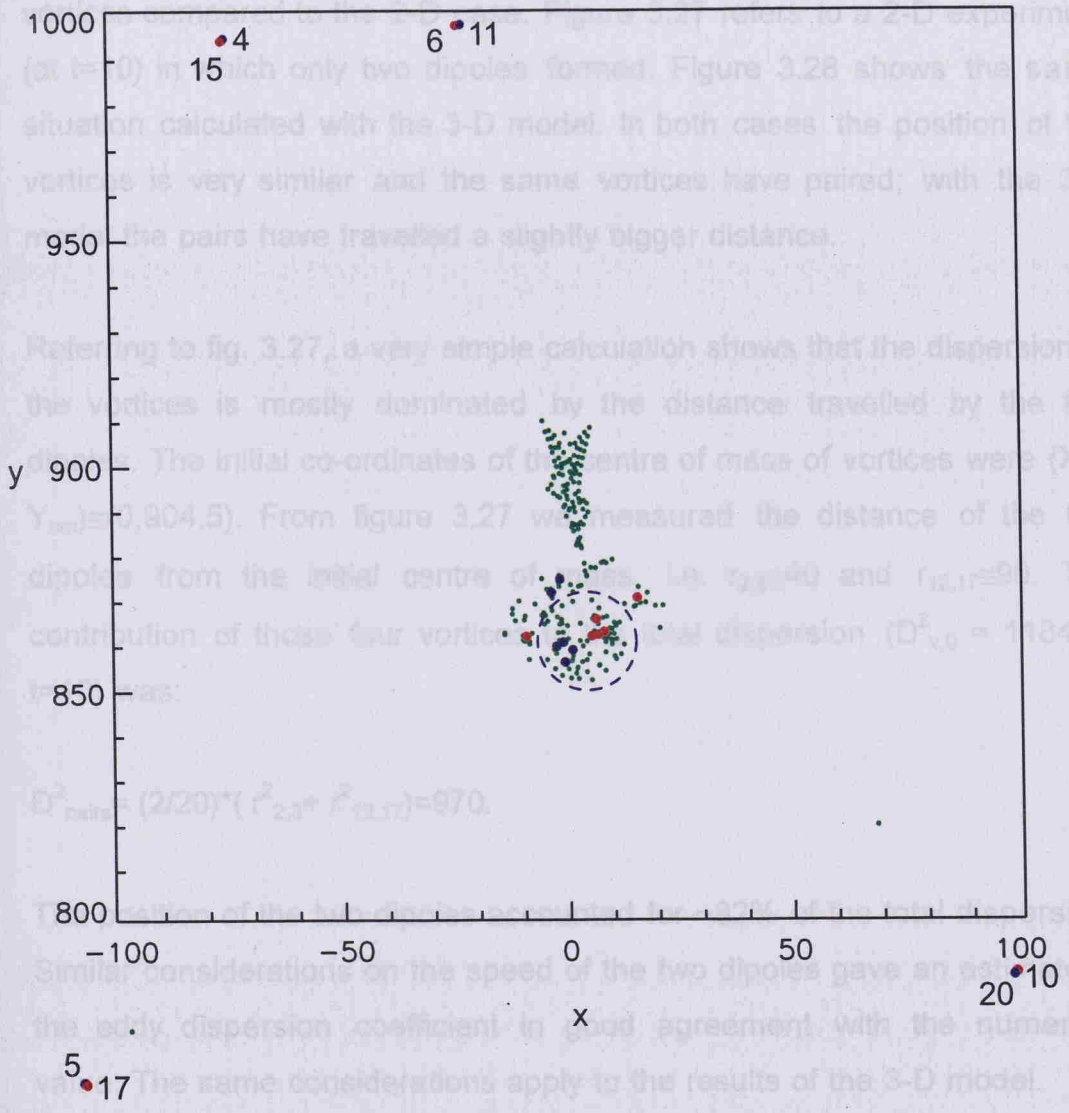

Fig 3.26: Evolution of the initial situation sketched in figure 3.24 (3-D model). The positive vortices are now indicated with red circles, the negative with blue circles. The tracer position is indicated by the green dots. The same number of dipoles of the corresponding 2-D simulation (fig. 3.25) formed but different vortices paired (20&10, 5&17, 4&15 and 11&6). As in the 2-D case the dispersion of vortices is dominated by the distance travelled by dipoles and dipolar structure (blue dashed circle) from the initial centre of mass of the vortices. This snapshot was taken at t=20 (non dimensional).

vortices compared to the 2-D case. Figure 3.27 refers to a 2-D experiment (at t=10) in which only two dipoles formed. Figure 3.28 shows the same situation calculated with the 3-D model. In both cases the position of the vortices is very similar and the same vortices have paired; with the 3-D model the pairs have travelled a slightly bigger distance.

Referring to fig. 3.27, a very simple calculation shows that the dispersion of the vortices is mostly dominated by the distance travelled by the two dipoles. The initial co-ordinates of the centre of mass of vortices were (X_{cm}, Y_{cm})≅(0,904.5). From figure 3.27 we measured the distance of the two dipoles from the initial centre of mass, i.e. $r_{2,3}$≅40 and $r_{12,17}$≅90. The contribution of those four vortices to the total dispersion ($D^2_{v,0}$ = 1184 at t=10) was:

$$D^2_{pairs}= (2/20)*(r^2_{2,3}+ r^2_{12,17})=970.$$

The position of the two dipoles accounted for ~82% of the total dispersion. Similar considerations on the speed of the two dipoles gave an estimate of the eddy dispersion coefficient in good agreement with the numerical value. The same considerations apply to the results of the 3-D model.

The dispersion of particles in the 2-D and in the 3-D cases was much smaller than the dispersion of vortices since only a small fraction of total number of particles was captured and carried away by the recirculation cell (see fig. 3.23 where the eddy dispersion coefficient, for vortices and particles are compared). A comparison between fig. 3.23 b and fig. 3.23 d shows that the rate of change with time of the dispersion of the tracer was faster for the 3-D model. One reason can be (see e.g. fig. 3.25, 2-D model) that most of the particles moved with the big cluster of vortices or were dispersed by them and left behind along the path followed by the cluster, while with the 3-D model (see fig. 3.26) the cluster of vortices moved a

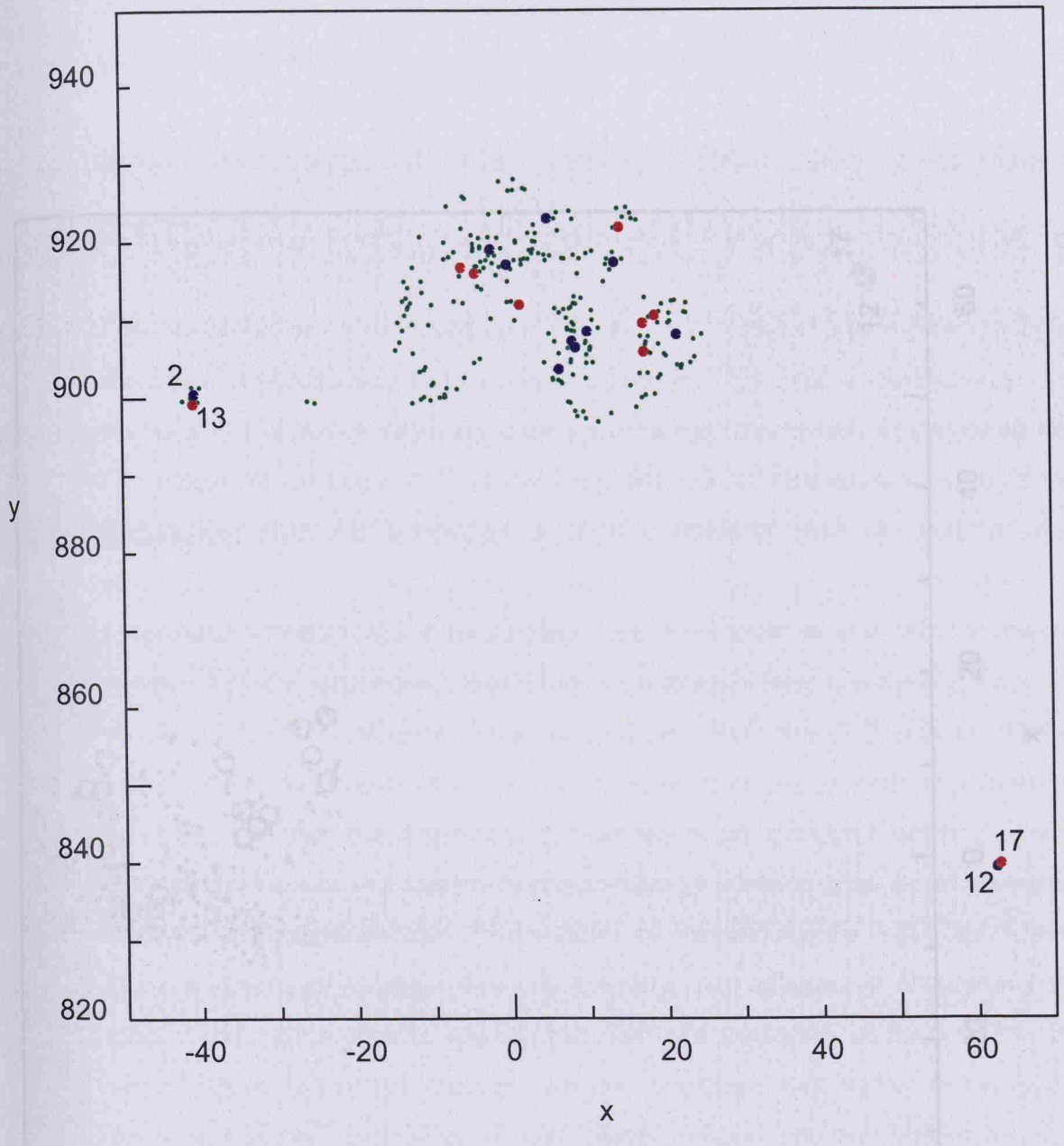

Fig 3.27: Evolution at t=10 (non dimensional) of an initial situation similar to the one illustrated in fig. 3.24 but now the net circulation is Γ=80. Only two dipoles (12&17 and 2&13) have formed. The rest of the vortices and particles are still close to the source area. The distance travelled by the two dipoles is the biggest contribution to the total dispersion of vortices (see section 3.4.2 d). 2-D model. The positive vortices are indicated with red circles, the negative with blue circles. The size of the vortices is not to scale in order to make them more visible. The tracer position is indicated by the green dots.

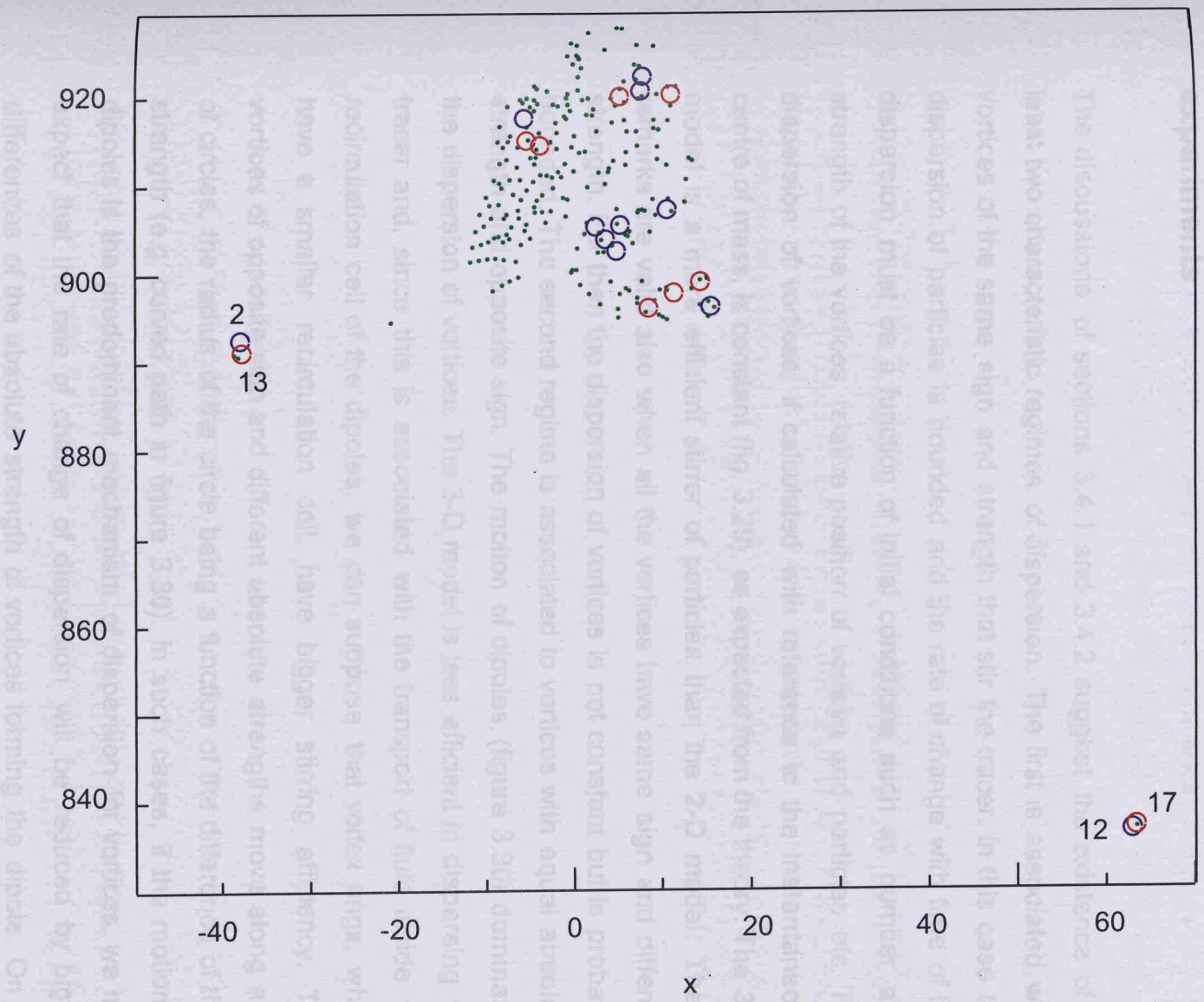

Fig 3.28: The same initial conditions (apart from the radius of the core) used for the experiment shown in fig. 3.27 were also used to run the 3-D model.This sketch shows the situation at t=10 (non dimensional, see fig. 3.27). The dipoles were formed by the same vortices of the 2-D case and moved in a very similar way.

shorter distance and much of the particles stayed close to their initial position. The dispersion of particles was almost isotropic for both models.

3.4.3 Summary of the results from the preliminary experiments

The discussions of sections 3.4.1 and 3.4.2 suggest the existence of at least two characteristic regimes of dispersion. The first is associated with vortices of the same sign and strength that stir the tracer. In this case the dispersion of particles is bounded and the rate of change with time of the dispersion must be a function of initial conditions such as number and strength of the vortices, relative position of vortices and particles etc. The dispersion of vortices, if calculated with reference to the instantaneous centre of mass, is constant (fig. 3.29), as expected from the theory. The 3-D model is a more efficient stirrer of particles than the 2-D model. These remarks are valid also when all the vortices have same sign and different strength. For then the dispersion of vortices is not constant but is probably bounded. The second regime is associated to vortices with equal absolute strength and opposite sign. The motion of dipoles (figure 3.30) dominates the dispersion of vortices. The 3-D model is less efficient in dispersing the tracer and, since this is associated with the transport of fluid inside the recirculation cell of the dipoles, we can suppose that vortex rings, which have a smaller recirculation cell, have bigger stirring efficiency. Two vortices of opposite sign and different absolute strengths move along arcs of circles, the radius of the circle being a function of the difference of their strength (e.g. curved path in figure 3.30). In such cases, if the motion of dipoles is the predominant mechanism of dispersion for vortices, we may expect that the rate of change of dispersion will be reduced by bigger differences of the absolute strength of vortices forming the dipole. On the contrary it will be greater if the vortices have the same absolute strength.

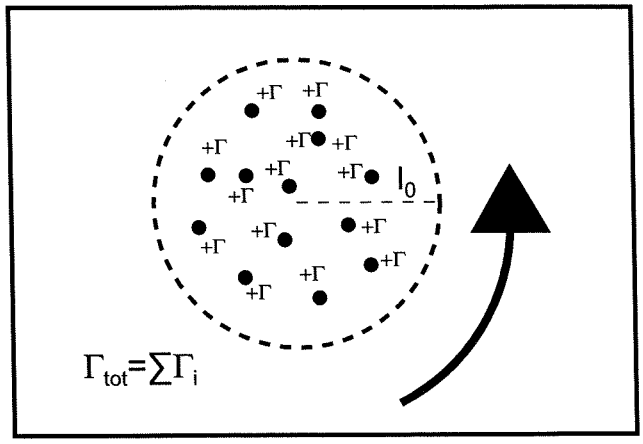

Fig 3.29: The dispersion of a system of positive (or negative) point vortices is bounded and of the same order of their initial dispersion (that is a function of the number of vortices and their relative position). The dispersion remains constant if the vortices are all equal. The area in which they are contained has a constant typical length scale l_0. The dispersion of a passive tracer is bounded too. The predominant mechanism of dispersion for particles is stirring by the vortices.

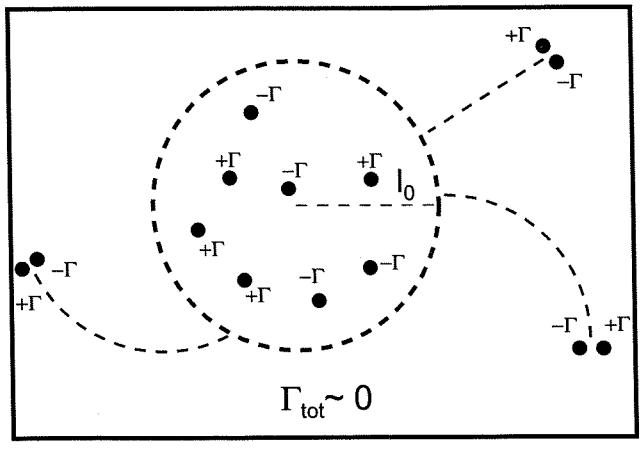

Fig 3.30: The dispersion of a system point vortices with $\Gamma_{tot} \cong 0$ is not bounded. The pairing of vortices of opposite sign is the dominant mechanism of dispersion for vortices. The associated transport of fluid is the corresponding mechanism of dispersion for particles.

3.5 Dispersion of vortices and mass near the wall- Case 1. Vortices and particles sharing the same surface

We now describe three sets of experiments that were designed to simulate the effect of a shoreline on the dispersion of vortices and tracer[10]. The vortices and the tracer are now close enough to the wall for the effect of the images to be of the same order as the mutual interaction of the real vortices. We shall compare the dispersion (of vortices and particles) in the direction normal to the shoreline with the dispersion in the direction parallel to the shoreline. We shall also compare the dispersion properties of the 2-D and 3-D models. We start by investigating a situation in which, at the beginning of the experiment, the vortices and the marked particles share the same surface. The distance and the area of this surface from the shore were changed between experiments. Different sets of experiments also have a different initial number of vortices. The experiments were designed to allow a statistical analysis of the results.

3.5.1 Experimental set-up

A typical initial situation, with 15 vortices and 676 marked particles is shown in figure 3.31. We created three different sets of initial conditions

---

[10]We are aware of the possibility to implement spatially periodic schemes using point vortex dynamics but it seems that a similar approach is not easily applied if vortex rings are used, or, more precisely, the required algorithm would increase the already long time for the execution of the program beyond acceptable limits. Since we want to compare the results from the two models, we do not use a periodic scheme in the x direction for the 2-D model even if it would probably be more appropriate. We would claim that, if we assume that the vortices are initially located near the centre of a near-shore circulation cell, so that the effect of neighbouring vortices could be neglected, our simulations would describe at least the initial trends in dispersion.

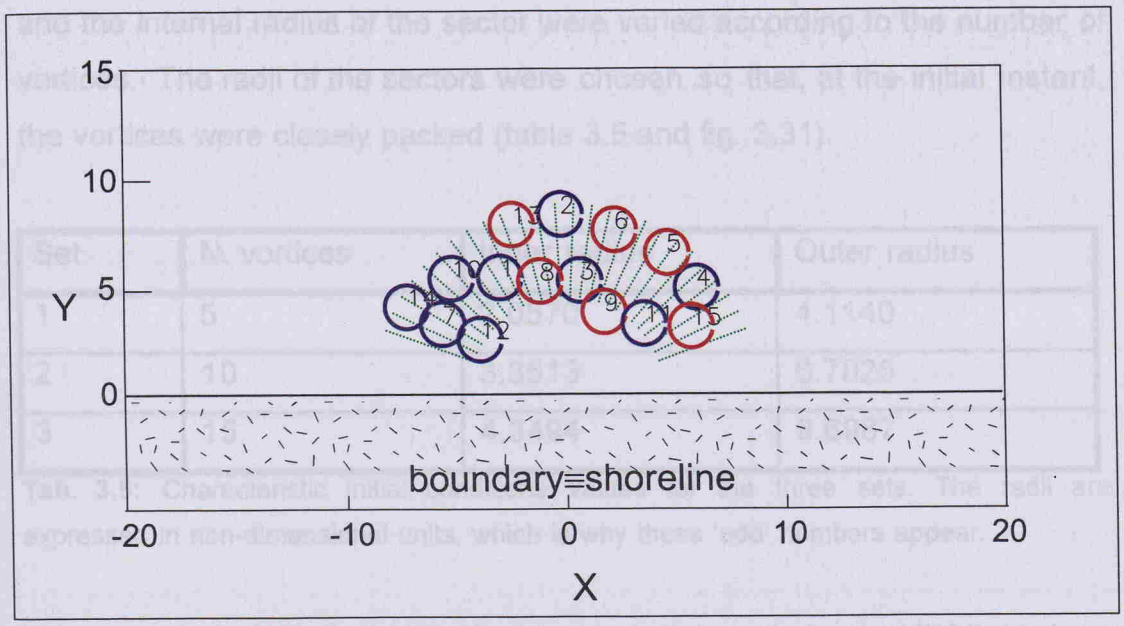

Fig. 3.31: Typical initial situation for the numerical experiments described in section 3.5. 15 vortices (red with positive circulation, blue with negative circulation) were randomly placed in a circular sector. A straight rigid boundary was coincident with the axis y=0. The distance is expressed in non-dimensional units.

characterised by a different initial number of vortices. Each set was made of 30 runs. For each run the initial position of the vortices was varied randomly inside a pre-fixed area (called source area) common to all the runs within a set as well as strength and radius of the vortices.

The source area was a sector of a circular annulus (fig. 3.31). The external and the internal radius of the sector were varied according to the number of vortices. The radii of the sectors were chosen so that, at the initial instant, the vortices were closely packed (table 3.5 and fig. 3.31).

Set	N. vortices	Inner radius	Outer radius
1	5	2.0570	4.1140
2	10	3.3513	6.7025
3	15	4.3494	8.6987

Tab. 3.5: Characteristic initial conditions values for the three sets. The radii are expressed in non-dimensional units, which is why these 'odd' numbers appear.

The tracer was initially located inside the sector and along radial lines (see fig. 3.31). The angular amplitude of the sector was constant for all the runs (140° for the tracer and 120° for the vortices).

For each set of experiments we created an ensemble of 30 initial conditions by varying the position of the vortices and their strength. The initial co-ordinates of the vortices were calculated with a generator of random numbers (see section 3A.1, appendix 3A). An auxiliary algorithm was designed to avoid significant vortex overlapping at the initial instant. The circulation of the vortices was varied with uniform probability by ± 10 % from the non-dimensional reference value of 2.5. The probability of having a positive or a negative vortex was 0.5. The initial radius of the vortices was 1.0 and the merging control parameter (see section 3.2.1 d) was f=0.5 for all the experiments.

The evolution of the position of vortices and tracer with time was calculated, for each different initial condition, with the 2-D model and the 3-D model. Both programs performed $1 \cdot 10^4$ time steps of fixed amplitude $\Delta t=0.01$ (corresponding to a non-dimensional time at the end of the run of $t_{max}=100$). The time step was chosen as a compromise between the pragmatic requirement of speed of the execution and accuracy of the results. Averaged values of μ for each set of initial conditions, are given in table 3.6. In this case μ represents the maximum variation of the Hamiltonian, relative to some initial values, between two collisions (see also section 3.2.2 c). The initial values were taken at the beginning of the run and updated after each collision.

Set	μ, 2-D model	μ, 3-D model
1	0.05	0.1
2	0.01	0.07
3	0.01	0.05

Table. 3.6: Characteristics values of μ for the three sets of experiments.

For set 1, when the 3-D model was used, the accuracy of the results was not very good. With $\Delta t=1 \cdot 10^{-5}$ we had an increase of a factor 10^3 of the execution time without a remarkable increase in the accuracy of the results. One possible reason could be that if vortex rings are close to the Hill's spherical vortex limit, our model, designed to deal with thin-cored rings, performs quite poorly.

3.5.2 Analysis tools and results

a. Animation of the output

A graphical routine was created to animate the changes in position of the vortices and of the marked particles. Up to 100 records with the position of vortices and of the tracer were stored in a output file. A graphical interface

was used to create a corresponding number of images with the position of the vortices and of the tracer. All the images were collated into an animated file. This tool was useful to get intuitive insights into the behaviour of the system (see e.g. figure 3.32). Two different characteristic types of motion for vortices were isolated with this tool (see fig. 3.33 to 3.35 and section 3.5.3 for further discussion).

b. Dispersion of vortices and particles

The results of our experiments are summarised by figures 3.36 to 3.41, appendix 3A.3, showing time series of the dispersion of vortices and particles from the initial and from the instantaneous centre of vorticity, with the 2-D model and the 3-D model. These are discussed in section 3.5.3.

c. Statistical analysis: comparison between dispersions from the same model

We used a one tail significance test (see e.g. Spiegel M.R., 1975), based on the Gaussian distribution, to verify the following set of hypothesis formulated on the appearance of the plots of the dispersions:

$$H_0: \overline{D'_{v,t}} > \overline{D'_{m,t}}; \tag{3.19 a}$$

$$H_0: \overline{DX'_{v,t}} > \overline{DX'_{m,t}} \tag{3.19 b}$$

$$H_0: \overline{DY'_{v,t}} > \overline{DY'_{m,t}} \tag{3.19 c}$$

$$H_0: \overline{DX'_{v,t}} > \overline{DY'_{v,t}} \tag{3.19 d}$$

$$H_0: \overline{DX'_{m,t}} > \overline{DY'_{m,t}} \tag{3.19 e}$$

We calculated the standardised variable:

$$Z = \frac{\overline{D_1} - \overline{D_2}}{\sigma_{\overline{D_1}-\overline{D_2}}}. \tag{3.20}$$

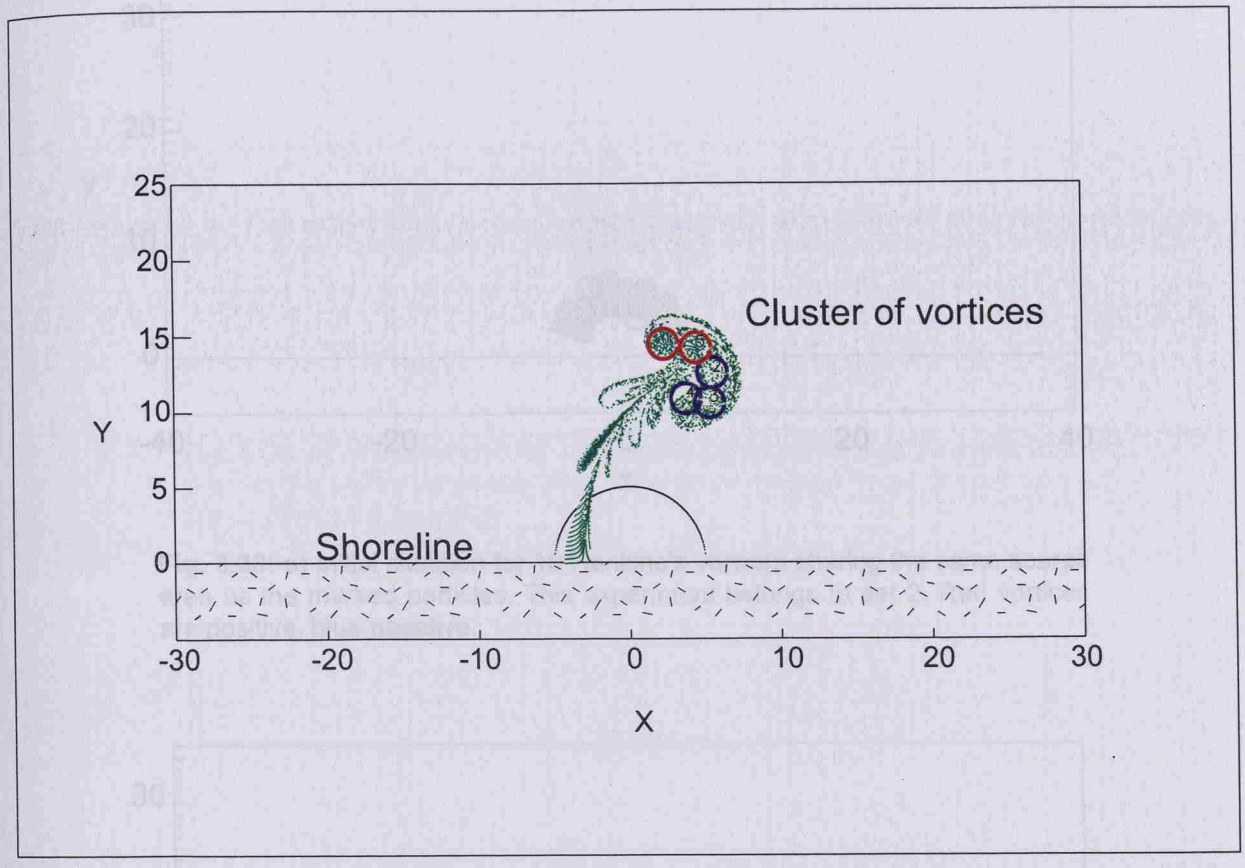

Fig. 3.32: Five Rankine's vortices (red positive, blue negative) may represent an uneven distribution of vorticity. The cluster is moving as a dipole. Since the net cisrculation is negative the group of vortices is moving along a curved path, marked by the tail of particles. The shape of the tracer (green dots) ejected from the recirculation cell of the dipole suggest the existence of filaments but the fluid there is irrotational. The distance is expressed in non-dimensional units. The radius of the core of the vortices is r=1 and the absolute reference circulation is $|\Gamma|=2.5$. The circulation of the vortices can differ up to 10% from the reference value.

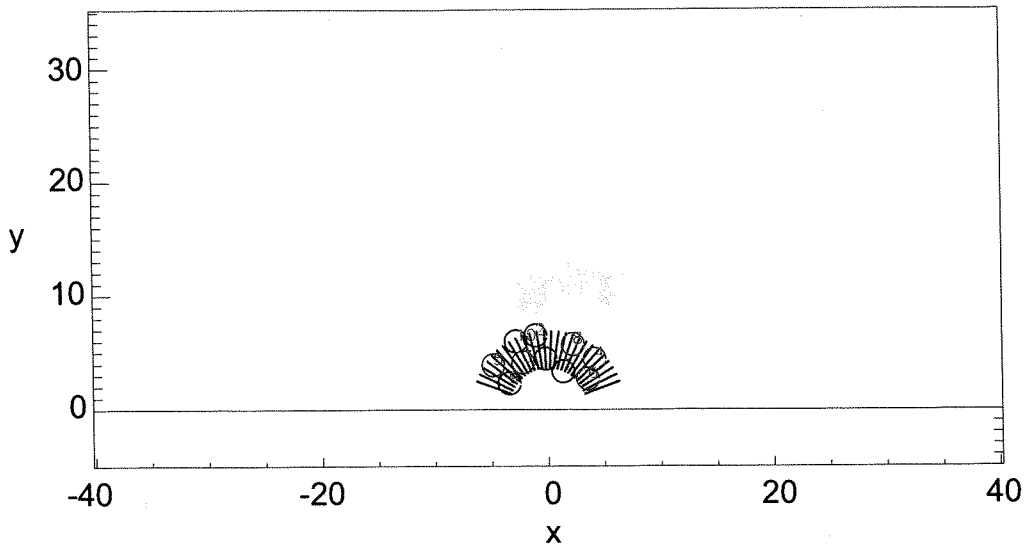

Fig. 3.33: a) Initial situation for 10 Rankine's vortices sharing the same source area as the marked particles. This experiment belongs to set 2. Red vortices are positive, blue negative.

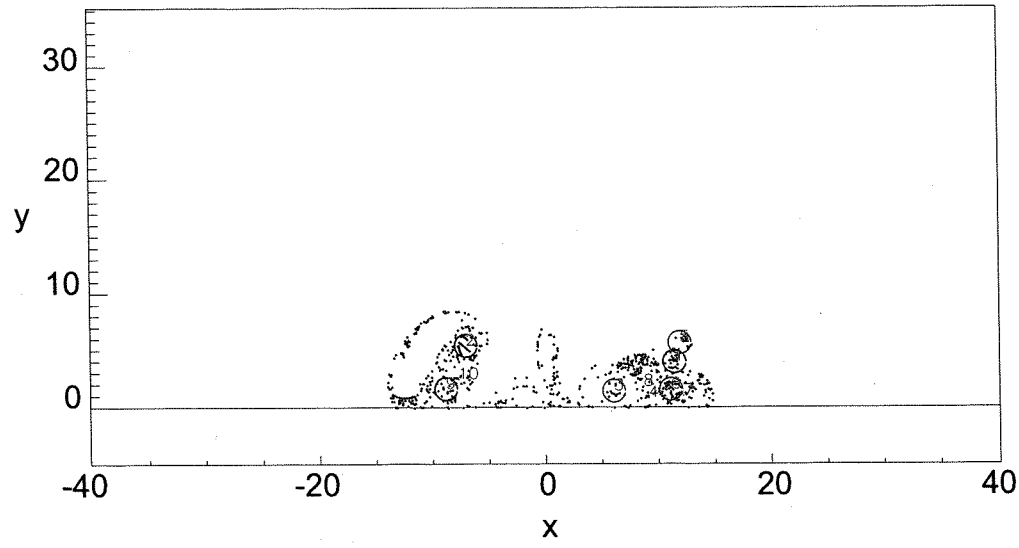

Fig. 3.33: b) Evolution of the system at t=100 (non dimensional). The surviving vortices are moving parallel to the boundary. Note that the surface occupied by the marked particles, at least in the x direction, is larger than the area occupied by the vortices. Some particles escape from the recirculating region and are left behind. Situation I.

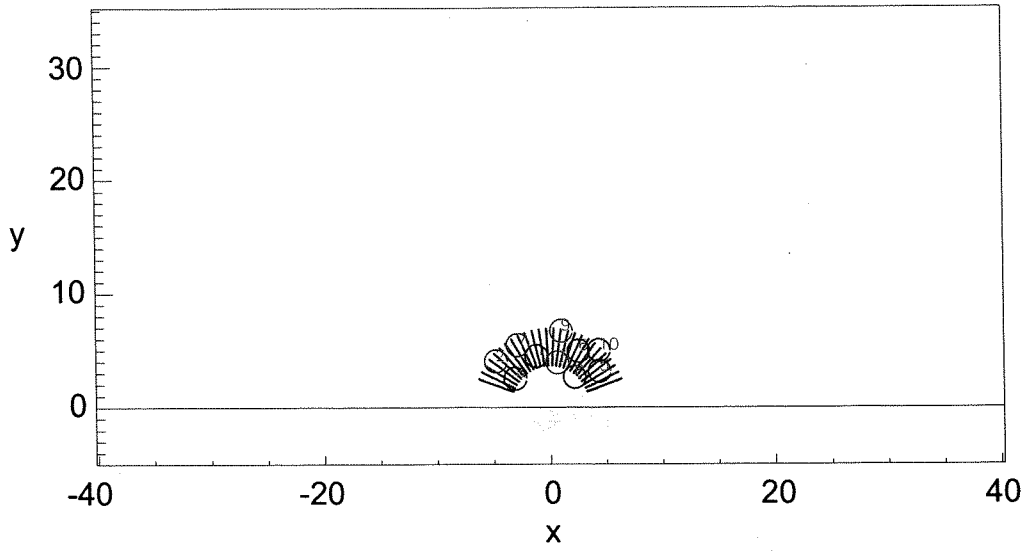

Fig. 3.34: a) Initial situation for 10 Rankine's vortices sharing the same source area as the marked particles. This experiment belongs to set 2. Red vortices are positive, blue negative.

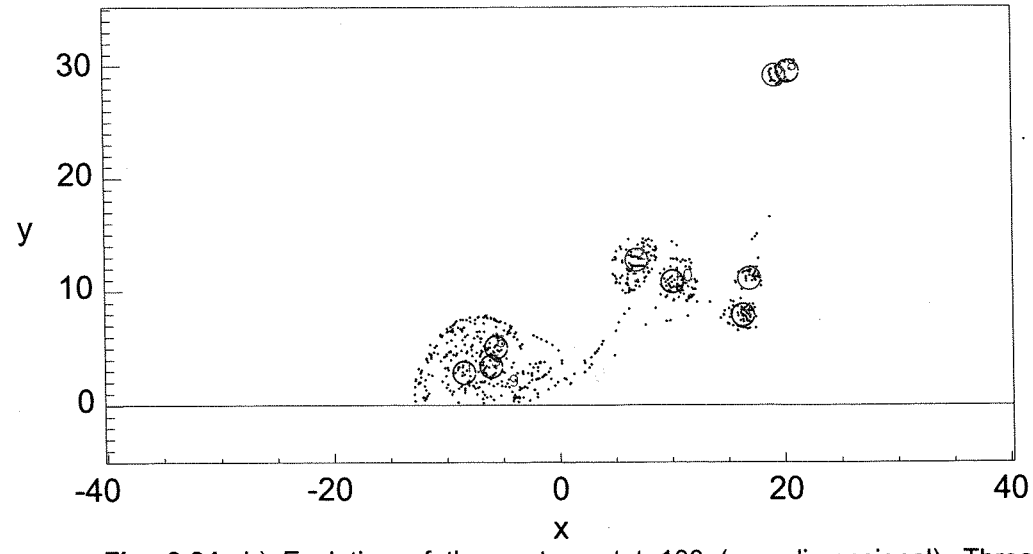

Fig. 3.34: b) Evolution of the system at t=100 (non dimensional). Three dipoles have formed and moved away from the boundary. The rest of the vortices are still near the source area and are stirring the particles. The cluster near the wall is formed by negative vortices (1,5,9) and therefore the centre of vorticity moves left. Situation I.

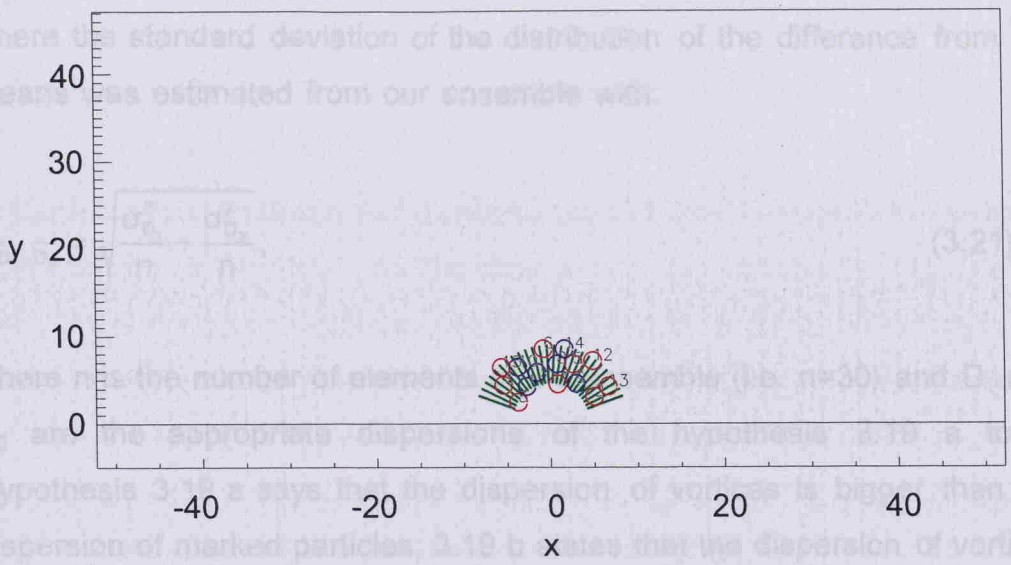

Fig. 3.35: a) Initial situation for 15 Rankine's vortices sharing the same source area as the marked particles. This experiment belongs to set 3. Red vortices are positive, blue negative.

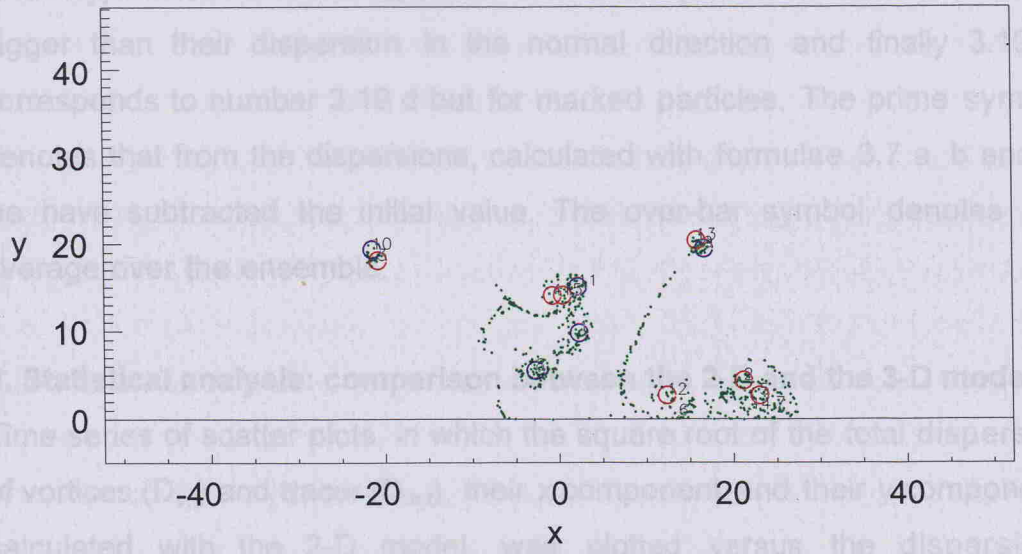

Fig. 3.35: b) Evolution of the system at t=100 (non dimensional). A large number of dipoles formed, either between real vortices or between a real vortex and its image. Particles are dispersed in both directions. They are also left behind by the dipoles (this reduces the stirring efficiency of the system). Situation II.

where the standard deviation of the distribution of the difference from the means was estimated from our ensemble with:

$$\sigma_{\overline{D_1}-\overline{D_2}} = \sqrt{\frac{\sigma_{D_1}^2}{n} + \frac{\sigma_{D_2}^2}{n}}, \qquad (3.21)$$

where n is the number of elements of the ensemble (i.e. n=30) and D_1 and D_2 are the appropriate dispersions of the hypothesis 3.19 a to e. Hypothesis 3.19 a says that the dispersion of vortices is bigger than the dispersion of marked particles; 3.19 b states that the dispersion of vortices in the direction parallel to the shoreline is bigger than the dispersion of marked particles in the same direction; hypothesis 3.19 c is the correspondent of 3.19 b but for the direction normal to the shoreline; 3.19 d is the hypothesis that the dispersion of vortices parallel to the shoreline is bigger than their dispersion in the normal direction and finally 3.19 e corresponds to number 3.19 d but for marked particles. The prime symbol denotes that from the dispersions, calculated with formulae 3.7 a, b and c, we have subtracted the initial value. The over-bar symbol denotes the average over the ensemble.

d. Statistical analysis: comparison between the 2-D and the 3-D models

Time series of scatter plots, in which the square root of the total dispersion of vortices ($D_{v,t}$) and tracer ($D_{m,t}$), their x component and their y component, calculated with the 2-D model, was plotted versus the dispersions calculated with the 3-D model, were used to formulate a second significance test. The plots are shown in figures from 3.42 to 3.47, appendix 3A.4.4. A two tails significance test, analogous to the one just described, was therefore performed to test the hypothesis of differences in the estimate of dispersion from the two models. A two tail test was necessary since we were testing the hypothesis of differences in the two estimates and not if one estimate was bigger or smaller than the other one. The results of the test are summarised in appendix 3A.4.

3.5.3 Discussion

a. Dispersion of vortices and particles parallel and normal to the shore

The analysis of the plots with the time series of dispersions (fig. 3.36 to 3.41, appendix 3A.3) suggests that the dispersion, whether of vortices or of particles, calculated with reference to the initial or to the instantaneous centre of vorticity do not differ greatly between experiments. The conclusions from the statistical analysis confirm this observation. From now we will refer only to the dispersion calculated with reference to the instantaneous centre of vorticity, e.g. $D_{v,t}$, $D_{m,t}$ etc. Most of the plots suggest that the dispersion of vortices and tracer parallel to the shoreline accounts for almost all the total dispersion. This is particularly clear if the 3-D model is considered; only figures 3.38 d, e and f and figures 3.38 j, k and l, referring to the 2-D model with 10 initial vortices, show that the average dispersion of vortices and particles along x may be only slightly bigger than the corresponding y component. A more definite answer can be obtained from the significance test and the five hypothesis 3.19 are discussed next.

The first three hypothesis, as already noted, state that the dispersion of vortices (total, x and y components) is bigger than the dispersions of marked particles. If the 2-D model is used and the total dispersion is considered, this hypothesis is generally accepted with a good level of confidence after a non-dimensional time of $t=0.6\ t_{max}$ (table 3A4.1). The same results are obtained for set 1 and 3 if the x component is considered. Set 2 appears to take more time to reach the same status, the hypothesis being accepted only at $t=t_{max}$. In the direction normal to the shore the dispersion of vortices and particle are similar only for set 1 and, again, the dispersion of vortices is generally larger than the dispersion of tracer for the other two sets.

The results are rather different if the 3-D model is used. The total dispersion of vortices appears to be larger than the total dispersion of particles only for set 3, i.e. for the highest number of vortices and when they are at a biggest distance form the shoreline. The results are unchanged if the x component is considered, as can be seen from fig. 3.37 and 3.39 (d,e,f and j,k,l), showing the predominance of the dispersion along the shoreline for both vortices and particles. As a consequence, if hypothesis 3.19 a is valid, it is very likely that hypothesis 3.19 b is valid too. The third hypothesis is strongly rejected for set 1, for which the opposite is true, i.e. that the dispersion of particles is bigger than the dispersion of vortices. The two dispersions are of the same order for set 2 and vortices disperse more than particles for set 3.

To summarise, the similarity between the dispersion of vortices and particles is a consequence of the initial nearly zero value of the total circulation, $\Gamma_{tot} \cong 0$, for which the centre of mass of vortices will stay close to its initial position (see section 3.4.2). These simulations have some similarities with the experiments discussed in section 3.4.2 for which the dispersion of vortices was generally bigger than the dispersion of particles due to the dominant effect of pairing vortices. This is true especially if the 2-D model is used.

We now address the question of whether there is a preferential direction for dispersion. The answer depends on the influence of the image vorticity compared with the mutual influence of the real vortices. Consider the 2-D model the system formed by the real vortices plus the images has two remarkable features: 1) it always has zero total circulation and 2) y=0 is by definition the permanent axis of symmetry. This implies that each real vortex has a natural dipolar structure (the other partner of the dipole being its image). As a consequence, if this effect dominates the contribution from the other neighbouring vortices in the real plane, the along-shore direction becomes the preferred direction of motion. This mode appears to be

favoured if the average distance of the vortices from the wall is small compared with the average spacing between real vortices and if the number of the vortices is not very big, so that the pairing between real vortices is not likely to happen. There is a close analogy if the 3-D model is considered since each element of an array of coaxial vortex ring has a persistent component of the velocity directed along the axis of symmetry. Therefore similar considerations apply. We can conclude that, whatever the preferred direction is, pairing is going to be the dominant mechanism for dispersion of vortices and the transport in the recirculation cell combined with stirring is the mechanism of dispersion for particles.

In the 2-D case the pairing of real vortices with their images is responsible for dispersing the vortices more than the tracer along the shoreline. The dipoles can move along-shore in both directions (depending on the sign of the vortices) and carry with them the tracer. The particles of fluid that are ejected from the recirculation cell are left behind in wake and this reduces their along-shore dispersion (see e.g. fig. 3.33). We call this situation of type I. The corresponding 3-D simulations suggest that this behaviour is still characteristic of set 3 but it is absent from set 1 and 2, i.e. when the vortices are initially closer to the boundary, for which there is no difference between the along-shore dispersion of vortices and particles. Therefore most of the particles move together with the vortices and the two dispersions are similar.[11]

---

[11]This result may be a consequence of the design of the program since: 1) the biggest contribution to the velocity of the particles that are inside the vortex core is the self-induced velocity of the vortex ring (i.e. the particles inside the core move together with it); 2) the core increases its area as the vortex moves towards shallow water (see section 3.3.1 d, formula 3.14) and more particles can be trapped inside it. Since the number of absorption events of vortices at the boundary, typically 2 events for set 1 and 4-5 events for set 2, is high compared with the corresponding 2-D runs, the stirring properties of the system are reduced. As a consequence, the particles are not ejected from the core of the vortex by the stirring activity of the system but move with it, therefore giving two similar estimates of the dispersion.

The dispersion of vortices and tracer in the direction normal to the shoreline are similar for set 1, with the 2-D model, and for sets 1 and 2, with the 3-D model. If fewer vortices are available the formation of real dipoles, able to migrate off-shore, is not frequent (see e.g. fig. 3.36 f, 3.37 f and 3.39 f, all showing a very small growth of the dispersion of vortices in the y direction). This scenario changes if set 3 is examined (with the 2-D model and the 3-D model). The larger initial number of vortices combined with their larger distance from the boundary favour the formation of real dipoles and we observe an increase in the dispersion of vortices in the direction normal to the shoreline. The dipoles also transport tracer off shore therefore enhancing its dispersion. We label this situation as type II (fig. 3.34 and 3.35). The dispersion of vortices and particles in this case can be, if not dominant, at least an important contribution to the total dispersion. On the other hand, differences in the absolute strength of the vortices will induce the dipoles to follow curved trajectories therefore making the pairing mechanism less efficient in promoting dispersion.

We now analyse the two last hypotheses, i.e. that the along-shore (x) direction is a preferential direction for dispersion of both vortices and particles. With the 2-D model both hypotheses (for vortices and particles) are accepted when set 1 and 3 are considered, while set 2 shows the same behaviour only toward the end of the runs. The same hypotheses are accepted without much to discuss if the 3-D model is used since the dispersion along x accounts for most of the total dispersion.

As a final remark, we should observe that we made only a comparison between dispersions and not commented on their absolute value. The straight boundary sets a preferential direction for the dispersion of vortices and particles but this does not imply that the dispersion in the direction normal to the shoreline is negligible.

b. Comparison between 2-D and 3-D models

Figures 3.42, 3.43, 3.44 and 3.45 suggest that for sets 1 and 2, the dispersion of vortices and particles should, on average, be bigger in the 3-D case than in the 2-D case. This appears to be true only for the x-component of the dispersion (i.e. for the total dispersion since this is dominated by the dispersion along the shoreline). In the direction across the shoreline the dispersion of vortices and tracer is larger if the 2-D model is used. The most likely explanation is that since fewer Rankine's vortices than vortex rings are subject to collisions (vortex rings moving towards shallow water increase their radius and are more prone to fulfil the conditions for collision and absorption, see section 3.3.1 d) more dipoles, responsible for the dispersion normal to the shoreline, can form in the 2-D case. If the number of vortices and their initial distance from the boundary is increased, i.e. if set 3 is considered, the estimates of dispersions for vortices and tracer are larger in the 3-D case.

The two-tail significance test (tables A3.3.1 to A3.3.3) show that the difference in the results is always significant, with the only exception of the total dispersion of vortices when set 2 is considered. For set 1 and 2 we therefore conclude that the total dispersions of vortices and particles (and their components along (x) and across (y) the shoreline) always differ. The total dispersion and its x component are larger if the 3-D model is used. The opposite is true for the y component of the total dispersion. For set 3 the dispersions of vortices and particles calculated with the 3-D model are always larger than the corresponding 2-D estimates.

3.5.4 Conclusions

We designed this experiment to study the effect of a straight and infinitely long shoreline on the dispersion of vortices and tracer initially sharing the same portion of fluid. The total initial circulation of the system was nearly zero. We investigated three different situations, starting with five vortices

close to the shoreline and increasing the number of vortices and their distance from the boundary. The results from the 2-D model and the 3-D model were compared. We observed that the dispersion of vortices is mainly dominated by the formation of vortex dipoles between real vortices or by their propagation along the shore. This can be explained by observing that: 1) the formation of dipoles between real vortices is favoured by the choice of a nearly null initial circulation; 2) the propagation of the vortices along the shoreline can also be interpreted as the formation of vortex dipoles formed by a real vortex and its mathematical image (since, again, the equivalent system, formed by the real vortices and the images, has exactly zero total strength and y=0 as an axis of symmetry). Mechanism 2) is more likely to be dominant if: a) the vortices are close to the boundary; b) the number of vortices is not large; 3) the differences of strength between vortices are significant and the real dipoles move along curved paths. The overall conclusion is that the shoreline is the preferential direction for the dispersion of vortices.

The velocity field generated by the group of vortices determines the dispersion of the passive tracer (i.e. of particles of fluid). The transport properties of the recirculation cell of a dipole and the stirring properties of a group of vortices are the combined mechanism through which the dispersion of tracer takes place. A (real) dipole moving off-shore and a vortex that moves parallel to the shore carry a volume of fluid and the remaining vortices act as stirrers. As a result the particles escape from the recirculating region (e.g. this is very apparent in the trail of particles left by the vortex cluster in fig 3.32) and the transport efficiency of the dipoles is reduced. The particles, like the vortices, are dispersed more in the direction parallel to the shoreline than in the normal direction. The dispersion in the normal direction in this case should be bounded. This scenario also supports the hypothesis that the dispersion of vortices is usually bigger that the dispersion of particles (we have found that this is

true for the highest number of vortices) but this seems to depend on the number of vortices and their distance from the boundary.

From the comparison of the dispersing properties of the two models we conclude that the 3-D model is more efficient in dispersing vortices and particles.

3.6 Dispersion of vortices and mass near the wall- Case 1. Vortices and particles starting in different areas

In this section we present the last set of experiments designed to study a situation in which the vortices and the particles occupy at the beginning of the run different portions of fluid. This initial configuration substantially leads to conclusions that are very similar to the ones obtained in section 3.5. The main differences in the initial conditions are: a) the particles are initially simulating the release of a line source of dye of finite length; b) the area initially occupied by the tracer is much bigger than the area occupied by the vortices.

3.6.1 Experiment set-up

A typical initial situation is shown in figure 3.48. In this experiments we discuss only one set of initial conditions. The initial position of the tracer is the same for all the experiments. The initial position of the vortices is varied randomly inside a rectangular area (which measures 24 x 10 and has an offset of 10 from the shoreline, see fig. 3.48). The box is initially filled with 20 vortices (with a reference strength of Γ=80 to which we add or subtract randomly 30% of this reference value). The probability to have a positive vortex is 0.5 (i.e. the total initial circulation is nearly zero). The initial reference value for the radius is r = 1 and the random variations are

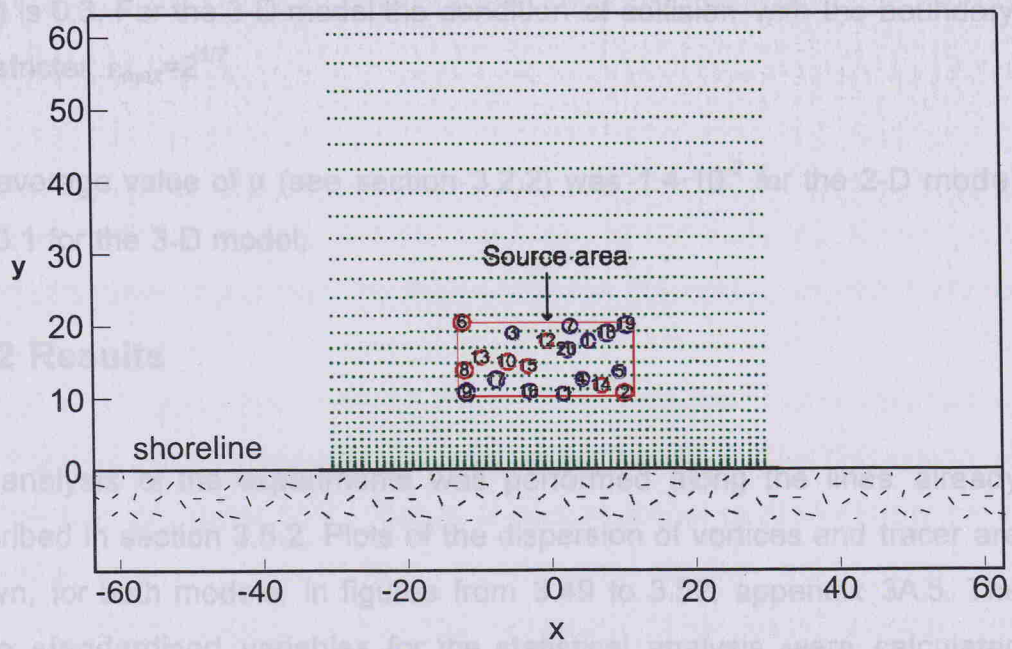

Fig. 3.48: typical initial situation with 20 vortices and 1800 marked particles that simulate a passive tracer.

contained within ±20%. The tracer is contained inside a box of 60 x 60; 1800 particle are located at the node of a grid evenly spaced in the x direction. The mesh size increases linearly in the y direction. The number of iterations performed is $4 \cdot 10^4$ and the time-step is $\Delta t = 5 \cdot 10^{-4}$ (equivalent to a non-dimensional execution time $t_{max}=20$). The parameter f (see section 3.2.1) is 0.3. For the 3-D model the condition of collision with the boundary was stricter: $\varepsilon_{max}=2^{1/2}$.

The average value of μ (see section 3.2.2) was $1.4 \cdot 10^{-2}$ for the 2-D model and 0.1 for the 3-D model.

3.6.2 Results

The analysis of the experiments was performed along the lines already described in section 3.5.2. Plots of the dispersion of vortices and tracer are shown, for both models, in figures from 3.49 to 3.52, appendix 3A.5. The same standardised variables for the statistical analysis were calculated (see sections 3.5.2 c and 3.5.2 d).

3.6.3 Discussion

a. Dispersion of vortices and particles parallel and normal to the shore

Since the total circulation of the system is nearly zero we consider the dispersion of vortices and particles from the instantaneous centre of vorticity (see sections 3.4.2 and 3.5.3 a).

The time series of the dispersion of vortices and particles (2-D model, fig. 3.49) suggest that the along-shore (x) component dominates the total dispersion. The y-component of the dispersion of vortices appears bounded (the maximum is reached at about $t=0.4t_{max}$). The y-component of the dispersion of particles decreases and reaches its minimum value at

$t=0.6t_{max}$). The results from the 3-D model (see fig. 3.50) suggest very similar conclusions (with the difference that, compared with the 2-D case, the total dispersion of vortices and particles is in general larger but the dispersion of vortices and particles in the normal direction is substantially smaller). The peaks in figure 3.50 f are due to dipoles that followed a curved path, moving first offshore and then back again toward the shoreline.

The significance test revealed that the hypotheses 3.19 are always accepted (with the 2-D and the 3-D models). We conclude that the vortices always disperse more than the tracer and the dispersion in the direction parallel to the shoreline is dominant for both vortices and particles. The dispersion of tracer decreases as the patch of particles is stretched along the boundary and compressed in the normal direction. The dispersion of vortices has an upper limit. This is a consequence of the differences in circulation between the vortices forming the dipoles, which therefore progress along curved paths and inevitably move back towards the boundary.

b. Comparison between 2-D and 3-D models

Scatter plots of the dispersion of vortices, figure 3.51, show that while the x-component of the dispersion (and the total value) are bigger if vortex rings are used, the y-component appears to be bigger if the 2-D model is used. The same observations are valid if the dispersion of particles is considered (figure 3.52) but now the dispersions in the normal direction seem to be very similar. The dispersion of tracer along y does not seem to be an important feature in this experiment.

For sake of completeness, we calculated the standardised variables to see whether the differences between the dispersions calculated with the two models are statistically significant. We do not show their values because the differences are always statistically significant for all the cases

but for the dispersion of tracer in the normal direction, for which the results from the two models do not differ.

3.6.4 Final remarks

We designed this experiment to study the dispersion of vortices and tracer when the vortices are initially contained in an area much smaller than the area that contains the tracer. We have increased the variability of the strength of the vortices (compared to section 3.5).

With these initial conditions the dispersion of vortices and particles in the x-direction always dominates the total dispersion. The dispersion of the vortices in the y direction is always bounded. This is a consequence of differences of the absolute circulation between the partners of vortex dipoles. On the contrary, the dispersion along the shoreline increases with time. The dispersion of the tracer in the direction normal to the shoreline is generally decreasing because the dispersion of vortices in the same direction is bounded and the area occupied by the tracer is much larger. Since many dipoles form during the evolution of the system, the dispersion of vortices is larger than the dispersion of particles. The 3-D model is more efficient in dispersing vortices and particles in all cases but for the dispersion of tracer in the y-direction.

3.7 Conclusions

The results from the numerical simulations have provided evidence of several interesting aspects of the mechanisms of dispersion of a system of vortices and passive particles.

We have discussed the importance of the choice of the measure of dispersion. If the dispersion for vortices is defined as the second order

moment of their position from the initial centre of mass and this migrates along the boundary (because of the effect of the image vorticity) the differences with the dispersion from the instantaneous centre of mass can be very large.

The dispersion of vortices and particles is dominated by the formation of dipoles between real vortices and between a real vortex and its image. The second kind of dipole moves along the axis of symmetry of the system (i.e. the shoreline). For this reason the dispersion in the direction parallel to the shoreline is normally dominant, whether tracer or particles are analysed. This is true until the velocity induced by the images on the real vortices is larger, or of the same order, of the velocity induced by the neighbouring vortices.

In our simulations we neglected the effect of viscosity and this may be a serious limit in our analysis. When a vortex is close to a boundary, the effect of viscosity (see e.g. Doligaski, 1994), is to generate of a counter-rotating secondary vortex at the boundary and to cause rebounding. The implications of this mechanism should be assessed if the dispersion parallel to the shore has to be quantified. Our laboratory experiments, to be discussed in the next chapters, show that rebounding is present also when a sloping bed is considered.

The dispersion of vortices in the direction normal to the shoreline is very large only if the differences in the absolute strength of the vortices are small: in this case dipoles can propagate in any direction and on almost straight paths. The bigger the differences the more curved the paths are, and, consequently, the dispersion of vortices will reach soon its maximum[12].

---

[12]Curved paths can also be induced by horizontal shear of the along-shore current (Garten et al, 1998).

The dispersion of the tracer is generally smaller than the dispersion of the vortices and its magnitude depends on the initial position of the particles with respect to the position of the vortices. The tracer transported by the dipoles inside the recirculation cell is also stirred by the remaining vortices. If the area is very rich in eddies the net dispersion may be reduced.

The 3-D model is in general more efficient in dispersing vortices and particles but this may not be true for dispersion in the direction normal to the shoreline.

There is need for a better understanding of the dynamics of vortices over a planar and sloping bed. In the rest of this dissertation we will describe a series of physical experiments aimed at disclosing to what extent the ring vortex model is suitable to study the dynamics of a vortex over a sloping bottom.

3.8 Summary

The main results are:

- The dispersion of vortices, for a system that has almost zero total circulation, is driven by the formation of dipoles either between real vortices and between a real vortex and its image. The dispersion of particles is dominated by transport inside the recirculation cell and stirring by the other vortices.
- The dispersion of vortices and particles is generally bigger in the direction parallel to the shore than in the normal direction; this is true when the effect of the shore, i.e. of the images, is of the same order, or bigger, than the effect of the other vortices.

- A dipole in which the two partners have different absolute strength follows a curved path. Therefore the dispersion of vortices and particles in the direction normal to the shoreline is bounded if vortices of opposite sign have large differences of absolute circulation (section 3.6.3 a).
- the 3-D model is generally more efficient than the 2-D model in dispersing vortices and particles; this may not be true for the dispersion of particles in the direction normal to the shoreline.

Chapter 4

Physical experiments

4.1 Introduction

4.1.1 Background and motivations

In chapter 2 we discussed how a sector of a vortex ring can be used to model a vortex in a wedge-like domain and we observed that this construct is mathematically exact. We also observed that this model could be seen as an extension to three dimensions of the two-dimensional model that uses parallel straight-line vortices, or, equivalently, point vortices. If point vortices are taken, the model is valid as it stands only if applied to unbounded fluids or if the vortices are in between two parallel planes (see e.g. Saffman, 1992, chapter 7), with the further assumption that the vortex lines must also be perpendicular to the latter. In other words, if the angle between any of the vortices and the planes is not 90°, image vorticity must be introduced in order to satisfy the boundary conditions. It follows that point vortices can no longer be used because two-dimensionality is lost. For this reason a model able to describe the dynamics of vortices in a shore environment, in which the sea floor is often gently sloping, requires an extension to three dimensions. To solve this problem we assumed that, if the seabed is not too steep and the depth is small compared with the radius of the vortex, a real vortex over a sloping bottom may be approximated with a sector of a vortex ring.

Following this idea, in chapter 3 we used the inviscid vortex ring model in a non-rotating system to investigate the combined effect of a shoreline and of a sloping bottom on the dispersion of vortices and particles of fluid in the

absence of other dynamical features, such as currents, horizontal shear and waves. A comparison was made with the 2-D model of a semi-infinite coastal ocean bounded by a vertical wall. We found that along-shore dispersion produced by vortices in a wedge exceeded that promoted by identical initial configurations of vortices near a vertical wall. The absence of background rotation is a good hypothesis. Recent observations made during the Sandy Duck '97 Experiment suggest that the characteristic radius R of coherent vortices near the surf zone is of the order of tens of metres with strength Γ of order 10 m^2 s^{-1} (Dr. Jerome Smith, 1998, personal communication). The Rossby number for these vortices, calculated as Ω/f, where Ω is the angular velocity of the core, assuming rigid rotation, and f is the Coriolis parameter, (see e.g. Gill, 1982, p. 498) becomes $R_o=2\Gamma/(\pi f R^2)$. Substituting, for mid latitudes, we find $R_o \sim 10^4$; thus, the Earth's rotation can be neglected.

The principal question that we now want to answer is: how good is our analytical model with vortex rings in predicting the dynamics of vortices over a gently sloping bed that, together with the fluid surface, bounds a wedge-like region of fluid (see section 2.3.3 and figure 2.13)? Therefore the behaviour of vortices moving over a planar sloping bottom is investigated with physical experiments and the results are compared, in a separate chapter, with the predictions of the analytical model. The idea is to generate a vortex dipole that, since it progresses along a straight path under the effect of its self-induced motion, can move from a region of constant depth towards a part of the tank where the depth is decreasing (see fig. 4.1). We are aware that the situation reproduced by the experiments may not occur frequently in nature or may not be a characteristic feature of the near-shore dynamics, but the apparatus is simple to build and the experiments represent a good way to validate (or otherwise) our theoretical model and to learn more of the processes which are not represented by the theory.

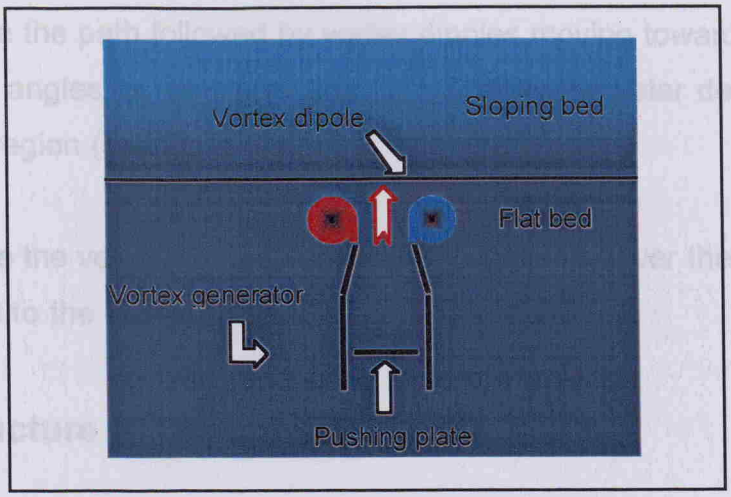

Fig. 4.1: Working principle of the vortex generator and schematic plan view from above of the experimental set-up. The dipole is generated over a flat bottom by pushing water out of a channel that is narrowing at one end. The dipole moves, by mutual interaction of the vortices, over a planar slope towards progressively shallow water. The horizontal black line indicates where the slope begins whilst the red arrow indicates the direction of motion of the dipole. The red vortex is positive (i.e. contains positive vorticity) and the blue is negative (for a side view see fig. 4.5).

In the past almost two dimensional vortex dipoles have been used to investigate the case of collision with solid boundaries, or walls, when the latter are parallel to the vortex lines (e.g. Barker and Crow, 1977). In our experiments the boundary is not parallel to the vortex lines but is inclined at an angle, therefore simulating a planar sloping beach (see figure 2.13).

4.1.2 Objectives

The main objectives of the experiments are:

- to describe the development of the flow as the vortices interact with a slope;

- to measure the path followed by vortex dipoles moving towards the shore, for different angles of the slope and for two different water depths beyond the wedge region (see fig. 4.6.a);

- to measure the velocity of the vortices, whilst moving over the sloping bed and parallel to the shore.

4.1.3 Structure of the chapter

The experimental apparatus is presented in section 4.2, where we also describe the flow visualisation techniques used. Section 4.3 contains an overview of experimental observations. In section 4.4 we discuss the techniques used to process the raw data from the experiments (images of the vortices when dye was employed and position of particles when particle image velocimetry was used). The measurement of other parameters and their analysis is the subject of section 4.5. Two experiments with the planar slope replaced with a vertical wall are the subject of section 4.6. Discussion and conclusions are in sections 4.7 and 4.8 respectively.

4.2 The apparatus

4.2.1 The vortex generator

Ideally, we only need to observe the motion of one vortex over a planar sloping bottom but the generation in the laboratory of isolated and coherent vortices in a homogeneous and non-rotating fluid is not a simple task.[13]

---

[13]In contrast, the case in which the Earth's rotation is simulated with the aid, for example, of a rotating table, is easier since the fluid can be forced to develop vortices

Barker and Crow (1977) designed a device to generate quasi two-dimensional vortex dipoles without using background rotation [this technique is the two-dimensional analogous of the puffing method used to produce a circular vortex ring (e.g. Maxworthy, 1974)]. The apparatus consisted of two thin plates spanning the depth of the fluid, to form a channel open at the two ends, and a third plate, normal to the first two, for pushing the fluid. The fluid pushed from the channel formed two symmetrical vortex sheets that immediately rolled-up to form a vortex dipole. With the pushing plate still moving, a trigger released a spring-loaded mechanism that quickly retracted the plate, so that the flow in the channel was free to evolve without being blocked by the plate itself. At this point, a fully developed dipole detached from the mouth of the generator and moved away along a straight path (see fig. 4.2). As reported by Barker and Crow (1977), as well as observed in our experiments, to obtain a long lasting dipole it is essential that the pushing plate is removed. The out-washed fluid is needed to fill the recirculation cell of the dipole. If the plate is not withdrawn but left to obstruct the channel the two vortices quickly draw together, amalgamate and disappear. We will see in the next sections that the structures obtained with this device are robust and can progress without losing coherence for distances that are long compared with the initial radius of the vortices.

---

by virtue of the Taylor-Proudman theorem. For this theorem to hold, the flow must be geostrophic and incompressible (i.e. Rossby number and Ekman number much smaller than 1 and zero divergence). If those condition are satisfied the vertical velocity shear is zero (see e.g. Tritton, 1988, chapter 16, pp 219-226). As a consequence an impulsive perturbation at the surface such as air jets, drops of fluid and submerged jets of water, will evolve so that the resulting vortical structure will span the depth of the tank, thus forming Taylor columns (see e.g. Carnevale et al, 1991, Fedorov et al, 1989, Whitehead, 1989, and Hopfinger and van Heijst, 1993, for a review).

Fig. 4.2.a

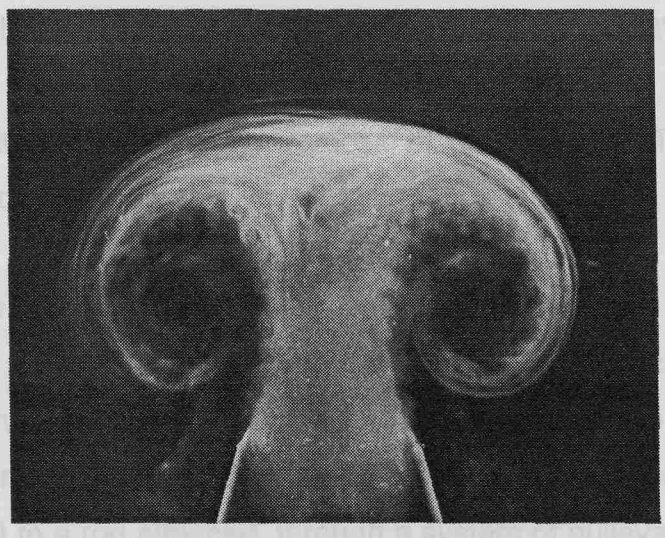

Fig. 4.2.b

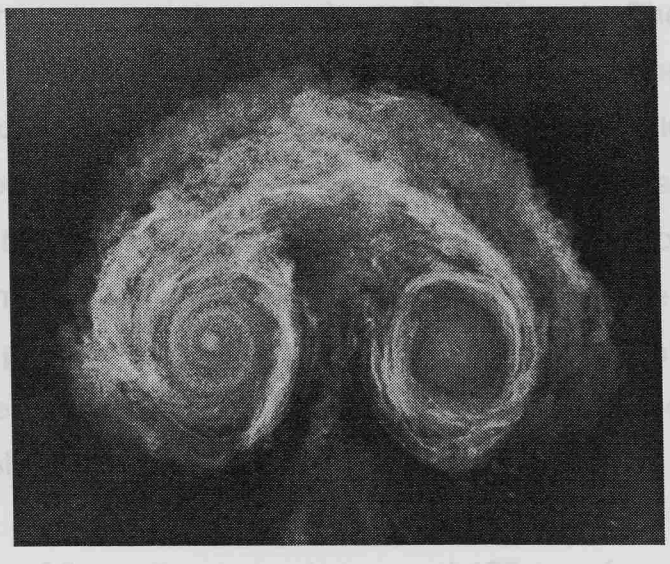

Fig. 4.2.c

Fig 4.2: This sequence of photographs (from Barker and Crow, 1977) illustrates the technique that we used in our experiments to create vortex dipoles. For a description of this technique see section 4.2.1. Water coloured with fluorescine was used to visualise the vortices. Fig 4.2.a shows the early stage of roll-up of the dipole that subsequently develops in the mushroom–like pattern shown in fig. 4.2.b. Small scale instabilities, i.e. small compared to the size of the dipole, prior to the transition to a turbulent core, can also be seen. The edges of the converging mouth of the vortex generator (with ~7 cm opening) are visible. The fully developed dipole, now detached from the generator, is shown in fig. 4.2.c. Since the two vortices have the same strength the dipole progresses along a straight path (see section 4.3.2).

We designed a vortex generator borrowing many characteristics from the device used by Barker and Crow (1977). Our apparatus, sketched in figure 4.3, consisted of a channel made of 1 mm thick stainless steel. With reference to figure 4.3, the length of the channel was AA" = 120 mm and the width at the back AB = 60 mm. The two lateral walls were bent in order to obtain a width at the mouth of 37 mm (A'B'). The channel was 60 mm deep. A plate obstructing the channel (CC' in fig. 4.3) was used to transfer momentum to the fluid and to push it through the mouth, A'B'. The width of the opening at the mouth allowed the generation of dipoles with an initial separation of the centres of the vortices of about 7 cm. The maximum working depth of the apparatus was 4.5 cm.

A sliding lid covered the top of the channel (fig. 4.4 b). The role of the lid was to support a frame to which the pushing plate was attached through a spring. The forward motion of the plate was obtained at the expense of a weight falling under the action of gravity. The back of the lid was connected (at B, fig. 4.4.b) to a rod attached, through a system of pulleys and levers, to a weight sliding over a sloping plane (not shown). The plane was lubricated with silicon grease to obtain a smooth movement. With the spring extended, a metallic pin (C in fig 4.4.b) was used to keep the plate in its lowered position, as shown in fig. 4.4.a. The pin was attached to the border of the tank with a string. When the maximum stroke of the lid (typically 2-3 cm) was reached, the pin was extracted from the hole (A in fig. 4.4.a) and the pushing plate was pulled upwards and out of the water by the spring. The upward motion of the plate was very fast and was guided by two lateral slots (see fig. 4.4.a).

The back edge of the vortex generator was at 160 mm from the border of the tank. The device had its plane of symmetry perpendicular to the longest side of the tank and was placed in the middle, so that side–wall effects, roughly estimated with the method of the images, were symmetric and

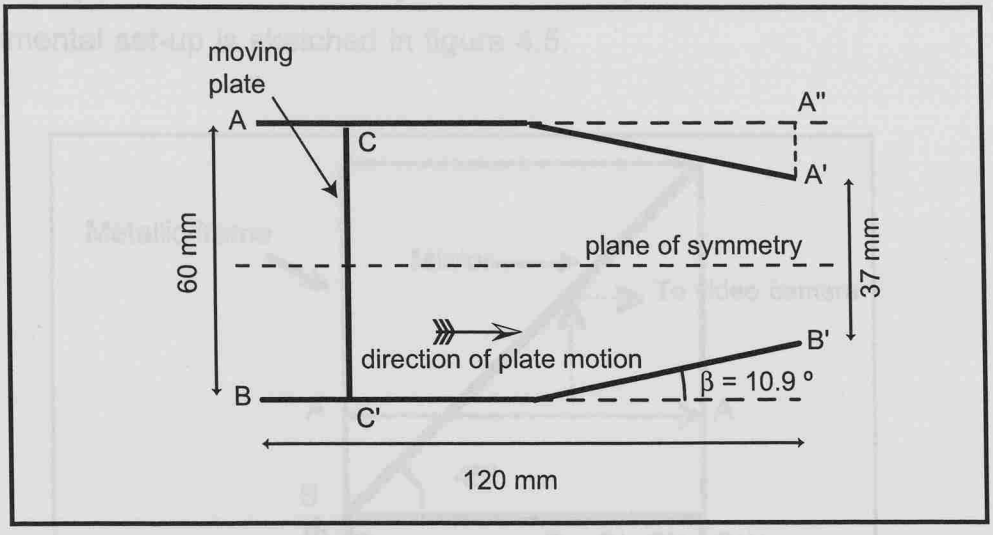

Fig.4.3: Schematic of the channel of the vortex generator. Plan view from above. The moving plate is attached to the lid (not shown, see below).

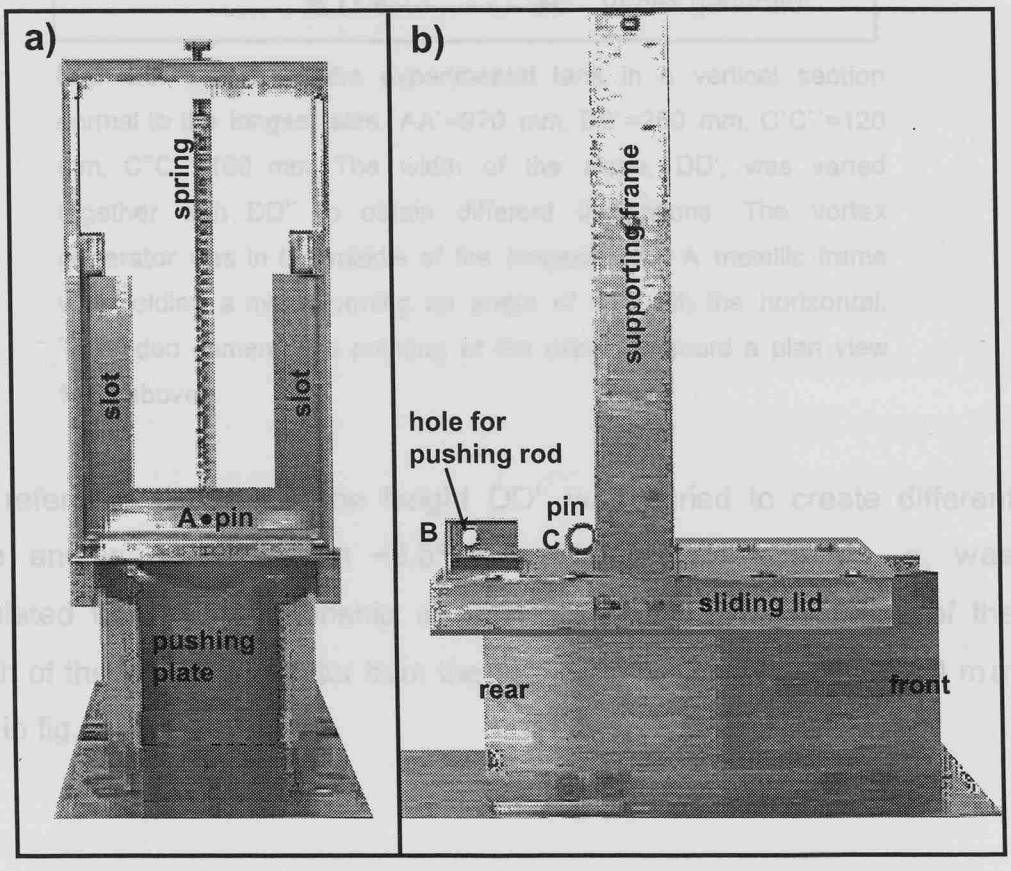

Fig. 4.4: a) Front view of the vortex generator. The spring mechanism, now loaded, is visible. The spring is attached to a frame mounted on the sliding lid. Two lateral slots guide the vertical motion of the plate. A metallic pin, passing through holes in the pushing plate and in the frame (A in figure) is used to keep the plate in its low position. b) Side view. The pin that keeps the pushing plate down is now visible. A string (not shown) is attached to the pin (at C) and to the border of the tank (not shown); when the maximum stroke is reached the pin is extracted from the hole and the pushing plate is free to move upwards. On the left is the small hole at which the rod that pushes the lid is attached.

small compared with the velocity field of the dipole[14]. A side view of the experimental set-up is sketched in figure 4.5.

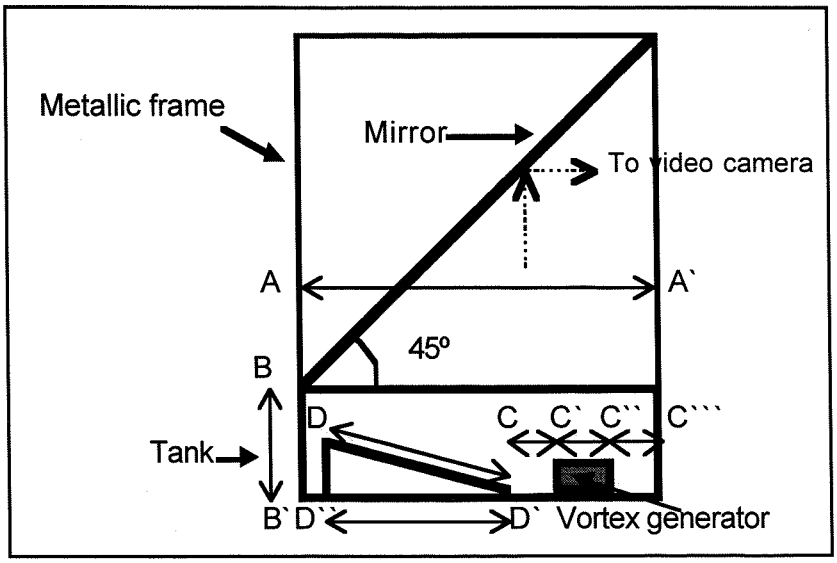

Fig. 4.5: Sketch of the experimental tank in a vertical section normal to the longest side. AA`=970 mm, BB`=250 mm, C`C``=120 mm, C''C'''=160 mm. The width of the slope, DD', was varied together with DD`` to obtain different inclinations. The vortex generator was in the middle of the longest side. A metallic frame was holding a mirror forming an angle of 45° with the horizontal. The video camera was pointing at the mirror to record a plan view from above.

With reference to fig. 4.5, the height DD'' was varied to create different slope angles, ranging from ~3.5° to ~45°. The slope angle, α, was calculated from the relationship α=arcsin(DD``/DD'). The distance of the mouth of the vortex generator from the beginning of the slope was 110 mm (CC' in fig. 4.5).

---

[14]The offshore velocity induced by the side borders where estimated with the method of the images (formula 2.11). Typical values are: $\Gamma \sim 10^2$ cm^2 s^{-1} and s~0.5 10^2 cm (see tables 4.5 and 4.8), giving a velocity of~0.15 cm s^{-1}. The typical along-shore speed is ~1 cm s^{-1}.

4.2.2 The tank

The experiments were made in a rectangular Perspex tank of 970 mm x 1470 mm and 250 mm deep. The water had a free surface. A planar sloping beach was simulated with two glass panels. The smaller panel (200 mm x 900 mm) was used for shallow water levels and for large angles. For deeper water and small angles we used a panel with sizes 458 mm x 1430 mm.

We should mention that the thickness of the Perspex material and the fact that the tank in which we conducted the experiments was not perfectly horizontal (we measured a difference of ~2 mm in water depth across the longest side at the position of the shoreline, see fig. 4.6 for a definition of the shoreline), made the measurement of the water depth a little ambiguous. For this reason we decided to estimate the water depth using the angle of the slope and the length R_i (see section 4.5.1 and fig. 4.21 for the definition of R_i) which was calculated as the average of the distances measured from the digitised images of the plan view from above of the tank at three different positions. This procedure yielded an accuracy on the water depth at the flat bottom of ~0.1 cm and on R_i of ~0.2 cm (see tables 4.1, 4.2 and 4.3 and tables 4.5 and 4.6).

4.2.3 Recording system, flow visualisation techniques and data acquisition

a. Recording system

We recorded the experiments with a 50 Hz shutter video camera. We used either a Cohu Cosmicar TV zoom lens, 8–48 mm f1.2 or a Rainbow TV zoom lens H6X8–II, 8–43 mm f1.0. The images were recorded with a S–VHS Panasonic VCR (model AG–7350). We regulated the iris

diaphragm of the lens by viewing the images on a TV monitor until the exposure looked correct. The recording frequency allowed a time resolution of the images of 0.04 s, adequate to measure the position of the centre of the vortices and to sample the velocity field. We used a digital timer to stamp the images with the time elapsed since the beginning of the experiment. A plan view of the experiments from above was obtained by suspending over the tank a mirror forming an angle of 45° with the horizontal, as shown in figure 4.5.

b. Flow visualisation and data acquisition. Method 1: dye

To visualise the vortices we injected a strong solution of yellow fluorescine into the channel of the vortex generator immediately before the run. The working fluid was fresh water. A black background was used to enhance the contrast of the coloured vortices. Two 500 W halogen lamps were attached to the metallic frame used to hold the mirror (see fig. 4.5). The lamps were suspended at about 50 cm from the water surface and were switched on only for the duration of the experiments to avoid non–uniform heating of the water which may promote convective motions. To reduce the number of air bubbles created by the gas dissolved in the pressurised tap water, we filled the tank with tepid fluid and we left it to cool overnight.

The data acquisition consisted of filming the surface of the fluid, as shown schematically in figure 4.5. Examples are shown in figures 4.6.a and 4.6.b. A grid with a mesh size of 1 cm, used to map a Cartesian frame of reference, was placed under the transparent bottom of the tank and filmed before the experiment (fig. 4.7).

c. Flow visualisation and data acquisition. Method 2: particles

The PIV (Particle Image Velocimetry) technique (e.g. Dalziel, 1993 and Adrian, 1991, for a review) was used to: a) visualise the features of the flow; b) to measure the position of the vortices; c) to measure the velocity field. The analysis consisted of the calculation of the velocity of some

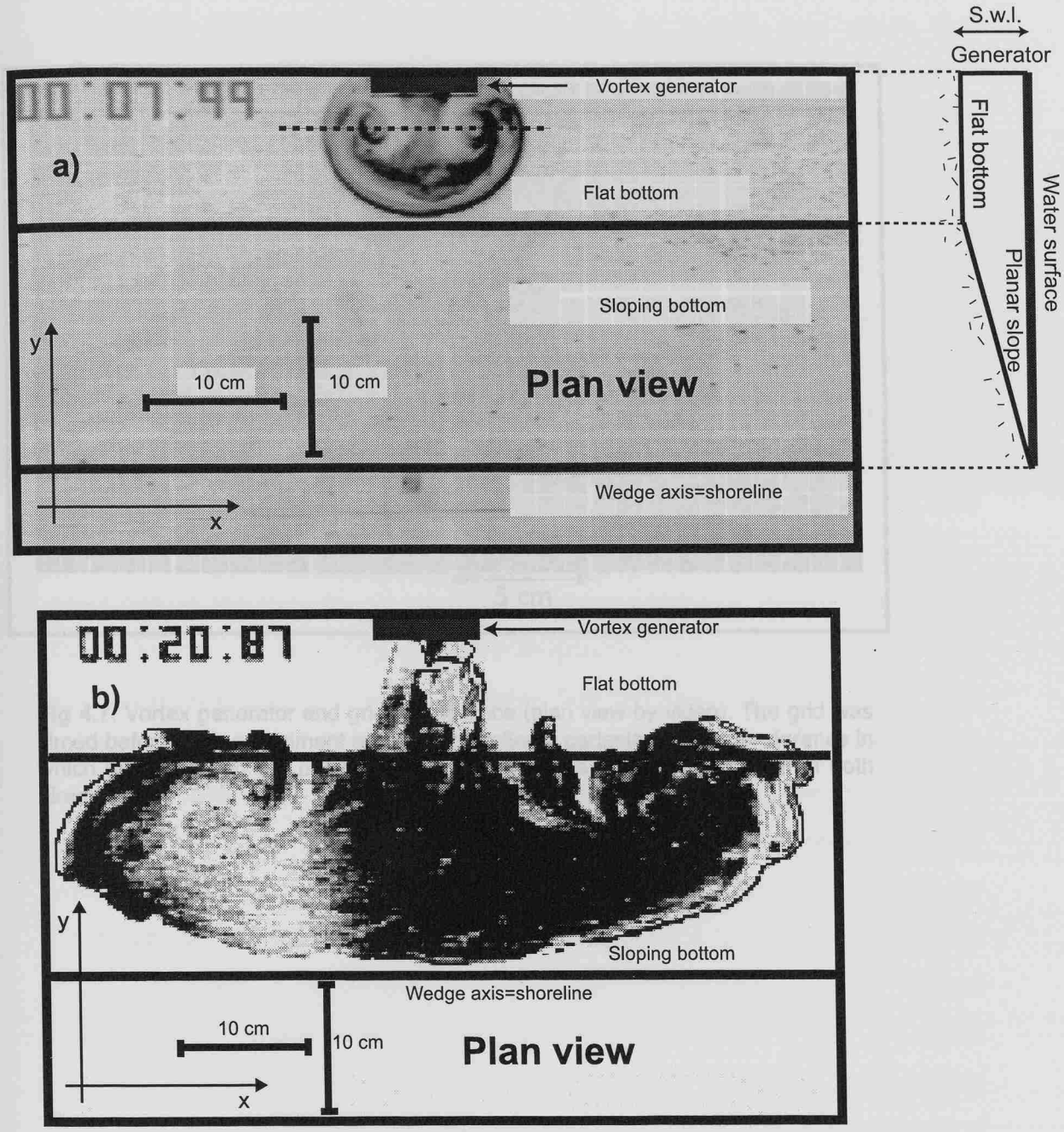

Fig. 4.6: a) a vortex dipole 1.45 s after its formation (plan view). Slope: $\alpha=(12.4\pm0.2)^{\circ}$, s.w.l. $=(3.8\pm0.1)$ cm. On the upper left corner is the time elapsed since the beginning of filming, which does not necessarily correspond with the beginning of the experiment. These images have been converted to negative and therefore the background (originally black) appears almost white. The non-uniform colour intensity of the patch of dye is due to non uniform lighting conditions and/or non uniform concentration of dye. The dipole was generated at t=6.45 s, which therefore is the time offset. In the analysis of all the experiments, the dashed line, passing trough the centre of the vortices, was assumed to be parallel to the axis of the wedge (shoreline), or, in other words, we neglected differences of the ordinates of the centres. b) Later evolution of the dipole shown above. The vortices are now moving apart from each other and almost parallel to the shoreline.

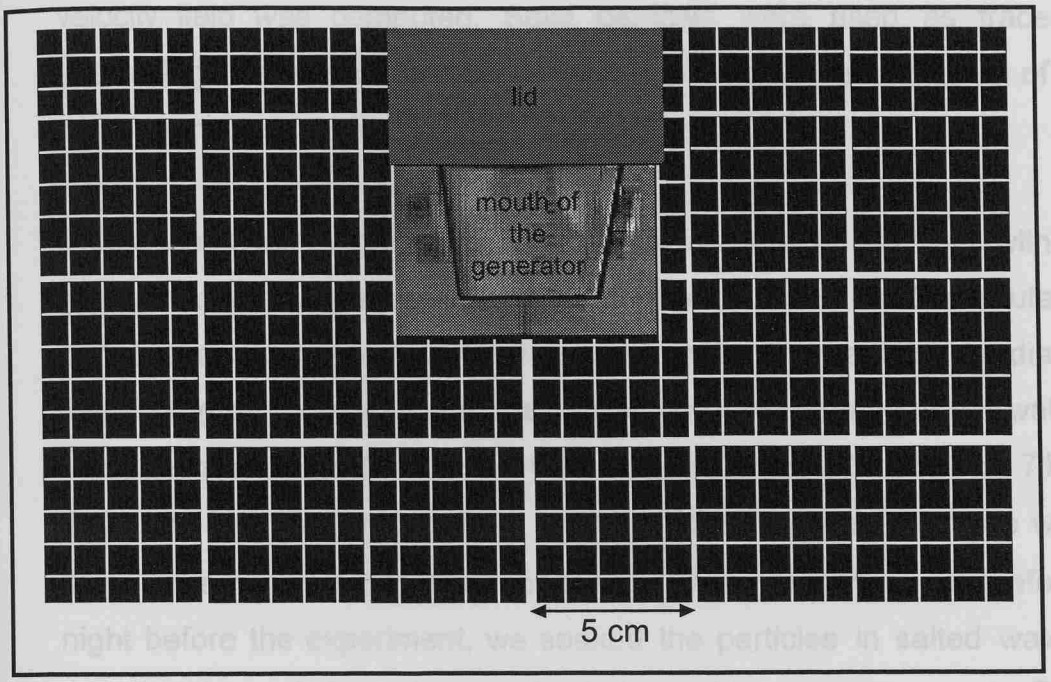

Fig 4.7: Vortex generator and grid of reference (plan view by video). The grid was filmed before each experiment and used to define a cartesian frame of reference in which we measured the position of the vortices. The mesh size is 1 cm in both directions.

particles of fluid, essentially a Lagrangian approach, and on the subsequent interpolation of the velocity data on a grid, over which the velocity field was computed. Solid particles were used as tracer. The underlying assumption is that a particle of water and a particle of tracer move in the same way.

Before each experiment, we seeded the surface of the fluid with white granules of the astyrene/acrylate interpolymer Pliolite AC 80 (manufactured by Goodyear). We previously sieved and sorted the particles by diameter. Depending on the distance of the camera from the surface of the water, we used particles with diameter in the ranges 500 μm-710 μm and 710 μm-1000 μm. The best results were obtained when the granules were wet and there were no air bubbles trapped on their rough surface. Therefore, the night before the experiment, we soaked the particles in salted water with the addition of few drops of photographic wetting agent. For the experiments we used only the particles that remained at the surface. The working fluid for this set of experiments was a mixture of water, salt, and blue food dye. The reason for adding salt was that, since the Pliolite granules are only slightly denser than fresh water, its greater density ensured that the particles did not sink. Furthermore, with the addition of blue dye, we obtained a dark fluid, ideal to achieve a high contrast with the white granules. The density of the water, measured with an optical refractometer before adding the colour, was about 1.04 g cm^{-3}. A small quantity of photographic wetting agent was finally added to the working fluid to reduce the surface tension and therefore to reduce the tendency of the particles to stick together and to form large lumps. As in the dye experiment, three 500 W halogen lamps were suspended at about 50 cm from the water surface and switched on only for the duration of the experiments, typically 2-3 minutes, in order to avoid heating of the working fluid.

The same data acquisition procedure already described for the experiments with fluorescine was employed here. For this set of experiments more care was put in avoiding reflections of light from the surface of the water, as it would induce errors during the velocimetry analysis. We always included in the images at least two white spots to be used later as anchor points for the images (as required by the software DIGIMAGE that performs the velocimetry analysis, Dalziel 1993). This is necessary in order to position the images in the same location relative to each other and to reduce the error. The lens of the camera was also kept slightly out of focus so that the images of the particles were bigger and the tracking process was more efficient. Since, for a fixed focal length, the spatial resolution of the velocity field is mainly a function of the number of particles recognised during the tracking phase, it was essential to record good quality pictures, i.e. with correct exposure time and with high contrast between the colour of the background and of the particles.

In fig. 4.8 we show an example of a streak photograph obtained with the PIV software DIGIMAGE (Dalziel 1993). The streak-lines clearly show the vortex dipole and the position of the centre of rotation relative to an observer fixed with respect to the tank. The streak lines, made by white particles, are now black because the picture was converted to negative.

4.3 The experiments

4.3.1 Plan of the experiments

Tables 4.1, 4.2 and 4.3 show the range of slope angles and depths used for the experiments with dye and with particles.

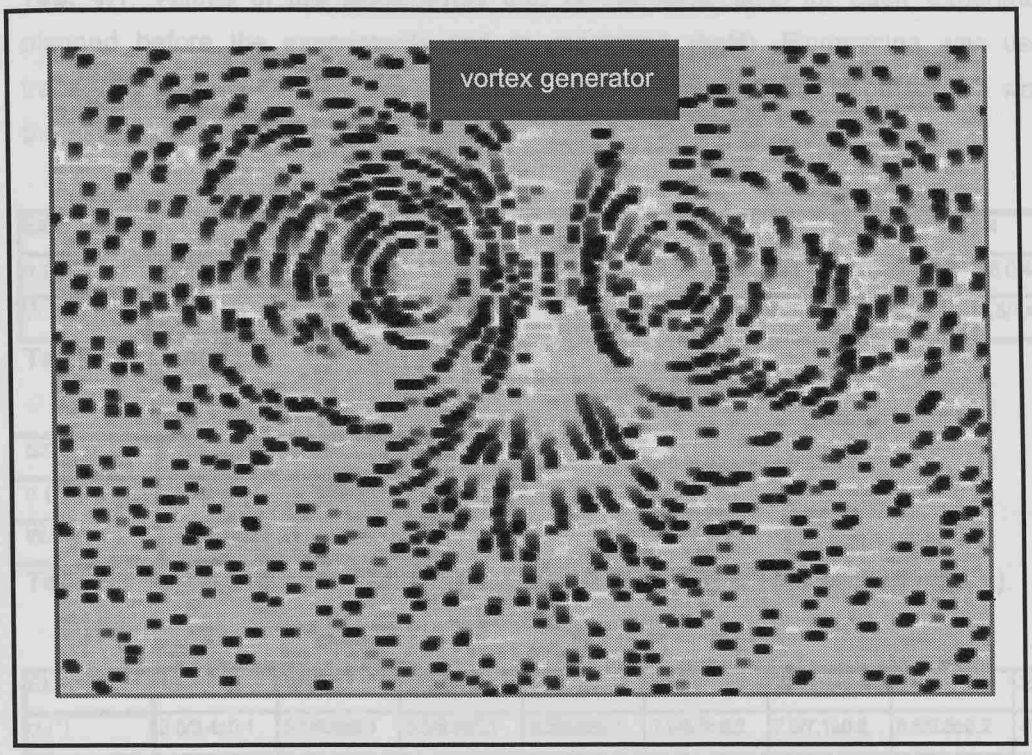

Fig 4.8: Streak picture of a vortex dipole immediately after its formation. The rectangle indicates the position of the vortex generator. The separation between the centres of the vortices is about 7 cm. The dipole is still moving over the flat bottom in a water depth of (4.1±0.1)cm. This picture is the result of a sophisticated image processing algorithm (Dalziel 1993) which has altered, but not distorted, some original features. For example only the particles that satisfy some threshold criteria are used to produce this picture. Also, the size of the particles shown in the picture does not correspond to the their real size.

EXP. N°	1	2	3	4	5	6	7
α (°)	3.5/**3.4±0.1**	5.5/**5.6±0.1**	5.5/**5.6±0.1**	7.0/**7.0±0.1**	7.0/**7.0±0.1**	8.5/**8.3±0.1**	8.5/**8.3±0.1**
W.L. (cm)	2.7/**2.7±0.1**	2.5/**2.7±0.1**	4.5/**4.3±0.1**	2.5/**2.7±0.1**	4.5/**4.4±0.1**	2.5/**2.7±0.1**	4.5/**3.7±0.1**

Tab. 4.1: Values of the slope angle and of the water level for each experiment as planned before the experiments and as measured (bold). Fluorescine was used as tracer (see section 4.2.3 b). For water level (W.L.) is intended the depth of the water off the slope, i.e. at the flat bottom region.

EXP. N°	8	9	10	11	12	13	14
α (°)	10.0/**9.9±0.1**	10.0/**9.9±0.1**	12.0/**12.4±0.1**	12.0/**12.4±0.1**	18.0/**17.5±0.4**	20.0/**20.4±0.2**	45.0/**45.6±0.7**
W.L. (cm)	2.5/**2.7±0.1**	4.5/**4.1±0.1**	2.5/**2.7±0.1**	4.5/**3.8±0.1**	4.5/**4.4±0.1**	4.5/**3.9±0.1**	4.5/**4.4±0.1**

Tab. 4.1: Continued.

EXP. N°	15a	15b
α (°)	90.0/90±1	90.0/90±1
W.L. (cm)	4.0/**3.6±0.1**	4.0/**3.9±0.1**

Tab. 4.2: As table 4.1 but with Pliolite AC80 used as tracer (see section 4.2.3.c).

EXP. N°	16	17 a	17 b	18	19	20	21	22
α (°)	3.5/**3.4±0.1**	5.5/**5.6±0.1**	5.5/**5.6±0.1**	5.5/**5.6±0.1**	7.0/**6.9±0.2**	7.0/**7.1±0.2**	8.5/**8.3±0.2**	8.5/**8.0±0.2**
W.L. (cm)	2.7/**2.7±0.1**	2.5/**2.5±0.1**	2.5/**2.7±0.1**	4.5/**4.5±0.1**	2.5/**2.7±0.1**	4.5/**4.3±0.1**	2.5/**2.7±0.1**	4.5/**4.3±0.1**

Tab. 4.3: As table 4.1 but with Pliolite AC80 used as tracer (see section 4.2.3.c).

EXP. N°	23	24	25	26	27
α (°)	10.0/**9.9±0.2**	10.0/**9.8±0.2**	12.0/**12.4±0.2**	12.0/**12.4±0.2**	18.0/**18.4±0.4**
W.L. (cm)	2.5/**2.7±0.1**	4.5/**4.3±0.1**	2.5/**2.7±0.1**	4.5/**4.4±0.1**	4.5/**4.5±0.1**

Tab. 4.3: continued.

The greatest water depth (4.5 cm) was the maximum working depth of the apparatus. Experiments 15a, 15b, and 15c (with the vertical wall) were made to check the behaviour of the vortices against the potential theory and other published experiments and are discussed in section 4.7.

4.3.2 Summary of observations

Time series of pictures from three experiments made using fluorescine are shown in plate 1 [slope angle α=3.4°, water depth 2.3 cm], plate 2 [slope angle α=7°, water depth 2.7 cm] and plate 3 [slope angle α=7°, water depth 4.4 cm].

An examination of the plates indicates that the motion of the dipole can be divided in four main phases. 1) After the generation of the dipole, at $t=t_0$, and while on the flat bottom, the vortices move almost parallel to each other along an approximately straight path. Their separation increases slowly with time. 2) When the vortices meet the slope, at $t=t_1$, they still progress forward along the straight path but their separation increases more rapidly until they reach a minimum distance (R_f) from the shore ($t=t_2$). 3) The vortices then move parallel to the shoreline and apart from each other until 4), at $t=t_3$, they start to move towards deeper water [this process is called rebounding (e.g. van Heijst and Flor, 1989 b, Orlandi, 1990)]. The rebounding consists in the pairing of secondary vortices, generated by viscous interaction of the main flow with the boundary, with the primary to form an unbalanced dipole. The division of the trajectory of the vortices in four phases can be seen more clearly in plots like the one shown in fig. 4.9 and corresponding to experiment 2 in tab. 4.1. The rebounding induced by the action of secondary vortices (not visible in plates 1 to 3 since there is no dye to mark them) can be seen, for example, in plate 2 by comparing the two images at t= 28 s and t=46 s.

Because of the diffusion of the tracer, the details of the centre of the vortices are lost in the very first seconds, therefore making the identification of their position at later times difficult. Streak photographs were also used to obtain a view of the flow at the fluid surface, as shown in plates from 4 to

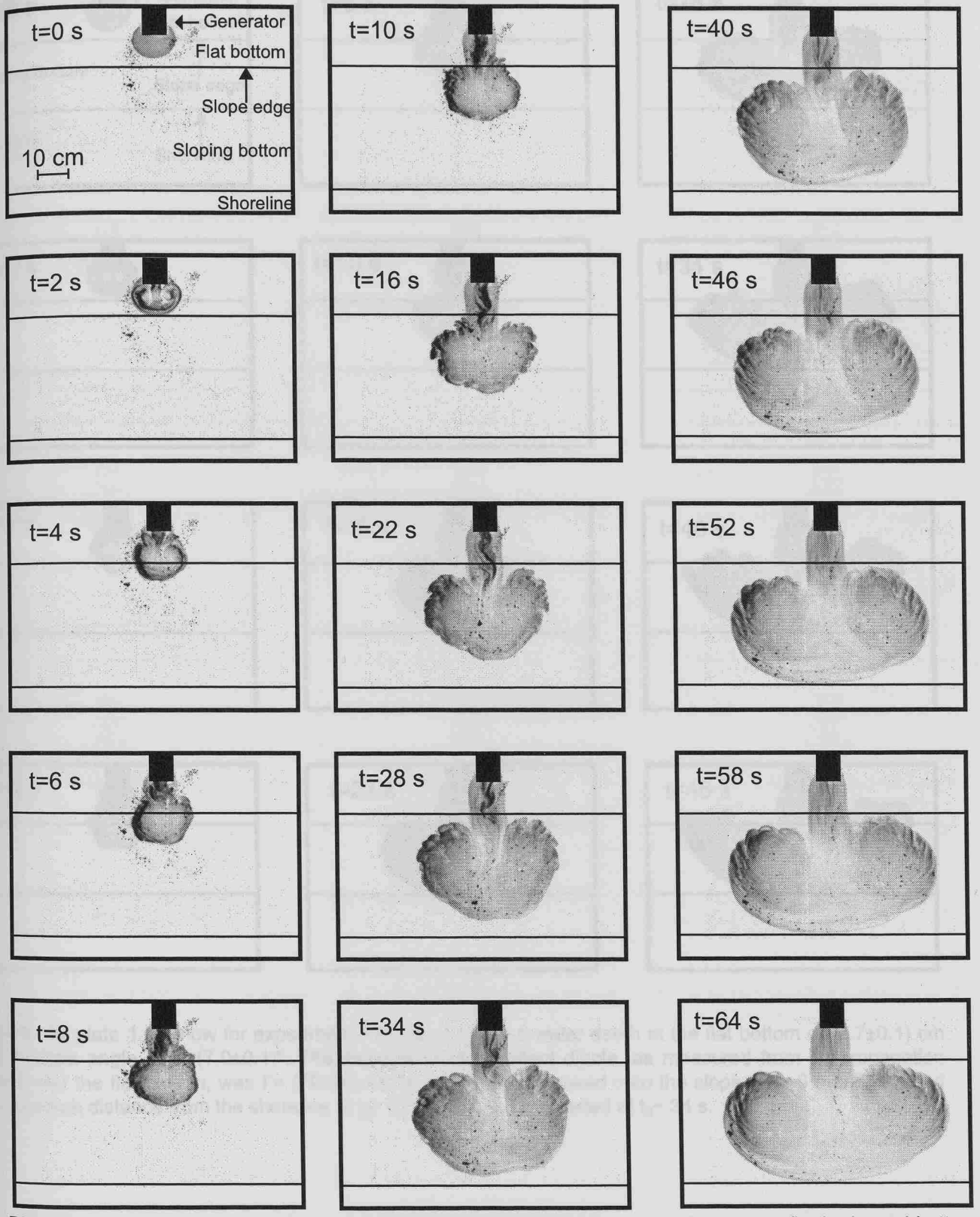

Plate 1: Evolution of a vortex dipole, for experiment 1 in table 4.1, progressing over a flat horizontal bottom (from t=0 s to t_1~5 s) and subsequently over a planar slope. The images are a plan view of the experimental tank from above. The position of the slope is indicated in the first frame. The water was coloured with fluorescine and a black background was used to enhance the contrast. The images shown in this plate are the result of a series of operation that are mainly: a) the use of an interlace filter; b) the subtraction of the background (as recorded before the run) from each image; c) conversion of the images to negative. Those operations are necessary to improve the quality of the images and to optimise the visibility of the tracer. The vortices reached the minimum distance from the shore line at t_2~44 s. Rebounding started at t_3~95 s (not shown. The water depth at the flat bottom was (2.3±0.1) cm for this experiment (1 in table 4.1) and the angle formed by the planar slope with the horizontal was α=(3.4±0.1)°. The strength of the incident dipole, as measured from its propagation speed over the flat bottom, was Γ= (94±36) cm^2s^{-1}.

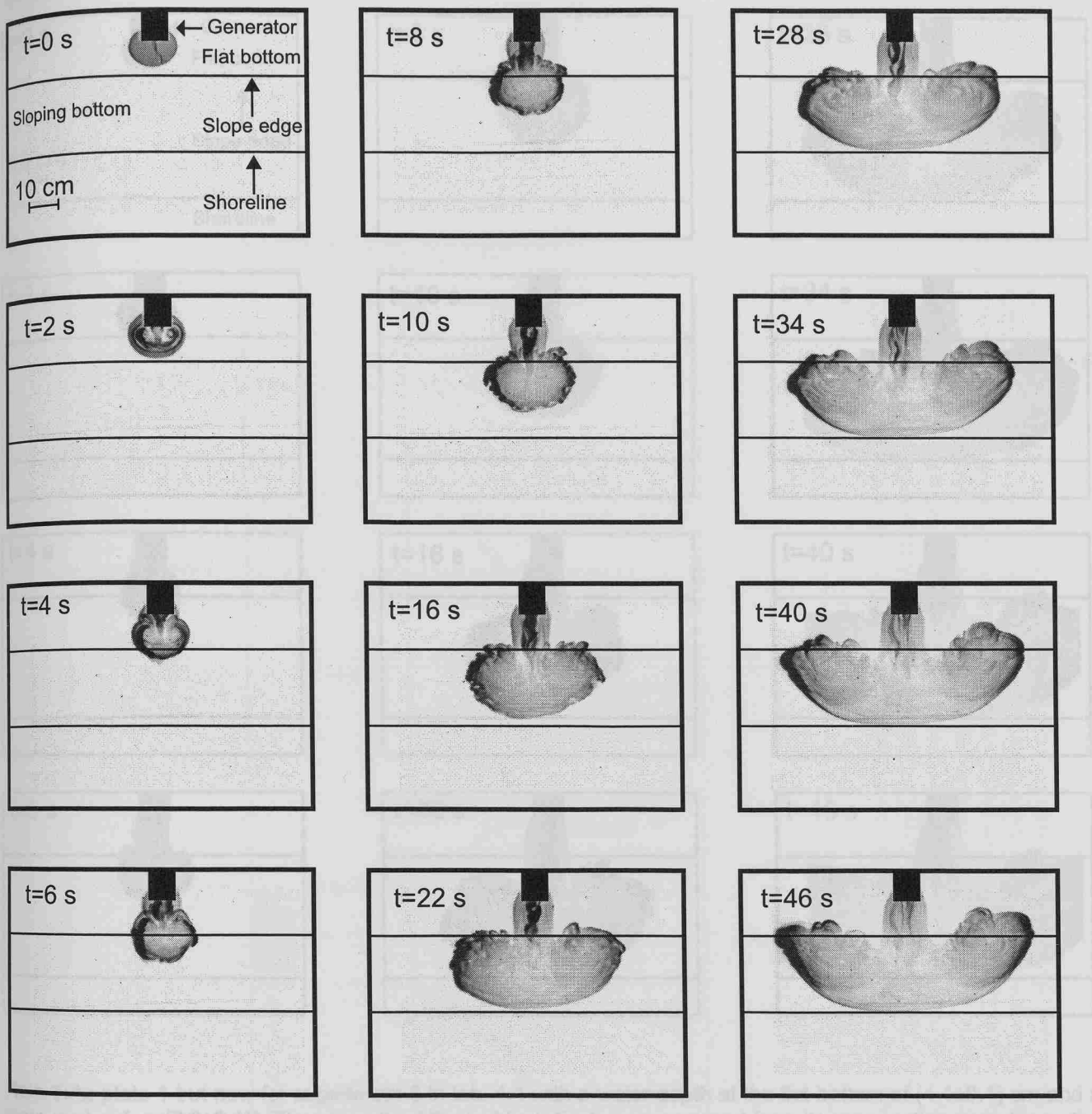

Plate 2: As plate 1 but now for experiment 4 in tab. 4.1 with a water depth at the flat bottom of (2.7±0.1) cm and a slope angle of α=(7.0±0.1)°. The strength of the incident dipole, as measured from its propagation speed over the flat bottom, was Γ= (79±34) cm^2s^{-1}. The dipole moved onto the slope at t_1~6 s and reached the minimum distance from the shoreline at t_2~14 s . Rebounding started at t_3~ 34 s.

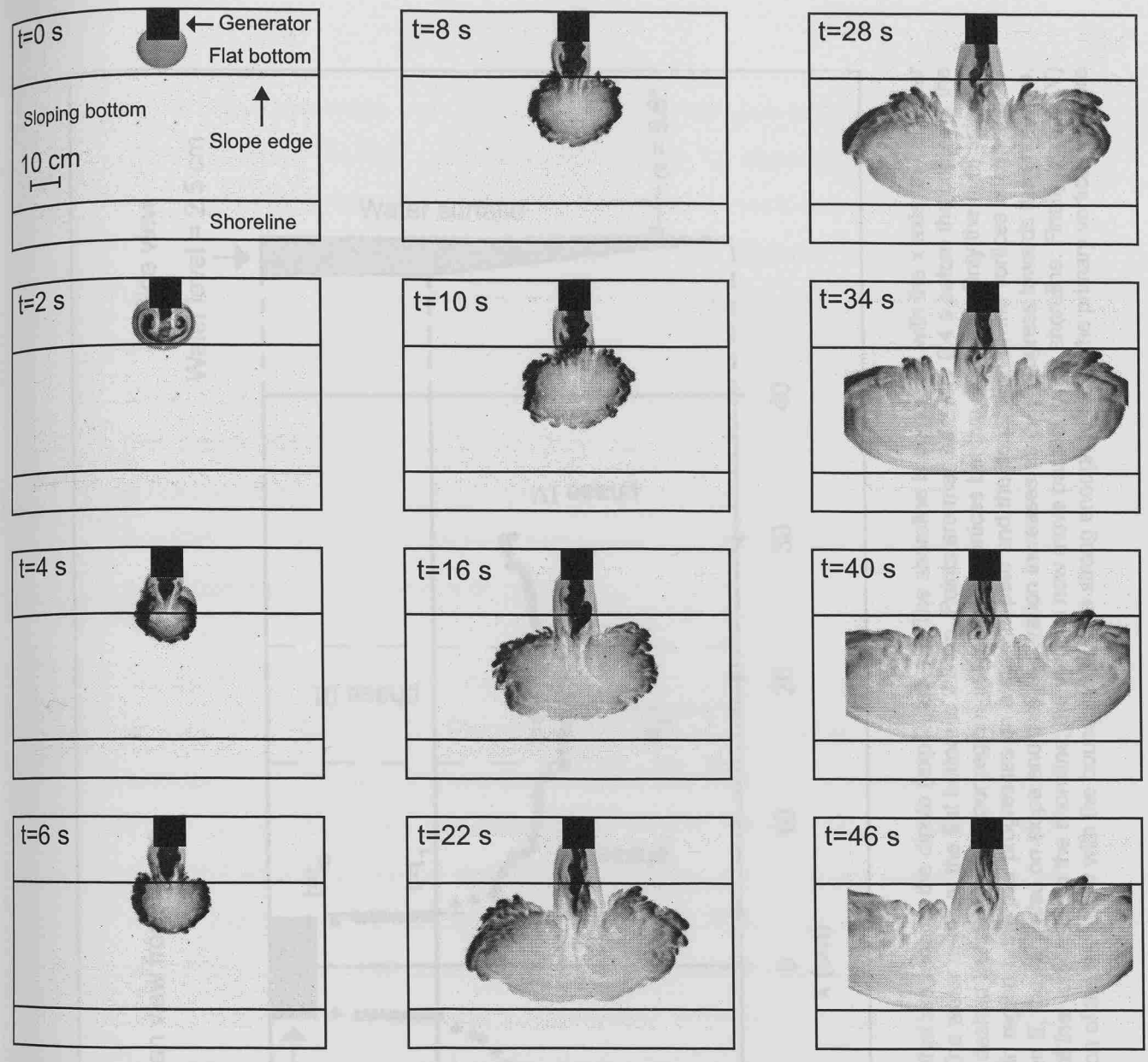

Plate 3: As plate 1 but now for experiment 5 in tab. 4.1 with a water depth at the flat bottom of (4.4±0.1) cm and a slope angle of α=(7.0±0.1)°. The strength of the incident dipole, as measured from its propagation speed over the flat bottom, was Γ= (129±41) cm^2s^{-1}. The dipole moved onto the slope at t_1~3 s and reached the minimum distance from the shoreline at t_2~17 s . Rebounding started at t_3~ 40 s.

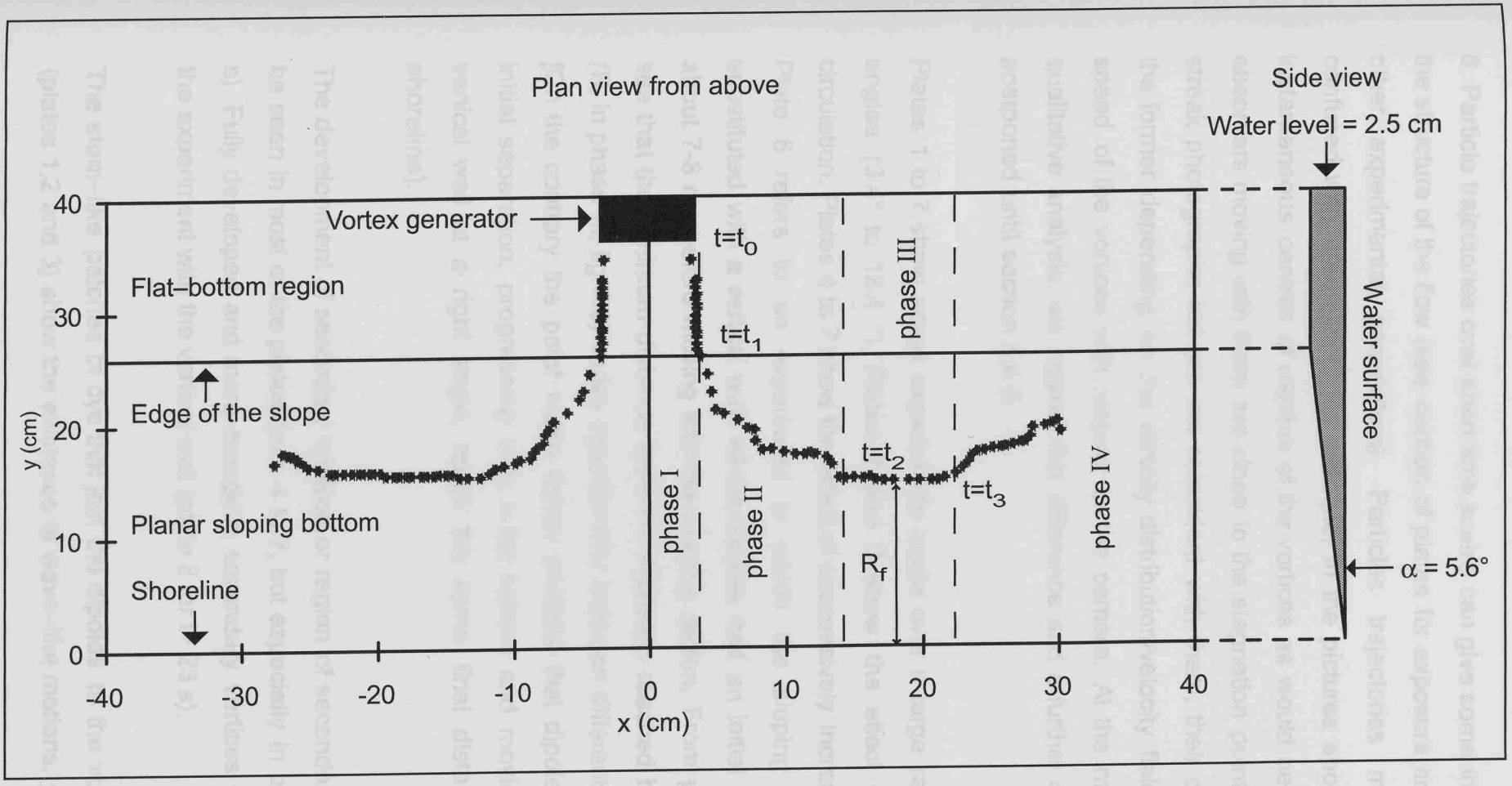

Fig. 4.9: Path followed by the centre of the two vortices that are forming the dipole (exp.2, tab 4.1. The shoreline is coincident with the x axis and a planar slope is used to simulating a beach with slope $\alpha = 5.6°$. The water depth at the flat bottom is 2.5 cm. Points are marked every 0.4 s before the centre of the vortices meets the slope and 0.8 s afterwards. The three dashed lines delimitate four regions in which the vortices behave differently. Only the right side has been marked to avoid confusion. When the vortices are in region I, the pair progresses on a straight path and the separation of the vortices is constant or slowly increasing with time. When the vortices enter region II, they are also on slope and their separation increases as they progress towards the shore-line. Region III is characterised by the minimum position (R_f) of the vortices from the shoreline; the vortices now move parallel to the shoreline. Finally (region IV) the secondary vortices generated by the viscous interaction of the main flow with the boundary become strong enough to move the primary vortices offshore (this process is called rebounding).

8. Particle trajectories over short time scales can give some information on the structure of the flow (see caption of plates for exposure time used and other experimental parameters). Particles trajectories must not be confused with streamlines. For example, in the pictures shown here, the instantaneous centres of rotation of the vortices as would be seen by two observers moving with them are close to the stagnation points showed by streak photographs but are not coincident with them, their distance from the former depending on the vorticity distribution/velocity field and on the speed of the vortices with respect to the camera. At the moment, for a qualitative analysis, we neglect this difference and a further discussion is postponed until section 4.4.3.

Plates 1 to 7 show some experiments made over a large range of slope angles (3.4° to 18.4 °). Plates 2 and 3 show the effect of increasing circulation. Plates 4 to 7 show the effect of successively increasing angles. Plate 8 refers to an experiment in which the sloping bottom was substituted with a vertical wall. All the dipoles had an initial separation of about 7-8 cm before moving into the sloping region. From plates 1-7 we see that the minimum distance from the shoreline reached by the vortices (R_f in phase III, fig 4.9) varies considerably between different experiments. [On the contrary the point vortex theory predicts that dipoles with equal initial separation, progressing over a flat bottom and moving towards a vertical wall at a right angle, reach the same final distance from the shoreline].

The development of secondary vortices or region of secondary vorticity can be seen in most of the plates from 4 to 7, but especially in plate 6 for t=16 s). Fully developed and more energetic secondary vortices were found in the experiment with the vertical wall (plate 8 for t> 23 s).

The stem–like patches of dye that join the dipoles to the vortex generator (plates 1,2 and 3) show the existence of wave–like motions, propagating in

the same direction of the dipole, with a wave–length of the order of the size of the dipole (e.g. plate 1 at t=22 s and t=64 s). Similar patterns are shown by plates 4, 5, 6, and 8.

The vortices are generally turbulent. The series of pictures in plates 1, 2 and 3 show for example that the outer border of the dipole undergoes different phases, starting with a smooth laminar motion during the roll-up of the vortices (e.g. plate 1 at t=2 s), which becomes irregular (plate 1 at t≥4 s) and eventually smooth again when the fluid slows down (plate 1 at t>40 s). Plate 1 also shows, for t>40 s, the development of ripples at the outer edge of the dipoles. This pattern is suggestive of the development of instabilities, probably shear instabilities of the Ekman flow, directed inwards along radial lines as required by the spin-down theory, in the bottom boundary layer (Greenspan and Howard, 1963 and section 2.4). The inner core of the vortices may be also turbulent (small eddies appear at the surface and near the centre of rotation in plate 4, for t=6 s until t=14 s, and plate 8, for t=8 and t=11 s). For example in plate 4, after the dipole crosses the border between the flat bottom region and the sloping bottom region the streamlines, so far circular and with only one centre of rotation (see pictures for t=4 s and t=6 s), change shape and each vortex appears to have two distinct centres of rotation. Far from the centres of rotation the streamlines are elliptical. The eccentricity e of the ellipses, roughly estimated from the pictures, varies from e~0.5 at t=6 to e~0.66 at t=10. At t=16 s the streamlines in proximity of the centre of the vortices are again almost circular.

Upward vertical motions inside the core of the vortices are required by mass conservation to balance the boundary layer radial flow towards the centre of the vortices (see section 2.4). To observe them we put an elongated streak of food dye at the bottom of the tank and approximately along the path followed by one of the two vortices forming the dipole. A time series of pictures taken while the dipole was progressing over the flat

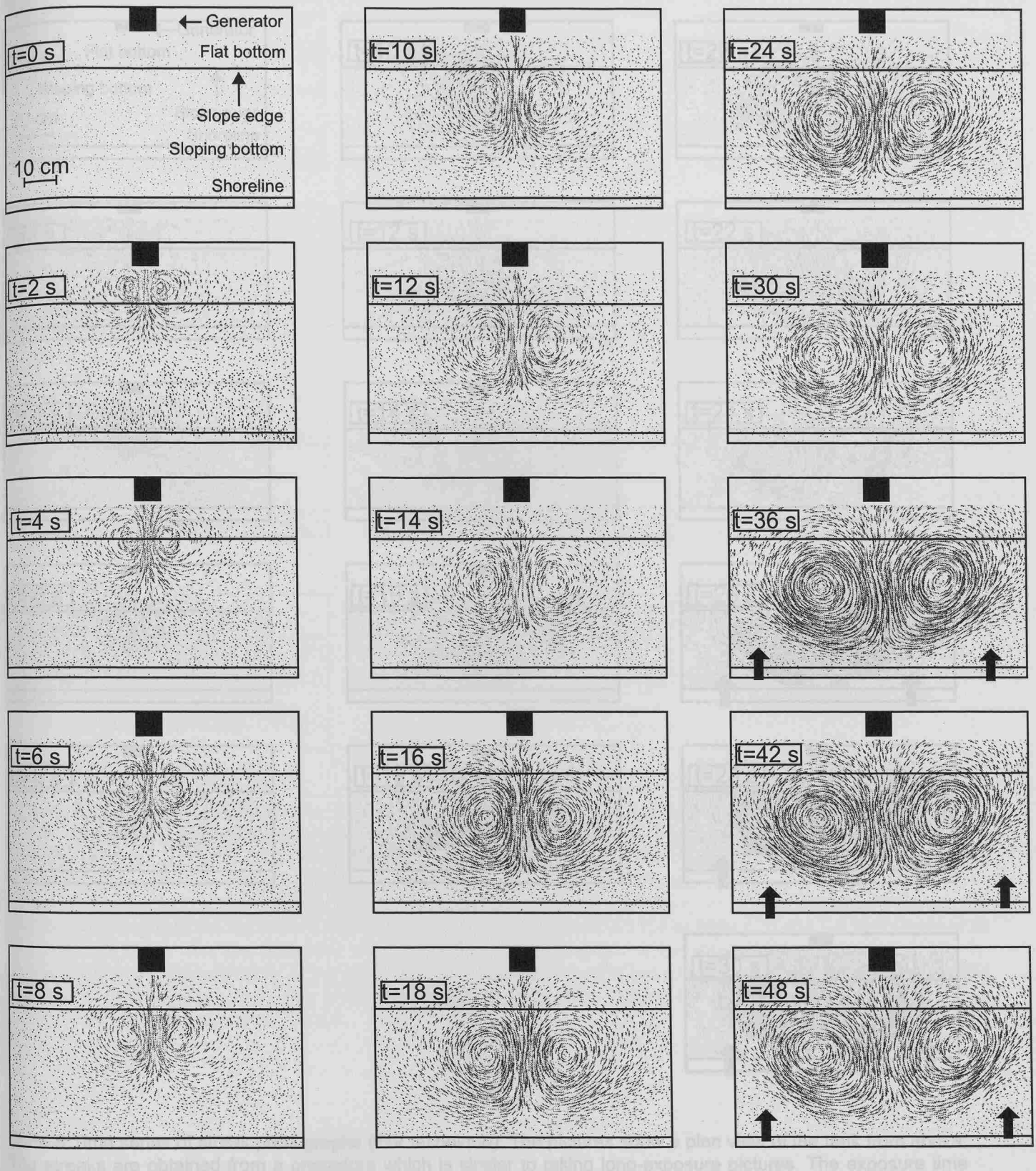

Plate 4: Time series of streak photographs (PIV technique). The pictures show a plan view of the tank from above. The streaks are obtained from a procedure which is similar to taking long-exposure pictures. The exposure time for frames from 0 s to 16 s is ~ 0.8 s, ~1.6s from 16 s to 24 s and ~3.2 s from 26 s to 30 s. The pictures do not show all the particles used to seed the fluid but only those that were satisfying the criteria imposed by the PIV analysis.

The water depth at the flat bottom was (2.7±0.1) cm for this experiment (16 in table 4.3) and the angle formed by the planar slope with the horizontal was α=(3.4±0.1)°. The strength of the dipole, as measured over the flat bottom, was Γ= (127±18) cm^2s^{-1}, then decreased to Γ= (90±13) cm^2s^{-1} when the vortices travelled almost parallel to the shoreline. Weak secondary vortices, or region of secondary vorticity, (arrows) developed as the main flow interacted with the apex of the wedge.

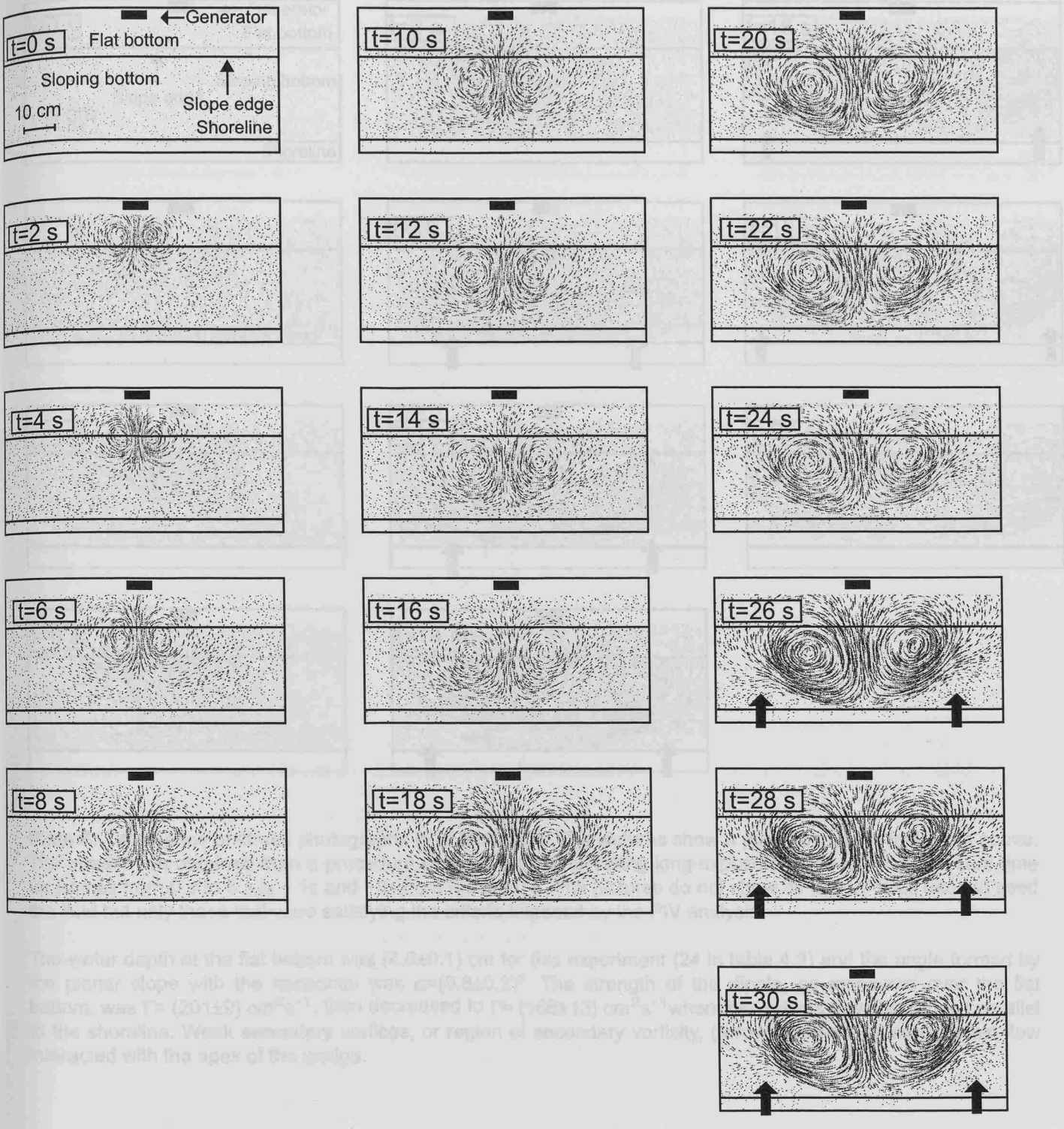

Plate 5: Time series of streak photographs (PIV technique). The pictures show a plan view of the tank from above. The streaks are obtained from a procedure which is similar to taking long-exposure pictures. The exposure time for frames from 0 s to 14 s is ~ 1s, ~2s from 16 s to 30 s and ~3s from 36 s to 48 s. The pictures do not show all the particles used to seed the fluid but only those that were satisfying the criteria imposed by the PIV analysis.

The water depth at the flat bottom was (2.7±0.1) cm for this experiment (17b in table 4.3) and the angle formed by the planar slope with the horizontal was $\alpha=(5.6\pm0.1)°$. The strength of the dipole, as measured over the flat bottom, was $\Gamma=(108\pm16)\ cm^2s^{-1}$, then decreased to $\Gamma=(91\pm13)\ cm^2s^{-1}$ when the vortices travelled almost parallel to the shoreline. Weak secondary vortices, or region of secondary vorticity, (arrows) developed as the main flow interacted with the apex of the wedge.

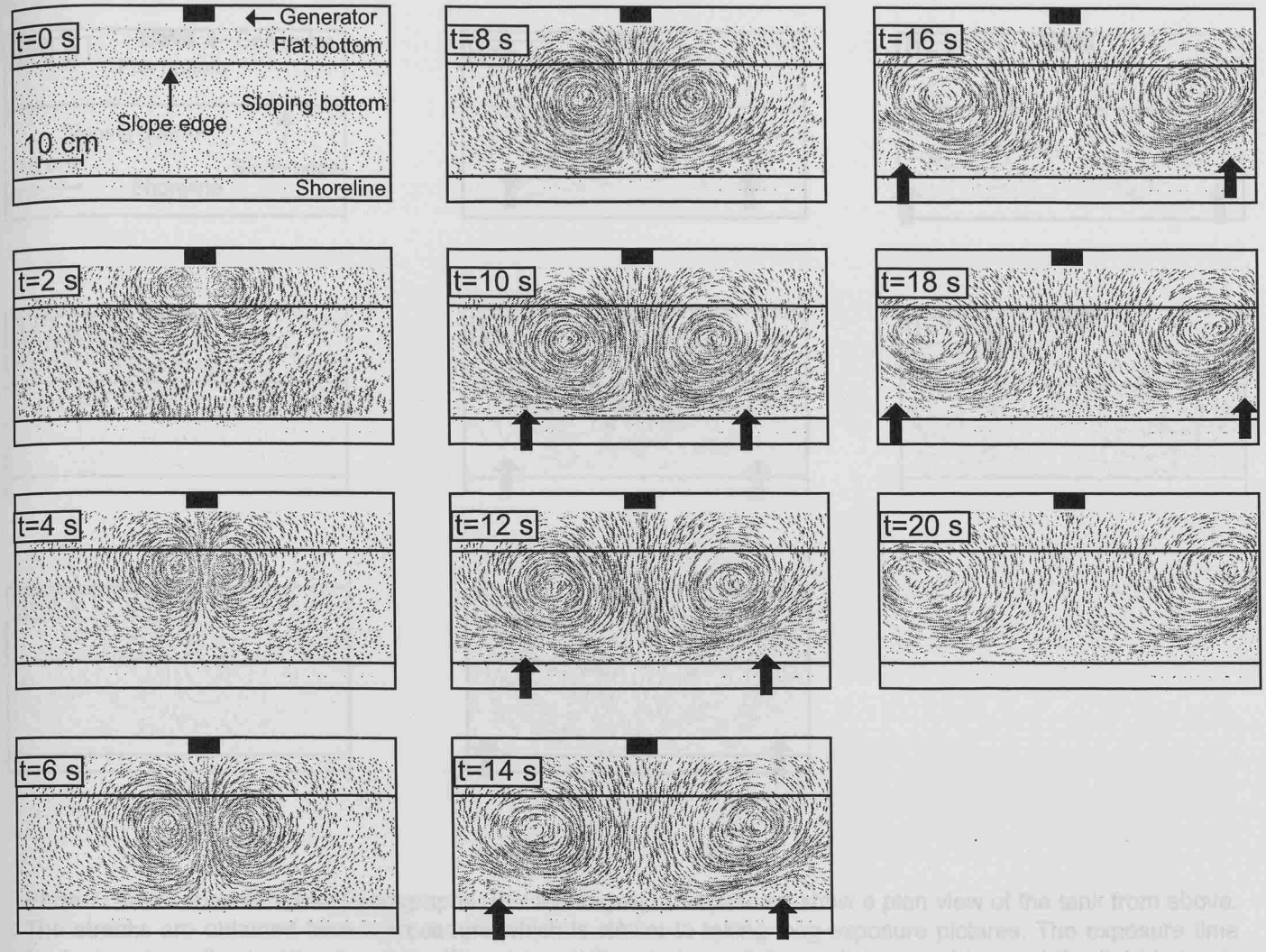

Plate 6: Time series of streak photographs (PIV technique. The pictures show a plan view of the tank from above. The streaks are obtained from a procedure which is simil)ar to taking long-exposure pictures. The exposure time for frames from 0 s to 6 s is ~ 1s and ~2s from 8 s to 20 s. The pictures do not show all the particles used to seed the fluid but only those that were satisfying the criteria imposed by the PIV analysis.

The water depth at the flat bottom was (4.6±0.1) cm for this experiment (24 in table 4.3) and the angle formed by the planar slope with the horizontal was α=(9.8±0.2)°. The strength of the dipole, as measured over the flat bottom, was Γ= (201±9) cm^2s^{-1}, then decreased to Γ= (186±13) $cm^2s^{-1}$when the vortices travelled almost parallel to the shoreline. Weak secondary vortices, or region of secondary vorticity, (arrows) developed as the main flow interacted with the apex of the wedge.

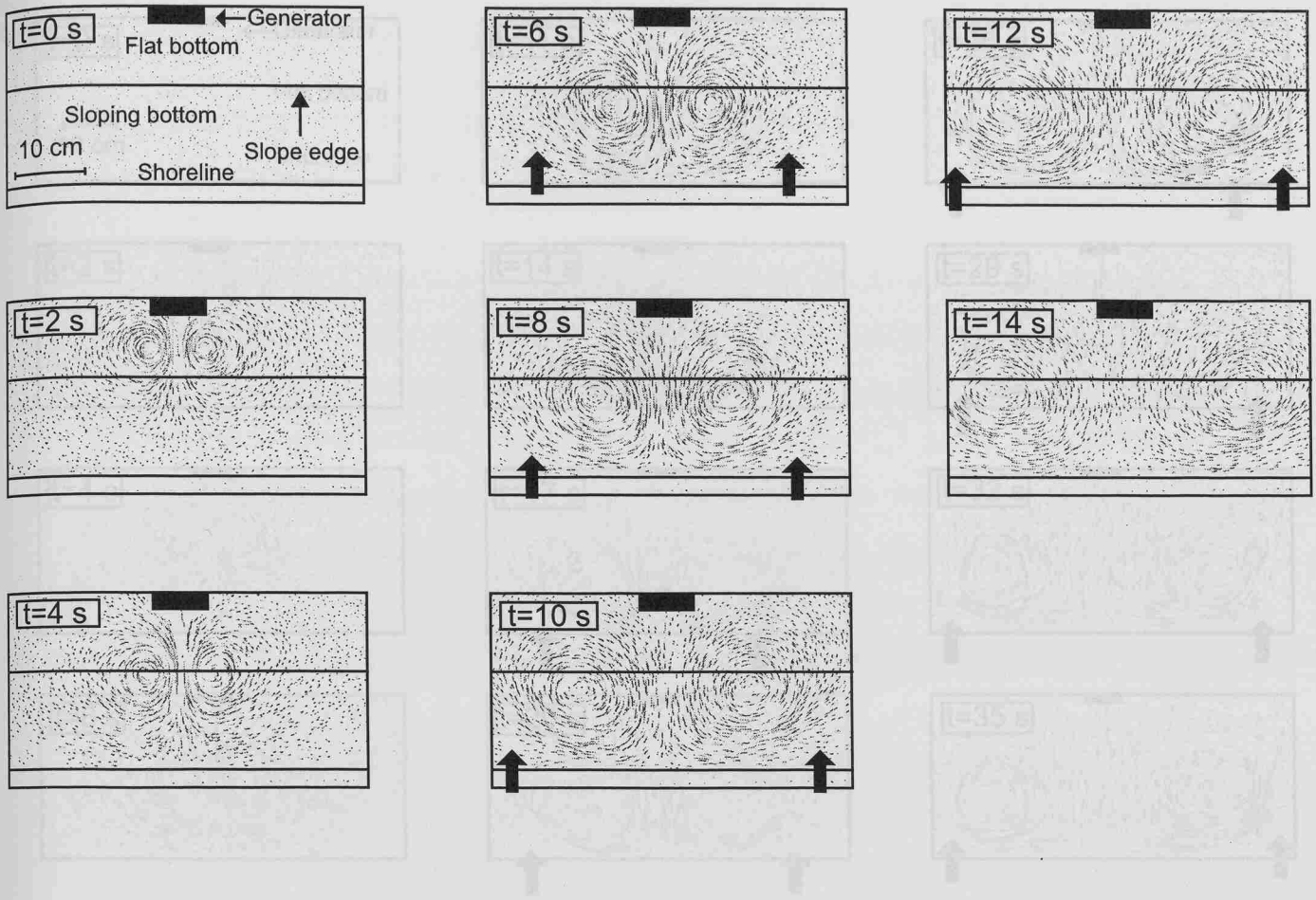

Plate 7: Time series of streak photographs (PIV technique). The pictures show a plan view of the tank from above. The streaks are obtained from a procedure which is similar to taking long-exposure pictures. The exposure time for frames from 0 s to 14 s is ~ 0.8s. The pictures do not show all the particles used to seed the fluid but only those that were satisfying the criteria imposed by the PIV analysis.

The water depth at the flat bottom was (4.5±0.1) cm for this experiment (27 in table 4.3) and the angle formed by the planar slope with the horizontal was α=(18.4±0.4)°. The strength of the dipole, as measured over the flat bottom, was Γ= (93±11) cm^2s^{-1}, then decreased to Γ= (89±10) $cm^2s^{-1}$when the vortices travelled almost parallel to the shoreline. Weak secondary vortices, or region of secondary vorticity, (arrows) developed as the main flow interacted with the apex of the wedge.

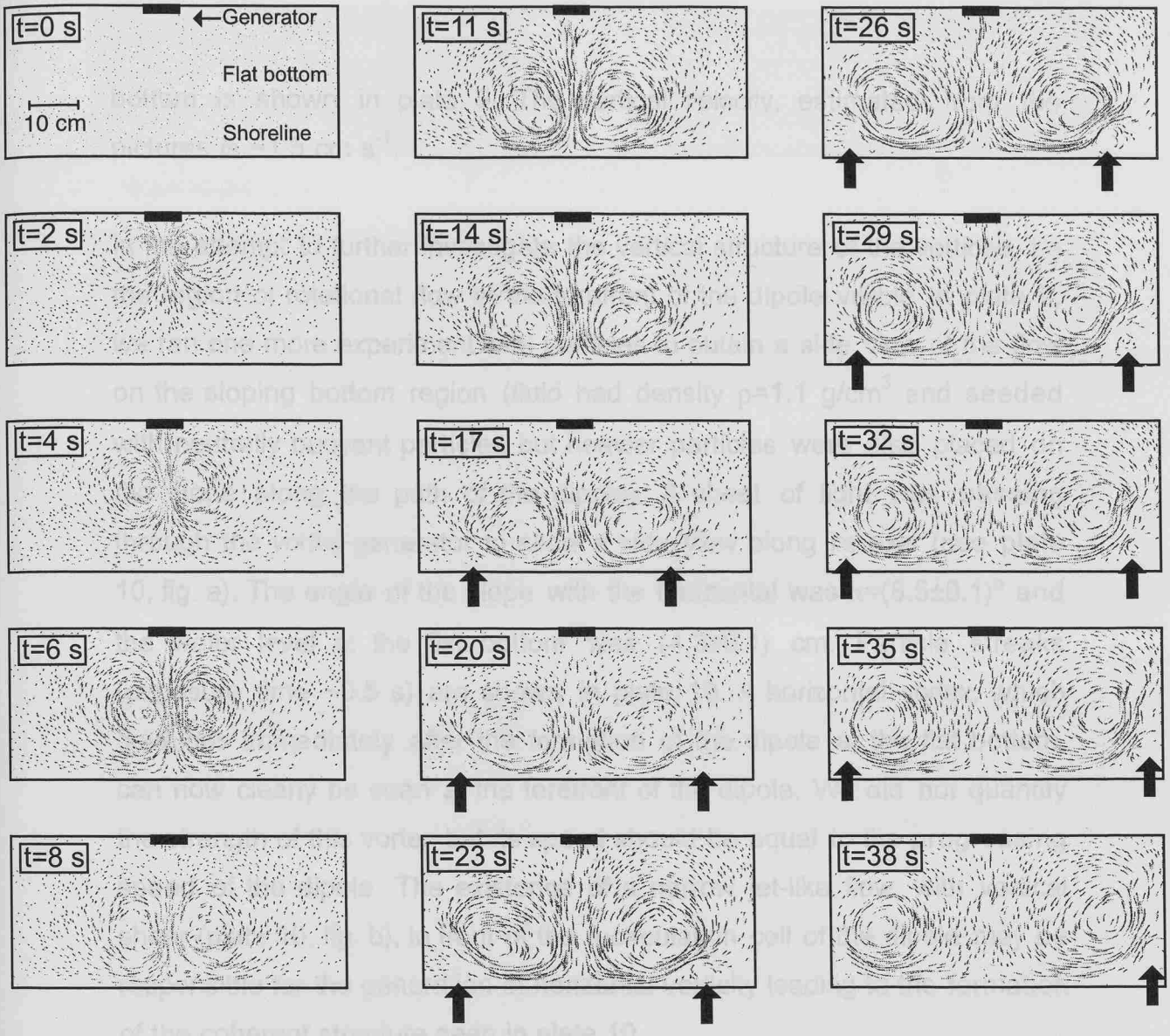

Plate 8: Time series of streak photographs (PIV technique). The pictures show a plan view of the tank from above. The exposure time for frames from 0 s to 8 s is ~ 0.8 s, ~ 1.6 s from 8 s to 20 s and ~ 3.2 s from 23 to 38 s. The pictures do not show all the particles used to seed the fluid but only those that were satisfying the criteria imposed by the PIV analysis.

The water depth at the flat bottom was (3.9±0.1) cm for this experiment (15 b in table 4.2) and the boundary is now a vertical wall (i.e. α=(90±1)°). The strength of the dipole, as measured at the beginning of the experiment, was Γ= (100±11) cm^2s^{-1}, then decreases to Γ= (73±8) $cm^2s^{-1}$when the vortices travel almost parallel to the shoreline. Weak secondary vortices, or region of secondary vorticity, (arrows) develop as the main flow interact with the apex of the wedge.

bottom is shown in plate 9. The vertical velocity, estimated from the pictures is ~1.5 cm s^{-1}.

In the attempt to further investigate the vertical structure of the vortices, i.e the region of rotational flow at the forefront of the dipole visible in plate 9, we ran one more experiment with particles to obtain a side view of the flow on the sloping bottom region (fluid had density ρ=1.1 g/cm^3 and seeded with neutrally buoyant particles but heavier particles were also placed on the slope along the path of the dipole). A sheet of light was passing through the vortex generator to allow a side view along its axis (see plate 10, fig. a). The angle of the slope with the horizontal was α=(8.5±0.1)° and the water level at the flat bottom was (4.3±0.1) cm. Particle streaks (exposure time ~0.5 s) are shown in plate 10. A horizontal vortex, which develops immediately after the formation of the dipole at the flat bottom, can now clearly be seen at the forefront of the dipole. We did not quantify the strength of this vortex but its speed should be equal to the progressing speed of the dipole. The existence of a narrow jet-like flow, with vertical shear (plate 10, fig. b), in front of the recirculation cell of the dipole may be responsible for the generation of horizontal vorticity leading to the formation of the coherent structure seen in plate 10.

4.4 Data processing

The images recorded from the experiments were used to: a) measure the displacement of the centre of the vortices; b) obtain snapshots of the velocity and of the vorticity fields at the surface of the fluid (only when PIV was used). Both tasks were performed with the aid of the software DIGIMAGE (Dalziel, 1993).

The co-ordinate system used to make our measurements was created 1) by filming a grid with mesh size of 1 cm x 1 cm and placed underneath the

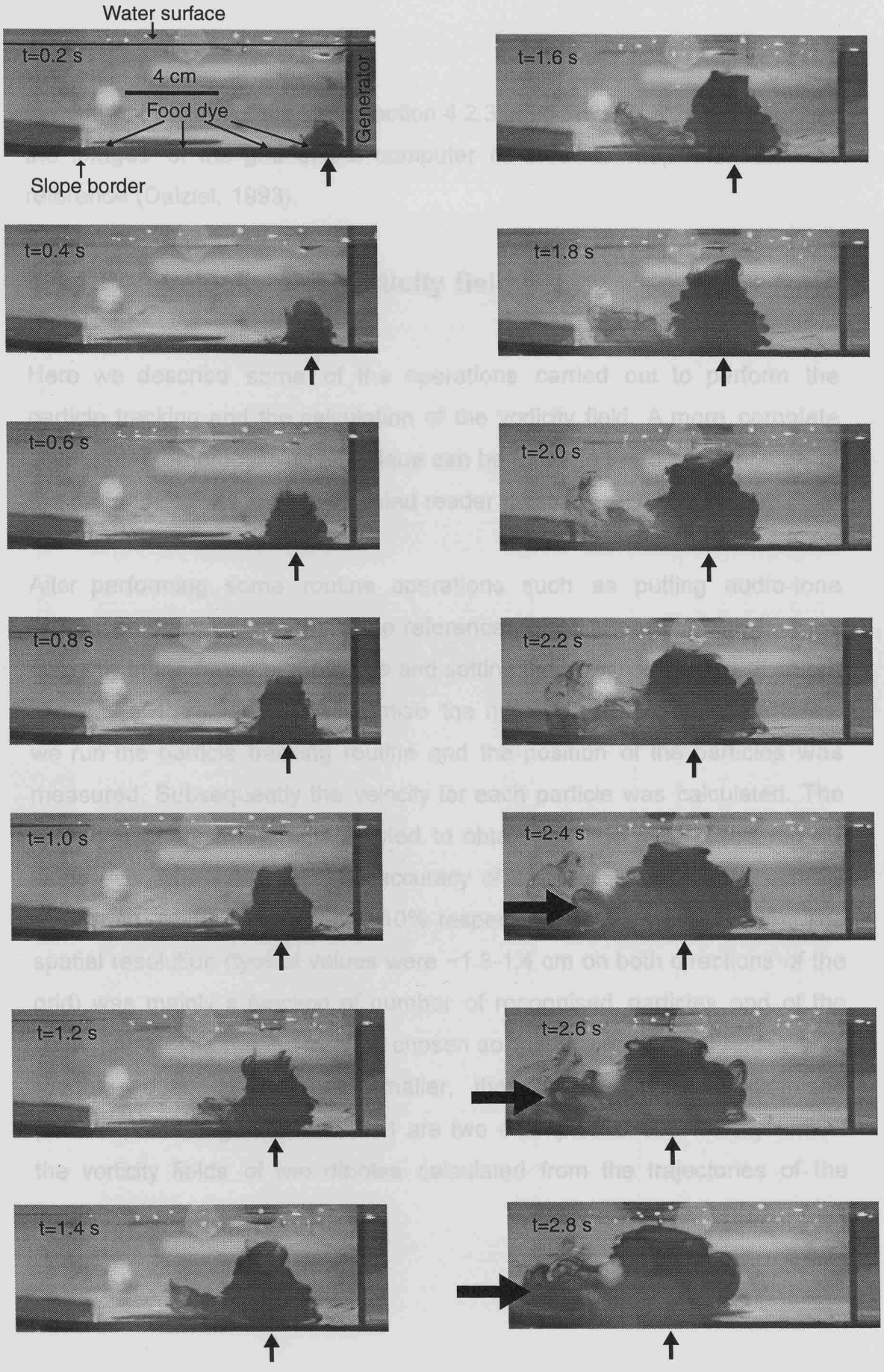

Plate 9: Vertical motions inside the vortex core. Side view of the experimental tank (flat bottom). An elongated streak of food dye, placed at the flat bottom of the tank along the path of one of the two vortices, shows that upward motions are present and that, as the vortex progresses towards the slope, its radius grows . The up pointing arrows mark roughly the position of the vortex advancing right to left. At the forefront of the vortex there is a region of rotational motion (arrows, see also plate 10).

transparent bottom of the tank (section 4.2.3.b, fig. 4.7), and 2) by importing the images of the grid in the computer in order to map the frame of reference (Dalziel, 1993).

4.4.1 PIV: velocity and vorticity field

Here we describe some of the operations carried out to perform the particle tracking and the calculation of the vorticity field. A more complete account on the processing technique can be found in the documentation of the program, to which the interested reader must refer (Dalziel, 1993).

After performing some routine operations such as putting audio-tone pulses on the tape, choosing the reference points to position the images correctly in the frame of reference and setting the threshold levels of colour intensity of the images to maximise the number of recognised particles, we run the particle tracking routine and the position of the particles was measured. Subsequently the velocity for each particle was calculated. The velocity data were then interpolated to obtain the velocity and the vorticity fields over a regular grid. The accuracy of the velocity and of the vorticity fields was estimated in 5% and 10% respectively (Linden et al. 1995). The spatial resolution (typical values were ~1.3-1.4 cm on both directions of the grid) was mainly a function of number of recognised particles and of the focal length. The mesh size was chosen so that the number of nodes was roughly equal, or eventually smaller, than the number of recognised particle paths. Fig. 4.10 and 4.11 are two examples of the velocity and of the vorticity fields of two dipoles calculated from the trajectories of the particle.

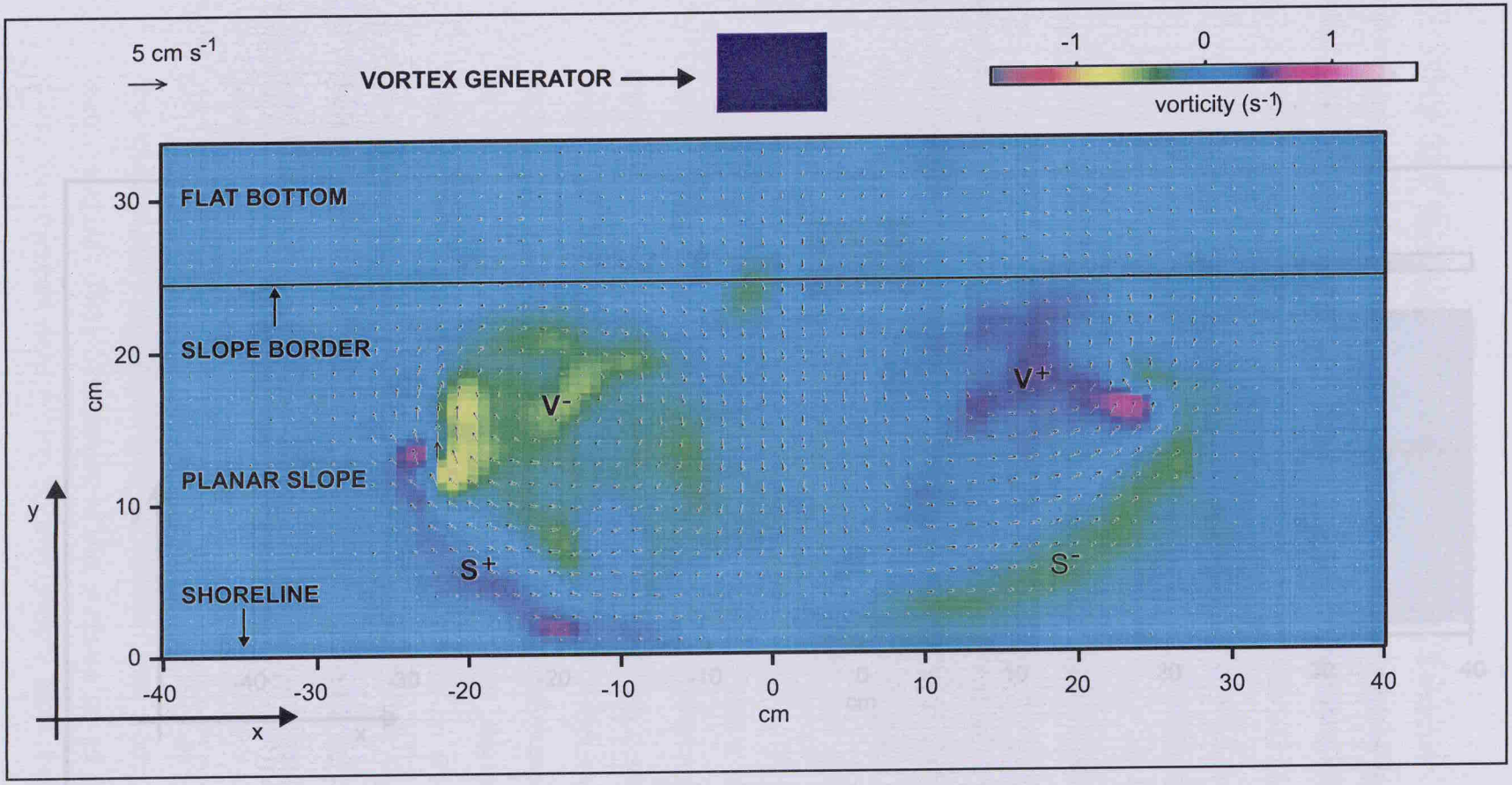

Fig 4.10: Velocity and vorticity fields of a vortex dipole moving over a planar sloping bottom 24 s after its formation. The shoreline is coincident with the x axis. The blue box marks the position of the vortex generator. The angle of the planar slope with the horizontal plane is (5.6±0.1)° and the water depth at the flat bottom is (2.4±0.1)cm (experiment 17 b in tab. 4.3). The velocity and the vorticity fields were computed with a PIV technique (see section 4.4.1). The snapshot was taken when the vortices were moving almost parallel to the shoreline and in opposite directions. The two main vortices are indicated with V+ and V-. The other two vortical regions (S+ and S-) are secondary vortices induced by the viscous interaction of the primary flow with the boundary. The secondary vortices are responsible for driving the main vortices offshore, a phenomenon called rebounding (see also section 4.3.2 , fig. 4.9 and fig. 4.13 a). The path followed by the vortices in this experiment is shown in fig. 4.13 a.

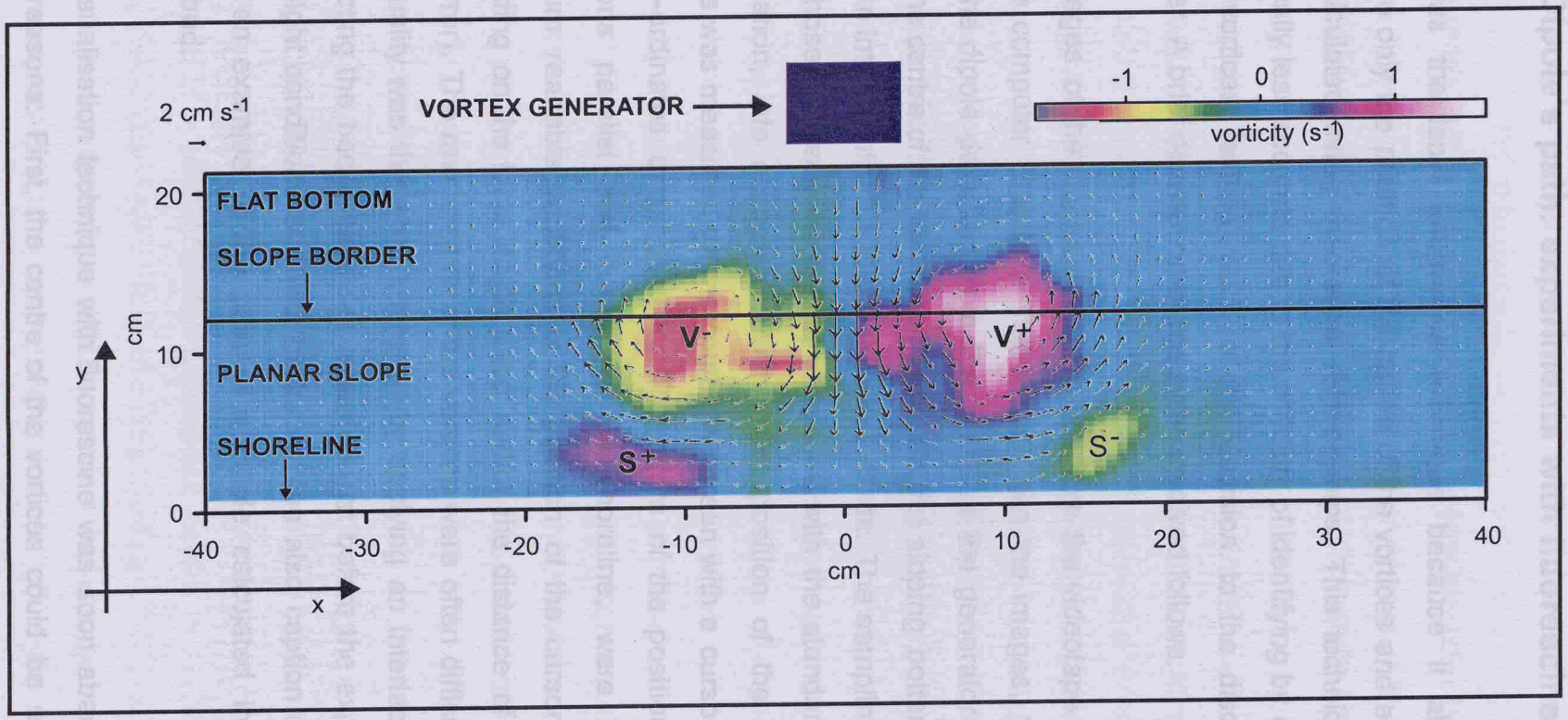

Fig 4.11: Velocity and vorticity fields of a vortex dipole moving over a planar sloping bottom 8.24 s after its formation. The shoreline is coincident with the x axis. The blue box marks the position of the vortex generator. The angle of the planar slope with the horizontal plane is (12.4±0.2)° and the water depth at the flat bottom is (2.7±0.1)cm (experiment 25 in tab. 4.3). The velocity and the vorticity fields were computed with a PIV technique (see section 4.4.3). This snapshot was taken when the vortices were moving almost parallel to the shoreline and in opposite directions. As in fig. 4.10, the two main vortices are indicated with V+ and V- and the other two vortical regions (S+ and S-) are secondary vortices induced by the viscous interaction of the primary flow with the boundary. The angle is now steeper compared with the situation shown in fig. 4.10 and therefore the centre of the vortices is just at the border of the planar slope with the flat bottom region. The path followed by the vortices in this experiment is shown in fig. 4.13 b. The two vortices are stronger than the ones shown in figure 4.10 and so are the secondary vortices, and that results in a stronger rebounding, as can be seen by comparing fig. 4.13 a and fig 4.13 b.

4.4.2 Dipole's path: experiments with fluorescine

This was the least informative technique because it allowed us to measure only the position of the centre of the vortices and everything else was calculated using theoretical relationships. This technique was also intrinsically less accurate due to the difficulty of identifying by eye the centre of the vortices, leaving much of the decision to the discretion of the observer. A brief description of the steps involved follows.

The images of the dipole were retrieved from the videotape and imported into the computer. The time interval between the images, from the time when the dipole detached from the mouth of the generator to the instant when the centre of the vortices moved into the sloping bottom region, was 0.4 s. An interval of 0.8 s was used afterwards. The sampling frequencies were chosen to keep the errors, calculated with the standard formulae of propagation, into acceptable limits. The position of the centre of the vortices was measured on the computer screen with a cursor that returned the co–ordinates of its position. The errors of the position, both in the directions parallel and normal to the shoreline, were taken as the minimum readable variations of the position of the cursor (~0.1-0.3 cm depending on the focal length used and/or the distance of the lens from the mirror). The raw images of the vortices were often difficult to interpret: their quality was therefore improved by applying an interlace filter and by subtracting the background (as recorded just before the experiment in the same light conditions and with no tracer, see also caption of plate 1). Fig. 4.9 is an example of the path of a dipole calculated in the way just described.

The visualisation technique with fluorescine was soon abandoned for two main reasons: First, the centre of the vortices could be easily localised whilst the vortices were rolling-up and shortly after, but their identification

became uncertain when the dye was diluted (see e.g. figure 4.6 b). The quality of the images was improved by filtering but this made the analysis extremely long and not practical. Second, and most important, only the position of the vortices could be measured but not the velocity field.

4.4.3 Dipole's path: experiments with particles (PIV)

Using the PIV data, we generated streak photographs as follows. We took the digitised snapshot of the seeded surface of the fluid at a particular instant, and averaged it with the 2, 3 or 5 images (depending on the flow speed) immediately before and with the same number of images immediately after. The images were spaced by 0.04 s, therefore making the corresponding exposure time 0.2 s, 0.28 s and 0.44 s. One example is shown in fig. 4.8. Once the streak photographs were created, the position of the centre of the vortices was measured in the same way explained in section 4.4.1. As before, the time interval between the streak-pictures was 0.4 s for the dipole on the flat bottom and 0.8 s afterwards. With this technique the localisation of the centres of the vortices was less ambiguous. The accuracy of the co-ordinates of the centres was estimated as ~0.1 - ~0.4 cm. However, streak photographs introduce a bias in the determination of the centre of rotation (i.e. the centre of the vortex) because the vortex also moves as a whole. The centre of rotation seen by an observer fixed with respect to the tank (we call it the apparent centre of rotation) is different from the one seen by another observer moving with the vortex (the true centre of rotation). The first observer will see the superposition of the rotational motion around the centre and the translational motion of the vortex. It follows that the distance between the two centres is a function of the translational speed of the vortex and of the velocity distribution inside the vortex core. Saffman (1979) studied a similar situation. He calculated the trajectories and the changes in shape of the apparent centre of rotation and of the true centre of rotation for a symmetric and two-dimensional vortex pair of elliptical shape and uniform vorticity

approaching a vertical wall (fig. 4.12). The true centre of rotation, or centroid, of the two-dimensional vortex, say (x_0,y_0), was defined as[15] (Saffman, 1979):

$$x_0 = \frac{\int_0^\infty \int_0^\infty y\omega dxdy}{\Gamma}, \qquad (4.1.a)$$

$$y_0 = -\frac{\int_0^\infty \int_0^\infty x\omega dxdy}{\Gamma}, \qquad (4.1.b)$$

where $\omega(x,y)$ is the vorticity and Γ is the strength of the vortex, i.e.,

$$\Gamma = \int_0^\infty \int_0^\infty \omega dxdy. \qquad (4.2)$$

We used the measurements of the vorticity field (see section 4.4.1) to estimate, using finite sums, the integrals 4.1.a, 4.1.b and 4.2. Two examples of trajectories calculated with formulae 4.1 and 4.2 are shown in fig. 4.13 a and fig. 4.13 b, where the average of the paths of the positive (main) vortex and of the negative (main) vortex is plotted. The same method was used to track the motion of the secondary vortices[16].

We now give a detailed description of the procedure used to calculate the position of the vortices. To estimate the integrals 4.1.a, 4.1.b and 4.2 we integrated the vorticity given by the PIV analysis. One possibility consisted

---

[15]Note the similarity between formulae 4.1 and 2.5. The analogy becomes very strong if the core of the vortex is thought as made of a cloud of point vortices, for which the two expressions becomes coincident (see also section 3.4.1).

[16]In doing so we assumed that the path followed by the two pairs of vortices was symmetric with respect to the axis of symmetry of the dipole (e.g. the axis x=0 in fig 4.13 a and b). This assumption was based on the exam of plots like the one shown in fig. 4.9

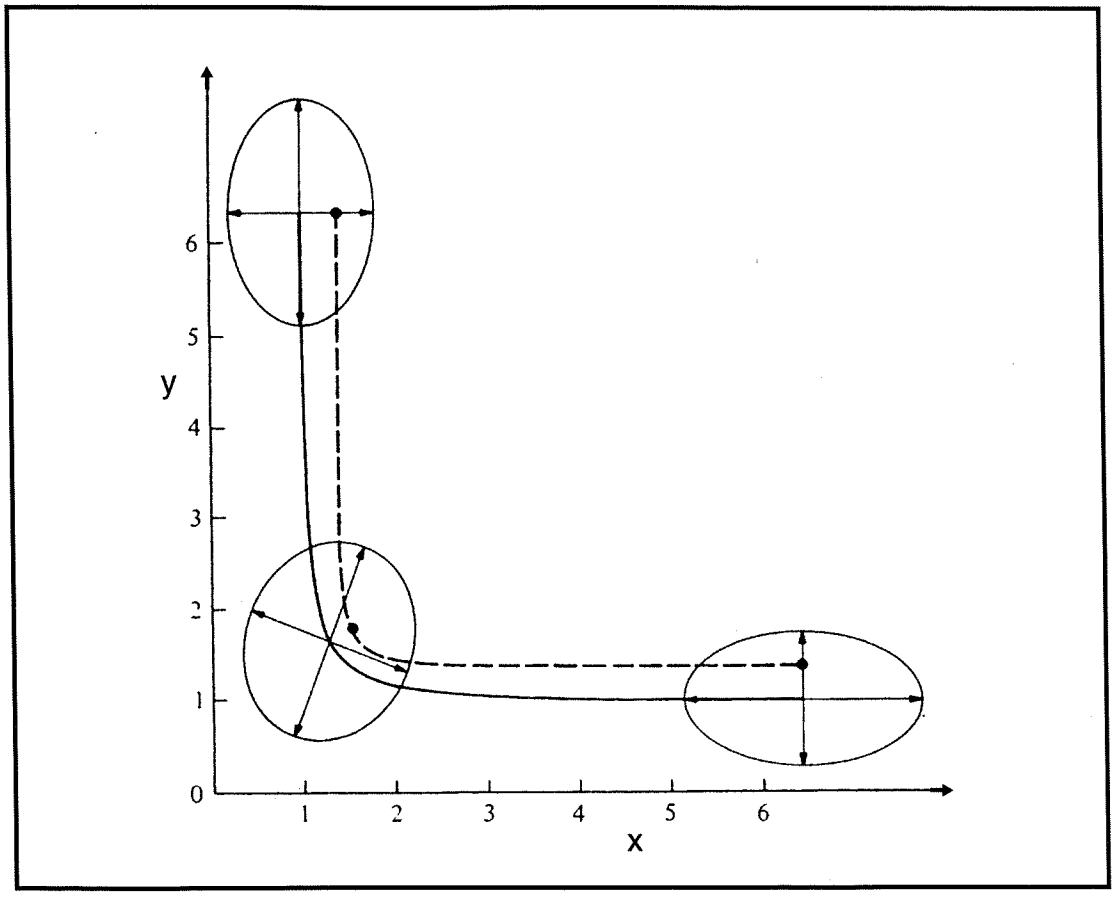

Fig 4.12: Path followed by the centre of rotation (solid line), as defined by 4.1.a and 4.1.b, and by the apparent centre of rotation (dashed line) of the positive vortex forming a dipole. A solid boundary is placed at y=0 and the negative vortex is not shown. x=0 is the axis of symmetry of the dipole. The black dot indicates the position of the apparent centre of rotation. (From Saffman, 1979).

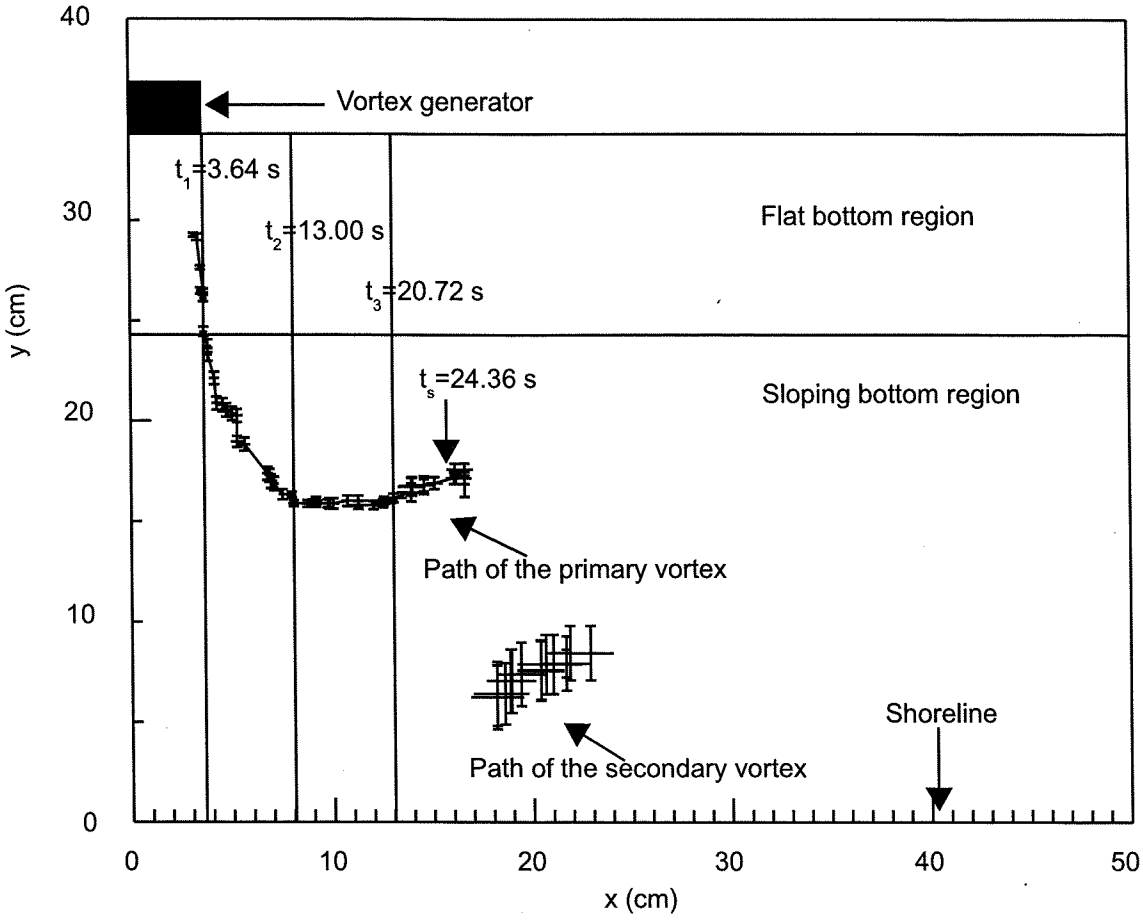

Fig. 4.13 a: Path followed by the primary and secondary vortices (exp. 17 b in tab. 4.3). The path of the primary vortex shown here is the average of the path of the positive and of the path of negative vortex. Likewise for the secondary vortex. We assumed that the flow is symmetric with respect to x=0 (see fig. 4.10). The time t_s corresponds to the sketch shown in fig. 4.10. The path of the secondary vortices is shown only for $t>t_3$.

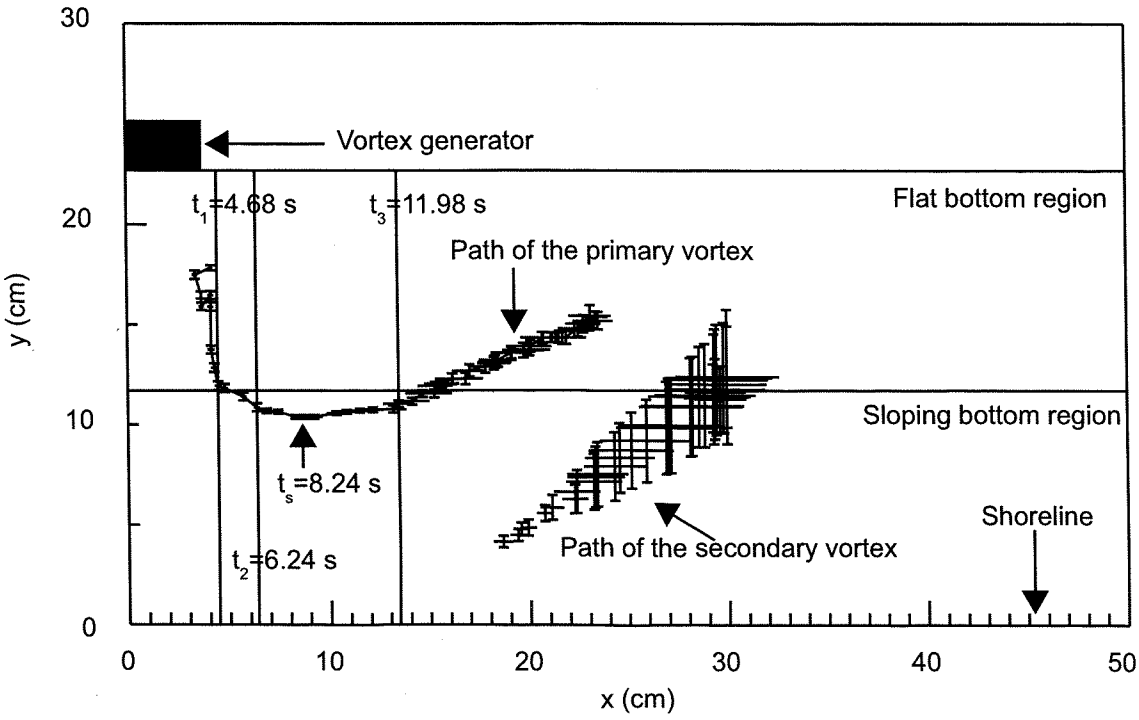

Fig. 4.13 b: As for fig. 4.13 a but for exp. 25 in tab 4.3. The time t_s corresponds to the sketch shown in fig. 4.11.

in defining *a priori* the regions of the fluid that contains the vortices and then estimate the integrals over this area. Another possibility was to estimate the integrals by considering only the vorticity values that were above (for positive vorticity) or below (for negative vorticity) a certain threshold and then repeat the procedure for a number of thresholds. We used the second method since in this way there is no need to define the boundary of the vortices. The integrals were estimated for the following set of thresholds: $\pm 12.0\ s^{-1}$, $\pm 11.9\ s^{-1}$, ..., $\pm 0.1\ s^{-1}$, $\pm 0.05\ s^{-1}$, $0.0\ s^{-1}$. By splitting the fluid domain in two (for example along the axis x=0 in fig. 4.14 a and b) we were able, for each threshold value, to isolate the vorticity (and the areas) forming the two main vortices and the two secondary vortices. This was possible because the flow had an axis of symmetry throughout the duration of the experiments. Fig. 4.14 shows the distribution of positive (negative) vorticity above (below) $0.1\ s^{-1}$ ($-0.1\ s^{-1}$). The integrals calculated with the lowest thresholds were probably contaminated with noise or smaller scale turbulent motions outside the vortex core. The 123 paths calculated between the positive and negative main vortices were then averaged into one single path and subsequently passed through a median filter to remove the spikes. The errors of the x and y co-ordinates of the path were taken as their standard deviation. The same procedure was used to track the movement of the secondary vortices.

A comparison of the track of the vortices (for experiment 27 in tab. 4.3) obtained using the integral method with the one obtained using the streak photographs method is shown in fig. 4.15. Some of the differences between the two paths can be explained qualitatively with the analysis of Saffman (1979, and fig. 4.12).

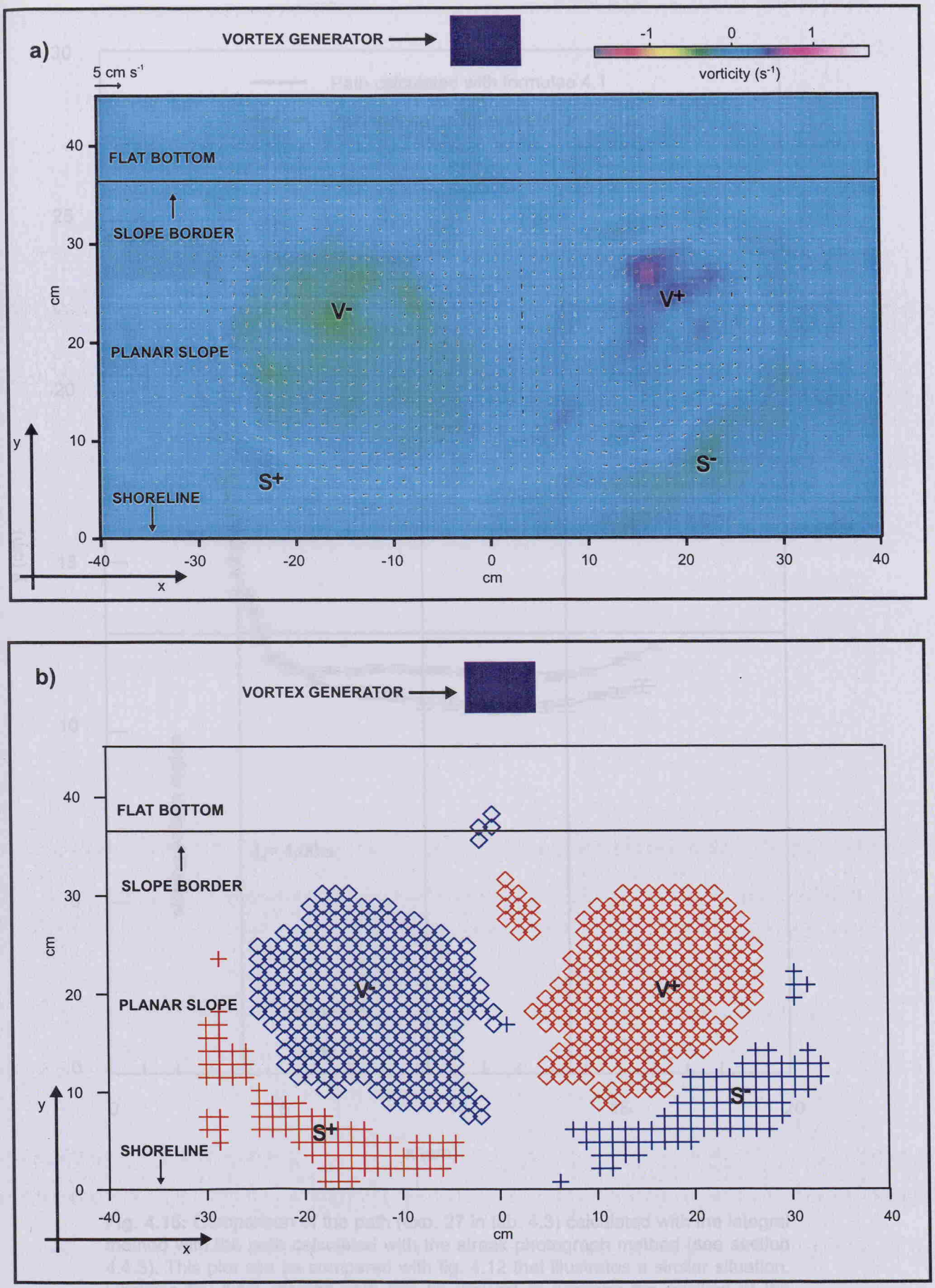

Fig. 4.14: The upper panel shows the velocity and the vorticity field for experiment 16 in tab. 4.3 at t=32.08 s. Below we show the distribution of vorticity, positive and negative, above 0.1 s^{-1}(◇ :V^+, + :S^+) and below -0.1 s^{-1}(◇ :V^-, + :S^-) as selected with a dedicated software. This operation enabled us to identify the areas over which the integrals 4.1.a, 4.1.b and 4.2 were estimated. The integrals were estimated for a number of thresholds (for vorticity) ranging from 0 s^{-1} to ±12 s^{-1} and for the whole duration of the experiments.

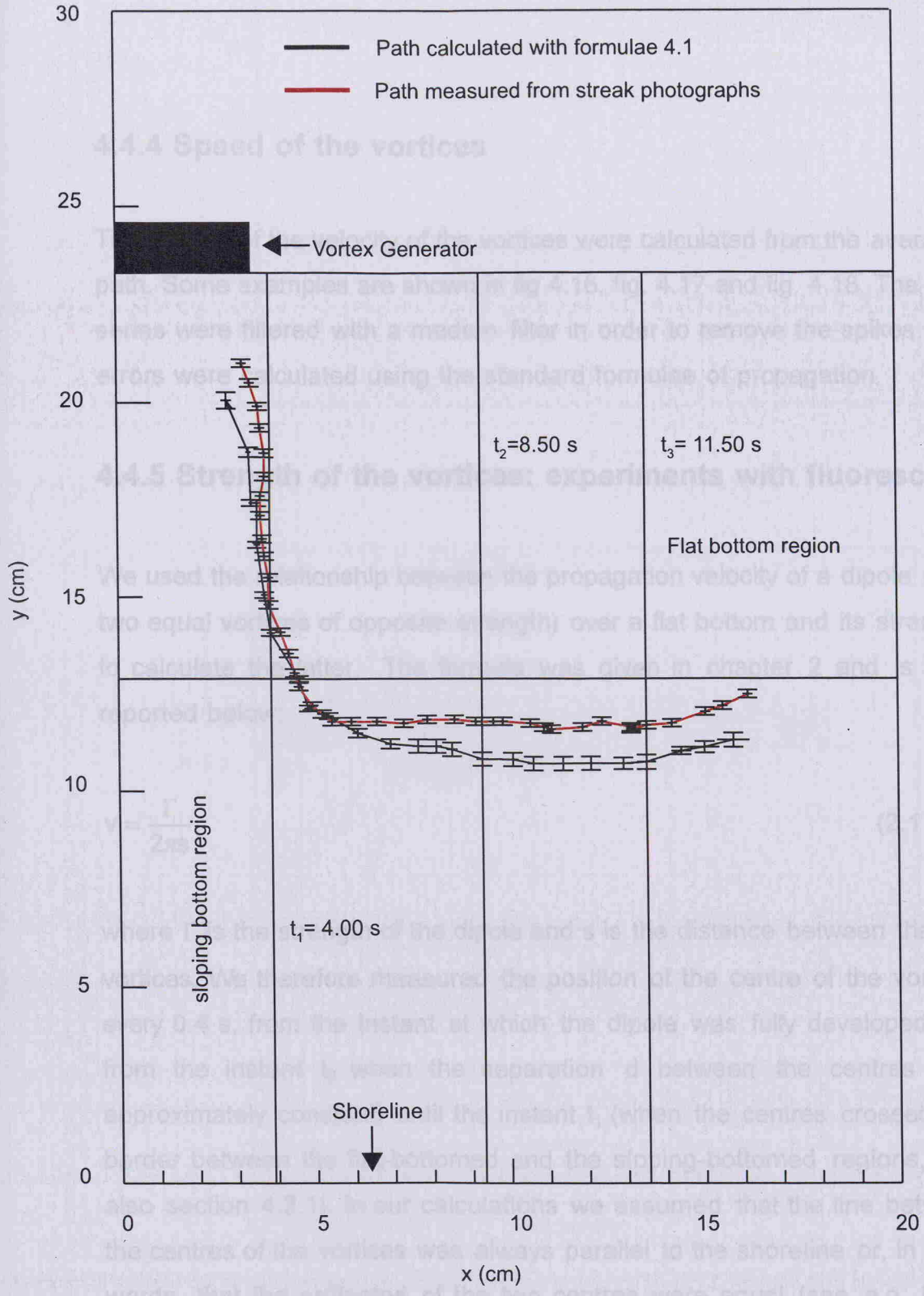

Fig. 4.15: Comparison of the path (exp. 27 in tab. 4.3) calculated with the integral method with the path calculated with the streak photograph method (see section 4.4.3). This plot can be compared with fig. 4.12 that illustrates a similar situation. Likewise fig. 4.12, the red path can be thought to describe the position of the instantaneous centre of rotation, and the black path the position of apparent centre of rotation.

4.4.4 Speed of the vortices

Time series of the velocity of the vortices were calculated from the averaged path. Some examples are shown in fig 4.16, fig. 4.17 and fig. 4.18. The time series were filtered with a median filter in order to remove the spikes. The errors were calculated using the standard formulae of propagation.

4.4.5 Strength of the vortices: experiments with fluorescine

We used the relationship between the propagation velocity of a dipole (with two equal vortices of opposite strength) over a flat bottom and its strength, to calculate the latter. The formula was given in chapter 2 and is also reported below:

$$v = \frac{\Gamma}{2\pi s}, \qquad (2.11)$$

where Γ is the strength of the dipole and s is the distance between the two vortices. We therefore measured the position of the centre of the vortices every 0.4 s, from the instant at which the dipole was fully developed (i.e. from the instant t_0 when the separation d between the centres was approximately constant) until the instant t_1 (when the centres crossed the border between the flat-bottomed and the sloping-bottomed regions, see also section 4.3.1). In our calculations we assumed that the line between the centres of the vortices was always parallel to the shoreline or, in other words, that the ordinates of the two centres were equal (see e.g. figure 4.6.a). The strength of the dipole was taken as the average of the values calculated every 0.4 s and the error was either the standard deviation or the maximum error of the calculated strengths, depending on whichever was

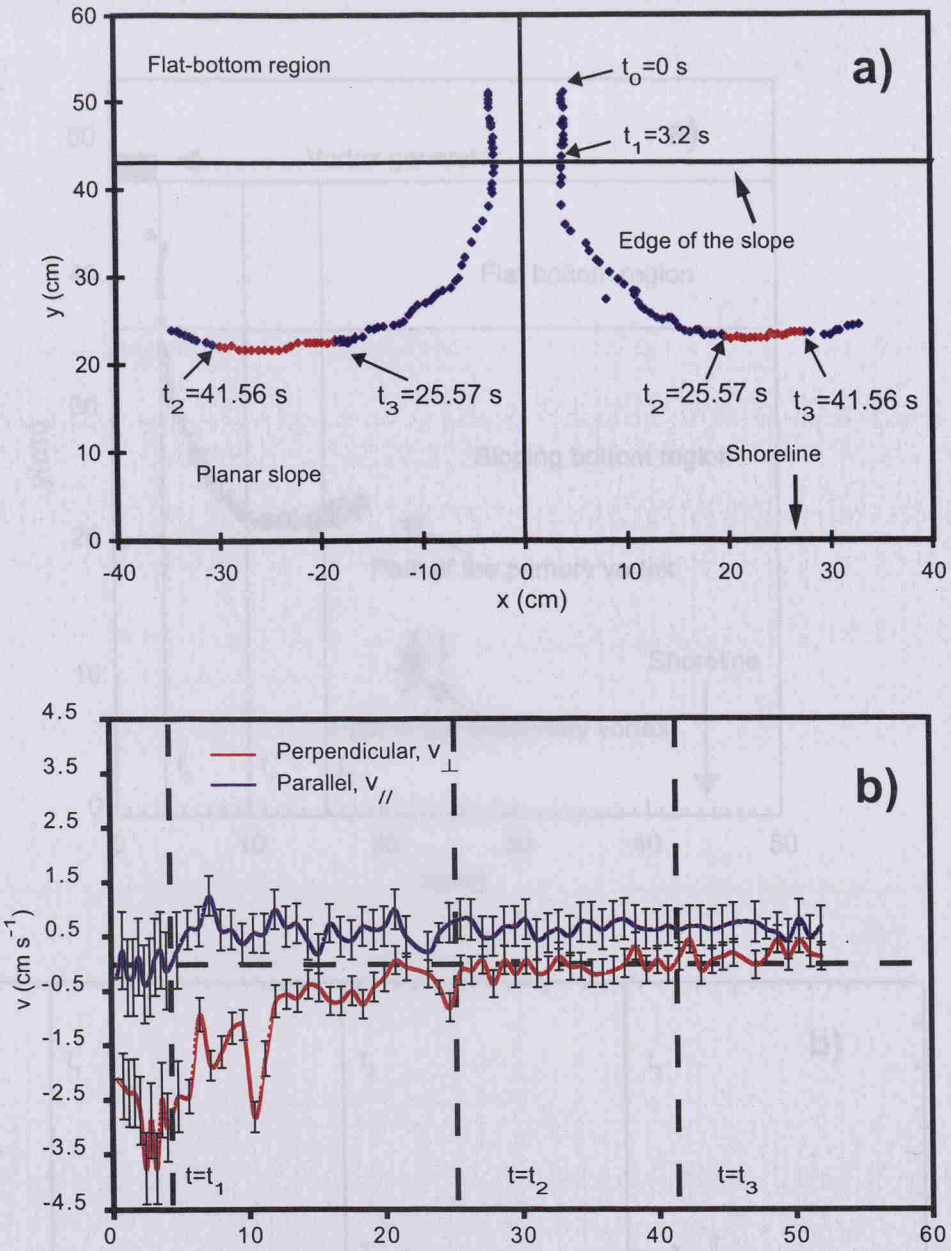

Fig. 4.16: a) Path followed by the vortices (exp. 3 in tab. 4.1). α= (5.6±0.1)°, water level at the flat bottom=(4.3±0.1) cm. The red dots indicate the portion of data used to compute the alongshore velocity. b) Time series of the average velocities in the directions parallel ($v_{//}$) and normal ($v_\perp$) to the shoreline . Note that in between the green lines (corresponding to the red dots in fig. a), $<v_\perp>$~0. At t~50 s, rebounding becomes important and $<v_\perp>$ is positive.

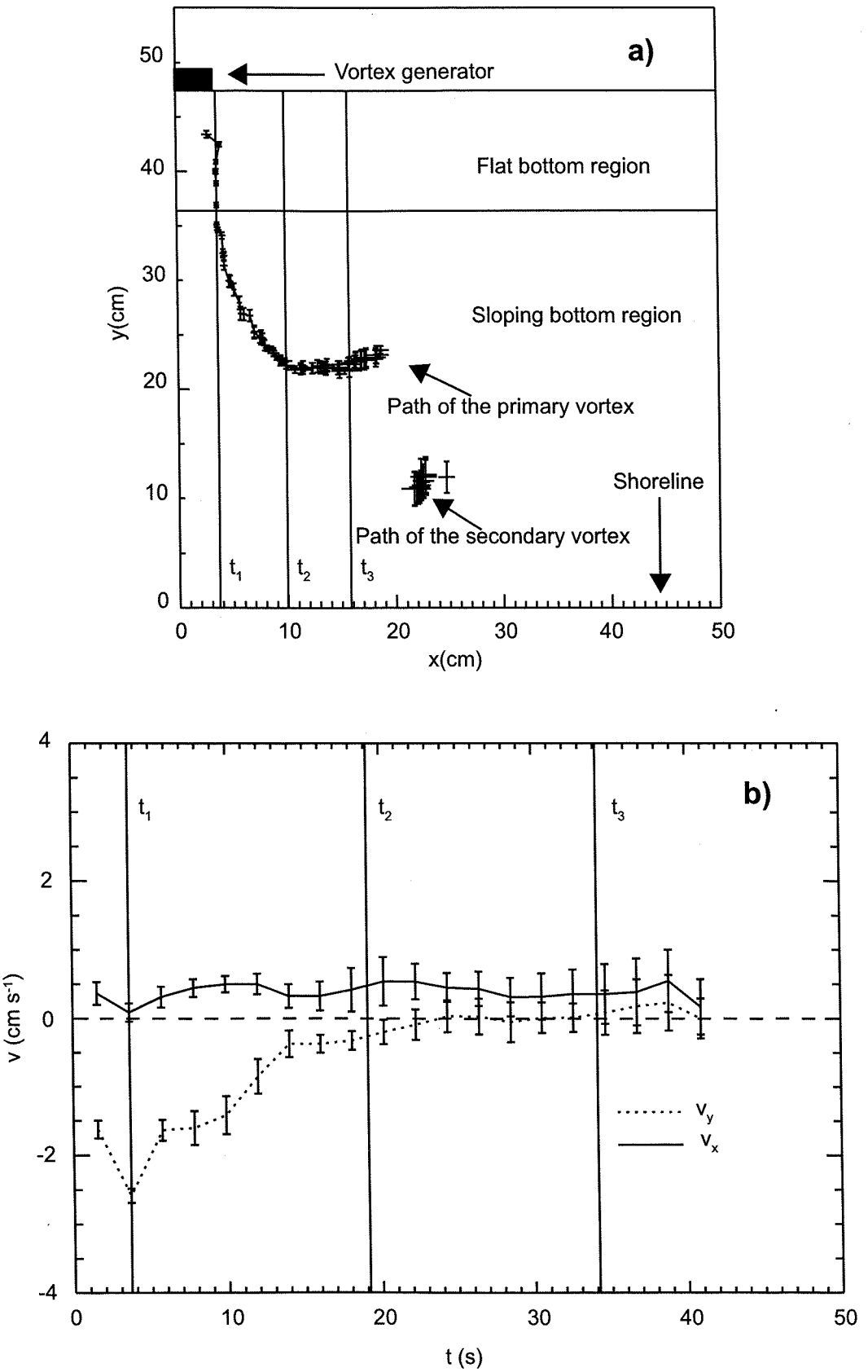

Fig. 4.17: a) Path followed by the main and by the secondary vortex (exp. 16 in tab. 4.3). The path followed by the secondary vortex is shown only for $t>t_3$. b) Velocity of the main vortex. The velocity was calculated from a subsample of the position time series in order to keep the error bars small. A weak rebounding can be seen when t>t3, when the y component of the velocity (dotted line) increases from near 0 values (for t2<t<t3) to a positive value. t_1=3.64 s, t_2=19.16 s, t_3=34.16 s.

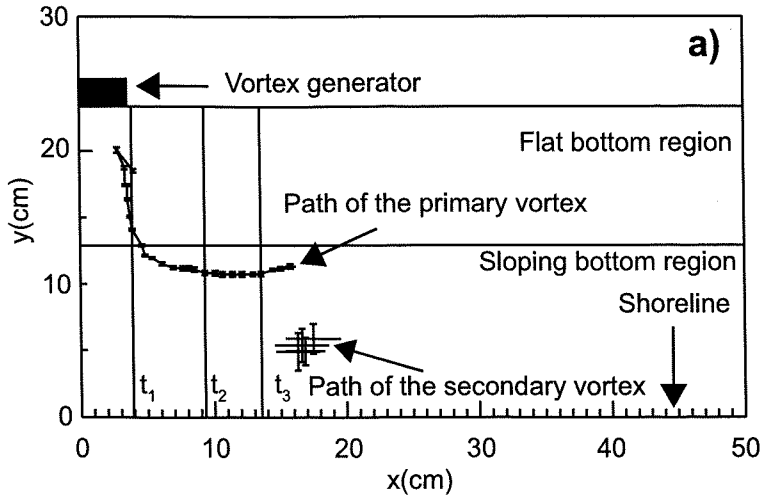

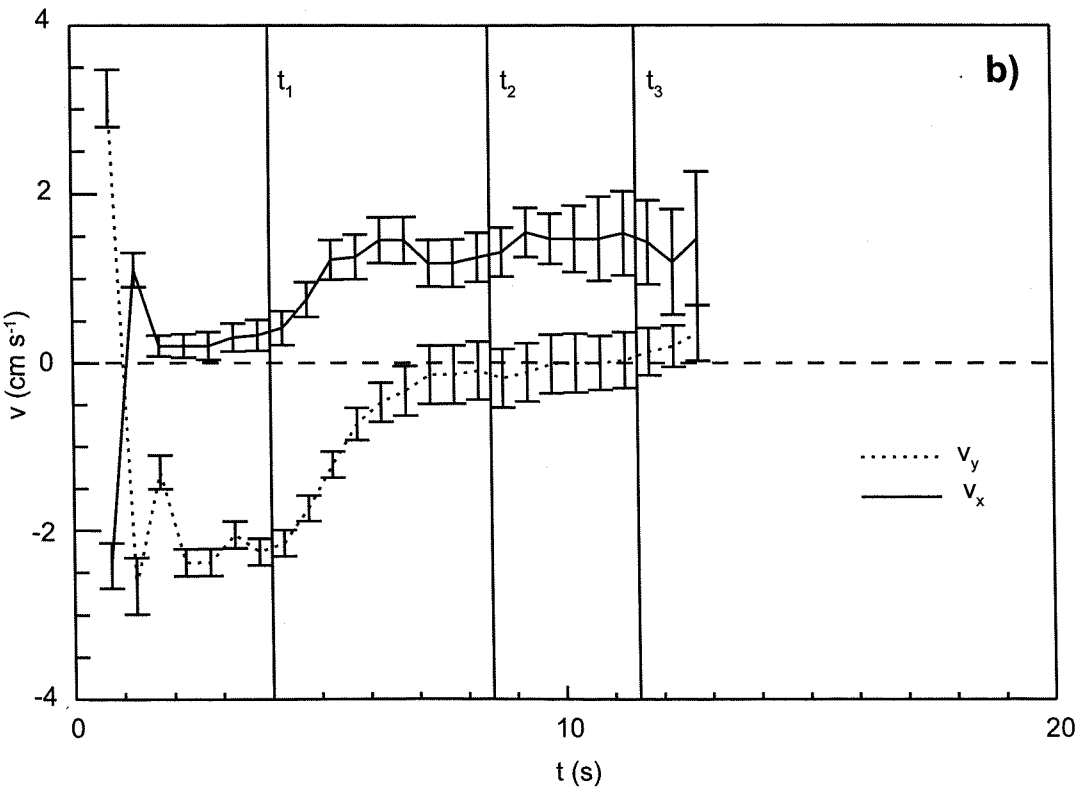

Fig. 4.18: As fig. 4.17 but now for exp. 27 in tab. 4.3. The large variation of velocity at the beginning of the time series is due to an uncorrect tracking of the vortex (see fig. a). t_1=4.00 s, t_2=8.50 s, t_3=11.50 s.

the greater. The calculated initial strengths are shown in table 4.4. With this method we could not follow the time evolution of the strength.

4.4.6 Strength of the vortices: experiments with particles

The procedure used to estimate the vortex strength from the distribution of vorticity at the surface was discussed in section 4.4.3. The total content of vorticity at the surface of the fluid, i.e. the integrals 4.2 estimated with a vorticity threshold of 0 and separated in 4 components (2 for the main vortices and two for the secondary vortices) were used to normalise the integrals 4.2 calculated with the other thresholds of vorticity. For the main vortices we took only the time series of the normalised strength for the percentiles 90%, 95% and 99%. For each percentile the average time series of absolute strength was calculated from the time series of the positive and of the negative main vortices. We indicate these with $\Gamma_{m,90}(t)$, $\Gamma_{m,95}(t)$ and $\Gamma_{m,99}(t)$. These parameters therefore represent the vortex made of a surface that contains 90%, 95% and 99% of the total vorticity. The error was calculated with the standard formulae of the propagation of the errors. The averaging procedure between the positive and the negative vortices was made possible because of the symmetry of the flow with respect to the axis of the dipole. Some examples of time series are shown in fig. 4.19. Time series of the strength of the secondary vortices were calculated in the same way and are indicated with $\Gamma_{s,90}(t)$ $\Gamma_{s,95}(t)$ and $\Gamma_{s,99}(t)$.

With this method there is no need to define the area core of the vortices (see also section 4.4.7). The initial strength of the dipole was calculated as the average value in an interval centred around t_1, i.e. the instant when the vortices cross the border with the planar slope, where the strength was greatest and almost constant (tab. 4.10).

Exp.	w.l. (cm)	α (°)	s_i (cm)	Γ (cm^2s^{-1})
1	2.3±0.1	3.4±0.1	6.8±0.3	94±36
2	2.7±0.1	5.6±0.1	6.8±0.3	101±32
3	4.3±0.1	5.6±0.1	7.1±0.3	105±33
4	2.7±0.1	7.0±0.1	6.7±0.3	79±34
5	4.4±0.1	7.0±0.1	7.4±0.3	129±41
6	2.7±0.1	8.3±0.1	7.0±0.3	89±33
7	3.7±0.1	8.3±0.1	7.1±0.2	106±28
8	2.7±0.1	9.9±0.1	7.1±0.3	96±29
9	4.1±0.1	9.9±0.1	7.2±0.3	134±39
10	2.7±0.1	12.4±0.2	6.6±0.3	80±31
11	3.8±0.1	12.4±0.2	6.8±0.3	104±28
12	4.4±0.1	17.5±0.4	7.3±0.3	114±34
13	3.9±0.1	20.4±0.2	7.3±0.3	117±40
14	4.4±0.1	45.6±0.7	7.8±0.3	104±37

Tab. 4.4: Experiments with fluorescine: w.l. is the water depth at the flat bottom; α is the slope angle, s_i is the separation of the vortices while moving over the flat bottom; Γ is the strength of the dipole calculated with formula 2.11.

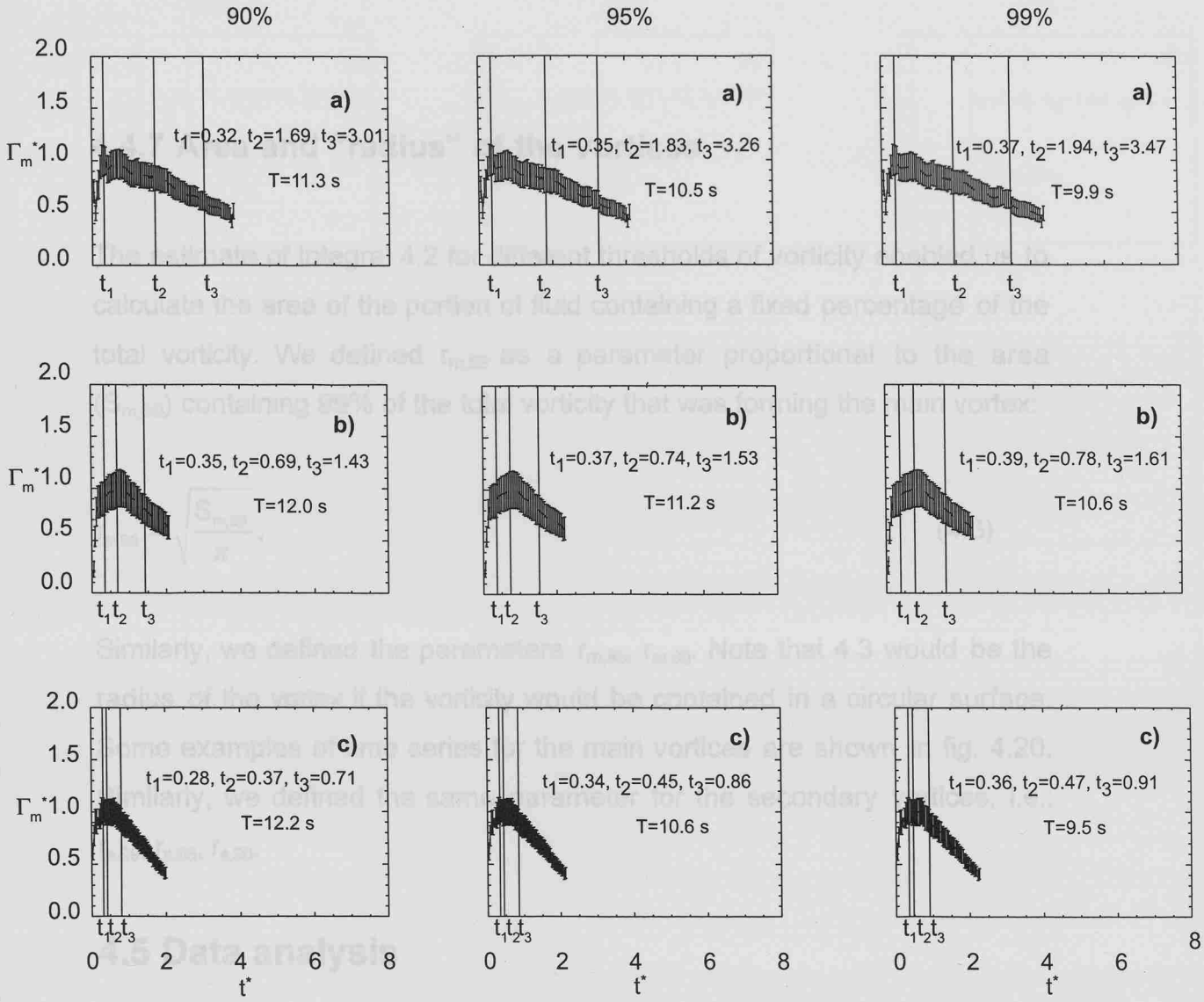

Fig. 4.19: Time series of the non-dimensional strength of the main vortices calculated for the three percentiles 90%, 95% and 99% as explained in section 4.4.6. Time was made non dimensional with the spin-down time scale T (see section 4.5.3). The strength was made non dimensional with the maximum of the time series. a) is experiment 16. b) is experiment 19, c) is experiment 25. The strength of the vortices is decreasing with time. Note the transient between the beginning of the experiment and the maximum of strength. This is a feature of the PIV processing which was unable to resolve the smaller spatial scales.

4.4.7 Area and "radius" of the vortices

The estimate of integral 4.2 for different thresholds of vorticity enabled us to calculate the area of the portion of fluid containing a fixed percentage of the total vorticity. We defined $r_{m,99}$ as a parameter proportional to the area ($S_{m,99}$) containing 99% of the total vorticity that was forming the main vortex:

$$r_{m,99} = \sqrt{\frac{S_{m,99}}{\pi}}, \qquad (4.3)$$

Similarly, we defined the parameters $r_{m,95}$, $r_{m,90}$. Note that 4.3 would be the radius of the vortex if the vorticity would be contained in a circular surface. Some examples of time series for the main vortices are shown in fig. 4.20. Similarly, we defined the same parameter for the secondary vortices, i.e.: $r_{s,99}$, $r_{s,95}$, $r_{s,90}$.

4.5 Data analysis

4.5.1 Minimum distance from the shoreline (R_f)

In section 4.3.2 we introduced the minimum distance from the shoreline (R_f). This was defined as the minimum distance reached by the vortices during the along-shore motion in the interval $t_2<t<t_3$ (see also in fig. 4.21). If we define the penetration depth, d, as the distance travelled by the vortices on the slope in the direction normal to the shoreline, then $R_f+d=R_i$, where R_i is the distance of the border of the slope from the shoreline.

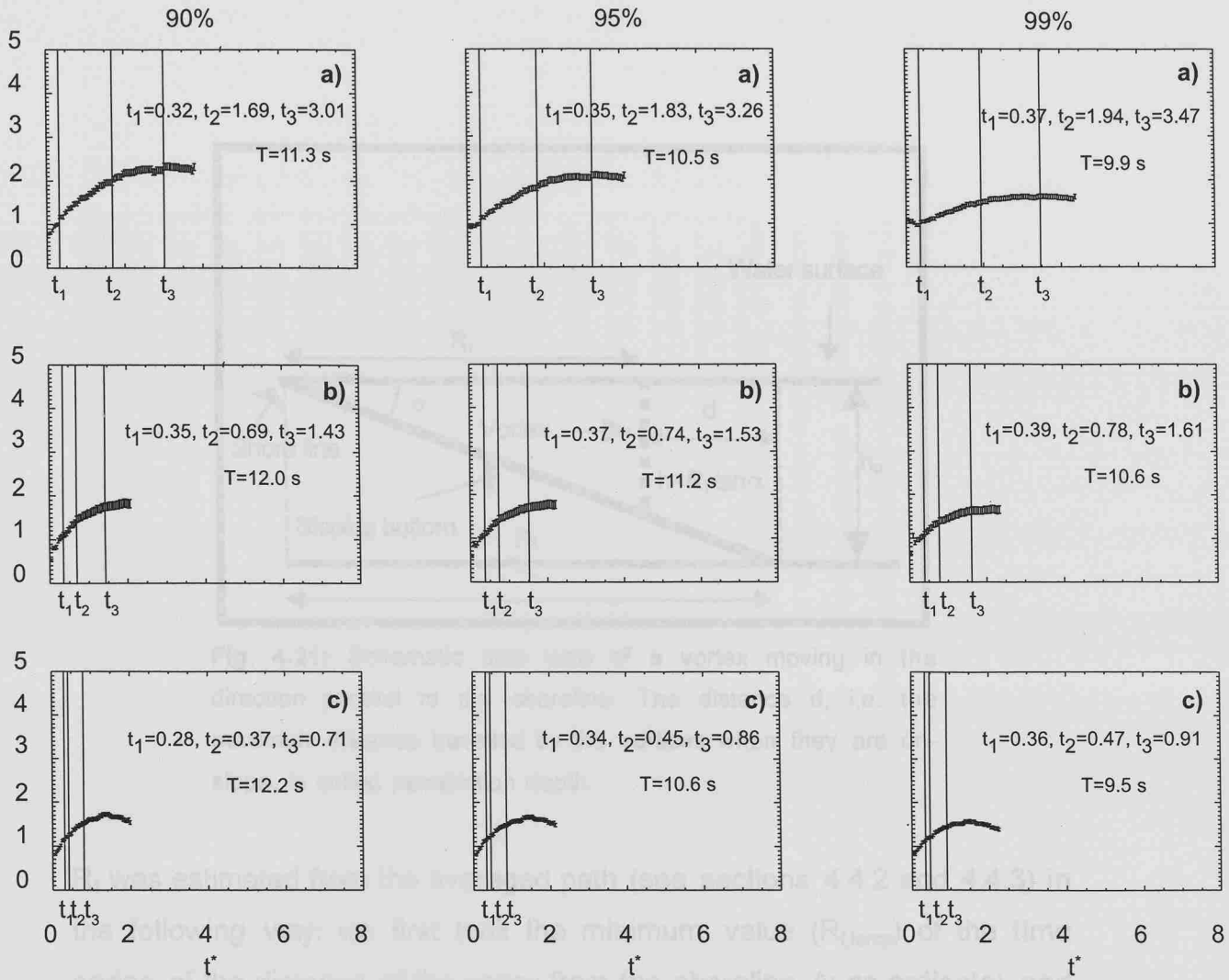

Fig. 4.20: Time series of the non-dimensional radius of the main vortices calculated for the three percentiles 90%, 95% and 99% as explained in section 4.4.7. Time was made non dimensional with the spin-down time scale T (see section 4.5.3). The radius was made non dimensional with the average of the time series calculated between 0 and t_1. a) is experiment 16. b) is experiment 19, c) is experiment 25.

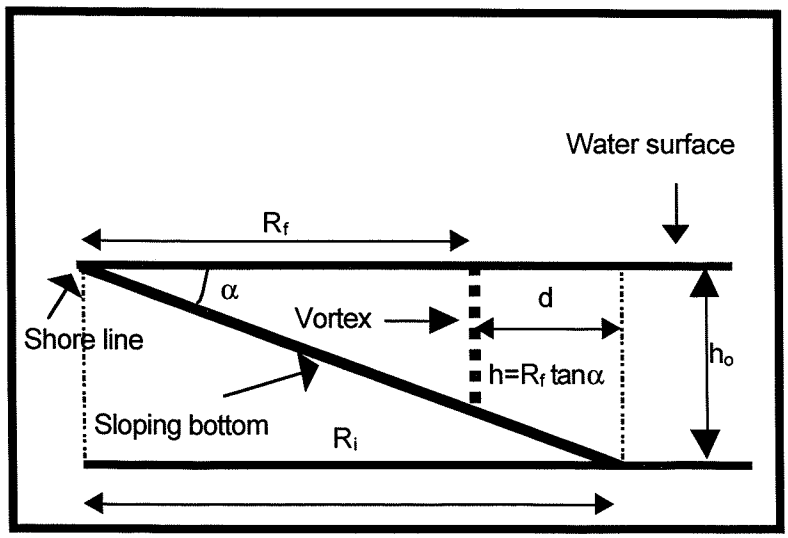

Fig. 4.21: Schematic side view of a vortex moving in the direction parallel to the shoreline. The distance d, i.e. the maximum distance travelled by the vortices when they are on-slope, is called penetration depth.

R_f was estimated from the averaged path (see sections 4.4.2 and 4.4.3) in the following way: we first took the minimum value ($R_{f,temp}$) of the time series of the distance of the vortex from the shoreline (y co-ordinate) and the maximum error ($D_{y,max}$) of the time series. Then we calculated the average, μ, and the standard deviation, σ, of the part of the y co-ordinate time series satisfying the condition: $R_{f,temp} < y < R_{f,temp} + D_{y,max}$. We then sub-selected the elements of the time series satisfying the second condition: $\mu-\sigma<y<\mu+\sigma$. R_f was calculated as the average of those elements. The error was taken as the standard deviation or the maximum error, depending on whichever was the greatest. The results from the experiments with fluorescine and from the experiments with particles are in tables 4.5 and 4.6 and plotted in fig. 4.22. Table 4.6 contains the final distance of the vortices from the shoreline (R_f) calculated with the integral method (formulae 4.1) as well as the one measured from streak photographs. The greatest difference between the two kind of measurements was (16±3)%.

Exp.	w.l. (cm)	α (°)	s_i (cm)	R_i (cm)	t_2 (s)	$0.5 \cdot s_2$ (cm)	t_3 (s)	$0.5 \cdot s_3$ (cm)	R_f (cm)
1	1.50±0.06	3.4±0.1	6.8±0.3	39.2±0.2	43.93±0.02	15.6±0.2	95.03±0.02	21.0±0.2	25.2±0.2
2	1.54±0.05	5.6±0.1	6.8±0.3	26.9±0.2	16.02±0.02	11.8±0.1	35.21±0.02	24.8±0.1	15.7±0.2
3	2.24±0.06	5.6±0.1	7.1±0.3	43.0±0.2	25.57±0.02	16.5±0.1	41.56±0.02	26.9±0.1	22.8±0.2
4	1.96±0.07	7.0±0.1	6.7±0.3	21.6±0.4	14.61±0.02	9.0±0.2	34.61±0.02	22.2±0.2	16.0±0.3
5	2.54±0.06	7.0±0.1	7.4±0.3	35.3±0.4	20.97±0.02	15.5±0.3	32.96±0.02	24.9±0.2	20.7±0.2
6	1.97±0.08	8.3±0.1	7.0±0.3	18.4±0.4	9.61±0.02	8.15±0.1	21.23±0.02	20.3±0.1	13.5±0.4
7	2.44±0.06	8.3±0.1	7.1±0.2	25.4±0.4	13.41±0.02	13.2±0.1	23.02±0.02	22.3±0.1	16.7±0.2
8	2.18±0.06	9.9±0.1	7.1±0.3	15.2±0.5	10.84±0.02	9.7±0.1	18.83±0.02	19.1±0.1	12.5±0.2
9	2.72±0.06	9.9±0.1	7.2±0.3	23.6±0.5	13.79±0.02	16.2±0.1	20.18±0.02	23.8±0.1	15.6±0.2
10	2.37±0.08	12.4±0.2	6.6±0.3	12.5±0.6	7.62±0.02	7.0±0.1	13.23±0.02	16.9±0.1	10.8±0.2
11	2.99±0.09	12.4±0.2	6.8±0.3	17.5±0.6	9.60±0.02	12.9±0.1	16.80±0.02	22.6±0.1	13.6±0.2
12	3.7±0.2	17.5±0.4	7.3±0.3	13.8±0.4	4.00±0.02	5.7±0.1	12.20±0.02	19.8±0.1	11.6±0.2
13	3.6±0.1	20.4±0.2	7.3±0.3	10.4±0.9	6.41±0.02	9.9±0.1	10.41±0.02	18.5±0.1	9.6±0.2
14	4.4±0.1	45.6±0.7	7.8±0.3	4.3±0.9	3.60±0.02	6.0±0.1	8.40±0.02	14.6±0.1	5.9±0.2

Tab. 4.5: Experiments with fluorescine: w.l. is the water depth at the distance R_f from the shoreline; α is the slope angle, s_i is the separation of the vortices while moving over the flat bottom; R_i is the distance in the horizontal plane, passing from the shoreline, from the projection of the beginning of the slope on that plane to the shore-line (see fig. 4.12); t_2 is the time at which the vortices start travelling at the minimum distance (R_f) from the shoreline and nearly parallel to it; s_2 is the separation of the vortices at the time $t=t_2$; t_3 is the time at which rebounding begins and the two vortices move off-shore; s_3 is the separation of the vortices at the time $t=t_3$; R_f is the minimum distance from the shoreline reached by the vortices.

Exp.	w.l. (cm)	α (°)	s_i (cm)	R_i (cm)	t_2 (s)	$0.5 \cdot s_2$ (cm)	t_3 (s)	$0.5 \cdot s_3$	R_f (cm)	R^*_f (cm)	Diff. (%)
16	1.31±0.07	3.4±0.1	7.6±0.3	36.4±0.2	19.16±0.02	9.9±0.8	34.16±0.02	15.8±0.7	22.1±0.3	24.1±0.4	9±3
17a	1.56±0.05	5.6±0.1	8.2±0.8	23.3±0.2	14.00±0.02	8.0±0.1	26.50±0.02	14.8±0.4	16.0±0.3	18.6±0.2	16±3
17b	1.57±0.06	5.6±0.1	7.0±0.3	24.3±0.2	13.00±0.02	8.1±0.3	20.72±0.02	13.0±0.7	16.0±0.2	17.5±0.2	9±3
18	Videotape corrupted: experiment not suitable for processing.										
19	1.70±0.08	6.9±0.2	7.4±0.7	19.0±0.2	8.32±0.02	7.2±0.2	17.16±0.02	16.4±0.9	14.0±0.4	15.2±0.2	9±5
20	2.5±0.1	7.1±02	6.8±0.6	32.6±0.2	12.48±0.02	9.6±0.1	18.20±0.02	24.2±0.3	20.2±0.1	Not meas.	***
21	2.15±0.7	8.3±0.2	8.1±0.5	17.8±0.2	7.80±0.02	7.1±0.1	15.60±0.02	16.8±0.8	14.7±0.5	Not meas.	***
22	3.0±0.1	8.0±0.2	7.2±0.7	32.3±0.2	10.92±0.02	11.0±0.1	17.16±0.02	18.7±0.4	21.3±0.2	22.4±0.3	5±2
23	2.24±0.08	9.9±0.2	7.9±0.5	14.6±0.2	7.28±0.02	6.1±0.3	18.20±0.02	23.6±0.3	12.8±0.5	12.9±0.2	1±5
24	3.5±0.1	9.8±0.2	8.2±0.5	26.5±0.2	6.24±0.02	8.8±0.2	17.16±0.02	32.1±0.9	20.0±0.4	20.6±0.2	3±3
25	2.36±0.07	12.4±0.2	8.1±0.5	11.7±0.2	6.24±0.02	6.4±0.1	11.96±0.02	13.4±0.8	10.7±0.2	11.7±0.2	9±4
26	2.9±0.1	12.4±0.2	7.6±0.4	18.6±0.2	7.80±0.02	10.8±0.2	11.44±0.02	17.3±0.4	13.2±0.1	14.5±0.2	10±2
27	3.6±0.1	18.4±0.4	7.3±0.5	12.9±0.1	8.50±0.02	9.3±0.1	11.50±0.02	13.5±0.2	10.7±0.2	11.7±0.1	9±3

Tab. 4.6: As in table 4.5 but for PIV. R^*_f is the position of the vortices obtained from streak photographs, as explained in section 4.4.3 and R_f is the position of the vortices calculated with 4.1. In the last column is the relative difference between the 2 measurements.

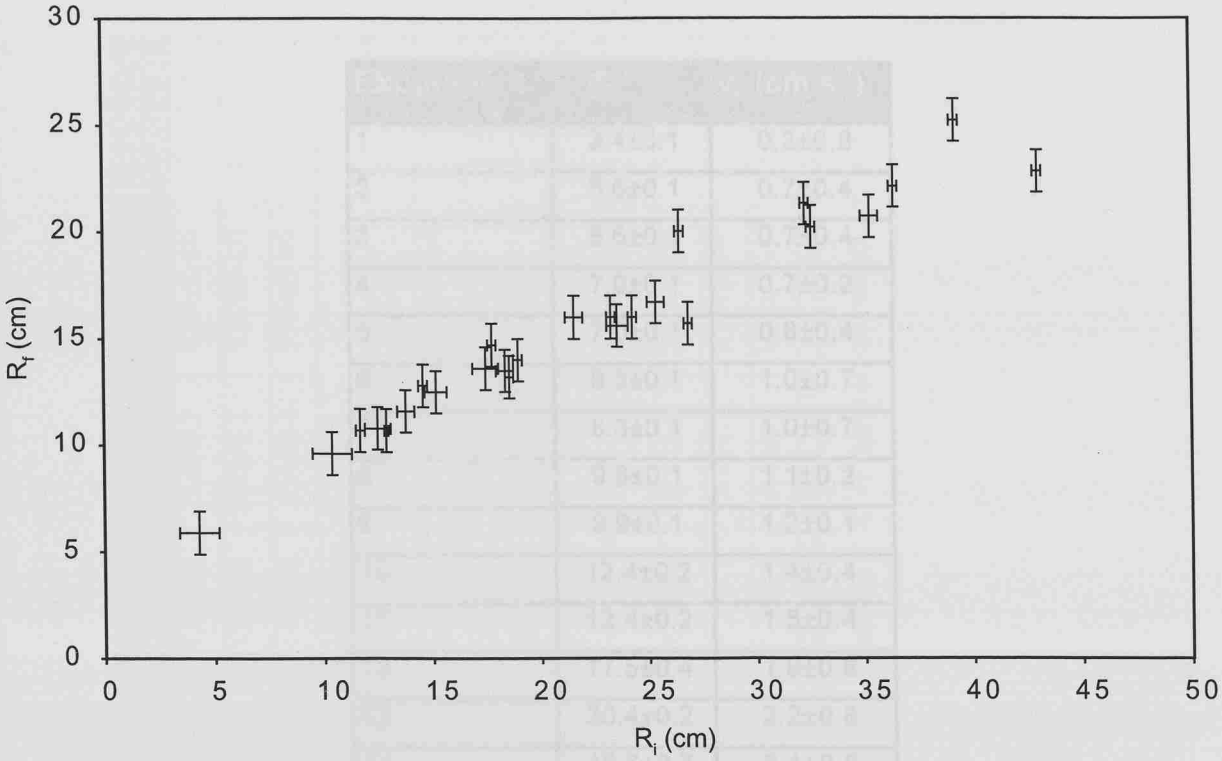

Fig. 4.22: Minimum (average) distance from the shoreline reached by the vortices (R_f) versus distance of the beginning of the planar slope from the shoreline (R_i). See tables 4.5 and 4.6.

Experiment	α (°)	$v_{//}$ (cm s^{-1})
1	3.4±0.1	0.3±0.8
2	5.6±0.1	0.7±0.4
3	5.6±0.1	0.7±0.4
4	7.0±0.1	0.7±0.2
5	7.0±0.1	0.8±0.4
6	8.3±0.1	1.0±0.7
7	8.3±0.1	1.0±0.7
8	9.9±0.1	1.1±0.2
9	9.9±0.1	1.2±0.1
10	12.4±0.2	1.4±0.4
11	12.4±0.2	1.5±0.4
12	17.5±0.4	1.8±0.8
13	20.4±0.2	2.2±0.8
14	45.6±0.7	2.1±0.8

Tab. 4.7: Velocity of the vortices in the direction parallel to the shore-line in the interval $[t_2,t_3]$. Experiments with fluorescine. The strength could not be measured for those vortices.

Exp.	α (°)	$\Gamma_{m,90}$ (cm^2 s^{-1})	$\Gamma_{m,95}$ (cm^2 s^{-1})	$\Gamma_{m,99}$ (cm^2 s^{-1})	$R_{e,90}$ 10^3	$R_{e,95}10^3$	$R_{e,99}10^3$	h(cm)	$v_{//}$ (cm s^{-1})
16	3.4±0.1	78±11	90±13	101±14	1.0±0.2	1.0±0.2	1.0±0.2	1.31±0.05	0.4±0.2
17 a	5.6±0.1	65±7	75±8	83±9	1.2±0.3	1.2±0.2	1.2±0.2	1.57±0.06	0.5±0.1
17 b	5.6±0.1	79±11	91±13	102±14	1.4±0.3	1.4±0.3	1.4±0.3	1.56±0.05	0.7±0.1
18	Videotape corrupted: experiment not suitable for processing.								
19	6.9±0.2	90±16	103±18	114±20	1.9±0.6	1.9±0.6	1.8±0.5	1.7±0.1	1.1±0.2
20	7.1±02	154±18	178±21	201±23	4.0±0.7	4.0±0.7	3.7±0.6	2.52±0.09	1.5±0.3
21	8.3±0.2	83±10	95±12	107±13	2.5±0.6	2.5±0.6	2.2±0.5	2.2±0.1	1.2±0.2
22	8.0±0.2	133±17	153±19	171±21	4.3±0.9	4.2±0.9	3.9±0.8	3.0±0.1	1.2±0.2
23	9.9±0.2	65±9	71±10	79±11	1.9±0.5	1.9±0.5	1.8±0.5	2.2±0.1	0.8±0.2
24	9.8±0.2	162±12	186±13	208±10	6±1	6±1	6±1	3.5±0.1	2.1±0.2
25	12.4±0.2	76±9	87±11	97±12	2.7±0.6	2.7±0.6	2.5±0.6	2.36±0.09	1.2±0.3
26	12.4±0.2	114±14	130±16	146±18	4.2±0.7	4.2±0.7	3.8±0.7	2.89±0.08	1.7±0.4
27	18.4±0.4	78±9	89±10	100±11	4.4±0.8	4.4±0.8	4.0±0.7	3.58±0.013	1.4±0.3

Tab. 4.8 Strength of the vortices ($\Gamma_{m,90}$, $\Gamma_{m,95}$, $\Gamma_{m,99}$, see section 4.4.6 for the definition), Reynold's numbers ($R_{e,90}$, $R_{e,95}$, $R_{e,99}$) and velocity ($v_{//}$) in the direction parallel to the shoreline. h is the water depth at a distance R_f from the shoreline, i.e. is the vertical length of the vortex. Experiments with particles.

4.5.2 Speed of the vortices in the direction parallel to the shoreline

From the time series of the speed of the vortices (section 4.4.4) we computed the mean along-shore speed between t_2 and t_3 (see section 4.3.2 for the definition of these characteristic times). This parameter was taken as the speed of an isolated vortex moving in the direction parallel to the shoreline over a planar slope. The error was the maximum error calculated with the formulae of propagation or the standard deviation of the time series between t_2 and t_3, depending on whichever was the greatest, although the two errors were usually very similar. For the PIV experiments we also computed the strengths ($\Gamma_{m,90}$, $\Gamma_{m,95}$, $\Gamma_{m,99}$, see section 4.4.6) of the main vortices in this time interval. The results are in tables 4.7 (experiments with fluorescine) and 4.8 (fig. 4.23, experiments with particles).

We have defined the Reynold's number of the vortices as:

$$R_e = \frac{\Gamma}{r}\frac{h}{\nu}, \qquad (4.4)$$

where Γ is the strength of the vortex, r is the radius, h is the local water depth and ν=0.011 cm^2 s^{-1} is the kinematic viscosity for water (e.g. Batchelor,1967). The ratio Γ/r gives a velocity scale. A Reynolds's number was calculated for each percentile (90%, 95% and 99% and only for the PIV experiments).

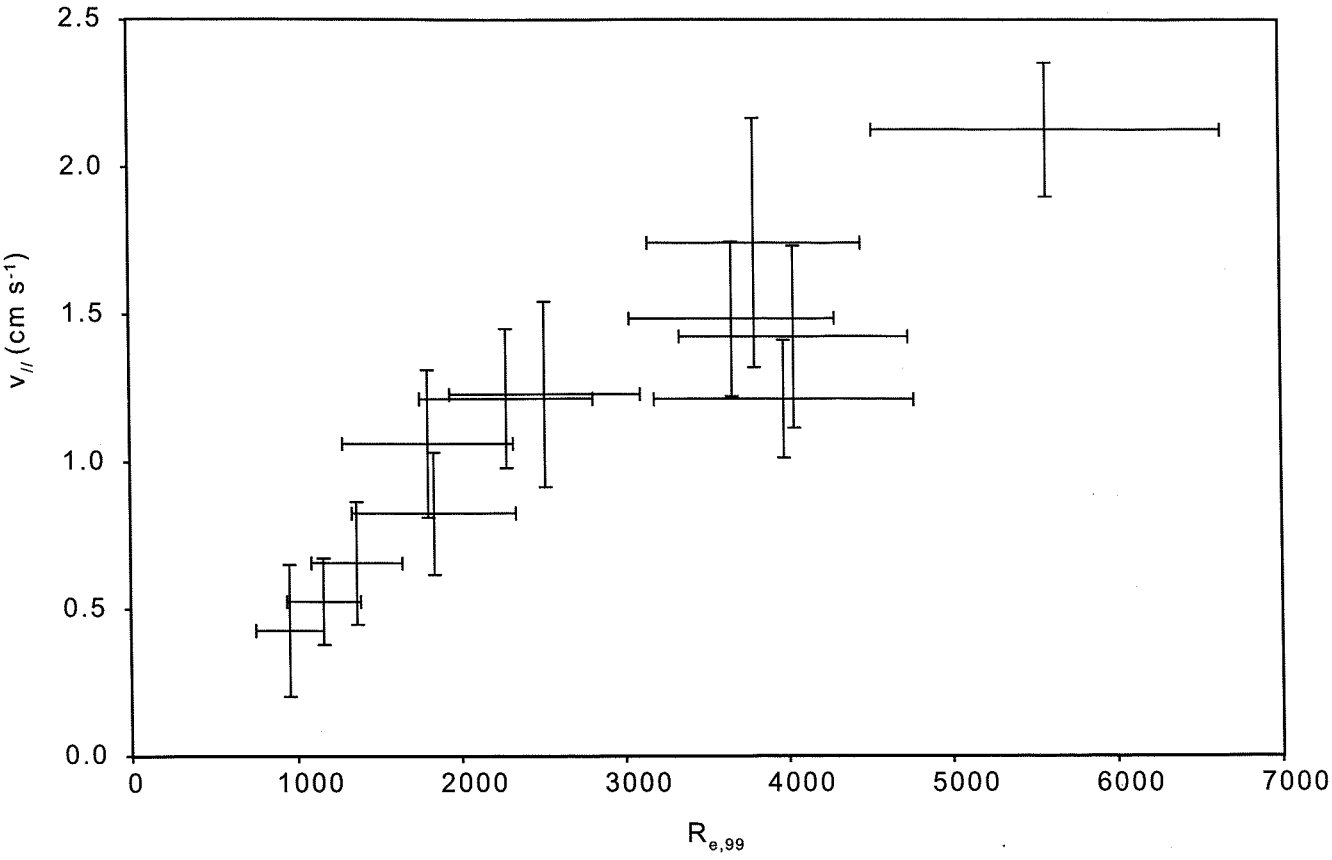

Fig. 4.23: Along-shore velocity of the vortices versus Reynold's number. Experiments with particles.

4.5.3 Time evolution of the radius of the vortices

In section 2.4 we discussed the mechanism that induces the spin-down of a vortex over a flat bottom. This model is a zero order approximation of the process since the viscosity is used only to establish an inflow of fluid with lower angular momentum into the main vortex (via a bottom boundary layer whose thickness is given by formula 2.56) and there is no dissipation of energy involved. This model has a strong analogy with the classical example of the ice-skaters that spins slower by extending his arms away from his body and vice-versa. The conservation of energy means that the strength must be conserved as can be easily seen from formulae 2.65 and 2.66. The spin-down time scale (T) is given by formula 2.55. T increases with depth, meaning that if the radius and the vorticity are kept constant and the depth is increased more fluid must be pumped into the constant depth boundary layer to obtain the same change of the rotation rate. Our vortices are climbing up a sloping plane (i.e. they are moving towards a decreasing depth) so we expect formula 2.55 to be an upper bound of the actual value. It follows that equation 2.65 should underestimate the growth of the radius of the vortex with time.

A second effect must be taken into account. This is the compression of the vortex column when the vortex moves up-slope (see section 3.3.1 d, formulae 3.13 and 3.14). Combining the two mechanisms, the growth of the radius, r, with time can be approximated by,

$$r(t) = r(t_0)\left[\left(1+\frac{t}{4T}\right)+\left(\frac{R(t_0)}{R(t)}\right)^{\frac{1}{2}}\right], \qquad (4.5)$$

where R is the distance of the vortex from the shoreline, t_0 is an arbitrary initial instant and T is the time scale given by 2.55, i.e.:

$$T = \left(\frac{h^2}{\nu \Omega_0} \right)^{\frac{1}{2}} \qquad (2.55)$$

with

$$\Omega_0 \approx \frac{\Gamma(t_0)}{2\pi r^2(t_0)} \qquad (4.6)$$

in which $\Gamma(t_0)$ is the initial strength. The same time series of fig. 4.20 are now shown in fig. 4.24 with the theoretical predictions of formula 4.5.

We defined the parameters (see section 4.4.7 for the definition of r_m):

$$\rho_{m,90} = \frac{r_{m,90}(t)}{r_{m,90}(t_0)},$$
$$\rho_{m,95} = \frac{r_{m,95}(t)}{r_{m,95}(t_0)}, \qquad (4.7\ a,b,c)$$
$$\rho_{m,99} = \frac{r_{m,99}(t)}{r_{m,99}(t_0)}.$$

The ratios 4.7 a, b and c, which represent the non-dimensional radius of the vortex for the three percentiles, were calculated for all the experiments during the motion of the vortices parallel to the shoreline (from t_2 to t_3) and these values are shown in table 4.9 together with the theoretical predictions from formula 4.5. The comparison of the experimental data with the theoretical prediction (i.e. their ratio) is shown in fig. 4.25. The agreement is a function of the percentile used to calculate the radius and of the Reynolds number. If the 90^{th} percentile is used, the agreement is in

Exp.	$R_{e,90}\ 10^3$	$\rho_{t,90}$	$\rho_{m,90}$	$\rho_{m,90}/\rho_{t,90}$	$R_{e,95}\ 10^3$	$\rho_{t,95}$	$\rho_{m,95}$	$\rho_{m,95}/\rho_{t,95}$	$R_{e,99}\ 10^3$	$\rho_{t,99}$	$\rho_{m,99}$	$\rho_{m,90}/\rho_{t,99}$
16	1.0±0.2	2.2	2.2±0.3	1.0±0.1	1.0±0.2	2.2	2.0±0.2	0.9±0.1	1.0±0.2	2.1	1.6±0.1	0.8±0.05
17 a	1.2±0.3	1.7	1.9±0.3	1.1±0.2	1.2±0.2	1.8	1.8±0.2	1.0±0.1	1.2±0.2	1.7	1.6±0.1	0.9±0.1
17 b	1.4±0.3	1.8	1.8±0.2	1.0±0.1	1.4±0.3	1.8	1.7±0.2	0.9±0.1	1.4±0.3	1.7	1.4±0.1	0.8±0.1
18	Videotape corrupted: experiment not suitable for processing.											
19	1.9±0.6	1.5	1.6±0.3	1.1±0.2	1.9±0.6	1.6	1.6±0.3	1.0±0.2	1.8±0.5	1.6	1.5±0.2	0.9±0.1
21	2.5±0.6	1.4	1.5±0.2	1.1±0.1	2.5±0.6	1.4	1.4±0.1	1.0±0.1	2.2±0.5	1.4	1.4±0.1	1.0±0.1
22	4.3±0.9	1.7	2.0±0.3	1.2±0.2	4.2±0.9	1.7	1.9±0.3	1.1±0.2	3.9±0.8	1.6	1.7±0.2	1.1±0.1
23	1.9±0.5	1.3	1.5±0.2	1.2±0.2	1.9±0.5	1.3	1.5±0.2	1.2±0.2	1.8±0.5	1.3	1.4±0.2	1.1±0.2
24	6±1	1.5	1.9±0.2	1.3±0.1	6±1	1.5	1.7±0.1	1.1±0.1	6±1	1.4	1.5±0.1	1.1±0.1
25	2.7±0.6	1.2	1.4±0.2	1.2±0.2	2.7±0.6	1.2	1.4±0.2	1.2±0.2	2.5±0.6	1.2	1.3±0.2	1.1±0.2
26	4.2±0.7	1.4	1.7±0.1	1.2±0.1	4.2±0.7	1.4	1.6±0.1	1.1±0.1	3.8±0.7	1.4	1.4±0.1	1.0±0.1
27	4.4±0.8	1.3	1.6±0.2	1.2±0.2	4.4±0.8	1.3	1.6±0.1	1.2±0.1	4.0±0.7	1.3	1.5±0.2	1.2±0.2

Tab. 4.9: Growth of the radius of the vortex measured from the experiments (ρ_m, see formulae 4.7 a,b,c) and predicted by the theory (ρ_t, see formulae 4.5) calculated for the three percentiles 90%, 95% and 99%. Their ratio and the corresponding Reynolds numbers are also shown. The values were averaged during the along-shore motion of the vortices, i.e. between t_2 and t_3.

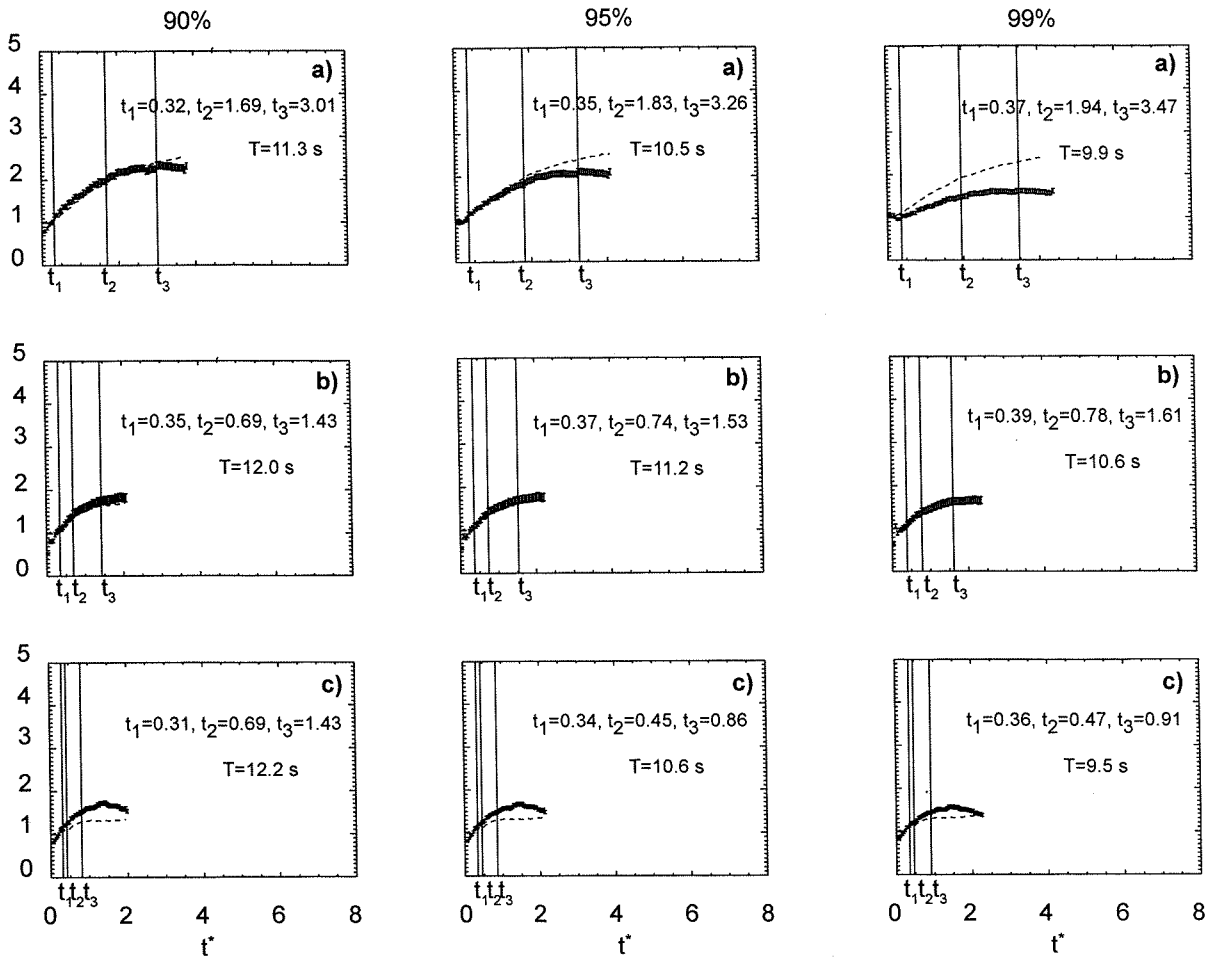

Fig. 4.24: Time series of the non-dimensional radius of the main vortices calculated for the three percentiles 90%, 95% and 99% as explained in section 4.4.7. The dashed line is the time series of the non dimensional radius [$r(t)/r(t_0)$] predicted by formula 4.5. Time was made non dimensional with the spin-down time scale T (see section 4.5.3). The experimental radius was made non dimensional with the average of the time series calculated between 0 and t_1. a) is experiment 16. b) is experiment 19, c) is experiment 25.

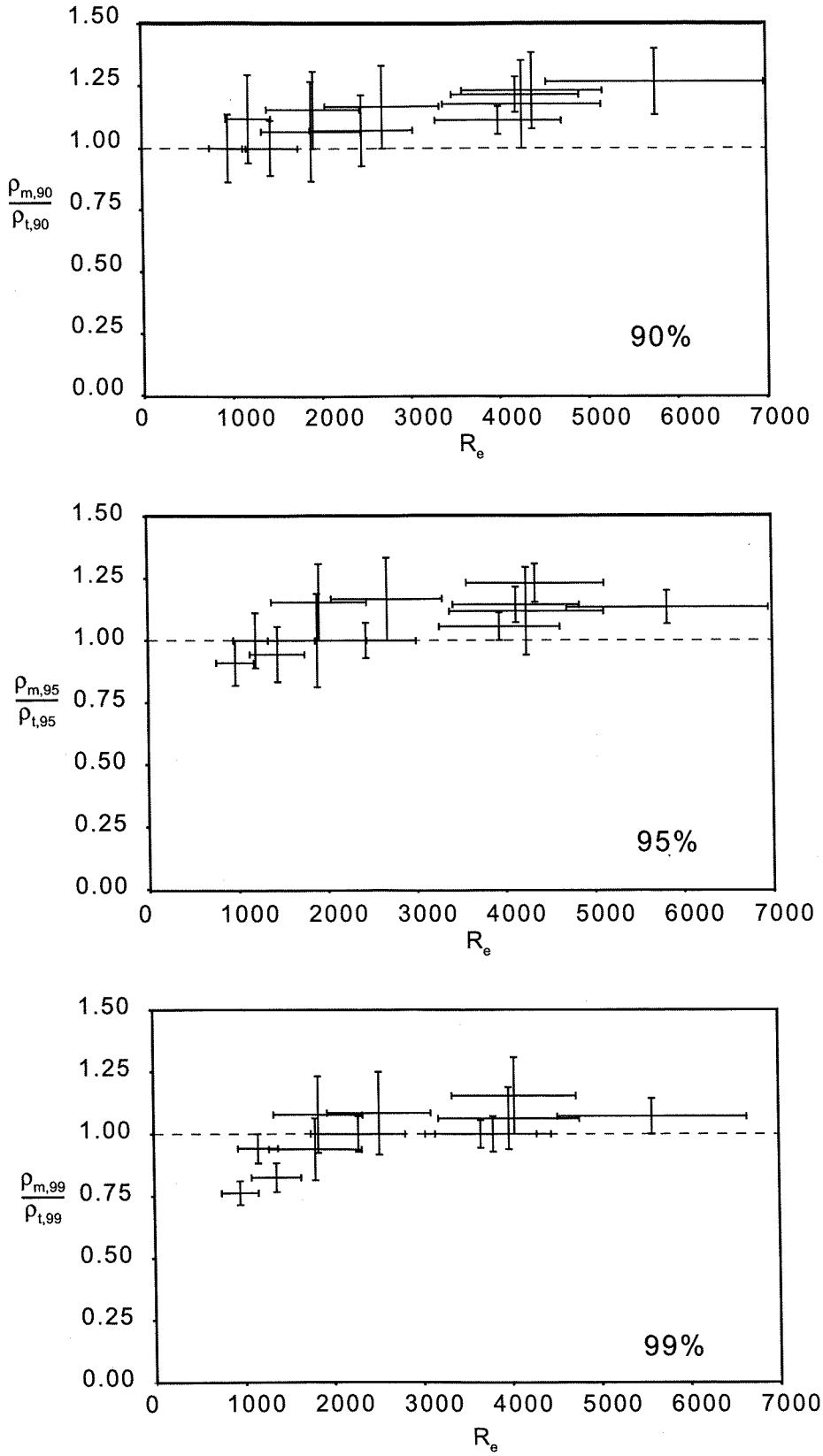

Fig. 4.25: Ratio of the non-dimensional experimental radius to the non dimensional theoretical radius calculated during the along-shore propagation (from t_2 to t_3) plotted against the Reynolds number (R_e). For the 90th percentile the theory generally underestimates the experimental data and the agreement is good only for low R_e. for the 90th and 99th percentiles the agreement is good for intermediate R_e.

within the error bars for lower Reynolds numbers but the theory underestimates the experimental values when the Reynolds number becomes greater. For the 95th and 99th percentiles the agreement is good for intermediate Reynolds numbers, while for smaller and greater Reynolds number we found, respectively, an overestimate and an underestimate of the experimental values.

4.5.4 Time evolution of the strength of the vortices

We conclude this section by presenting the dissipation of energy of the dipole. This was measured with the ratio, η, between the strength of the dipole just before it moves onto the planar slope (at the time t_1) and the strength of the vortices during the along shore propagation (i.e. between the times t_2 to t_3):

$$\eta_{90} = \frac{\Gamma_{i,90}}{\Gamma_{f,90}},$$
$$\eta_{95} = \frac{\Gamma_{i,95}}{\Gamma_{f,95}}, \qquad (4.8\ a,b,c)$$
$$\eta_{99} = \frac{\Gamma_{i,99}}{\Gamma_{f,99}}.$$

The ratios (see tab. 4.10) are almost independent from the percentile used to measure the strength. Fig. 4.26 is a plot of η versus the angle, α, of the planar slope. The dissipation is biggest when α is small.

4.6 The vertical wall case

We present the results from two experiments (15a and 15b, tab. 4.2) in which the planar slope was substituted with a vertical wall. These

Exp.	α (°)	$\Gamma_{i,90}$	$\Gamma_{f,90}$	η_{90}	$\Gamma_{i,95}$	$\Gamma_{f,95}$	η_{95}	$\Gamma_{i,99}$	$\Gamma_{f,99}$	η_{99}
16	3.4±0.1	109±15	78±11	0.7±02	127±18	90±13	0.7±02	144±20	101±14	0.7±02
17 a	5.6±0.1	78±9	65±7	0.8±0.2	90±10	75±8	0.8±0.2	100±11	83±9	0.8±0.2
17 b	5.6±0.1	93±13	79±11	0.9±0.2	108±16	91±13	0.8±0.2	123±18	102±14	0.8±0.2
18	Videotape corrupted: experiment not suitable for processing.									
19	6.9±0.2	100±18	90±16	0.9±0.3	114±20	103±18	0.9±0.3	127±23	114±20	0.9±0.3
20	7.1±02	162±19	154±18	1.0±0.2	188±22	178±21	0.9±0.2	213±25	201±23	0.9±0.2
21	8.3±0.2	94±11	83±10	0.9±0.2	107±13	95±12	0.9±0.2	121±15	107±13	0.9±0.2
22	8.0±0.2	138±17	133±17	1.0±0.2	160±20	153±19	1.0±0.2	181±23	171±21	0.9±0.2
23	9.9±0.2	67±9	65±9	0.9±0.3	77±11	71±10	0.9±0.3	87±12	79±11	0.9±0.3
24	9.8±0.2	175±8	162±12	0.9±0.1	201±9	186±13	0.9±0.1	225±10	208±10	0.9±0.1
25	12.4±0.2	78±20	76±9	1.0±0.2	89±11	87±11	1.0±0.2	100±12	97±12	1.0±0.2
26	12.4±0.2	114±11	114±14	1.0±0.2	133±13	130±16	1.0±0.2	153±15	146±18	1.0±0.2
27	18.4±0.4	81±9	78±9	1.0±0.2	93±11	89±10	1.0±0.2	104±12	100±11	1.0±0.2

Tab 4.10: Initial strength (Γ_i) averaged around the time t_1 when the dipole crosses the border with the planar slope, final strength (Γ_f) averaged during the along-shore propagation (between the times t_2 and t_3) and their ratio (η) calculated for the 90th, 95th and 99th percentiles. The ratio η is almost independent from the percentile used. The average of the ratios is plotted in fig. 4.26 against the angle of the planar slope with the horizontal (α).

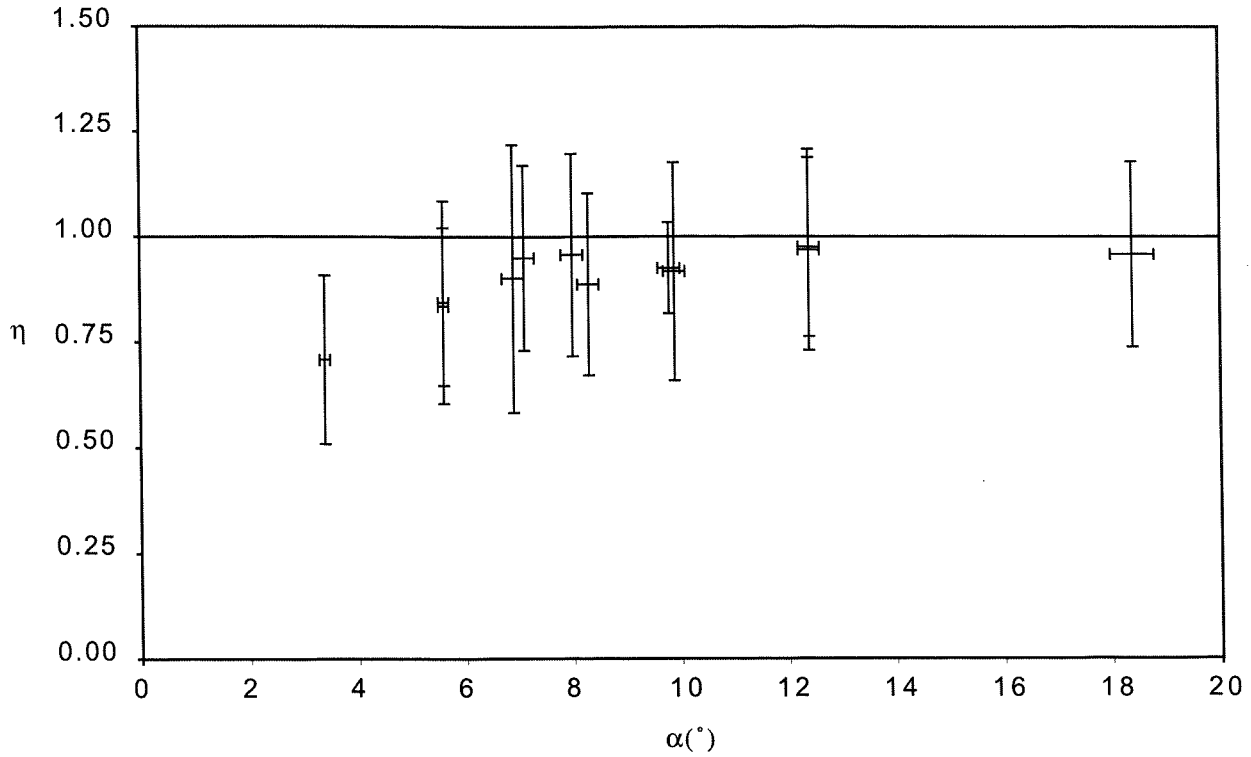

Fig. 4.26: Plot of the dissipation ratio (η) versus the angle of the planar slope with the horizontal (α). η was averaged for the three percentiles (90%, 95% and 99%). The largest dissipation (smallest η) occurs for the smallest values of α.

experiments are very similar to the ones discussed by Barker and Crow (1977).The results are in tables 4.11.1 to 4.11.4. For the two experiments the dissipation of energy (i.e. the loss of circulation) quantified in 30% of the initial value (η in tab. 4.11.2 to 4.11.4). Barker and Crow (1977) found the loss of circulation in their experiments to be ~20%. The generation of secondary vortices was always observed (see plate 7). They induced rebounding of the main vortices for $t > t_3$.

4.6.1 Final distance from the shore-line

The point vortex theory that describes this experiment was reviewed in section 2.2.2 b. The theory predicts that if the dipole is initially at an infinite distance from the wall the final distance of the vortices from the wall, when they have moved infinitely apart, must be half of their initial separation. The ratio of these two quantities, R_f/s_i, from the experiments is shown in tab. 4.1.1, last column, and is greater than 1. The final distance from the wall is therefore greater than the theoretical prediction. Since the radius of the vortices increases as they spin down, the centres of mass of vorticity of the two partner of the dipole also move apart, thus resulting in values of R_f larger than the prediction. This can be seen in fig. 4.27 that shows the trajectory followed by the dipole. The spin down theory slightly underestimates the growth of the radius.

4.6.2 Speed of the vortices along the shoreline.

The experimental values of the along-shore speed were compared with the predictions of the point vortex theory (see section 2.2.2 a). The comparison (ϖ) was made for the three percentiles and is shown in the last columns of tables 4.11.2, 4.11.3 and 4.11.4. Although the experimental error is quite large, the theory seems to overestimate the experimental values.

Exp.	w.l. (cm)	α (°)	s_i (cm)	R_i (cm)	t_2 (s)	t_3 (s)	R_f (cm)	$v_{//}$ (cm s^{-1})	R_f/s_i
15a	3.6±0.1	90±1	3.9±0.4	40.1±0.2	23.64±0.01	33.00±0.01	6.7±0.2	0.6±0.1	1.7±0.2
15b	3.9±0.1	90±1	4.5±0.1	40.0±0.2	14.04±0.01	20.80±0.01	6.1±0.2	0.9±0.2	1.4±0.1

Tab. 4.11.1: Water level: w.l.. Angle of the wall with the horizontal: α. Initial separation of the vortices after the generation: s_i. Distance of the vortex generator from the wall: R_i. Time at which the along-shore propagation begins: t_2. Time at which rebounding begins: t_3. Average distance from the shoreline during along-shore propagation: R_f. Average speed during along-shore propagation: $v_{//}$.

Exp.	Γ_i (cm^2s^{-1})	r_i (cm)	Γ_f (cm^2s^{-1})	r_f (cm)	R_e 10^3	v_t (cm s^{-1})	T (s)	η	ρ	ρ_t	ϖ
15a	98±12	4.5±0.8	67±8	7.8±0.2	2.8±0.4	0.8±0.1	17.1	0.7±0.2	1.7±0.4	1.4	1.3±0.4
15b	100±11	5.1±0.6	73±8	7.3±0.2	3.6±0.5	1.0±0.1	21.0	0.7±0.2	1.4±0.2	1.2	1.1±0.4

Tab. 4.11.2: 90th percentile. Initial strength of the vortices; Γ_i: Initial radius of the vortices: r_i. Final strength of the vortices: Γ_f. Final radius of the vortices r_f: Reynolds number: R_e. Point vortex velocity: v_t. Spin-down time scale: T. Dissipation ratio: η. Radius ratio (r_f/r_i): ρ. Radius ratio (non dimensiuonal) from spin-down theory: ρ_t. Ratio of point vortex velocity to experimental velocity (v//): ϖ.

Exp.	Γ_i (cm^2s^{-1})	r_i (cm)	Γ_f (cm^2s^{-1})	r_f (cm)	R_e 10^3	v_t (cm s^{-1})	T (s)	η	ρ	ρ_t	ϖ
15a	114±14	5.3±0.8	77±10	8.9±0.2	2.8±0.4	0.9±0.1	17.1	0.7±0.2	1.7±0.3	1.4	1.5±0.4
15b	115±12	6.1±0.7	83±9	8.3±0.2	3.5±0.5	1.1±0.2	21.0	0.7±0.2	1.4±0.2	1.2	1.2±0.5

Tab. 4.11.3: 95th percentile. As tab. 4.11.2

Exp.	Γ_i (cm^2s^{-1})	r_i (cm)	Γ_f (cm^2s^{-1})	r_f (cm)	R_e 10^3	v_t (cm s^{-1})	T (s)	η	ρ	ρ_t	ϖ
15a	130±16	6.6±0.8	87±11	10.4±0.3	2.7±0.4	1.0±0.2	17.1	0.7±0.2	1.6±0.2	1.5	1.7±0.6
15b	128±14	7.5±0.8	93±10	9.8±0.2	3.4±0.5	1.2±0.2	21.0	0.7±0.2	1.3±0.2	1.2	1.3±0.5

Tab. 4.11.4: 99th percentile. As tab. 4.11.2.

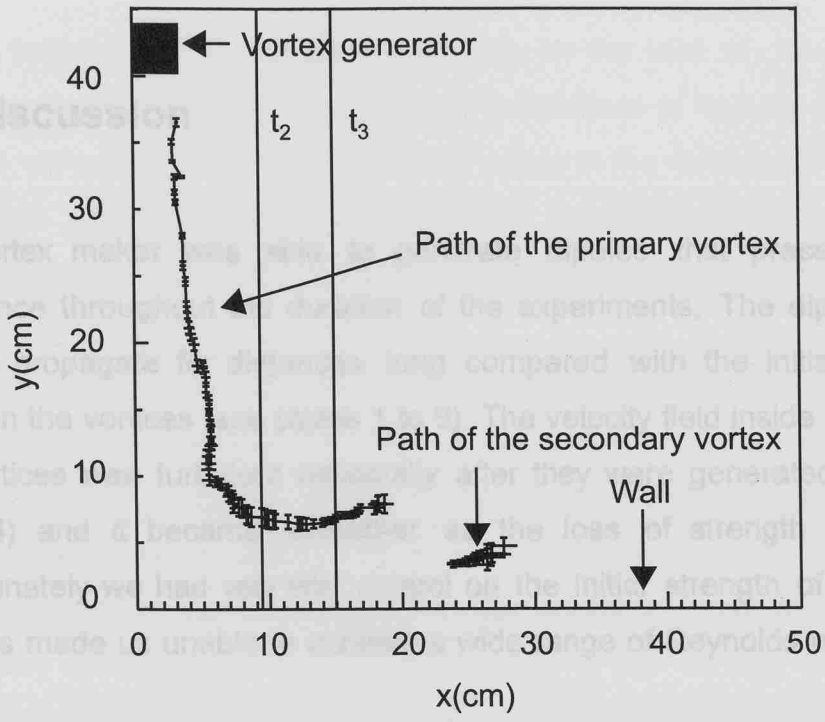

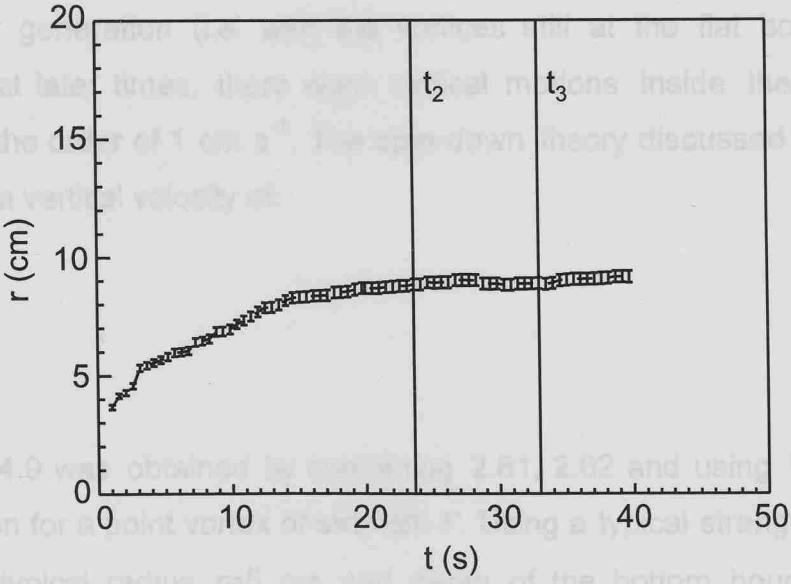

Fig. 4.27: a) Path follwed by the vortices (exp 15 a). t_2=23.64, t_3=33.00. Time series of the radius of the vortices (95th percentile).

4.7 Discussion

The vortex maker was able to generate dipoles that preserved their coherence throughout the duration of the experiments. The dipoles were able to propagate for distances long compared with the initial distance between the vortices (see plates 1 to 8). The velocity field inside the core of the vortices was turbulent especially after they were generated (see e.g. plate 4) and it became smoother as the loss of strength increased. Unfortunately we had very little control on the initial strength of the dipole and this made us unable to achieve a wide range of Reynolds numbers.

The vortices were not truly two-dimensional. Our qualitative investigation on the vertical structure of the vortices has shown that, at least immediately after their generation (i.e. with the vortices still at the flat bottom) and possibly at later times, there were vertical motions inside the core with speed of the order of 1 cm s^{-1}. The spin-down theory discussed in section 2.4 gives a vertical velocity of:

$$w = \frac{\Gamma \delta_E}{2\pi r^2} \qquad (4.9)$$

Formula 4.9 was obtained by combining 2.61, 2.62 and using the velocity expression for a point vortex of strength Γ. Using a typical strength of $\Gamma=10^2$ cm^2 s^{-1}, typical radius r=5 cm and depth of the bottom boundary layer $\delta_E=10^{-1}$ cm, formula 4.9 yields a vertical velocity w=0.06 cm s^{-1}, which is more that one order of magnitude smaller than our estimate. A strong pumping mechanism that cannot be fully explained with the spin-down model characterises our vortices. Barker and Crow (1977), who generated dipoles between two rigid boundaries, did not observe vertical motions but our experiments are different since our dipoles had a free surface. Intense

vertical motions are a possible explanation for the loss of circulation and for a growth of the radius bigger than the predictions of formula 4.5. Vertical motions were also observed in form of a vortex at the forefront of the dipole (see plate 10). This feature was analysed only qualitatively and we are unable to assess how much energy it eventually extracts from the dipole.

Two different visualisation techniques were adopted: one used yellow fluorescine and the other Pliolite particles for PIV analysis. The PIV technique gave by far the best results since it allowed us to build a coherent framework to analyse the experiments, especially in following the time evolution of the parameters of the vortices. However the spatial resolution achieved (~1 cm) and the error of the vorticity field (~10%) translated into rather large error bars. The essentially two-dimensional data acquisition (i.e. only a top view from above of the experiments) made a further interpretation of the result matter for speculation (see next chapter). The PIV analysis mainly aimed at avoiding absolute definition for the radius and the strength of the vortices since the concept of core of a vortex cannot be clearly defined. Instead we defined these quantities relative to the total vorticity at the surface of the fluid. In chapter 6 we will show that the main conclusions are independent of the way the radius and the strength are defined. The invaluable advantage of the PIV analysis was also to enable us to identify correctly the true centre of rotation of the vortices (i.e with formulae 4.1, see also fig. 4.15) and therefore their trajectory. This technique gave us the freedom to follow with a relatively inexpensive procedure the path of the vortices, while the manual equivalent using streak photograph, apart from giving biased results since only the apparent centre of rotation was measured, was also very time consuming.

The trajectory and the parameters of the positive rhs vortex were averaged with the ones of its negative partner since the flow preserved its symmetry throughout the experiments, as shown by the figures in this chapter. This does not restrict the analysis of our results. The evolution of the flow in our

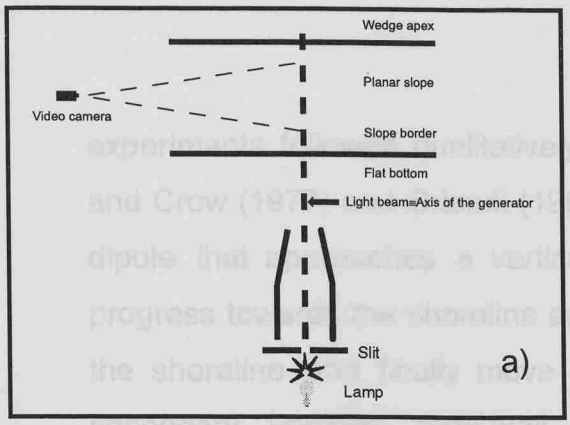

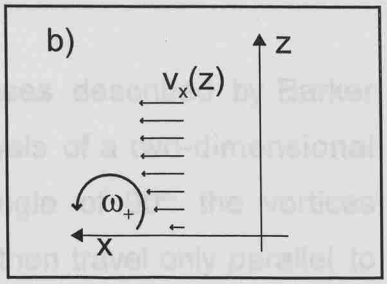

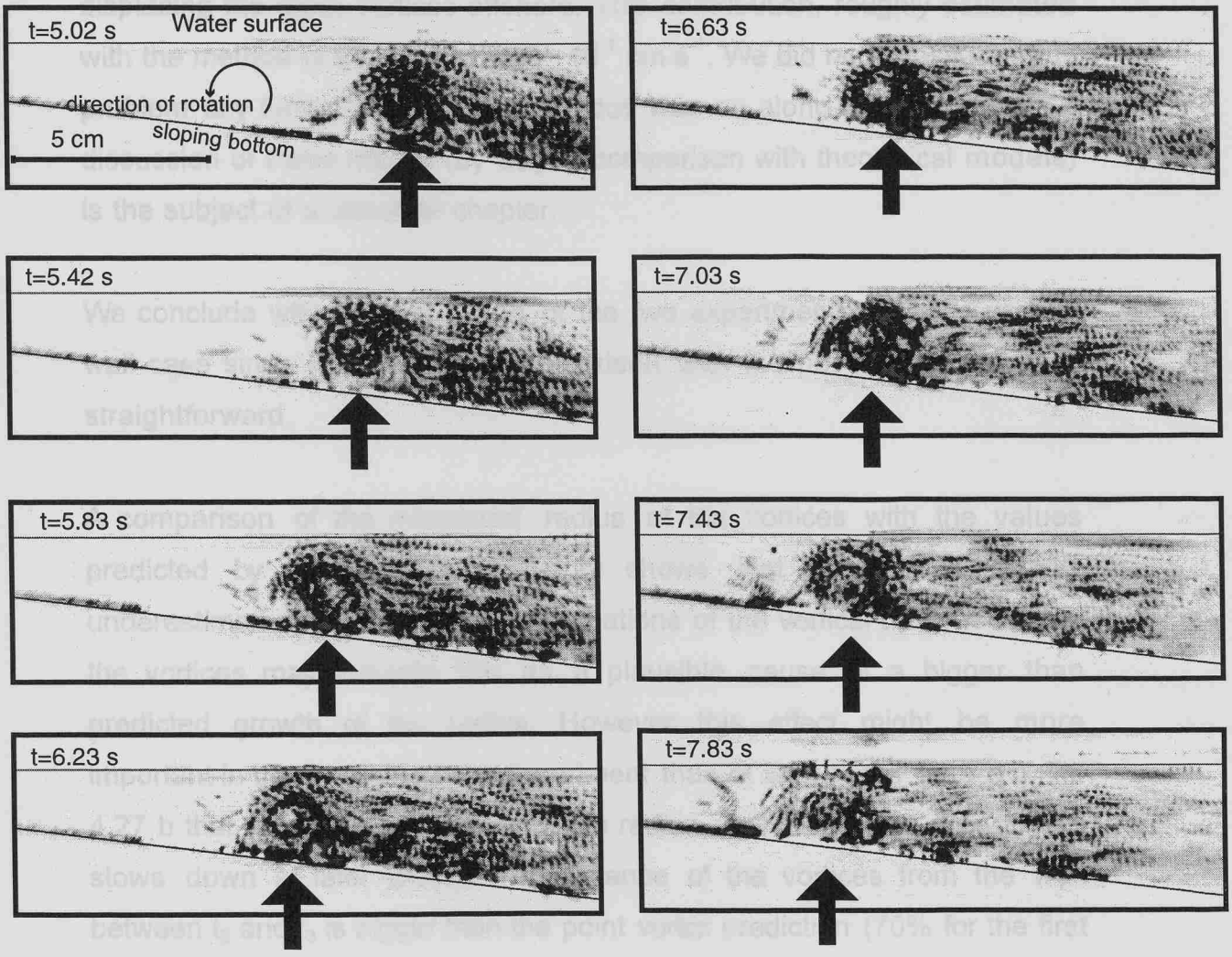

Plate 10: a) Experimental set-up to look at vertical motions along the horizontal axis of the dipole (plan view from above). The angle of the slope was $\alpha=(8.5\pm0.1)^{\circ}$, the density of the water was $\rho=1.1$ g/cm^3 and the water depth at the flat bottom was (4.3±0.1) cm.

Vortical motions at the forefront of the dipole. Side view. Particles were placed at the bottom of the tank. The fluid was also seeded with neutrally buoyant particles The time series of streak photographs shows an horizontal vortex running up-slope (arrows). The vortices develops at the very beginning of the experiment when the dipole is still on the flat bottom. In the upper lhs. corner is the time elapsed since the beginning of the experiment.

b) A possible mechanism to explain the development of this vortical structure is the existence of a jet-like region at the forefront of the recirculation cell with a vertical shear (i.e. positive vorticity in fig. b).

experiments followed qualitatively the same phases described by Barker and Crow (1977) and Orlandi (1990) in their analysis of a two-dimensional dipole that approaches a vertical wall at an angle of 90°: the vortices progress towards the shoreline and move apart, then travel only parallel to the shoreline and finally move away from it driven by newly generated secondary vortices. Side-wall effects can also be responsible for displacing the main vortices offshore. This contribution, roughly estimated with the method of the images was $\sim 10^{-1}$ cm s^{-1}. We did not investigate this problem any further since the main focus was on along-shore motions. A discussion of these results (by way of comparison with theoretical models) is the subject of a separate chapter.

We conclude with the discussion of the two experiments with the vertical wall case since in this case a comparison with the point vortex theory is straightforward.

A comparison of the measured radius of the vortices with the values predicted by the spin down theory shows that the first is slightly underestimated. Our qualitative observations of the vertical motions inside the vortices may indicate this as a plausible cause of a bigger than predicted growth of the radius. However this effect might be more important in the first part of the experiment than at later times (see e.g. fig. 4.27 b that show a quick growth of the radius until t~13 s; the growth rate slows down at later times). The distance of the vortices from the wall between t_2 and t_3 is bigger than the point vortex prediction (70% for the first experiment and 40% for the second, unfortunately no similar estimates were provided by Barker and Crow, 1977). This should be interconnected with the growth of the radius of the vortices which causes the two centres of rotation to move apart at a faster rate than the point vortex model predictions (Peace and Riley, 1983).

The experimental velocities along the shoreline are also underestimated by the point vortex model although the accuracy of ~1/3 of the measured values prevented us from being more assertive (average ratio of theoretical velocity to experimental velocity of 1.4±0.5).

Chapter 5

Comparison with theory

5.1 Objectives and structure of the chapter

5.1.1 Objectives

We compare the results of the experiments described in chapters 4 with the theory discussed in chapter 2, i.e. the theory of vortex rings. The main objectives of this experiment are:

- to compare the distance of the vortices from the shoreline (R_f) when they move parallel to it (see chapter 4, section 4.5.1) with the predictions of our analytical model;

- to compare the speed of the vortices (see chapter 4, section 4.5.2), moving over the sloping bed and parallel to the shoreline, with the one predicted by the vortex ring-theory;

- to give an explanation of the differences between theory and observations.

5.2 Distance of the vortices from the shoreline: the prediction of the inviscid vortex ring model (model 1)

5.2.1 Introduction

In section 2.3.2 we used the principle of the conservation of the kinetic energy to calculate the asymptotic value of the radius (R_f) of two equal coaxial inviscid vortex rings of opposite sign and initial separation s_i that

move infinitely apart (see fig. 5.1 a). This situation was described with equation 2.47 (reported below) that gives R_f as a function of the initial relative distance of the vortices (s_i), the initial radius (R_i) of the rings, and the initial and final radius of the core (r_i and r_f respectively).

$$R_i\left[\log\left(\frac{8R_i}{r_i}\right)-\frac{7}{4}\right]-\left(s_i+\sqrt{s_i^2+4R_i^2}\right)\left[K(\lambda)-E(\lambda)\right]=R_f\left[\log\left(\frac{8R_f}{r_f}\right)-\frac{7}{4}\right]. \quad (2.47)$$

λ was given by formula 2.46:

$$\lambda=\frac{\sqrt{s_i^2+4R_i^2}-s_i}{\sqrt{s_i^2+4R_i^2}+s_i}. \quad (2.46)$$

Since the flow is assumed to be non-viscous the circulation (Γ) of the two rings is conserved and equation 2.47 is independent of this parameter. The dependence of the right hand side of equation 2.47 from the final radius of the core r_f, was eliminated by using the conservation of volume of the vortex (eq. 2.43), which has a simple form if the rings are approximated by two tori of circular cross-section:

$$r_f=r_i\left(\frac{R_i}{R_f}\right)^{\frac{1}{2}}. \quad (2.43)$$

The substitution of 2.43 in 2.47 leads to the following expression:

$$R_i\left[\log\left(\frac{8R_i}{r_i}\right)-\frac{7}{4}\right]-\left(s_i+\sqrt{s_i^2+4R_i^2}\right)\left[K(\lambda)-E(\lambda)\right]=R_f\left[\log\left(\frac{8R_f^{3/2}}{r_iR_i^{1/2}}\right)-\frac{7}{4}\right].$$

The situation to which the formula above applies is sketched in figures 5.1.a and 5.1.b. Bearing in mind the discussion of section 2.3.3, when the idea of using a sector of a vortex ring as a model for a vortex over a planar

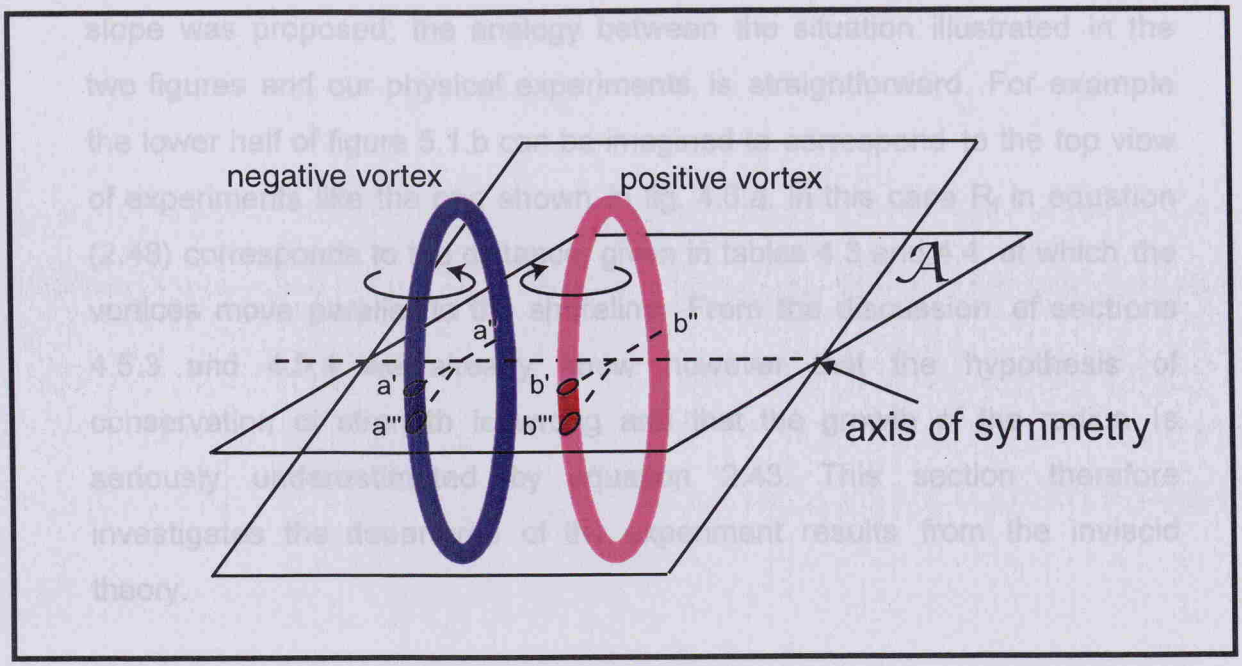

Fig. 5.1.a: Two axisymmetric circular vortex ring, of equal strength and opposite sign, are at an initial distance s_i (indicated in the panel below). In this configuration the vortices move apart symmetrically in opposite directions and their radius decreases. The motion is completely axisymmetric and can be described with the position of the intersections of the rings with the plane $\mathcal{A}$. Therefore the problem can be considered completely two-dimensional. If the two planes shown in figure are replaced with two solid boundaries, the two portion of the vortices a'a''' (dark blue) and b'b''' (dark red) can be considered as an approximation of the vortex dipole on the planar slope. The vortex lines a'a''a''' (light blue) and b'b''b''' (light red) are the images of the system.

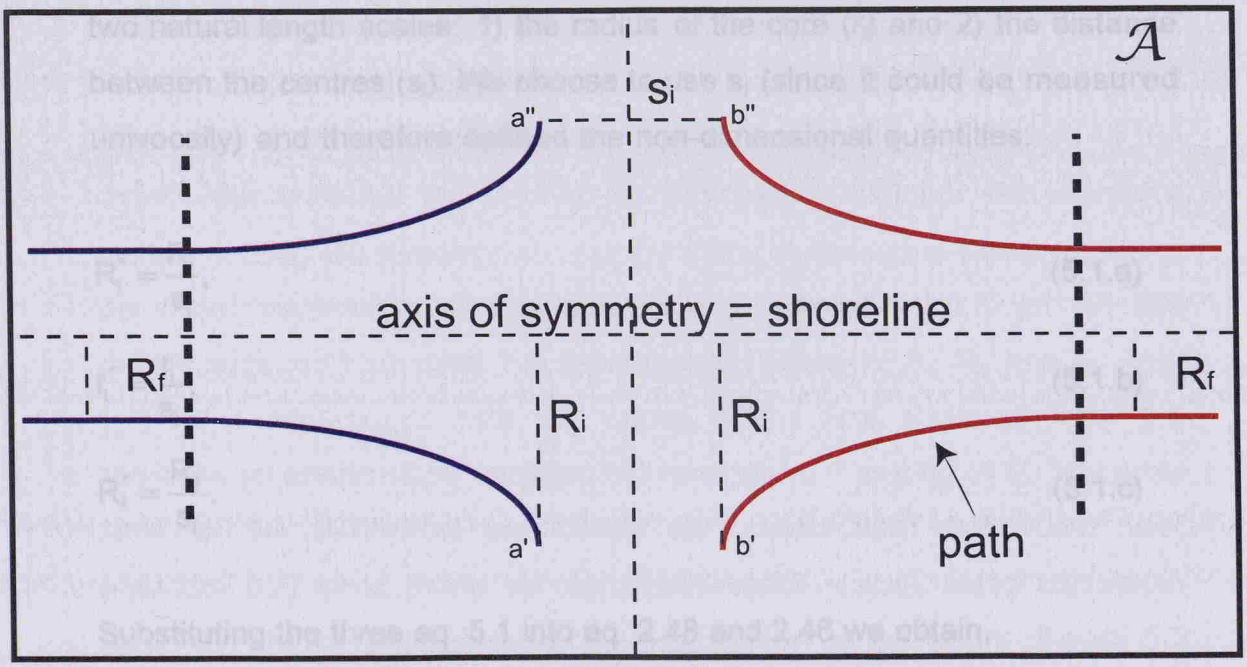

Fig. 5.1.b: Sketch of the path followed by the intersections of the vortex rings with the plane $\mathcal{A}$. The lower half of the figure corresponds to our experimental set-up. When the vortices are far enough to be considered independent (beyond the blue dashed lines) they continue moving along-shore under the effect of their self-induced velocity, as discussed in chapter 2.

slope was proposed, the analogy between the situation illustrated in the two figures and our physical experiments is straightforward. For example the lower half of figure 5.1.b can be imagined to correspond to the top view of experiments like the one shown in fig. 4.6.a. In this case R_f in equation (2.48) corresponds to the distance, given in tables 4.3 and 4.4, at which the vortices move parallel to the shoreline. From the discussion of sections 4.5.3 and 4.5.4 we already know however that the hypothesis of conservation of strength is wrong and that the growth of the radius is seriously underestimated by equation 2.43. This section therefore investigates the departures of the experiment results from the inviscid theory.

5.2.2 Comparison with theory

Eq. 2.48 reveals that the distance R_f (at which the vortices move parallel to the shoreline) must be independent not only of the strength Γ of the dipole but also of the angle that the planar slope forms with the horizontal. We now seek a suitable parameter to scale equation 2.48. The problem has two natural length scales: 1) the radius of the core (r_i) and 2) the distance between the centres (s_i). We choose to use s_i (since it could be measured univocally) and therefore defined the non-dimensional quantities:

$$R_i^* = \frac{R_i}{s_i}, \qquad (5.1.a)$$

$$r_i^* = \frac{r_i}{s_i}, \qquad (5.1.b)$$

$$R_f^* = \frac{R_f}{s_i}. \qquad (5.1.c)$$

Substituting the three eq. 5.1 into eq. 2.48 and 2.46 we obtain,

$$R_i^*\left(\log 8\frac{R_i^*}{r_i^*}-\frac{7}{4}\right)-\left(1+\sqrt{1+4\left(R_i^*\right)^2}\right)\left[K\left(\lambda^*\right)-E\left(\lambda^*\right)\right]=R_f^*\left\{\log\left[8R_f^*\left(\frac{R_f^*}{R_i^*}\right)^{\frac{1}{2}}\right]-\frac{7}{4}\right\},$$

(5.2)

and,

$$\lambda^*=f\left(R_i^*\right)=\frac{\sqrt{1+4\left(R_i^*\right)^2}-1}{\sqrt{1^2+4\left(R_i^*\right)^2}+1}=\lambda. \qquad (5.3)$$

Equation 5.2 was solved numerically for $R_i^* \in [1,6]$ and $r_i^* \in [0.2,1.3]$. The parameter $R_i^*=1$ corresponds to a dipole for which the initial distance from the shoreline is equal to the initial separation of the vortices. The parameter $r_i^*=0.2$ corresponds to a dipole for which the initial radius of the core is 1/5 of the initial separation of the vortices. The solutions for this range of values are shown in fig. 5.2. The relationship of R_f^* with R_i^* becomes less sensitive to r_i^* when r_i^* increases and R_i^* is small.

The radius of the vortices is difficult to identify since the boundaries of the region that contains the vorticity are not clearly defined. We therefore started making the assumption that the initial radius (r_i) is equal to half of the initial separation of the vortices (s_i), i.e. $r_i^*=r_i/s_i=0.5$ for all the experiments, and we used the experimental values of R_i, R_f, and s_i, (tab. 4.4) for a comparison with the values of the final distance from the shoreline as predicted by equation 5.2 (see tab. 5.1 and fig. 5.3). The error bars for the theoretical predictions were calculated numerically with equation 5.2, while those for the experimental values were calculated using the standard formulae for the propagation of the errors. Figure 5.3 shows that for almost all the experiments, except n. 1 and n. 14, the theoretical predictions overestimate the experimental measurements, (but note that the experimental data points are consistent with the predictions if

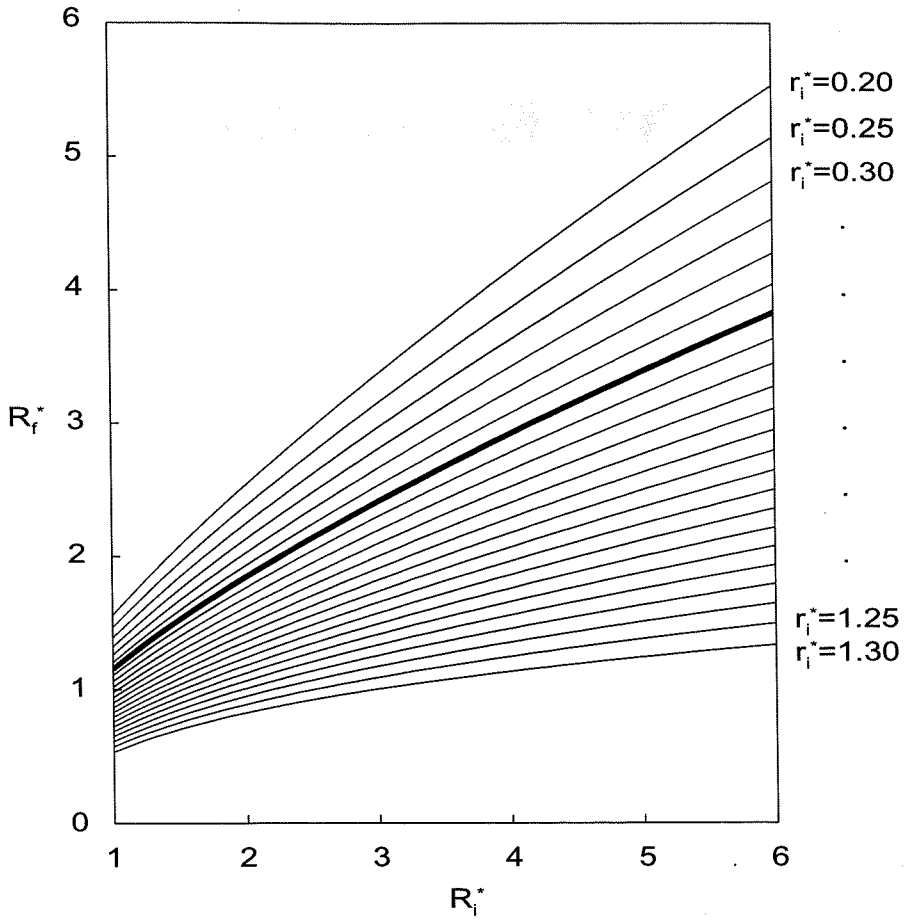

Fig. 5.2: Two co-axial equal vortex rings of opposite sign at an initial distance si and with initial radius R_i move apart from each other. When si tends to ∞ the radius of the rings tends to R_f (see fig. 5.1). R_f^* (see def. 5.1.c) was calculated numerically from equation 5.2, parametrised with the non dimensional radius of the cross-section of the rings (see def. 5.1.b), as a function of the non-dimensional initial radius (see def. 5.1.a). Since the parameters are scaled with the initial separation of the vortices, s_i, the condition R_i^*=1 means that the initial radius of the rings is equal to their initial separation and the conditions r_i^*=0.5 (bold line) means that the initial radius of the circular cross-section of the vortices is half their separations.

Exp.	s_i	r^*_i	R^*_i	$R^*_{f,e}$	$R^*_{f,t}$	ΔE
1	6.8±0.3	0.5	5.8±0.3	3.7±0.2	3.7±0.4	0.1
2	6.8±0.3	0.5	4.0±0.2	2.3±0.1	2.9±0.3	1.5
3	7.1±0.3	0.5	6.1±0.3	3.2±0.2	3.9±0.4	1.8
4	6.7±0.3	0.5	3.2±0.2	2.4±0.2	2.5±0.3	0.4
5	7.4±0.3	0.5	4.8±0.2	2.8±0.1	3.3±0.4	1.3
6	7.0±0.3	0.5	2.6±0.2	1.9±0.1	2.2±0.3	0.7
7	7.1±0.2	0.5	3.6±0.2	2.4±0.1	2.7±0.2	0.9
8	7.1±0.3	0.5	2.1±0.2	1.8±0.1	1.9±0.2	0.4
9	7.2±0.3	0.5	3.3±0.2	2.2±0.1	2.6±0.3	1.0
10	6.6±0.3	0.5	1.9±0.2	1.6±0.1	1.8±0.3	0.3
11	6.8±0.3	0.5	2.6±0.2	2.0±0.1	2.2±0.3	0.4
12	7.3±0.3	0.5	1.9±0.1	1.6±0.1	1.8±0.2	0.4
13	7.3±0.3	0.5	1.4±0.2	1.3±0.1	1.5±0.3	0.3
14	7.8±0.3	0.5	0.6±0.1	0.8±0.1	0.8±0.2	0.0
16	7.3±0.5	0.5	5.0±0.3	2.9±0.3	3.3±0.6	0.2
17a	8.2±0.8	0.5	2.9±0.3	2.0±0.2	2.3±0.5	0.4
17b	7.0±0.3	0.5	3.4±0.2	2.3±0.1	2.6±0.3	0.3
18	Videotape corrupted: not processed.					
19	7.4±0.7	0.5	2.6±0.3	1.9±0.2	2.2±0.5	0.3
20	6.8±0.6	0.5	4.8±0.5	3.0±0.3	3.3±0.7	0.2
21	8.1±0.5	0.5	2.2±0.2	1.8±0.2	2.0±0.3	0.2
22	7.2±0.7	0.5	4.5±0.4	3.0±0.3	3.2±0.7	0.1
23	7.9±0.5	0.5	1.8±0.1	1.6±0.2	1.7±0.3	0.2
24	8.2±0.5	0.5	3.2±0.2	2.4±0.2	2.5±0.4	0.1
25	8.2±0.5	0.5	1.4±0.1	1.3±0.1	1.5±0.2	0.3
26	7.6±0.4	0.5	2.4±0.2	1.7±0.1	2.1±0.3	0.4
27	7.3±0.3	0.5	1.8±0.1	1.5±0.1	1.7±0.2	0.4

Tab 5.1: s_i: initial separation of the vortices. This was used as length scale; r^*_i: non-dimensional radius of the vortices. This was set to 0.5 for all the experiments; R^*_i: non-dimensional initial radius from the experiments; $R^*_{f,e}$: non-dimensional final radius from the experiments; $R^*_{f,t}$: non-dimensional final radius from eq. 5.2; ΔE: ratio of the difference between the final theoretical kinetic energy and the final experimental kinetic energy (calculated with the rhs term of equation 5.2) to the final theoretical kinetic energy (see formula 5.4).

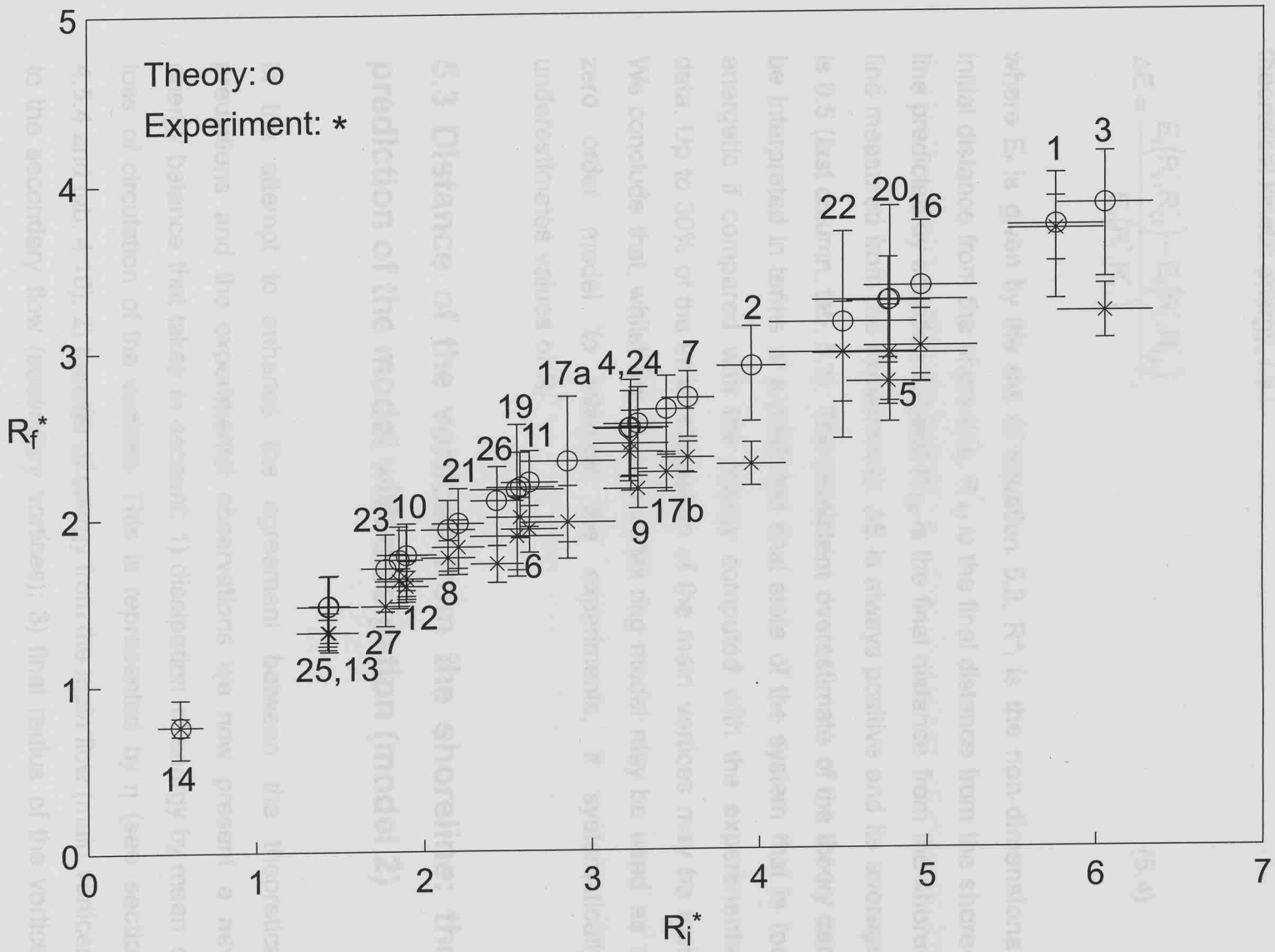

Fig. 5.3: Comparison of the experimental final distance from the shore-line (R_f^*) with the predictions of the two-dimensional energy conserving inviscid model 5.2. The final distance is expressed as a function of the distance of the border between the flat bottom region and the beginning of the planar slope from the shoreline (R_i^*). Both quantities were made nondimensional with the initial separation of the vortices (s_i).

the error bars are taken into account). The last column of table 5.1 shows the ratio ΔE of the difference between the final (or initial) theoretical kinetic energy and the final experimental kinetic energy to the final (or initial) theoretical kinetic energy, i.e.:

$$\Delta E = \frac{E_f\left(R_i^*, R_{f,t}^*\right) - E_f\left(R_i^*, R_{f,e}^*\right)}{E_f\left(R_i^*, R_{f,t}^*\right)}, \tag{5.4}$$

where E_f is given by the rhs of equation 5.2, R^*_i is the non-dimensional initial distance from the shore-line, $R^*_{f,t}$ is the final distance from the shore-line predicted by equation 5.2 and $R^*_{f,e}$ is the final distance from the shore-line measured from the experiments. ΔE is always positive and its average is 0.5 (last column, tab. 5.1). The persistent overestimate of the theory can be interpreted in terms of a predicted final state of the system that is too energetic if compared with the energy computed with the experimental data. Up to 30% of the initial circulation of the main vortices may be lost. We conclude that, whilst the inviscid vortex ring model may be used as a zero order model to interpret the experiments, it systematically underestimates values of R_f^*.

5.3 Distance of the vortices from the shoreline: the prediction of the model with dissipation (model 2)

In the attempt to enhance the agreement between the theoretical predictions and the experimental observations we now present a new energy balance that takes in account: 1) dissipation of energy by mean of loss of circulation of the vortices. This is represented by η (see section 4.5.4 and tab. 4.10); 2) transfer of energy from the main flow (main vortices) to the secondary flow (secondary vortices); 3) final radius of the vortices

bigger than the prediction of the compression mechanism (eq. 2.43). The new energy balance is therefore written as:

$$E_i=E_{f,1}+E_{f,2}, \tag{5.5}$$

where:

$$E_i = \alpha\Gamma_i^2 R_i\left[\log\left(\frac{8R_i}{r_i}\right)-\frac{7}{4}\right]-\alpha\Gamma_i^2\left(s_i+\sqrt{s_i^2+4R_i^2}\right)\left[K(\lambda)-E(\lambda)\right] \tag{5.6}$$

is the initial kinetic energy of the flow (i.e. when the vortices impinge on the slope forming an angle α with the horizontal);

$$E_{f,1} = \alpha\left(\eta\Gamma_i\right)^2 R_f\left[\log\left(\frac{8R_f}{r_f}\right)-\frac{7}{4}\right] \tag{5.7}$$

is the kinetic energy of the vortices when they move parallel to the shoreline at a distance R_f and parallel to it, which take in account the effect of the final radius of the vortices, r_f, and the loss of strength, η;

$$E_{f,2} = \Phi_s + \Phi_{lost} \tag{5.8}$$

is a term that represents the transfer of energy from the primary to the secondary flow (Φ_s) plus the energy dissipated and lost in small-scale turbulence (Φ_{lost}).

We estimated Φ_s by making the gross assumption that the secondary vortices behave like Hill's spherical vortices of strength Γ_s and with kinetic energy (e.g. Saffman, 1992, p. 199):

$$E_{f,s} = \frac{4}{70}\pi\Gamma_s^2 r_s, \tag{5.9}$$

where r_s and Γ_s are respectively the radius and the circulation of the secondary vortices. This assumption is probably not very precise, since the secondary vortices do not exhibit axial symmetry (e.g. fig. 4.10 and 4.11) but it should give at least the order of magnitude of the energy extracted by the secondary vortices from the main flow.

If the term Φ_{lost} is assumed to be small, R_f can be found by solving the equation:

$$R^*_i\left[\log\left(\frac{8R^*_i}{r^*_i}\right)-\frac{7}{4}\right]-\left(1+\sqrt{1+4R^{*2}_i}\right)\left[K(\lambda)-E(\lambda)\right]=\eta^2 R^*_f\left[\log\left(\frac{8R^*_f}{r^*_f}\right)-\frac{7}{4}\right]+\frac{4}{70}\pi\beta^2 r^*_s \tag{5.10}$$

with $\beta=\Gamma_s/\Gamma_i$. Equation 5.10 was obtained by substituting eq. 5.6, 5.7 and 5.8 into 5.4 and the initial separation of the vortices s_i was used to make equation 5.10 non-dimensional (the dimensional quantities are indicated with the symbol *). The parameters used to solve eq. 5.10 are in tab. 5.2. Γ_s and r_s were estimated during the along-shore propagation in the same way described for the main vortices (sections 4.5.3 and 4.5.4). For η and r_f we used the average of the values calculated for the 90th, 95th and 99th percentiles. The theoretical predictions of the final distance from the shore-line, $R^*_{f,t}$, are shown in fig. 5.4. As in the previous section, we have calculated the relative difference of final kinetic energy from theory and experiments, i.e.:

$$\Delta E = \frac{E_f\left(\eta^2,\beta^2,r^*_f,r^*_s,R^*_i,R^*_{f,t}\right)-E_f\left(\eta^2,\beta^2,r^*_f,r^*_s,R^*_i,R^*_{f,e}\right)}{E_f\left(\eta^2,\beta^2,r^*_f,r^*_s,R^*_i,R^*_{f,t}\right)}, \tag{5.11}$$

Exp.	s_i	r^*_i	R^*_i	η^2	β^2	r^*_f	r^*_s	$R^*_{f,e}$	$R^*_{f,t}$	σ^+	σ^-	$E_{s,f}/E_{p,f}$	ΔE (%)
16	7.3±0.5	0.8±0.1	5.0±0.3	0.5±0.3	0.07±0.04	1.5±0.1	1.2±0.1	3.0±0.2	3.6	1.9	1.0	0.01	0.3
17a	8.2±0.8	0.6±0.1	2.9±0.3	0.7±0.3	0.05±0.03	1.1±0.2	0.8±0.1	2.0±0.2	2.4	1.4	0.6	0.01	0.3
17b	7.0±0.3	0.8±0.1	3.4±0.2	0.7±0.4	0.10±0.06	1.3±0.1	1.1±0.1	2.3±0.1	2.2	1.6	0.6	0.02	-0.05
18	Videotape corrupted: not processed.												
19	7.4±0.7	0.7±0.1	2.6±0.3	0.8±0.6	0.06±0.05	1.1±0.2	0.8±0.1	1.9±0.2	1.9	1.5	0.6	0.01	-0.01
20	6.8±0.6	0.8±0.1	4.8±0.5	0.9±0.4	0.02±0.01	1.6±0.2	0.9±0.1	3.0±0.3	2.6	1.2	0.5	0.003	-0.3
21	8.1±0.5	0.7±0.1	2.2±0.2	0.8±0.4	0.09±0.05	1.0±0.1	0.9±0.1	1.8±0.2	1.7	1.0	0.4	0.01	-0.2
22	7.2±0.7	0.8±0.1	4.5±0.4	0.9±0.5	0.15±0.07	1.4±0.2	1.2±0.1	3.0±0.3	2.5	1.7	0.7	0.02	-0.4
23	7.9±0.5	0.7±0.1	1.8±0.1	0.8±0.5	0.08±0.06	1.0±0.1	0.7±0.1	1.6±0.2	1.5	1.1	0.4	0.01	-0.2
24	8.2±0.5	0.7±0.1	3.2±0.2	0.9±0.2	0.11±0.07	1.2±0.2	0.9±0.1	2.4±0.2	2.1	0.5	0.4	0.01	-0.3
25	8.2±0.5	0.6±0.1	1.4±0.1	0.9±0.5	0.06±0.04	0.9±0.1	0.6±0.1	1.3±0.1	1.2	0.7	0.3	0.01	-0.2
26	7.6±0.4	0.7±0.1	2.4±0.2	1.0±0.4	0.08±0.04	1.1±0.1	0.8±0.1	1.7±0.1	1.7	0.7	0.3	0.01	-0.09
27	7.3±0.3	0.6±0.1	1.8±0.1	0.9±0.4	0.02±0.01	0.9±0.1	0.7±0.1	1.5±0.1	1.5	0.8	0.3	0.003	0.02

Tab. 5.2: See caption of table 5.1 for the definitions of s_i, r^*_i, R^*_i, $R^*_{f,e}$ and $R^*_{f,t}$. η represents the loss of strength by the main vortices and was defined by formulae 4.8. The values in the tables are the average of the 90th, 95th and 99th percentiles. β is the strength of the secondary vortex divided by the initial strength of the primary vortex. r^*_f is the non-dimensional radius of the primary vortices while they move along the shoreline and r^*_s is the radius of the secondary vortices (see section 4.5.3). σ^+ and σ^- are the upper and lower accuracy of R*f,t calculated with eq. 5.10. $E_{s,f}/E_{p,f}$ is the ratio of the second term of the rhs of equation 5.10 to the first term and represents the ratio of the energy of the secondary vortex to the energy of the primary vortex. For the definition of ΔE see formula 5.11.

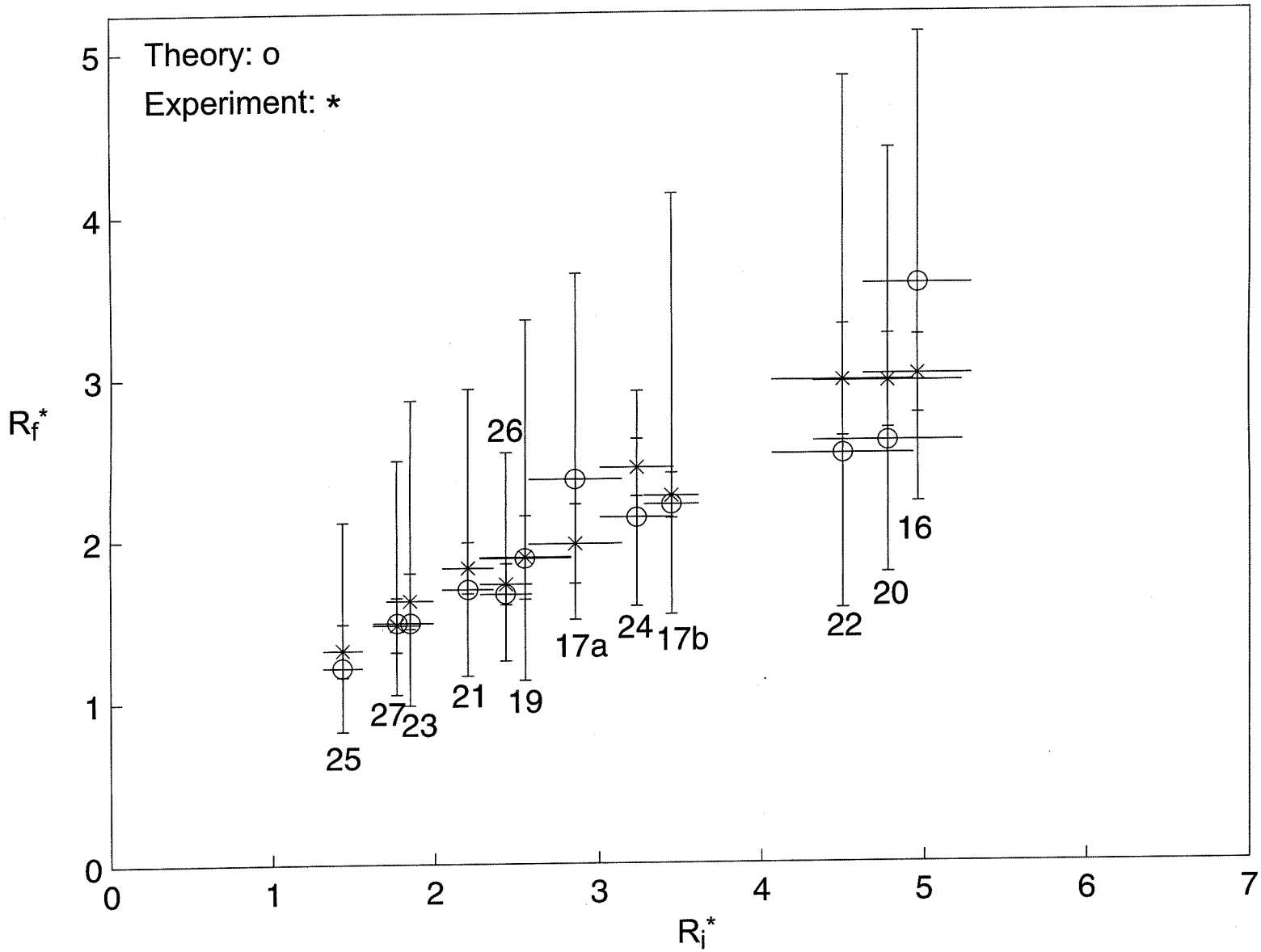

Fig. 5.4: Comparison of the experimental final distance from the shore-line (R_f^*) with the predictions of model 5.10. The final distance is expressed as a function of the distance of the border between the flat bottom region and the beginning of the planar slope from the shoreline (R_i^*). Both quantities were made nondimensional with the initial separation of the vortices (s_i). We note that now the tendency of the theory to systematically overestimate the experiments, showed in fig. 5.3, has disappeared.

where now E_f is the rhs of equation 5.10. The average absolute value of ΔE is now 0.2. For the majority of the experiments ΔE is negative, indicating that the kinetic energy calculated from the experiments is greater than the theoretical kinetic energy. The measurements that are most likely to lead to this inaccurate conclusion are the dissipation of energy, η, and the final radius of the main vortex, r_f. Our estimate of the relative importance of the two terms of the rhs of equation 5.10, i.e. the ratio of the kinetic energy of the secondary vortex to the kinetic energy of the primary vortex ($E_{s,f}/E_{p,f}$) is ~ 1%, thus suggesting that the energy of the secondary flow can be neglected in the computation of R_f. Note that the term Φ_{lost} in eq 5.8 was arbitrarily neglected. An estimate of the energy dissipated by small-scale turbulence could help to improve the predictions of equation 5.10, but given the accuracy of our estimates of η and r_f we cannot be more assertive. However the average value of ΔE passes from 0.5 (inviscid model 5.2) to 0.2, and therefore model 5.10 represents an improvement as can be seen from fig 5.5 that shows a comparison of the predictions from model 1 (equation 5.2) and model 2 (equation 5.10). We note that eq.4.5, or a similar refined version, may be used to predict the final value of the radius, r_f. We should also note from fig 5.5 a that there is a remarkably good agreement with the predictions for those vortices which still cross the border between the slope and the flat bottom regions but have a large portion of the core on the flat bottom (experiments 25, 26 and 27)[17]. Computation of R_f^* from equation 5.10 using values of r_f and h calculated using the 90th, 95th and 99th percentile criteria (not shown) did not lead to different conclusions. The new model accounts for the loss of circulation of the main vortices and, on the other hand, it reduces the loss of energy of

[17]We can justify this result theoretically by noting that (see fig. 6.2) for a small initial radius, R_i^*, the predicted value of R_f^* is less sensitive to the size of the radius of the core, r_i^*, i.e. the range of values that R_f^* can assume is much narrower if compared with the predictions for large R_i^*.

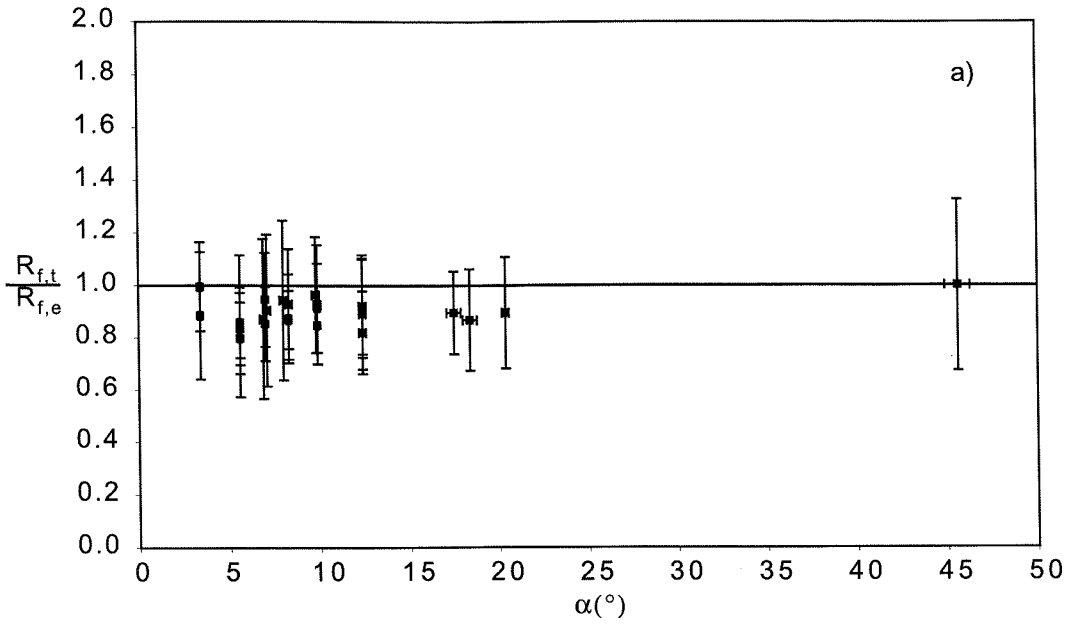

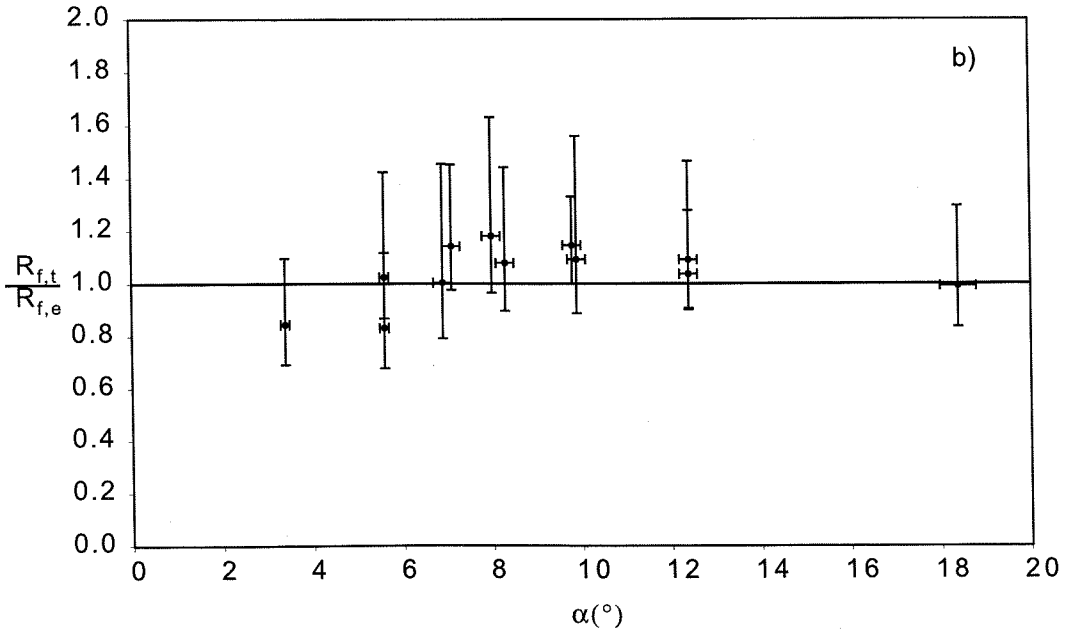

Fig 5.5: a) Comparison between final distance from the shoreline as predicted by model 1 (eq. 5.2), Rf,t, and the experimental observations. With the exceptions of experiments 14 (45°) and 1 (3.4°) the theory systematically overestimate the experiments (but is in agreement within the experimental error.

b) As a) but now the comparison is made with the predictions from model 2 (eq. 5.10). This models shows a better agreement. A more correct energy balance was used.

the main flow by including, via the bigger-than-predicted final radius of the vortices, a larger volume of rotational flow.

5.4 Speed of the vortices parallel to the shoreline during their along-shore motion. Comparison with theory

5.4.1 Introduction

In section 4.5.2 we measured the speed of the vortices in the direction parallel to the shoreline ($v_{//}$) in the interval $[t_2,t_3]$. For the PIV experiments we were able to compute a Reynolds number (R_e, formula 4.4). We showed that $v_{//}$ is almost proportional to R_e (fig. 4.23). In this section we shall not discuss the experiments with fluorescine since from them we could not measure the strength and the radius of the vortices during their along-shore motion. Fig. 5.6 a, 5.6 b and 5.6 c shows the range of R_e achieved in our PIV experiments as a function of α for the three percentiles used. The three figures are almost identical (see also tab. 4.8) and we conclude that our estimate of R_e (i.e. of Γ/r) is independent from the percentile used.

In this section we compare the speed measurements with two models: 1)the analytical formula for the speed of a thin cored vortex ring (i.e. rings for which the condition $\varepsilon<<1$ should be verified, where ε is the ratio of the radius of the core to the radius of the ring (see also section 2.3.1 and formula 2.28). We call this model A but it is consistent with the formulation of model 1, section 5.2, since eq. 2.30 and eq. 5.2 are obtained from the theory of inviscid thin cored vortex rings); 2)the numerical results computed by Norbury (1973) that apply to rings for which the less stringent condition $0.1 \leq \varepsilon \leq 2^{1/2}$ is true (model B, tab. 5.3).

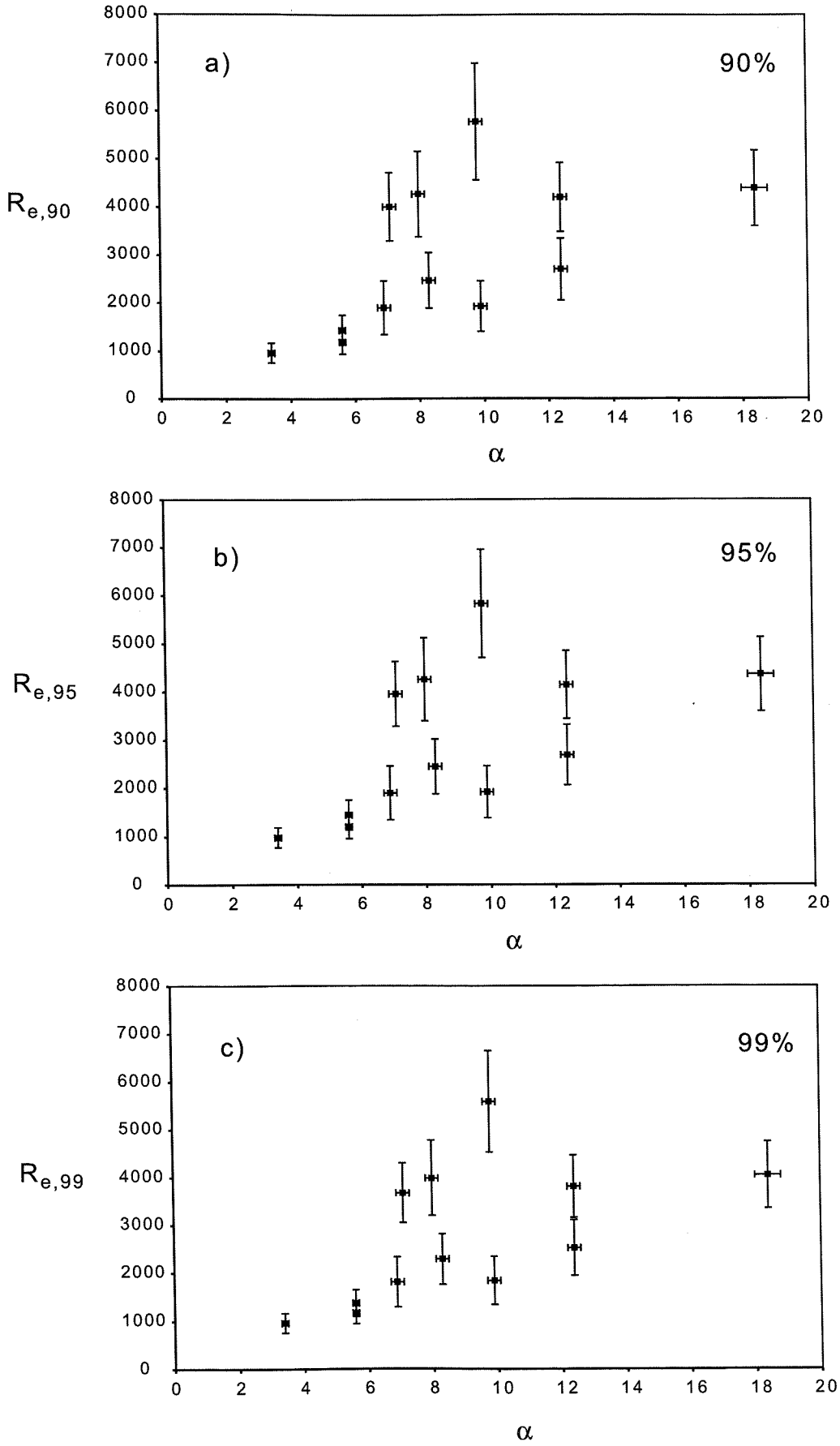

Fig 5.6: Range of Reynolds numbers for the PIV experiments as a function of the angle of the planar slope with the horizontal. The estimates made with the three percentiles are very similar. Unfortunately we were unable to achieve high Reynolds number at small angles.

α ...	0·1	0·2	0·3	0·4	0·5	0·6	0·7	0·8
W	1·0195	0·8488	0·7402	0·6586	0·5922	0·5357	0·4863	0·4428
α ...	0·9	1·0	1·1	1·2	1·3	1·35	$\sqrt{2}$	
W	0·4043	0·3703	0·3402	0·3136	0·2901	0·2793	0·2667	

Tab. 5.3: Table showing the numerical results for the non-dimensional speed of a vortex ring, made non dimensional with the ratio $\Gamma/(\pi R_f)$, as a function of the ratio, α, of the cross section area to the ring area (i.e. $\varepsilon \sim \alpha$, with ε given by formula 6.12). From Norbury, 1973.

For both models we show a comparison of the quantities measured with the three percentiles and averaged in the three time intervals $[t_2, t_3]$, $[t_2, t_2+0.5\Delta t]$ and $[t_2+0.5\Delta t, t_3]$, where $\Delta t=t_3-t_2$, to show that the conclusions are always consistent amongst them.

5.4.2 Comparison with vortex ring and Norbury theory

The self-induced velocity of an inviscid circular vortex ring with circular cross section of area πr_f^2 (e.g. Lamb, 1932) was given by formula 2.30, which is reported once more below:

$$v_c = \frac{\Gamma_f}{4\pi R_f}\left\{\log\frac{8}{\varepsilon_f} - \frac{1}{4} + \varepsilon_f^2\left[-\frac{3}{8}\log\frac{8}{\varepsilon_f} + \frac{15}{32}\right] + o\left(\varepsilon_f^4 \log\frac{8}{\varepsilon_f}\right)\right\}, \qquad (2.30)$$

where Γ_f is the strength of the vortex, R_f is the radius of the ring, r_f is the radius of the cross section and ε_f is defined by:

$$\varepsilon_f = \frac{r_f}{R_f}. \qquad (5.12)$$

The formula was obtained with the assumption $\varepsilon_f << 1$ (see e.g. Saffman, 1992 , p. 195-201). If formula 2.30 can explain our results, the speed of the vortices in the direction parallel to the shoreline, $v_{//}$ (see section 4.5.2) must be independent of the angle of the planar slope with the horizontal.

When the condition $\varepsilon_f << 1$ is relaxed the results of Norbury (1973) can be used. The author calculated numerically the solution of the speed of rings with ε in the interval $[0.1, 2^{0.5}]$, i.e. for a family of rings ranging from thin cored rings ($\varepsilon=0.1$) to Hill's spherical vortices ($\varepsilon=2^{0.5}$). The non-dimensional speeds are shown in table 5.3. Interpolated values were

used for comparison with our experimental results and were made dimensional with the factor: $\frac{\Gamma}{\pi R_f}$.

The results are shown in tables 5.4, 5.5 and 5.6 for the 90th, 95th and 99th percentiles respectively. The measured quantities shown in the tables were averaged in the interval t_2,t_3. The ratio between the experimental speed and the predictions of equation 2.30 and the ratio between the experimental speed and the predictions of tables 5.3, 5.4 and 5.5 are plotted in figures 5.7 (90%), 5.8 (95%) and 5.9 (99%) as a function of the Reynolds number and for the 3 time intervals mentioned in section 5.4.1. All the plots indicate that for low Reynolds numbers (R_e<$R_{e,b}$, with $R_{e,b}$~1500-2000) both models overestimate the experimental data but the agreement improves for larger values of R_e. A dependence on other parameters, the most likely being the angle of the planar slope α, could also be possible but the size of the error bars only allows us to speculate and prevents us from being assertive.

We conclude that either model A or model B can explain our experimental results when $R_e > R_{e,b}$, where $R_{e,b}$ is of the order $2 \cdot 10^3$. The conclusion is 'robust' in that it is not sensitive to the definition of the strength and of the radius (in the sense explained in sections 4.4.6 and 4.4.7), or on the time interval used for the average.

5.6 Conclusion

In sections 5.2 and 5.3 we have shown that model 1 and model 2, both based on the vortex ring theory, are able to explain the observed final distance from the shoreline within the experimental errors. Model 2 is a development of the first, which was modified to take in account energy dissipation. A different form of energy distribution, represented by a volume

Exp.N	α (°)	$\Gamma_{m,90}$ ($cm^2\ s^{-1}$)	$r_{f,90}$ (cm)	R_f (cm)	h (cm)	ε_{90}	$R_{e,90}\ 10^3$	$v_{//}$ ($cm\ s^{-1}$)	v_{ring} ($cm\ s^{-1}$)	v_{norb} ($cm\ s^{-1}$)	ρ_1	ρ_2
16	3.4±0.1	78±11	9.7±0.3	22.1±0.3	1.31±0.05	0.44±0.02	1.0±0.2	0.4±0.2	0.7±0.2	0.7±0.1	0.6±0.5	0.6±0.4
17a	5.6±0.1	65±7	7.8±0.5	16.0±0.3	1.57±0.06	0.49±0.04	1.2±0.3	0.5±0.1	0.8±0.3	0.8±0.1	0.6±0.4	0.7±0.3
17b	5.6±0.1	79±11	7.8±0.4	16.0±0.2	1.56±0.05	0.49±0.03	1.4±0.3	0.7±0.2	1.0±0.3	0.9±0.2	0.7±0.4	0.7±0.3
18	Videotape corrupted: not processed.											
19	6.9±0.2	90±16	7.3±0.5	14.0±0.4	1.7±0.1	0.52±0.05	1.9±0.6	1.1±0.2	1.3±0.5	1.2±0.3	0.8±0.6	0.9±0.4
20	7.1±0.2	154±18	8.8±0.2	20.2±0.1	2.52±0.09	0.44±0.01	4.0±0.7	1.5±0.3	1.6±0.3	1.5±0.2	0.9±0.4	1.0±0.3
21	8.3±0.2	83±10	6.6±0.4	14.7±0.5	2.2±0.1	0.45±0.04	2.5±0.6	1.2±0.2	1.2±0.5	1.1±0.2	1.0±0.6	1.1±0.4
22	8.0±0.2	133±17	8.5±0.4	21.3±0.2	3.0±0.1	0.40±0.02	4.3±0.9	1.2±0.2	1.4±0.4	1.3±0.2	0.9±0.4	0.9±0.3
23	9.9±0.2	62±9	6.5±0.5	12.8±0.5	2.2±0.1	0.51±0.06	1.9±0.5	0.8±0.2	1.0±0.4	0.9±0.2	0.9±0.6	0.9±0.4
24	9.8±0.2	162±12	8.8±0.9	20.0±0.4	3.5±0.1	0.44±0.05	6±1	2.1±0.2	1.7±0.7	1.6±0.2	1.2±0.6	1.3±0.3
25	12.4±0.2	76±9	6.0±0.5	10.7±0.2	2.36±0.09	0.56±0.06	2.7±0.6	1.2±0.3	1.3±0.5	1.2±0.3	0.9±0.6	1.0±0.4
26	12.4±0.2	114±14	7.1±0.2	13.2±-.1	2.89±0.08	0.54±0.02	4.2±0.7	1.7±0.4	1.7±0.4	1.6±0.2	1.0±0.5	1.1±0.4
27	18.4±0.4	78±9	5.7±0.2	10.7±0.2	3.6±0.1	0.53±0.02	4.4±0.8	1.4±0.3	1.4±0.3	1.3±0.2	1.0±0.5	1.1±0.4

Tab 5.4: α: angle of the planar slope with the horizontal; $\Gamma_{m,90}$: circulation of the vortices measured for the 90th percentile; $r_{f,90}$: radius of the vortices measured for the 90th percentile; R_f: Final distance from the shoreline; h: local water depth; ε_{90}: ratio $r_{f,90}/R_f$; $R_{e,90}$: Reynolds number calculated for the 90th percentile; $v_{//}$: measured along-shore speed; v_{ring}: self-induced speed of a vortex ring (formula 2.30); v_{norb}: self induced speed of a fat vortex ring calculated numerically by Norbury (1973); ρ_1: ratio $v_{//}/v_{ring}$; $\rho 2$: ratio $v_{//}/v_{norb}$. Γ and r were averaged in the interval $[t_2,t_3]$.

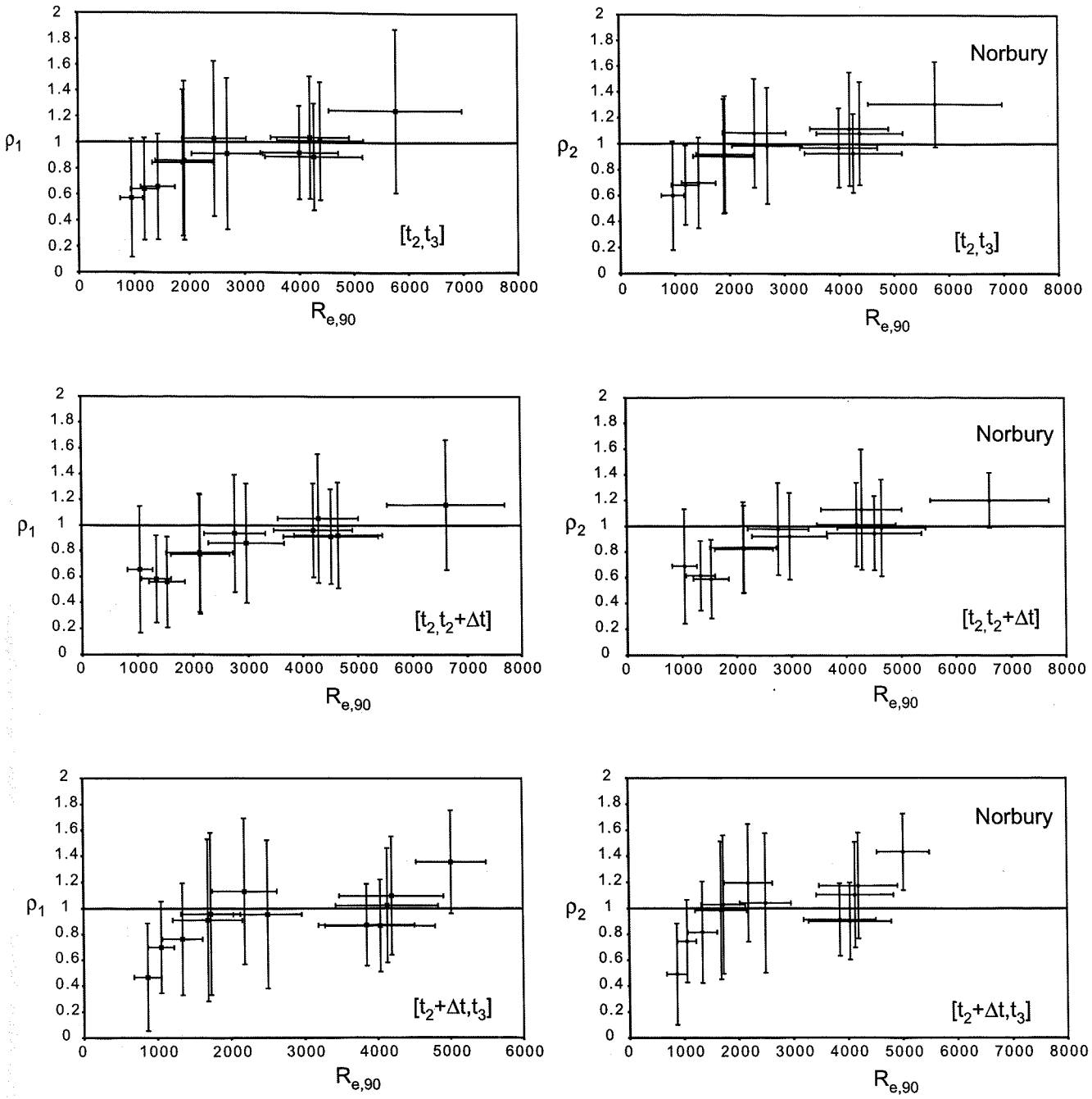

Fig 5.7: Speed of the vortices in three time ranges. 90th percentile. Comparison of the experimental data with theory (see caption of table 5.4 for a definition of ρ_1 and ρ_2). The agreement between theory and experiments is good for $R_{e,90}>R_{e,b}$, with $R_{e,b}\sim1500$. $\Delta t=t_3-t_2$.

Exp.N	α (°)	$\Gamma_{m,95}$ (cm^2 s^{-1})	$r_{f,95}$ (cm)	R_f (cm)	h (cm)	ε_{95}	$R_{e,95}10^{-3}$	$v_{//}$(cm s^{-1})	v_{ring} (cm s^{-1})	v_{norb} (cm s^{-1})	ρ_1	ρ_2
16	3.4±0.1	90±13	11.0±0.4	22.1±0.3	1.31±0.05	0.50±0.02	1.0±0.2	0.4±0.2	0.8±0.2	0.8±0.1	0.5±0.4	0.6±0.4
17a	5.6±0.1	75±8	8.9±0.5	16.0±0.3	1.57±0.06	0.55±0.04	1.2±0.2	0.5±0.1	0.9±0.3	0.8±0.1	0.6±0.3	0.6±0.3
17b	5.6±0.1	91±13	9.0±0.4	16.0±0.2	1.56±0.05	0.56±0.03	1.4±0.3	0.7±0.2	1.1±0.3	1.0±0.2	0.6±0.4	0.6±0.3
18	Videotape corrupted: not processed.											
19	6.9±0.2	103±18	8.3±0.5	14.0±0.4	1.7±0.1	0.59±0.05	1.9±0.6	1.1±0.2	1.4±0.6	1.3±0.3	0.8±0.5	0.8±0.4
20	7.1±0.2	178±21	10.4±0.2	20.2±0.1	2.52±0.09	0.51±0.01	4.0±0.7	1.5±0.3	1.8±0.3	1.6±0.2	0.8±0.3	0.9±0.3
21	8.3±0.2	95±12	7.6±0.4	14.7±0.5	2.2±0.1	0.52±0.04	2.5±0.6	1.2±0.2	1.3±0.5	1.2±0.2	0.9±0.5	1.0±0.4
22	8.0±0.2	153±19	9.8±0.4	21.3±0.2	3.0±0.1	0.46±0.02	4.2±0.9	1.2±0.2	1.5±0.4	1.4±0.2	0.8±0.4	0.9±0.3
23	9.9±0.2	71±10	7.5±0.6	12.8±0.5	2.2±0.1	0.58±0.07	1.9±0.5	0.8±0.2	1.0±0.5	1.0±0.2	0.8±0.6	0.9±0.4
24	9.8±0.2	186±13	10.0±0.8	20.0±0.4	3.5±0.1	0.50±0.05	6±1	2.1±0.2	1.9±0.6	1.8±0.2	1.1±0.5	1.2±0.3
25	12.4±0.2	87±11	6.9±0.5	10.7±0.2	2.36±0.09	0.65±0.06	2.7±0.6	1.2±0.3	1.5±0.5	1.3±0.3	0.8±0.5	0.9±0.4
26	12.4±0.2	130±16	8.3±0.2	13.2±0.1	2.89±0.08	0.63±0.02	4.2±0.7	1.7±0.4	1.8±0.4	1.6±0.2	1.0±0.4	1.1±0.4
27	18.4±0.4	89±10	6.7±0.2	10.7±0.2	3.6±0.1	0.62±0.02	4.4±0.8	1.4±0.3	1.5±0.3	1.4±0.2	0.9±0.4	1.0±0.4

Tab 5.5: α: angle of the planar slope with the horizontal; $\Gamma_{m,90}$: circulation of the vortices measured for the 95th percentile; $r_{f,90}$: radius of the vortices measured for the 95th percentile; R_f: Final distance from the shoreline; h: local water depth; ε_{90}: ratio $r_{f,90}/R_f$; $R_{e,90}$: Reynolds number calculated for the 95th percentile; $v_{//}$: measured along-shore speed; v_{ring}: self-induced speed of a vortex ring (formula 2.30); v_{norb}: self induced speed of a fat vortex ring calculated numerically by Norbury (1973); ρ_1: ratio $v_{//}/v_{ring}$; $\rho 2$: ratio $v_{//}/v_{norb}$. Γ and r were averaged in the interval $[t_2,t_3]$.

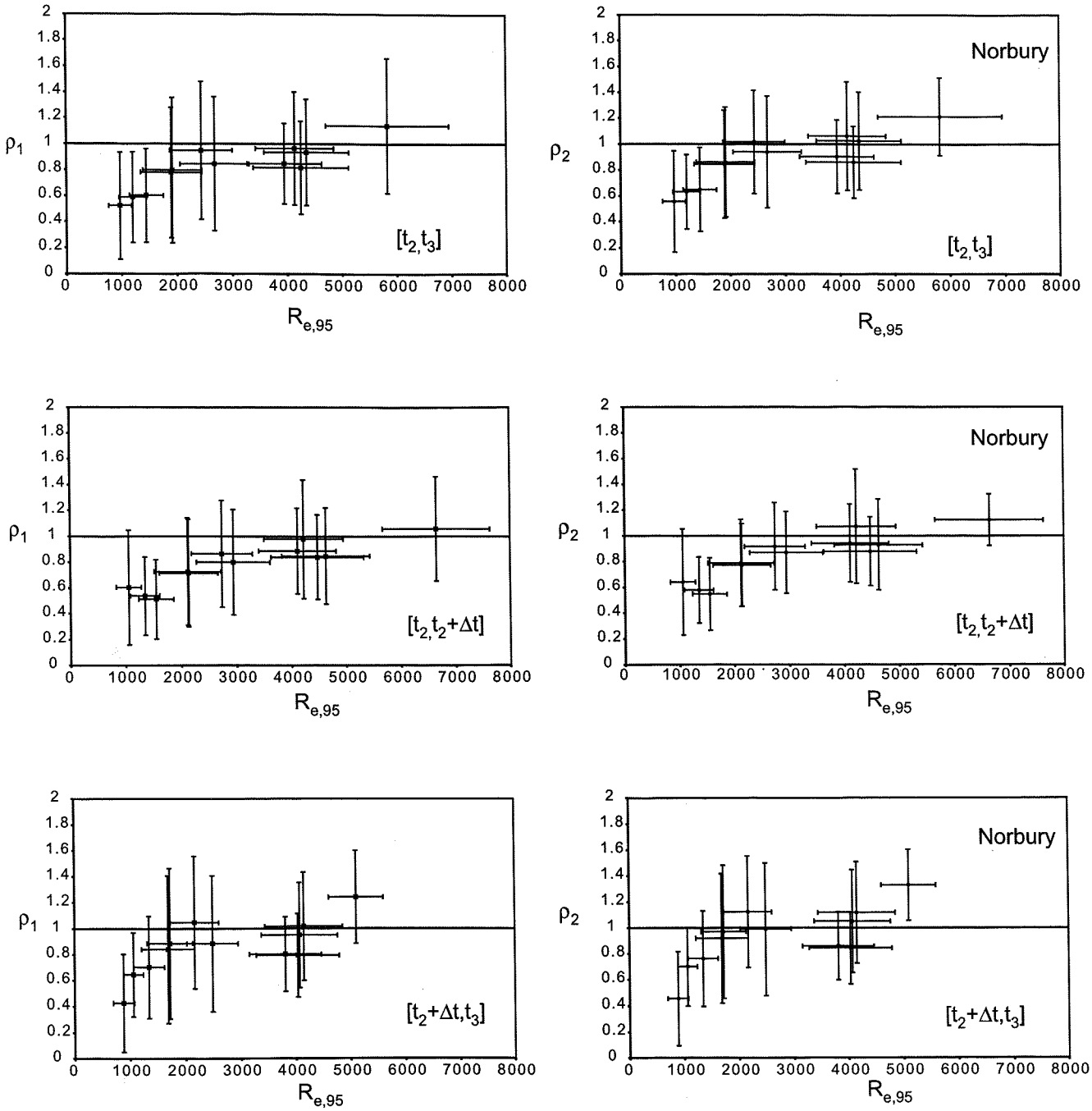

Fig 5.8: Speed of the vortices in three time ranges. 95th percentile. Comparison of the experimental data with theory (see caption of table 5.4 for a definition of ρ_1 and ρ_2). The agreement between theory and experiments is good for $R_{e,90}>R_{e,b}$, with $R_{e,b}\sim1500$. $\Delta t=t_3-t_2$.

Exp.N	α (°)	$\Gamma_{m,99}$ ($cm^2\ s^{-1}$)	$r_{f,99}$ (cm)	R_f (cm)	h (cm)	ε_{99}	$R_{e,99}\ 10^3$	$v_{//}$ ($cm\ s^{-1}$)	v_{ring} ($cm\ s^{-1}$)	v_{norb} ($cm\ s^{-1}$)	ρ_1	ρ_2
16	3.4±0.1	101±14	12.5±0.4	22.1±0.3	1.31±0.05	0.57±0.03	1.0±0.2	0.4±0.2	0.9±0.2	0.8±0.1	0.5±0.4	0.5±0.4
17a	5.6±0.1	83±9	10.2±0.5	16.0±0.3	1.57±0.06	0.64±0.04	1.2±0.2	0.5±0.1	0.9±0.3	0.8±0.1	0.6±0.3	0.6±0.3
17b	5.6±0.1	102±14	10.6±0.4	16.0±0.2	1.56±0.05	0.67±0.03	1.4±0.3	0.7±0.2	1.1±0.3	1.0±0.2	0.6±0.3	0.6±0.3
18	Videotape corrupted: not processed.											
19	6.9±0.2	114±20	9.8±0.5	14.0±0.4	1.7±0.1	0.70±0.06	1.8±0.5	1.1±0.2	1.4±0.5	1.3±0.3	0.7±0.5	0.8±0.4
20	7.1±0.2	201±23	12.6±0.3	20.2±0.1	2.52±0.09	0.62±0.02	3.7±0.6	1.5±0.3	1.8±0.3	1.7±0.2	0.8±0.3	0.9±0.3
21	8.3±0.2	107±13	9.1±0.5	14.7±0.5	2.2±0.1	0.62±0.05	2.2±0.5	1.2±0.2	1.3±0.5	1.2±0.2	0.9±0.5	1.0±0.4
22	8.0±0.2	171±21	11.7±0.4	21.3±0.2	3.0±0.1	0.55±0.03	3.9±0.8	1.2±0.2	1.5±0.4	1.4±0.2	0.8±0.3	0.8±0.3
23	9.9±0.2	79±11	8.7±0.6	12.8±0.5	2.2±0.1	0.68±0.07	1.8±0.5	0.8±0.2	1.1±0.5	1.0±0.2	0.8±0.5	0.8±0.4
24	9.8±0.2	208±10	11.7±0.9	20.0±0.4	3.5±0.1	0.58±0.06	6±1	2.1±0.2	2.0±0.6	1.8±0.3	1.1±0.5	1.2±0.3
25	12.4±0.2	97±12	8.3±0.6	10.7±0.2	2.36±0.09	0.77±0.07	2.5±0.6	1.2±0.3	1.5±0.5	1.3±0.3	0.8±0.5	0.9±0.4
26	12.4±0.2	146±18	10.1±0.2	13.2±0.1	2.89±0.08	0.76±0.03	3.8±0.7	1.7±0.4	1.8±0.4	1.6±0.3	0.9±0.4	1.1±0.4
27	18.4±0.4	100±11	8.0±0.2	10.7±0.2	3.6±0.1	0.75±0.03	4.0±0.7	1.4±0.3	1.6±0.3	1.4±0.2	0.9±0.4	1.0±0.4

Tab 5.6: α: angle of the planar slope with the horizontal; $\Gamma_{m,90}$: circulation of the vortices measured for the 99th percentile; $r_{f,90}$: radius of the vortices measured for the 99th percentile; R_f: Final distance from the shoreline; h: local water depth; ε_{90}: ratio $r_{f,90}/R_f$; $R_{e,90}$: Reynolds number calculated for the 99th percentile; $v_{//}$: measured along-shore speed; v_{ring}: self-induced speed of a vortex ring (formula 2.30); v_{norb}: self induced speed of a fat vortex ring calculated numerically by Norbury (1973); ρ_1: ratio $v_{//}/v_{ring}$; $\rho 2$: ratio $v_{//}/v_{norb}$. Γ and r were averaged in the interval $[t_2,t_3]$.

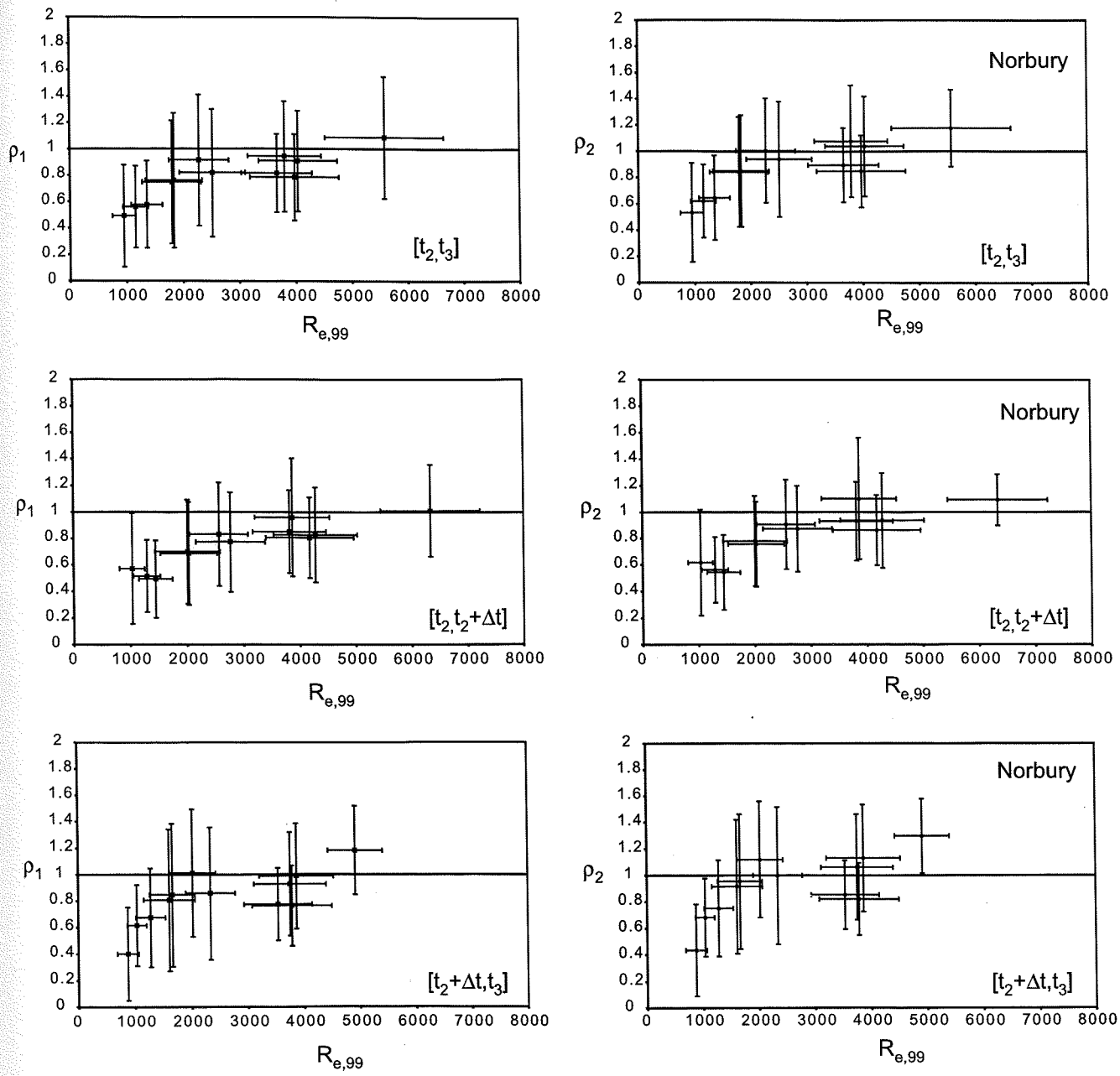

Fig 5.9: Speed of the vortices in three time ranges. 99th percentile. Comparison of the experimental data with theory (see caption of table 5.4 for a definition of ρ_1 and ρ_2). The agreement between theory and experiments is good for $R_{e,90}>R_{e,b}$, with $R_{e,b}\sim1500$. $\Delta t=t_3-t_2$.

of rotational flow different from the predictions of the spin-down/compression equation (eq. 4.5) was also included by using the experimental observations. The angle of the planar slope does not necessarily have to be small to give a good agreement between theory and observations. On the contrary the model seems to perform better for intermediate angles. The dissipation of vortex strength is largest for small angles (fig 5.10). If the plot of $R_{f,t}/R_{f,e}$ versus the Reynolds number, shown in fig. 5.11, is compared with fig. 5.5 b) the conclusion is that the predictions worsen when R_e is low, i.e. when dissipation is high, for then the physics behind model 5.10 appears inadequate. The arbitrarily neglected term Φ_{lost} may become important and/or the estimate 5.9 may be wrong.

The predictions of the vortex-ring theory of the speed of a vortex ring (models A and B) is consistent with the experiments if R_e is greater than about 1500. The model performs better when the dissipation is low. Experiments conducted with a wider range of (α,R_e) would provide further test and insights into the limitation of the theory.

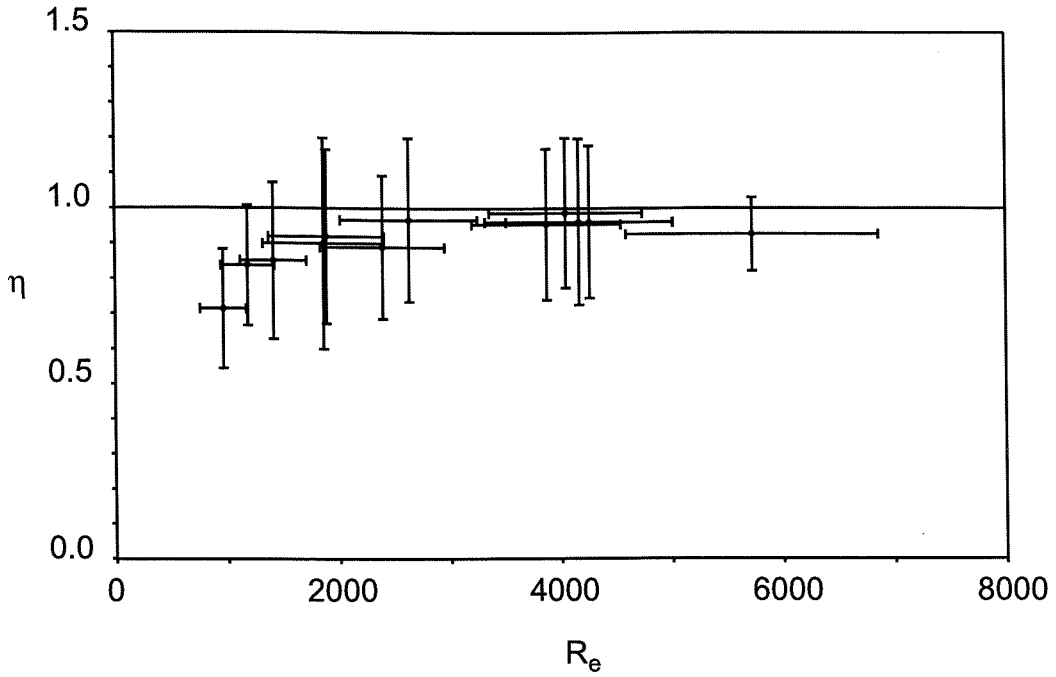

Fig. 5.10: Dissipation of strength as a function of the Reynolds number. Average for the 90th, 95th and 99th percentiles and over the interval $[t_2,t_3]$.

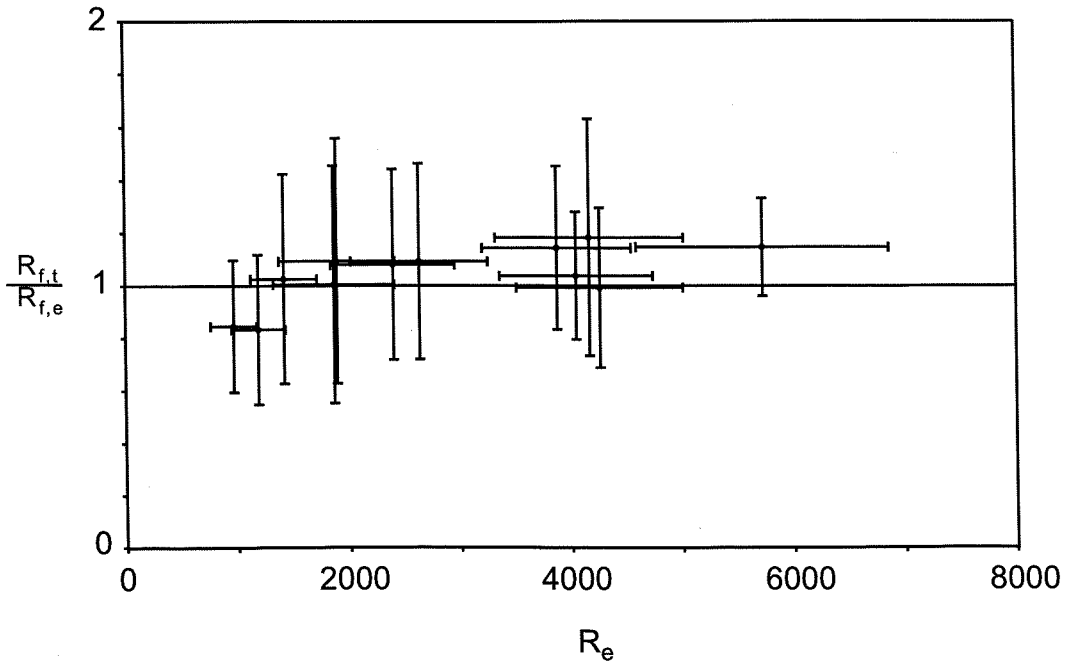

Fig. 5.11: Ratio of the final distance from the shoreline from model 5.10 to the experimental observations as a function of the Reynolds number. Average for the 90th, 95th and 99th percentiles and over the interval $[t_2,t_3]$.

Chapter 6

Conclusions

6.1 Dispersion

- We have performed a series of numerical tests made with two models reproducing vortices in a coastal sea, one with a step-like shoreline and a flat bottom and the other with a uniformly sloping bottom. Both models had a very simplified physics. They revealed that a system of near-shore vortices, in which the vortices are the only dynamical features, has a tendency to disperse in a direction parallel to the shoreline. Dispersion in the direction normal to the shoreline is possible, especially when two vortices pair to form a dipole. For then the dipole can move offshore. If the two partners of the dipole have the same circulation the dipole moves on a straight path. If the dipole is unbalanced, the path will be curved, the radius of curvature depending on the difference of strength of the two vortices. If the radius of curvature is large, the ability of the vortices to migrate offshore is seriously reduced. However, this transport process could be regarded as a mechanism for transporting water off shore where stronger currents may overcame the self-driving effect of the dipole and set up a different dispersion regime. Transport of fluid by the recirculation cell of a vortex seems to be the most likely mechanism for dispersion of pollutants in a direction normal to the shoreline.

6.2 Comparison of theory and observations

- The numerical model mentioned above of a coastal sea with a planar sloping bottom used an array of co-axial vortex rings as a model for the vortices in the wedge of fluid delimited by the sea surface and the bottom. We have conducted an investigation with laboratory experiments to test the validity of the analytical vortex ring model. The experiments have confirmed that the vortex ring can be used, especially for situations in which dissipation is not too high (i.e. large R_e). The influence of the angle, α, which the planar slope makes with the horizontal, is still not clear. We were unable to achieve high R_e at small α.

6.3 Applications and related observations

- Maps of the velocity and vorticity fields obtained with two sector scanning Doppler sonar during the Sandy Duck 97 experiment (unpublished data, courtesy of Dr. J. Smith, 1988) suggest the existence of an intense vortex dipole propagating offshore. The dipole was probably originated by a rip current event. The slope of the beach was α ($\approx \tan \alpha$) ~ 0.011 rad (~0.6°) and the dipole was at about 250 m from the shoreline. The strength of the dipole was ~ 20 $m^2 s^{-1}$, its radius ~10 m and the water depth ~ 2 m. If we assume that these measurements describe a typical near-shore vortex, its Reynolds number, calculated with formula 4.4, is R_e~ 1 10^6. This implies that, if our results are correct, the vortex ring theory applies. For such a vortex, the theory (formula 2.30), predicts a speed in the along-shore direction of ~ 3 cm s^{-1}.

6.4 Directions for further research

- Perhaps the most pressing are experiments to test theoretical predictions at high Reynolds numbers and small α. The study of eddies in shallow water with a sloping bed is important in relation to the transfer of near-shore pollution and sediments, and further field observations are merited.

Appendix 2A

2A.1 Boundary layer velocities, volume flux into the bottom boundary layer and vertical velocity

The velocities in the bottom boundary later are described by the Ekman spiral (e.g. Pedlosky, 1987):

$$u = V(\rho)\left(1 - e^{\frac{-z}{\delta_E}} \cos\frac{z}{\delta_E}\right), \tag{2A.1}$$

$$v = V(\rho)e^{\frac{-z}{\delta_E}} \sin\frac{z}{\delta_E}, \tag{2A.2}$$

with

$$V(\rho) = \frac{\Gamma}{2\pi\rho} = \frac{\omega\rho}{2} = \Omega\rho, \tag{2A.3}$$

representing the two dimensional velocity field induced by the vortex at a distance $\rho = \sqrt{x^2 + y^2}$ from the centre of the vortex (a Cartesian x,y,z system with origin at the centre of the vortex and z pointing upwards is assumed here), and,

$$\delta_E = \left(\frac{2\nu}{\omega}\right)^{\frac{1}{2}}. \tag{2.A.4}$$

The bottom boundary layer volume flux in the radial direction per unit length is maximum at ρ=r and is expressed by:

$$T'_M = \int_0^\infty v(r,\zeta)d\zeta = V(\rho)\int_0^\infty e^{-\frac{\zeta}{\delta_E}} \sin\frac{\zeta}{\delta_E} d\zeta = V(r)\delta_E \int_0^\infty e^{-\lambda} \sin\lambda d\lambda = \frac{V(r)\delta_E}{2}, \quad (2A.5)$$

since,

$$\int_0^\infty e^{-\lambda} \sin\lambda d\lambda = \frac{1}{2}.$$

Here ζ is the vertical co-ordinate. The total volume flux inside the vortex bottom boundary layer is therefore:

$$T_M = T'_M \, 2\pi r = \pi r V(r)\delta_E \quad (2A.6)$$

For the conservation of volume, T_M must therefore be equal to the volume of fluid moving upwards that is entering the interior vortex from the bottom boundary layer, e.g.:

$$T_M = w\pi r^2, \quad (2A.7)$$

where w is the velocity of the water entering the inviscid interior of the vortex.

Assuming a constant gradient for w and with the condition of w=0 at the surface, we also have:

$$\frac{\partial w}{\partial z} = -\frac{T_M}{\pi h r^2} = -\frac{V(r)\delta_E}{hr}. \quad (2A.8)$$

2A.2 Vorticity equation.

The vorticity equation is (e.g. Tritton, 1988, p. 85):

$$\frac{\partial\vec{\omega}}{\partial t}+\vec{u}\cdot\nabla\vec{\omega}=\vec{\omega}\cdot\nabla\vec{u}+\nu\nabla^2\vec{\omega} \qquad (2A.9)$$

[with $\vec{u}=(u,v,w)$ and $\omega=\left(0,0,\omega_z\right)$]. If we impose the additional condition:

$\omega_z(x,y,z)$=const., (2A.10)

equation 2A.9 reduces to the first equation of system 2A.11 with the addition of formulae 2A.3, 2A.4 and 2A.8:

$$\begin{cases}\dfrac{\partial\omega}{\partial t}=\omega\dfrac{\partial w}{\partial z},\\ V(r)=\dfrac{\omega r}{2},\\ \delta_E=\left(\dfrac{2\nu}{\omega}\right)^{\frac{1}{2}},\\ \dfrac{\partial w}{\partial z}=-\dfrac{V(r)\delta_E}{hr}.\end{cases} \qquad (2A.11)$$

The system reduces to 2A.12 with the addition of the initial value of the spatially constant vorticity at t=0:

$$\begin{cases}\dfrac{\partial\omega}{\partial t}=-\dfrac{(2\nu)^{\frac{1}{2}}\omega^{\frac{3}{2}}r}{2hr},\\ \omega(0)=\omega_0.\end{cases} \qquad (2A.12)$$

Renaming the integral variables, $\xi=\omega$ and $\tau=t$, the solution for the vorticity is found by solving:

$$\int_{\omega_0}^{\omega}\frac{\delta\xi}{\xi^{\frac{3}{2}}}=-\frac{(2\nu)^{\frac{1}{2}}}{2h}\int_0^t\delta\tau, \qquad (2A.13)$$

which has solution given by:

$$2\xi^{-\frac{1}{2}}\Big|_{\omega_0}^{\omega} = \frac{(2\nu)^{\frac{1}{2}}}{2h}\tau\Big|_0^t, \tag{2A.14}$$

$$\frac{1}{\sqrt{\omega}} - \frac{1}{\sqrt{\omega_0}} = \frac{(2\nu)^{\frac{1}{2}}}{4h}t, \tag{2A.15}$$

$$\frac{1}{\sqrt{\omega}} = \frac{1}{\sqrt{\omega_0}} + \frac{(2\nu)^{\frac{1}{2}}}{4h}t = \frac{4h + (2\omega_0\nu)^{\frac{1}{2}}t}{4h\sqrt{\omega_0}} \tag{2A.16}$$

$$\omega = \omega_0\left(\frac{1}{1+\frac{(2\omega_0\nu)^{\frac{1}{2}}t}{4h}}\right)^2 = \omega_0\left(\frac{1}{1+\frac{t}{4T}}\right)^2 \tag{2A.17}$$

where T is:

$$T = \frac{h}{(2\omega_0\nu)^{\frac{1}{2}}}.$$

2A.3 Radius of the vortex

The decrease in vorticity (i.e. the "spin-down of the vortex) must be accompanied by an increase of the (supposed) circular area that contains the vorticity, i.e. of the radius of the vortex. The growth of the radius is a consequence of the volume flux directed from the bottom boundary layer into the inviscid interior of the vortex (note that fluid with zero angular momentum must be sucked from outside the vortex if the vortex has to spin-down without loosing energy).

The time evolution of the radius of the vortex can be calculated from the law of conservation of the volume Δ (first equation of the system 2A.18):

$$\begin{cases} \dfrac{\partial \Delta}{\partial t} = T_M, \\ \Delta = \pi r^2 h, \\ T_M = \pi r V(r) \delta_E, \\ V(r) = \dfrac{\omega}{2} r, \\ \delta_E = \left(\dfrac{2\nu}{\omega} \right)^{\frac{1}{2}}. \end{cases} \qquad (2A.18)$$

Here h is the water depth. Substituting we obtain, by adding the initial condition for the radius at t=0,

$$\begin{cases} \dfrac{\partial r}{\partial t} h = \dfrac{\omega}{4} r \left(\dfrac{2\nu}{\omega} \right)^{\frac{1}{2}}, \\ r(0) = r_0. \end{cases} \qquad (2A.19)$$

The first equation becomes:

$$\frac{\delta r}{r} = \frac{\omega^{\frac{1}{2}}}{4h} (2\nu)^{\frac{1}{2}} \delta t, \qquad (2A.20)$$

which, by using 2A.17 and renaming the integral variables, ρ=r and τ=t, leads to:

$$\int_{r_0}^{r} \frac{\delta\rho}{\rho} = \frac{\left(2\nu\omega_0\right)^{\frac{1}{2}}}{4h} \int_0^t \frac{1}{1+\frac{\tau}{4T}} \delta\tau . \qquad \text{(2A.21)}$$

Equation 2A.21 has solution given by:

$$\ln r\Big|_{r_0}^{r} = \int_1^{1+\frac{t}{4T}} \frac{\delta\kappa}{\kappa}, \qquad \text{(2A.22)}$$

i.e.:

$$\ln\frac{r}{r_0} = \ln\kappa\Big|_1^{1+\frac{t}{4T}}, \qquad \text{(2A.23)}$$

$$\ln\frac{r}{r_0} = \ln\left(1+\frac{t}{4T}\right), \qquad \text{(2A.24)}$$

$$r = r_0\left(1+\frac{t}{4T}\right). \qquad \text{(2A.25)}$$

Appendix 3A

3A.1 2-D model. Input-output structure

At the beginning of the execution the program reads from a file that contains the position, the intensity and the radius of the vortices, and from another one with the position of the particles of fluid that are tracked during the evolution of the system. To generate the input files we have written several programs designed to fill a rectangular or semi-circular portion of the fluid, of arbitrary size, with vortices and marked particles.

The programs that initiate the position of the vortices use a generator of uniformly distributed random numbers: the same algorithm is used to calculate random variations of strength, sign and radius of the core.

The programs that generate the position of the marked particles are designed to fill a region of fluid that is not necessarily coincident with the region in which the vortices are: at the beginning of the run the particles can either be evenly spaced or be arranged in a way to simulate the release of a tracer from a point source or a finite line source.

Characteristic time and length scales, number of iterations, time step, parameter f that controls the collision between vortices and length of the output are retrieved from a different file.

The output of the program consists of several files that contain, at a common and constant interval of time the following parameters:

- position and circulation of the vortices;
- position of the marked particles;

- dispersion of the vortices in the direction parallel (x) and normal (y) to the boundary, together with the total dispersion, with reference to the initial centre of mass of the vortices, (X_{cm},Y_{cm}); those parameters are indicated with $DX^2_{v,0}$, $DY^2_{v,0}$ and $D^2_{v,0}$, respectively, and are defined as the variances of the x and y co-ordinates of the vortices:

$$DX^2_{v,0} = \frac{\sum_{i=1}^{n}\left(x_i - X_{cm}\right)^2}{n},$$

$$DY^2_{v,0} = \frac{\sum_{i=1}^{n}\left(y_i - Y_{cm}\right)^2}{n}, \qquad (3.7\ a,b,c)$$

$$D^2_{v,0} = DX^2_{v,0} + DY^2_{v,0},$$

where,

$$X_{cm} = \frac{\sum_{i=1}^{n} x_i}{n},$$

$$Y_{cm} = \frac{\sum_{i=1}^{n} y_i}{n}. \qquad (3.8\ a,b)$$

Here n is the number of vortices, (x_i,y_i) are the co-ordinates of the centre of the vortices and X_{cm} and Y_{cm} are calculated at the instant t=0.

The same quantities calculated for the marked particles are indicated with the following symbols: $DX^2_{m,0}$, $DY^2_{m,0}$ and $D^2_{m,0}$: the definitions 3.7 and 3.8 given for the vortices apply when the word "vortex" is replaced with "particle".

The same quantities defined above are also calculated with respect to the instantaneous centre of mass. Those are indicated in the following

text with $DX^2_{v,t}$, $DY^2_{v,t}$, $D^2_{v,t}$ for the vortices and $DX^2_{m,t}$, $DY^2_{m,t}$ and $D^2_{m,t}$ for the marked particles.

- the time derivatives of the twelve dispersions defined above; those have the meaning of a parameter proportional to an eddy dispersion coefficient and are indicated by $kx_{v,0}$, $ky_{v,0}$, $k_{v,0}$ and so on, with obvious meaning of the symbols;
- the distance between each pair of vortices.

One file also contains a summary of the initial conditions of the run and, finally, the last file keeps record of collisions between vortices and absorption events at the boundary.

3A.2 Dispersion of a group of sign-like vortices far from the boundary

We start from the definition:

$$k_{v,0} = \frac{\partial D^2_{v,0}}{\partial t},$$

where $D^2_{v,0}$ is given by 3.7 c. Substituting we have:

$$k_{v,0} = \frac{\partial D^2_{v,0}}{\partial t} = \frac{\partial}{\partial t} \frac{\sum_{i=1}^{n} \left[\left(x_i(t) - X_{cm}(t_0) \right)^2 + \left(y_i(t) - Y_{cm}(t_0) \right)^2 \right]}{n},$$

$$k_{v,0} = \frac{\partial}{\partial t} \frac{\sum_{i=1}^{n} \left\{ \left[\left(x_i(t) - X_{cm}(t) \right) + \left(X_{cm}(t) - X_{cm}(t_0) \right) \right]^2 + \left[\left(y_i(t) - Y_{cm}(t) \right) + \left(Y_{cm}(t) - Y_{cm}(t_0) \right) \right]^2 \right\}}{n},$$

$$k_{v,0} = \frac{\partial}{\partial t}\left\{D^2 + \left(X_{cm}(t) - X_{cm}(t_0)\right)^2 + \left(Y_{cm}(t) - Y_{cm}(t_0)\right)^2 + \right.$$
$$\left. + \frac{1}{n}\sum_{i=1}^{n} 2\left(x_i(t) - X_{cm}(t)\right)\left(X_{cm}(t) - X_{cm}(t_0)\right) + \frac{1}{n}\sum_{i=1}^{n} 2\left(x_i(t) - X_{cm}(t)\right)\left(X_{cm}(t) - X_{cm}(t_0)\right)\right\}.$$

where:

$$X_{cm}(t) = \frac{\sum_{i=1}^{n} x_i(t)}{n},$$
$$Y_{cm}(t) = \frac{\sum_{i=1}^{n} y_i(t)}{n}.$$

The distance of the vortices from the boundary is such that D^2 is constant in time (see section 2.2). Therefore its time derivative is zero.

We also have:

$$\frac{\partial}{\partial t}\left[\frac{1}{n}\sum_{i=1}^{n} 2\left(x_i(t) - X_{cm}(t)\right)\left(X_{cm}(t) - X_{cm}(t_0)\right)\right] = 2\left[\sum_{i=1}^{n} v_{x,i}(t) - V_{x,cm}(t)\right]\left(X_{cm}(t) - X_{cm}(t_0)\right) +$$
$$+ V_{x,cm}(t)\sum_{i=1}^{n}\left(x_i(t) - X_{cm}(t)\right) = 0,$$

because:

$$\frac{1}{n}\sum_{i=1}^{n} v_{x,i}(t) - V_{x,cm}(t) = \frac{1}{n}\left[\sum_{i=1}^{n} v_{x,i}(t)\right] - V_{x,cm}(t) = V_{x,cm}(t) - V_{x,cm}(t) = 0,$$
$$V_{x,cm}(t)\frac{1}{n}\sum_{i=1}^{n}\left(x_i(t) - X_{cm}(t)\right) = V_{x,cm}(t)\left\{\left[\frac{1}{n}\sum_{i=1}^{n} x_i(t)\right] - X_{cm}(t)\right\} = X_{cm}(t) - X_{cm}(t) = 0,$$

where

$$\frac{\partial}{\partial t}\left[X_{cm}(t)\right] = V_{x,cm} = \frac{\partial}{\partial t}\left[\frac{\sum_{i=1}^{n} x_i(t)}{n}\right] = \frac{\sum_{i=1}^{n} \frac{\partial}{\partial t}\left[x_i(t)\right]}{n},$$

$$\frac{\partial}{\partial t}\left[Y_{cm}(t)\right] = V_{y,cm} = \frac{\partial}{\partial t}\left[\frac{\sum_{i=1}^{n} y_i(t)}{n}\right] = \frac{\sum_{i=1}^{n} \frac{\partial}{\partial t}\left[y_i(t)\right]}{n}.$$

Similarly we can show that:

$$\frac{\partial}{\partial t}\left[\frac{1}{n}\sum_{i=1}^{n} 2\left(y_i(t) - Y_{cm}(t)\right)\left(Y_{cm}(t) - Y_{cm}(t_0)\right)\right] = 2\left[\sum_{i=1}^{n} v_{y,i}(t) - V_{y,cm}(t)\right]\left(y_{cm}(t) - Y_{cm}(t_0)\right) +$$

$$+V_{y,cm}(t)\sum_{i=1}^{n}\left(y_i(t) - Y_{cm}(t)\right) = 0.$$

Therefore, the only contributions left are:

$$k_{v,0} = \frac{\partial}{\partial t}\left[\left(X_{cm}(t) - X_{cm}(t_0)\right)^2 + \left(Y_{cm}(t) - Y_{cm}(t_0)\right)^2\right] =$$

$$2\left(X_{cm}(t) - X_{cm}(t_0)\right)\frac{\partial}{\partial t}X_{cm}(t) + 2\left(Y_{cm}(t) - Y_{cm}(t_0)\right)\frac{\partial}{\partial t}Y_{cm}(t) =$$

$$2\left(X_{cm}(t) - X_{cm}(t_0)\right)V_{x,cm}(t),$$

since

$$\frac{\partial}{\partial t}Y_{cm}(t) = V_{y,cm} \approx 0.$$

3A.3 Plots of dispersion (see chapter 3, sections 3.5 and 3.6)

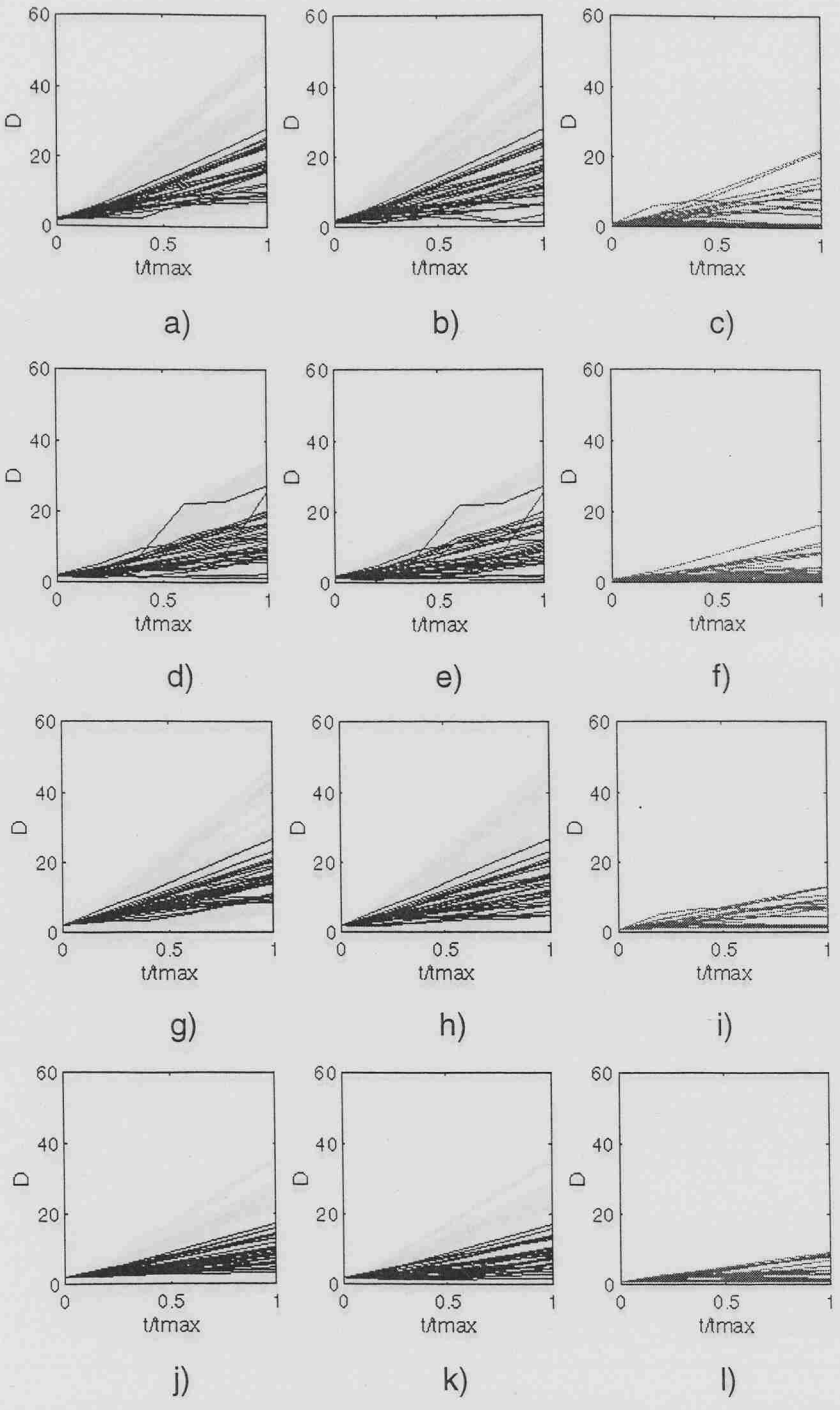

Fig 3.36: 2-D model. Dispersion of vortices and particles. Set 1: 5 vortices. Time series of: a) $D_{v,0}$; b) $DX_{v,0}$,; c) $DY_{v,0}$; d) $D_{v,t}$; e) $DX_{v,t}$,; f) $DY_{v,t}$; g) $D_{m,0}$; h) $DX_{m,0}$,; i) $DY_{m,0}$; j) $D_{m,t}$; k) $DX_{m,t}$,; l) $DY_{m,t}$. See appendix 3A.1 for a definition of the dispersion.

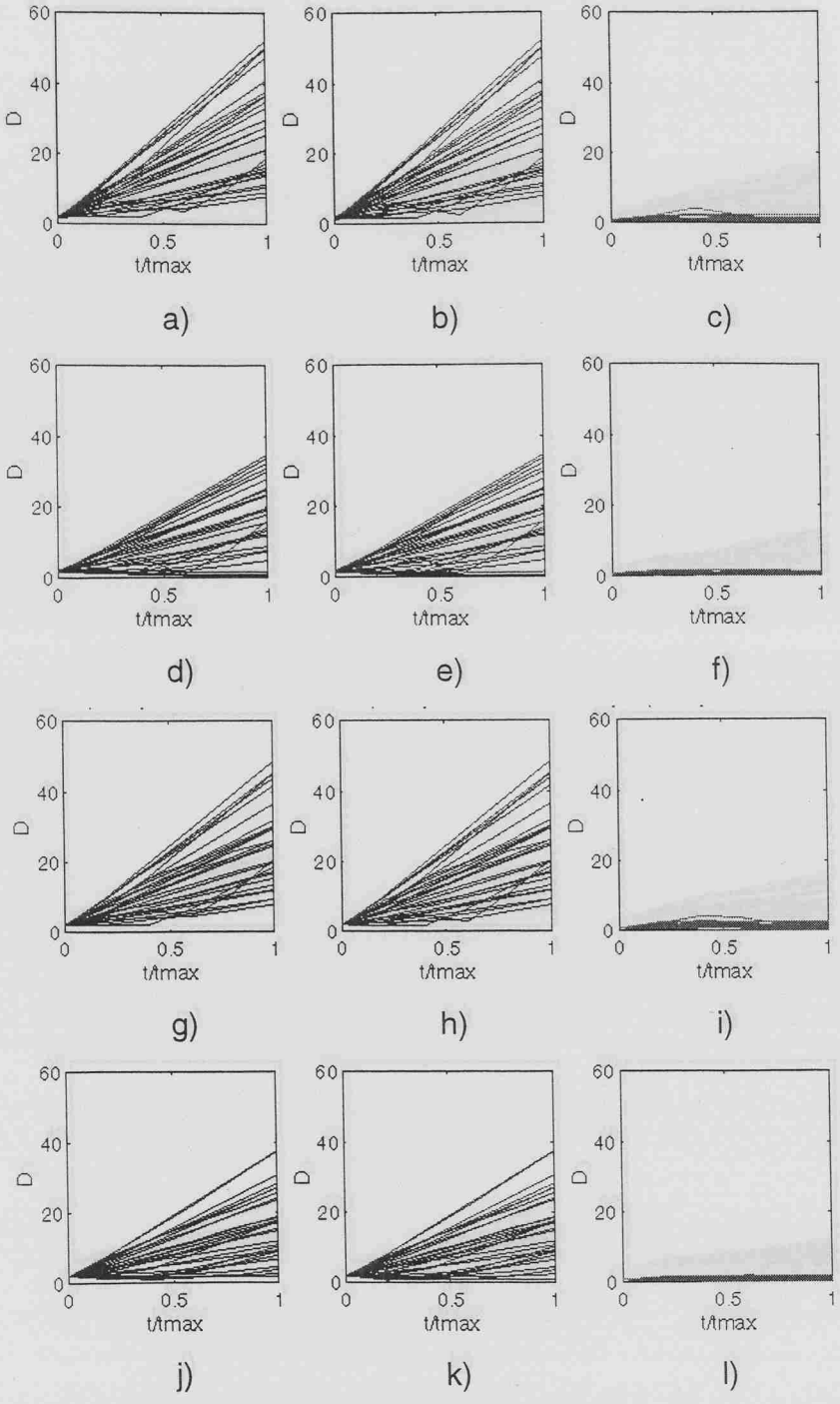

Fig 3.37: 3-D model. Dispersion of vortices and particles. Set 1: 5 vortices. Time series of: a) $D_{v,0}$; b) $DX_{v,0}$,; c) $DY_{v,0}$; d) $D_{v,t}$; e) $DX_{v,t}$,; f) $DY_{v,t}$; g) $D_{m,0}$; h) $DX_{m,0}$,; i) $DY_{m,0}$; j) $D_{m,t}$; k) $DX_{m,t}$,; l) $DY_{m,t}$. See appendix 3A.1 for a definition of the dispersion.

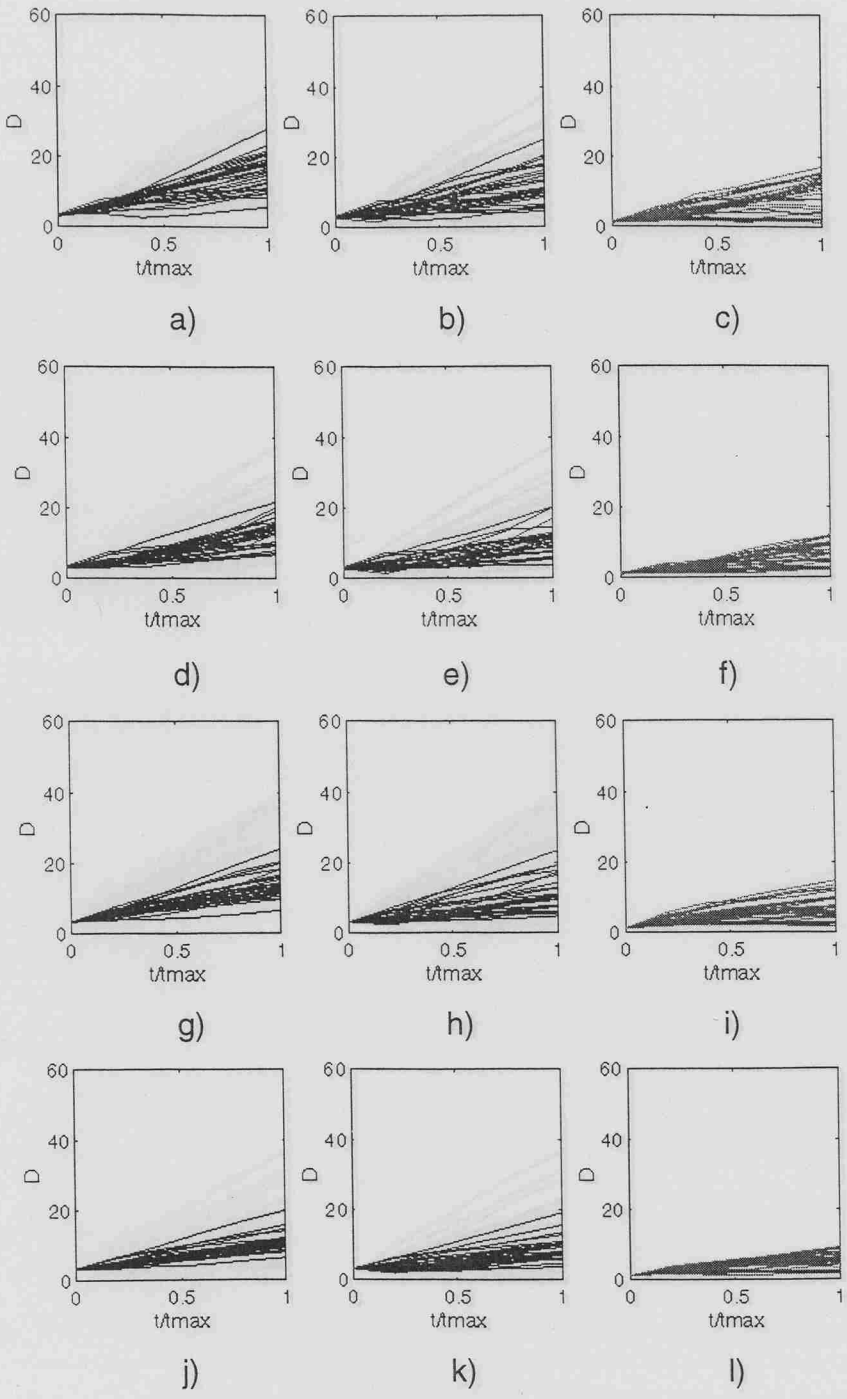

Fig 3.38: 2-D model. Dispersion of vortices and particles. Set 2: 10 vortices. Time series of: a) $D_{v,0}$; b) $DX_{v,0}$,; c) $DY_{v,0}$; d) $D_{v,t}$; e) $DX_{v,t}$,; f) $DY_{v,t}$; g) $D_{m,0}$; h) $DX_{m,0}$,; i) $DY_{m,0}$; j) $D_{m,t}$; k) $DX_{m,t}$,; l) $DY_{m,t}$. See appendix 3A.1 for a definition of the dispersion.

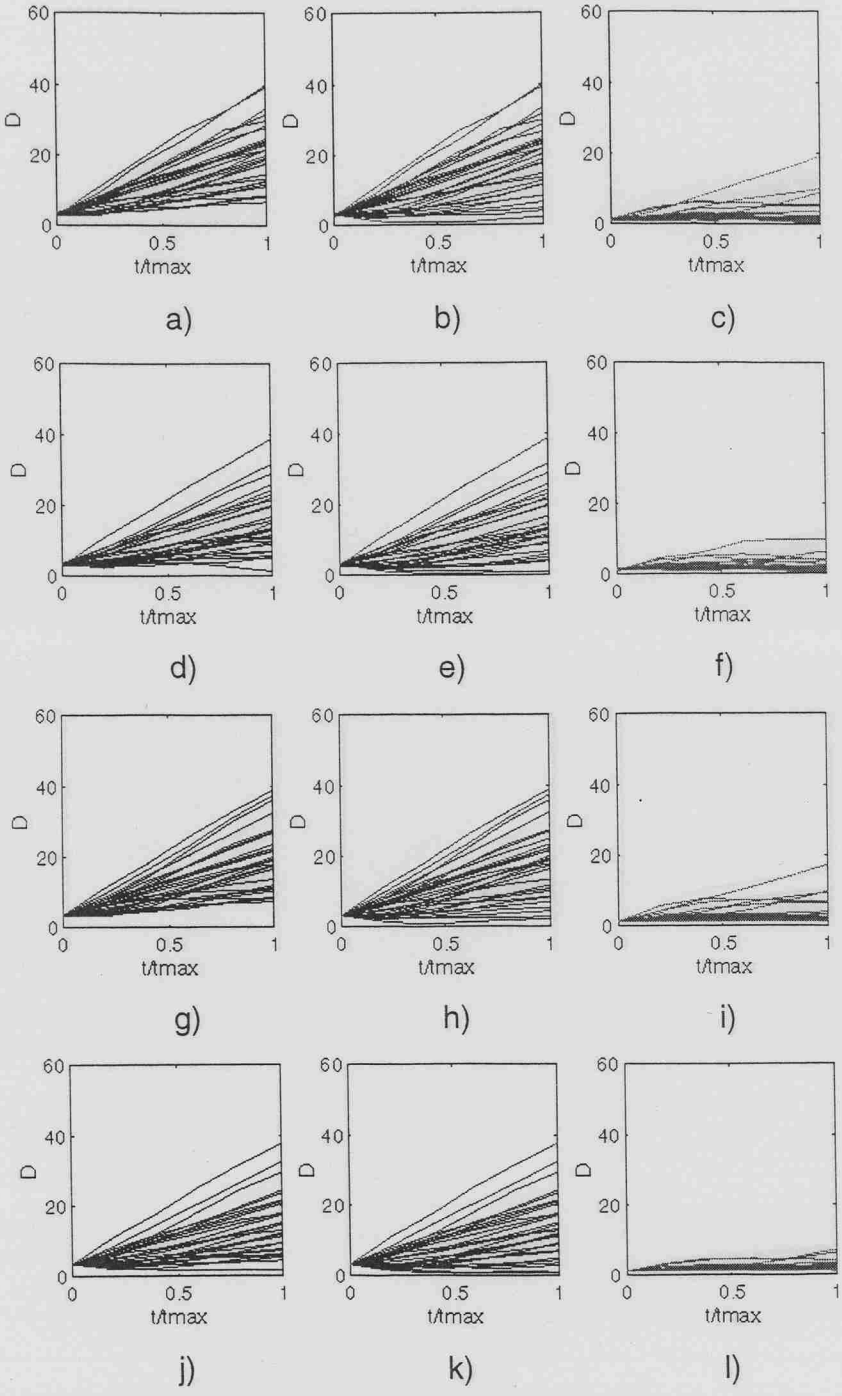

Fig 3.39: 3-D model. Dispersion of vortices and particles. Set 2: 10 vortices. Time series of: a) $D_{v,0}$; b) $DX_{v,0}$,; c) $DY_{v,0}$; d) $D_{v,t}$; e) $DX_{v,t}$,; f) $DY_{v,t}$; g) $D_{m,0}$; h) $DX_{m,0}$,; i) $DY_{m,0}$; j) $D_{m,t}$; k) $DX_{m,t}$,; l) $DY_{m,t}$. See appendix 3A.1 for a definition of the dispersion.

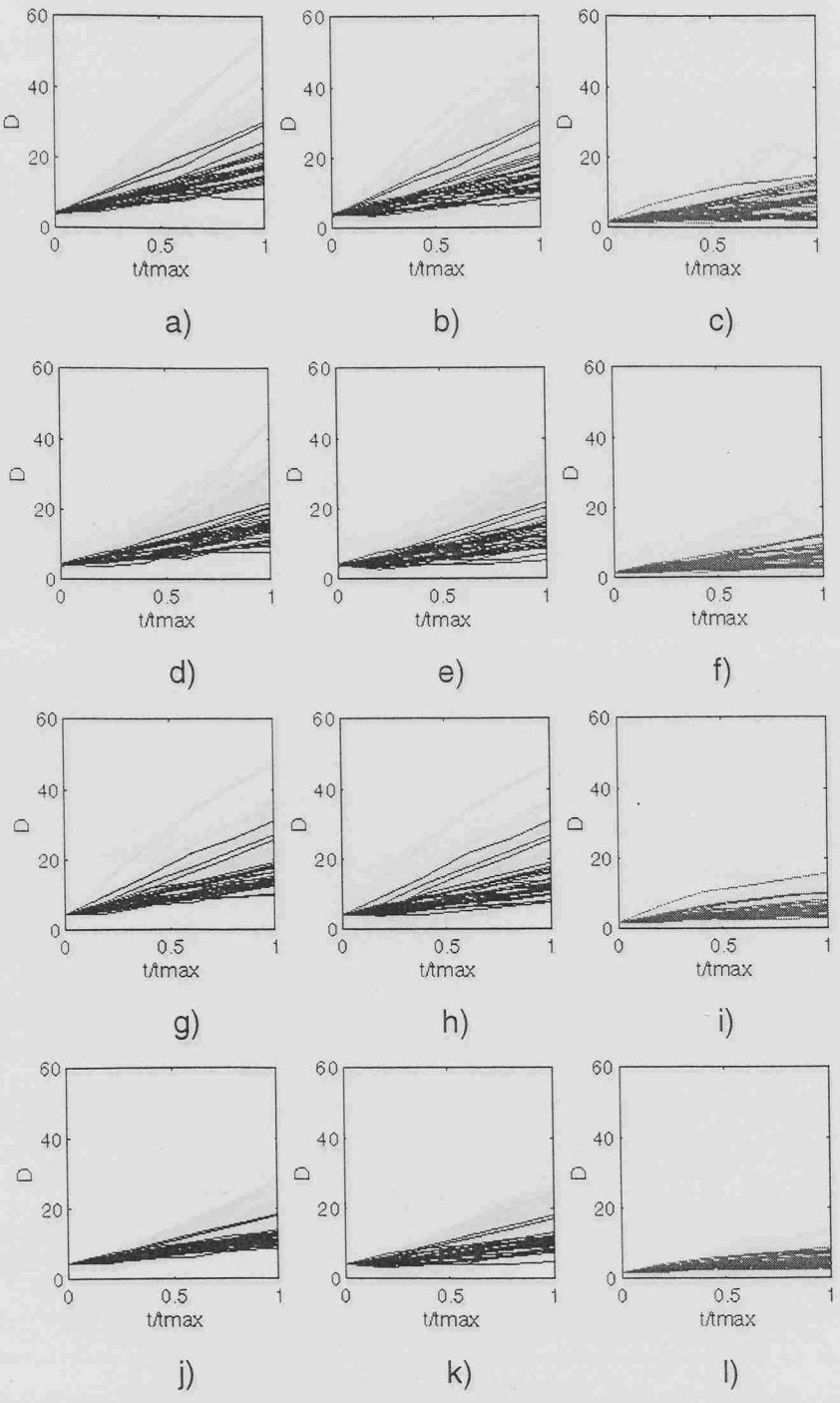

Fig 3.40: 2-D model. Dispersion of vortices and particles. Set 3: 15 vortices. Time series of: a) $D_{v,0}$; b) $DX_{v,0}$,; c) $DY_{v,0}$; d) $D_{v,t}$; e) $DX_{v,t}$,; f) $DY_{v,t}$; g) $D_{m,0}$; h) $DX_{m,0}$,; i) $DY_{m,0}$; j) $D_{m,t}$; k) $DX_{m,t}$,; l) $DY_{m,t}$. See appendix 3A.1 for a definition of the dispersion.

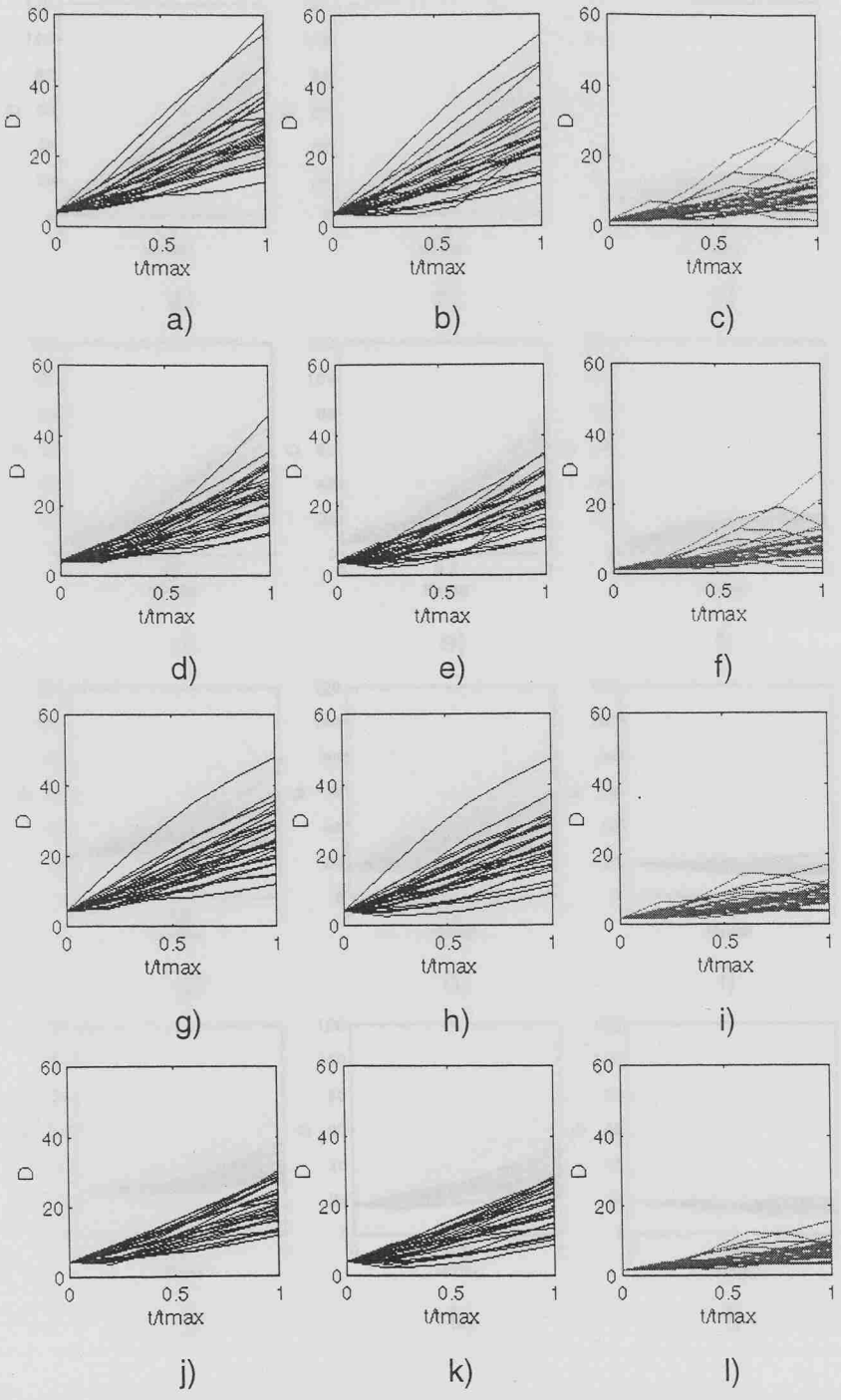

Fig 3.41: 3-D model. Dispersion of vortices and particles. Set 3: 15 vortices. Time series of: a) $D_{v,0}$; b) $DX_{v,0}$,; c) $DY_{v,0}$; d) $D_{v,t}$; e) $DX_{v,t}$,; f) $DY_{v,t}$; g) $D_{m,0}$; h) $DX_{m,0}$,; i) $DY_{m,0}$; j) $D_{m,t}$; k) $DX_{m,t}$,; l) $DY_{m,t}$. See appendix 3A.1 for a definition of the dispersion.

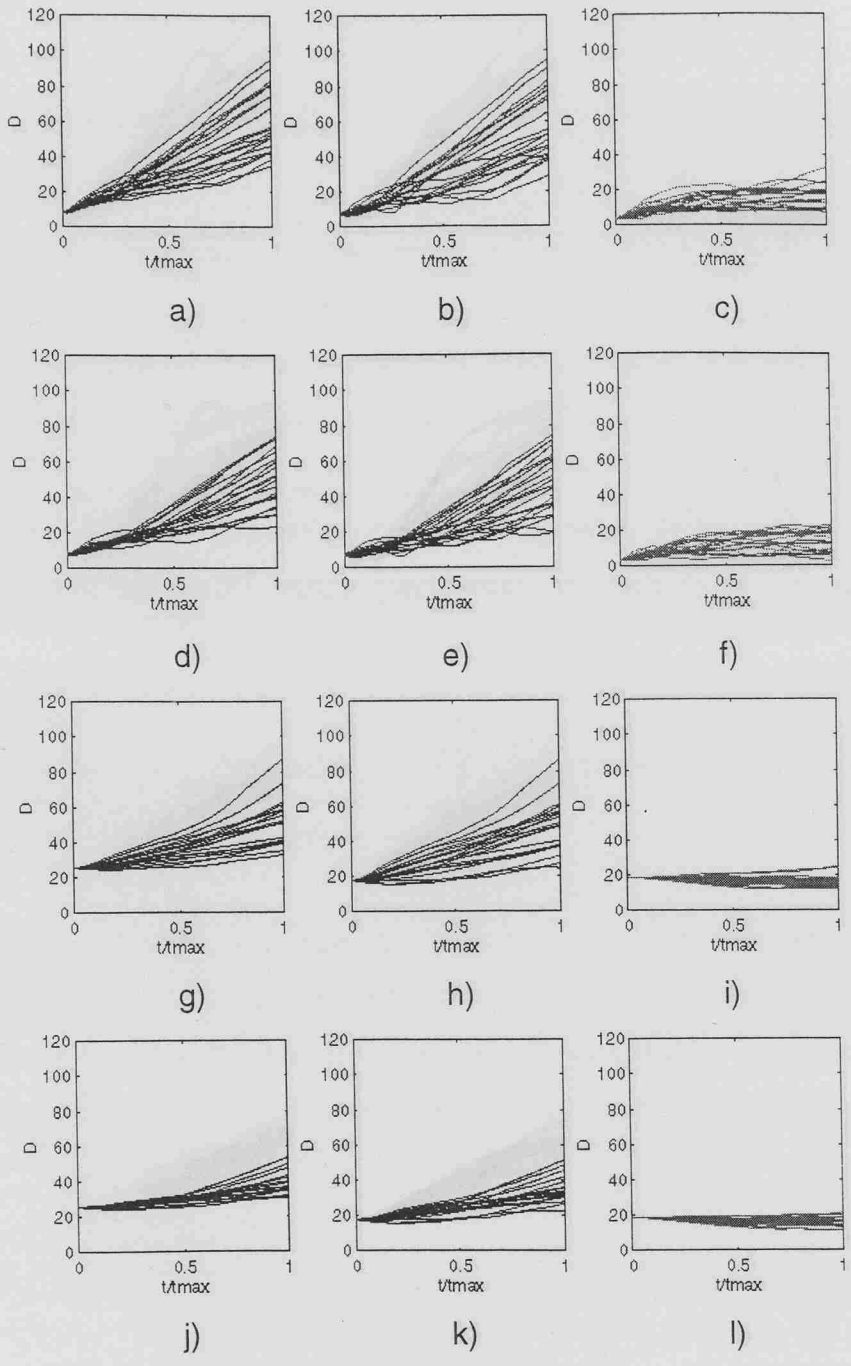

Fig 3.49: 2-D model. Dispersion of vortices and particles. 20 vortices. Time series of: a) $D_{v,0}$; b) $DX_{v,0,}$; c) $DY_{v,0}$; d) $D_{v,t}$; e) $DX_{v,t,}$; f) $DY_{v,t}$; g) $D_{m,0}$; h) $DX_{m,0,}$; i) $DY_{m,0}$; j) $D_{m,t}$; k) $DX_{m,t,}$; l) $DY_{m,t}$.

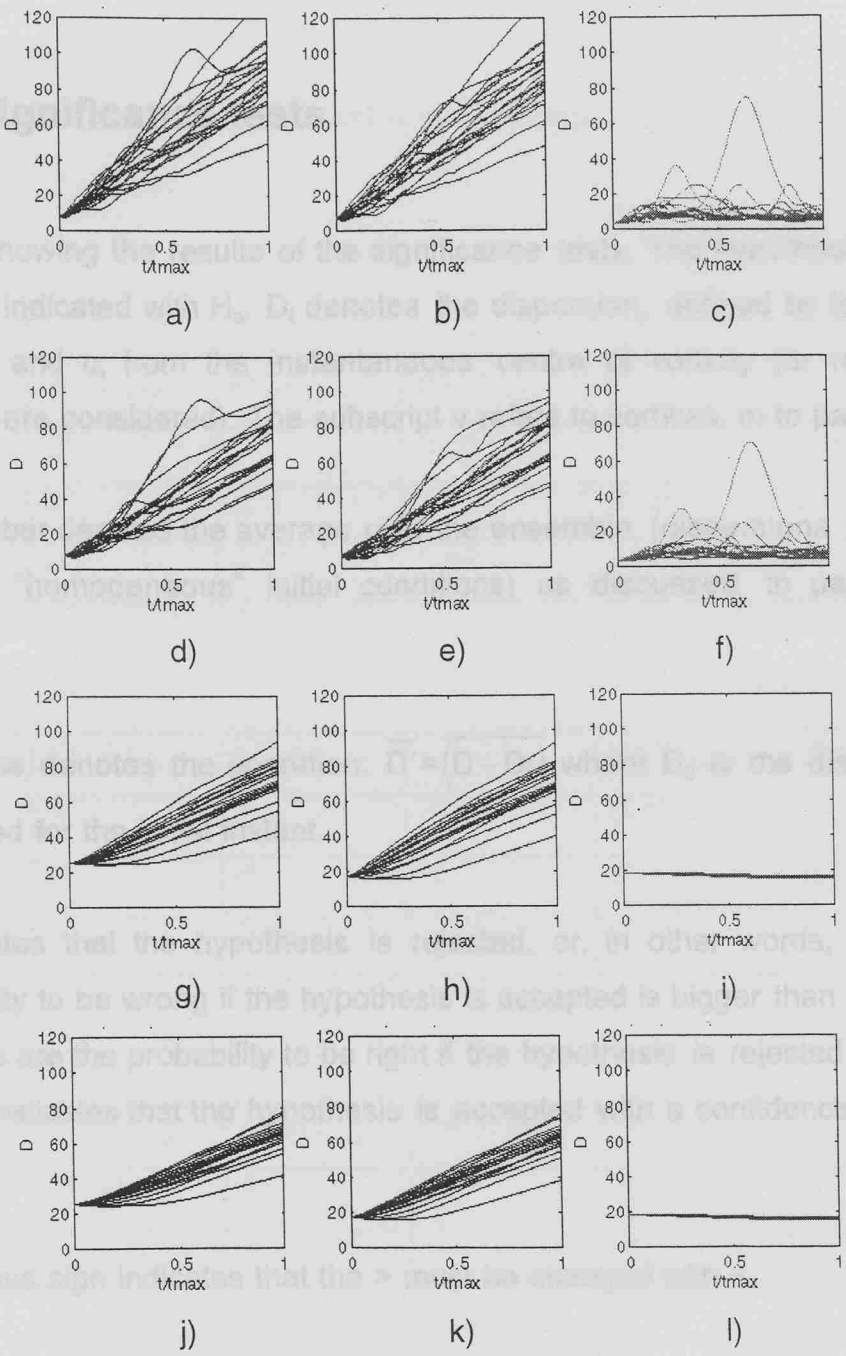

Fig 3.50: 3-D model. Dispersion of vortices and particles. 20 vortices. Time series of: a) $D_{v,0}$; b) $DX_{v,0}$,; c) $DY_{v,0}$; d) $D_{v,t}$; e) $DX_{v,t}$,; f) $DY_{v,t}$; g) $D_{m,0}$; h) $DX_{m,0}$,; i) $DY_{m,0}$; j) $D_{m,t}$; k) $DX_{m,t}$,; l) $DY_{m,t}$.

3A.4 Significance tests

Tables showing the results of the significance tests. The hypothesis to be tested is indicated with H_0. D_t denotes the dispersion, defined by formulae 3.7 a, b and c, from the instantaneous centre of vorticity (or mass, if particles are considered). The subscript v refers to vortices, m to particles.

The overbar denotes the average over the ensemble (dispersions from 30 run with "homogeneous" initial conditions) as discussed in paragraph 3.5.1.

The prime denotes the operation: $\overline{D'} = \overline{(D - D_0)}$ where D_0 is the dispersion calculated for the initial instant.

R indicates that the hypothesis is rejected, or, in other words, that the probability to be wrong if the hypothesis is accepted is bigger than 0.1. The numbers are the probability to be right if the hypothesis is rejected and the letter A indicates that the hypothesis is accepted with a confidence level of 0.002.

The minus sign indicates that the > must be changed with <.

3A.4.1 2-D model. Comparison between dispersions from the same model

H_0: $\overline{D'_{v,t}} > \overline{D'_{m,t}}$ Table 3A.3.1

# of vort.	t=0.2 t_{max}	t=0.4 t_{max}	t=0.6 t_{max}	t=0.8 t_{max}	t= t_{max}
5	-0.1	R	0.05	0.05	0.05
10	R	R	0.1	0.05	0.005
15	R	0.05	0.05	A	A

H_0: $\overline{DX'_{v,t}} > \overline{DX'_{m,t}}$ Table 3A.3.2

# of vort.	t=0.2 t_{max}	t=0.4 t_{max}	t=0.6 t_{max}	t=0.8 t_{max}	t= t_{max}
5	R	R	0.05	0.05	0.05
10	R	R	R	R	0.05
15	R	0.05	0.05	0.05	A

H_0: $\overline{DY'_{v,t}} > \overline{DY'_{m,t}}$ Table 3A.3.3

# of vort.	t=0.2 t_{max}	t=0.4 t_{max}	t=0.6 t_{max}	t=0.8 t_{max}	t= t_{max}
5	-0.005	R	R	R	R
10	R	R	R	0.05	0.05
15	R	R	0.005	A	A

H_0: $\overline{DX'_{v,t}} > \overline{DY'_{v,t}}$ Table 3A.3.4

# of vort.	t=0.2 t_{max}	t=0.4 t_{max}	t=0.6 t_{max}	t=0.8 t_{max}	t= t_{max}
5	R	A	A	A	A
10	-0.1	R	R	R	0.05
15	R	0.01	A	A	A

H_0: $\overline{DX'_{m,t}} > \overline{DY'_{m,t}}$ Table 3A.3.5

# of vort.	t=0.2 t_{max}	t=0.4 t_{max}	t=0.6 t_{max}	t=0.8 t_{max}	t= t_{max}
5	R	0.05	A	A	A
10	-0.01	R	R	0.1	0.05
15	-A	R	0.005	A	A

3A.4.2 3-D model. Comparison between dispersions from the same model

H_0: $\overline{D'_{v,t}} > \overline{D'_{m,t}}$ Table 3A.3.6

# of vort.	t=0.2 t_{max}	t=0.4 t_{max}	t=0.6 t_{max}	t=0.8 t_{max}	t= t_{max}
5	R	R	R	R	R
10	R	R	R	R	R
15	R	R	0.1	0.05	0.05

H_0: $\overline{DX'_{v,t}} > \overline{DX'_{m,t}}$ Table 3A.3.7

# of vort.	t=0.2 t_{max}	t=0.4 t_{max}	t=0.6 t_{max}	t=0.8 t_{max}	t= t_{max}
5	R	R	R	R	R
10	R	R	R	R	R
15	R	R	R	0.1	0.05

H_0: $\overline{DY'_{v,t}} > \overline{DY'_{m,t}}$ Table 3A.3.8

# of vort.	t=0.2 t_{max}	t=0.4 t_{max}	t=0.6 t_{max}	t=0.8 t_{max}	t= t_{max}
5	0.05	0.01	A	A	A
10	0.1	0.1	R	R	R
15	R	R	0.1	0.05	0.05

H_0: $\overline{DX'_{v,t}} > \overline{DY'_{v,t}}$ Table 3A.3.9

# of vort.	t=0.2 t_{max}	t=0.4 t_{max}	t=0.6 t_{max}	t=0.8 t_{max}	t= t_{max}
5	A	A	A	A	A
10	R	A	A	A	A
15	0.05	A	A	A	A

H_0: $\overline{DX'_{m,t}} > \overline{DY'_{m,t}}$ Table 3A.3.10

# of vort.	t=0.2 t_{max}	t=0.4 t_{max}	t=0.6 t_{max}	t=0.8 t_{max}	t= t_{max}
5	A	A	A	A	A
10	R	A	A	A	A
15	0.05	A	A	A	A

3A.4.3 Comparison between the two models

Set 1: 5 vortices, 676 particles. 2-D/3-D comparison Table 3A.3.11

H_0:	t=0.2 t_{max}	t=0.4 t_{max}	t=0.6 t_{max}	t=0.8 t_{max}	t= t_{max}
$\overline{D^{2D}_{v,t}} \neq \overline{D^{3D}_{v,t}}$	A	0.05	R	0.1	0.1
$\overline{DX^{2D}_{v,t}} \neq \overline{DX^{3D}_{v,t}}$	A	0.01	0.05	0.05	0.05
$\overline{DY^{2D}_{v,t}} \neq \overline{DY^{3D}_{v,t}}$	A	A	A	A	A
$\overline{D^{2D}_{m,t}} \neq \overline{D^{3D}_{m,t}}$	0.05	0.01	A	A	A
$\overline{DX^{2D}_{m,t}} \neq \overline{DX^{3D}_{m,t}}$	0.01	A	A	A	A
$\overline{DY^{2D}_{m,t}} \neq \overline{DY^{3D}_{m,t}}$	A	A	A	A	A

Set 2: 10 vortices, 676 particles. 2-D/3-D comparison Table 3A.3.12

H_0:	t=0.2 t_{max}	t=0.4 t_{max}	t=0.6 t_{max}	t=0.8 t_{max}	t= t_{max}
$\overline{D^{2D}_{v,t}} \neq \overline{D^{3D}_{v,t}}$	R	R	R	R	R
$\overline{DX^{2D}_{v,t}} \neq \overline{DX^{3D}_{v,t}}$	R	0.1	0.05	0.05	0.05
$\overline{DY^{2D}_{v,t}} \neq \overline{DY^{3D}_{v,t}}$	0.1	A	A	A	A
$\overline{D^{2D}_{m,t}} \neq \overline{D^{3D}_{m,t}}$	R	R	0.1	0.1	0.05
$\overline{DX^{2D}_{m,t}} \neq \overline{DX^{3D}_{m,t}}$	R	0.1	0.05	0.05	0.01
$\overline{DY^{2D}_{m,t}} \neq \overline{DY^{3D}_{m,t}}$	A	A	A	A	A

Set 3: 15 vortices, 676 particles. 2-D/3-D comparison Table 3A.3.13

H_0:	t=0.2 t_{max}	t=0.4 t_{max}	t=0.6 t_{max}	t=0.8 t_{max}	t= t_{max}
$\overline{D^{2D}_{v,t}} \neq \overline{D^{3D}_{v,t}}$	0.05	A	A	A	A
$\overline{DX^{2D}_{v,t}} \neq \overline{DX^{3D}_{v,t}}$	0.05	A	A	A	A
$\overline{DY^{2D}_{v,t}} \neq \overline{DY^{3D}_{v,t}}$	R	R	0.05	0.01	0.01
$\overline{D^{2D}_{m,t}} \neq \overline{D^{3D}_{m,t}}$	0.005	A	A	A	A
$\overline{DX^{2D}_{m,t}} \neq \overline{DX^{3D}_{m,t}}$	0.01	A	A	A	A
$\overline{DY^{2D}_{m,t}} \neq \overline{DY^{3D}_{m,t}}$	R	R	0.05	A	A

3A.4.3 Comparison between the two models: plots (see chapter 3, sections 3.5 and 3.6)

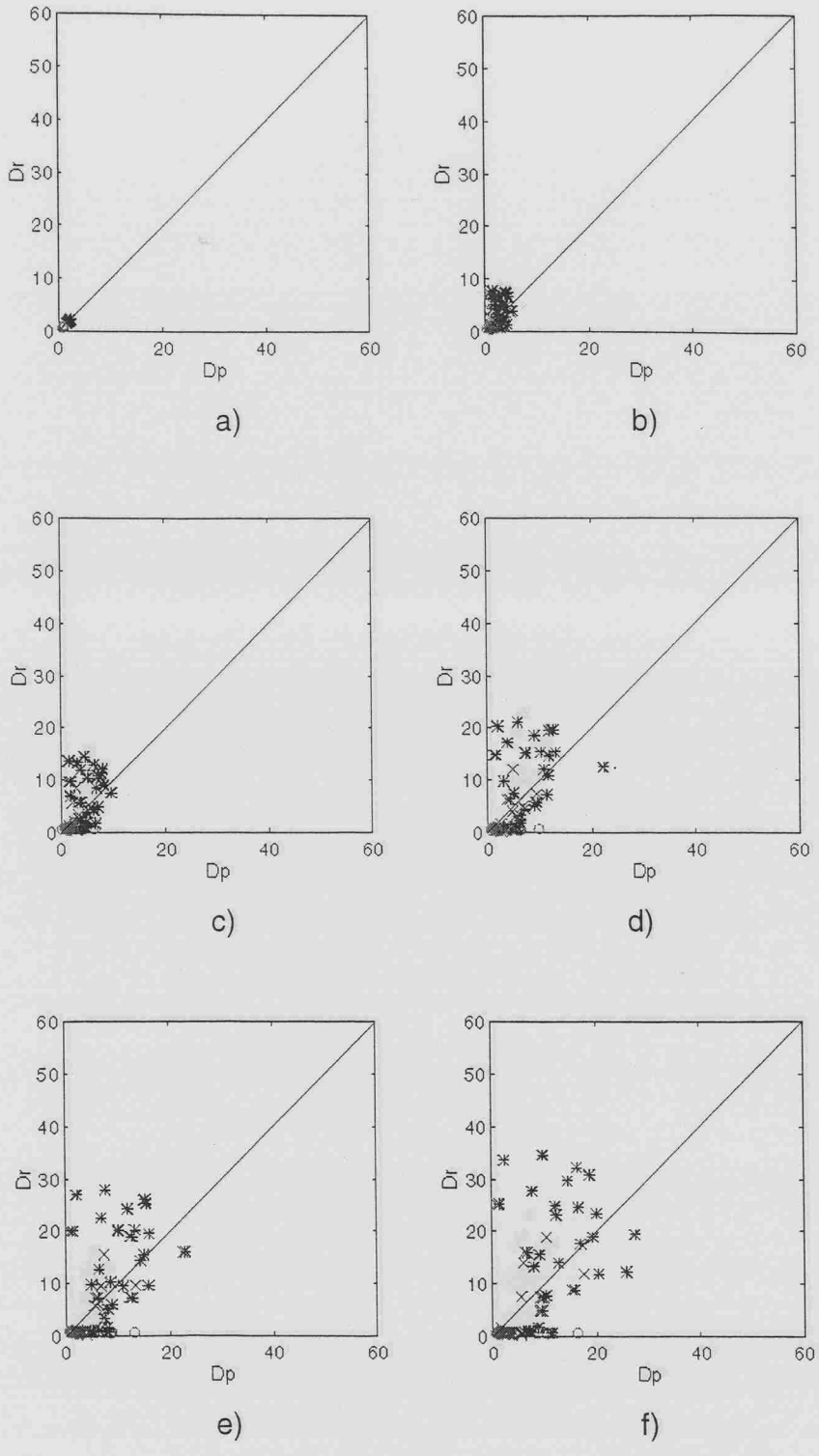

Fig 3.42: Set 1: 5 vortices. Comparison between the two models. Dispersion of vortices. Time evolution of the scatter-plot of $D_{v,t}$ (*), $DX_{v,t}$ (x) and $DY_{v,t}$ (o) from 2-D model (Dp) versus $D_{v,t}$, $DX_{v,t}$ and $DY_{v,t}$, respectively, from 3-D model (Dr). a) t=0; b) $t=0.2 \cdot t_{max}$; c) $t=0.4 \cdot t_{max}$; d) $t=0.6 \cdot t_{max}$; e) $t=0.8 \cdot t_{max}$; f) $t=t_{max}$.

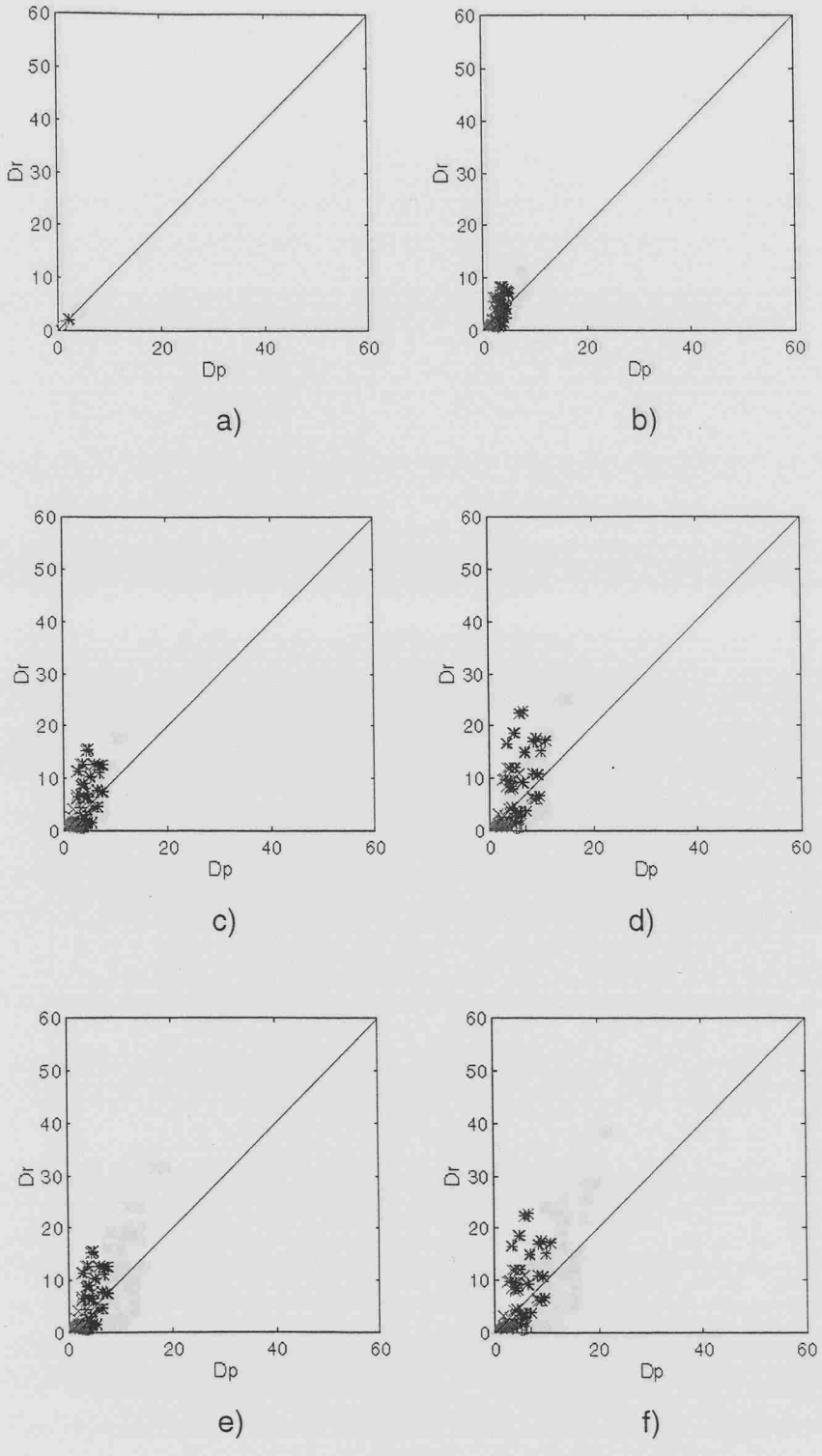

Fig 3.43: Set 1: 5 vortices. Comparison between the two models. Dispersion of particlesTime evolution of the scatter-plot of $D_{m,t}$ (*), $DX_{m,t}$ (x) and $DY_{m,t}$ (o) from 2-D model (Dp) versus $D_{m,t}$, $DX_{m,t}$ and $DY_{m,t}$, respectively, from 3-D model (Dr). a) t=0; b) $t=0.2 \cdot t_{max}$; c) $t=0.4 \cdot t_{max}$; d) $t=0.6 \cdot t_{max}$; e) $t=0.8 \cdot t_{max}$; f) $t=t_{max}$

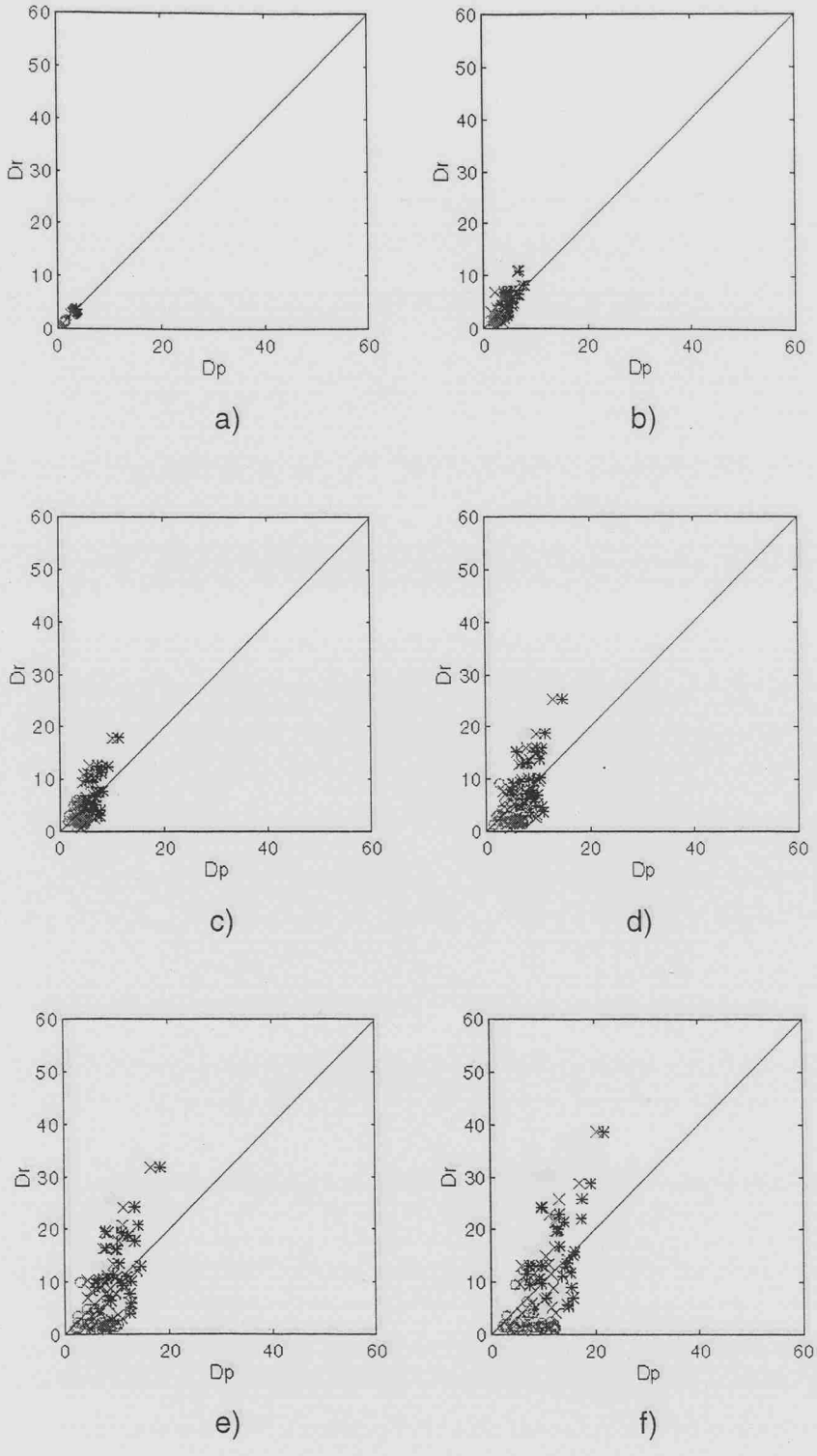

Fig 3.44: Set 2: 10 vortices. Comparison between the two models. Dispersion of vortices. Time evolution of the scatter-plot $D_{v,t}$ (*), $DX_{v,t}$ (x) and $DY_{v,t}$ (o) from 2-D model (Dp) versus $D_{v,t}$, $DX_{v,t}$ and $DY_{v,t}$, respectively, from 3-D model (Dr). a) t=0; b) $t=0.2 \cdot t_{max}$; c) $t=0.4 \cdot t_{max}$; d) $t=0.6 \cdot t_{max}$; e) $t=0.8 \cdot t_{max}$; f) $t=t_{max}$

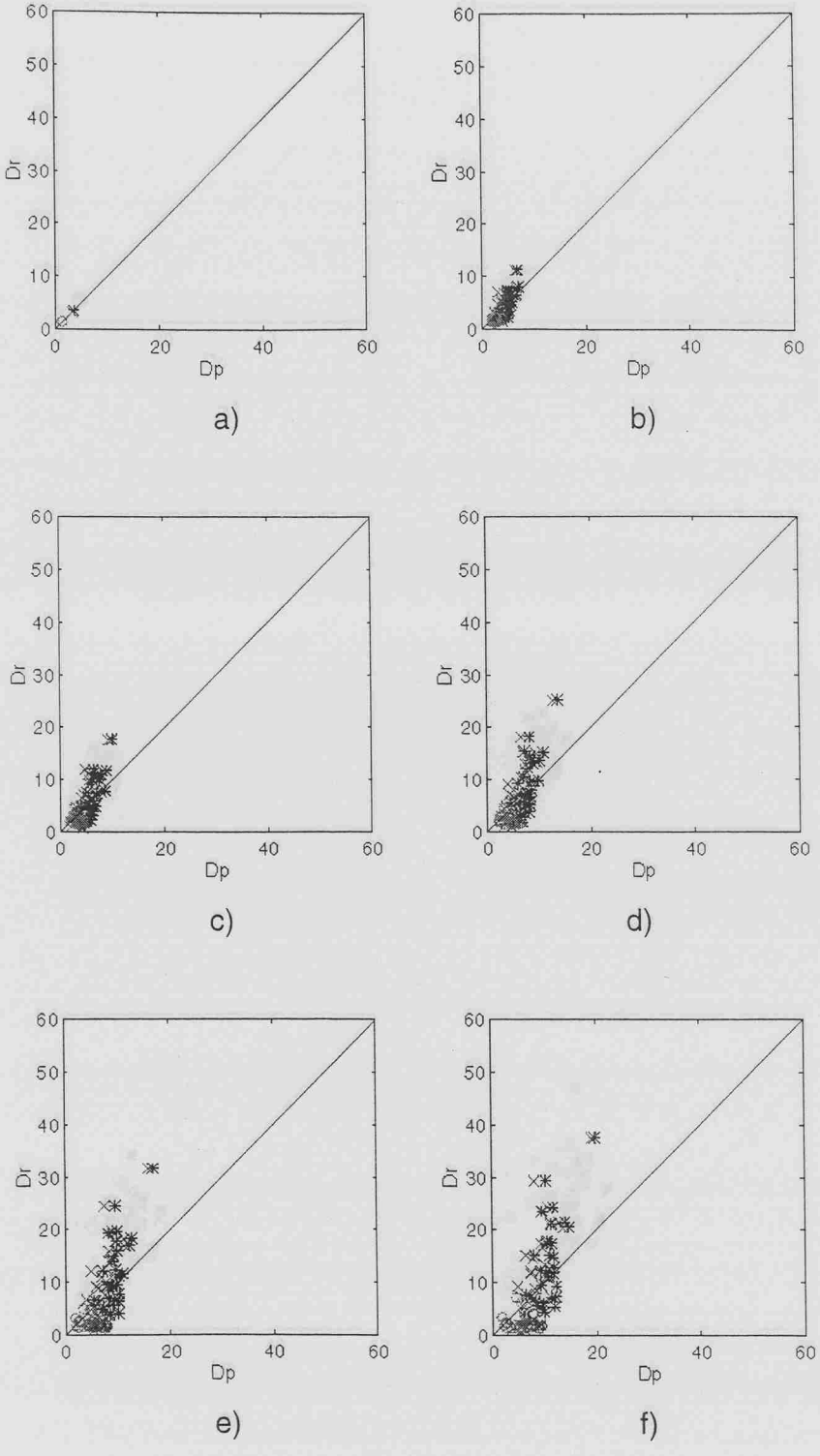

Fig 3.45: Set 2: 10 vortices. Comparison between the two models. Dispersion of particles. Time evolution of the scatter-plot of $D_{m,t}$ (*), $DX_{m,t}$ (x) and $DY_{m,t}$ (o) from 2-D model (Dp) versus $D_{m,t}$, $DX_{m,t}$ and $DY_{m,t}$, respectively, from 3-D model (Dr). a) t=0; b) $t=0.2 \cdot t_{max}$; c) $t=0.4 \cdot t_{max}$; d) $t=0.6 \cdot t_{max}$; e) $t=0.8 \cdot t_{max}$; f) $t=t_{max}$

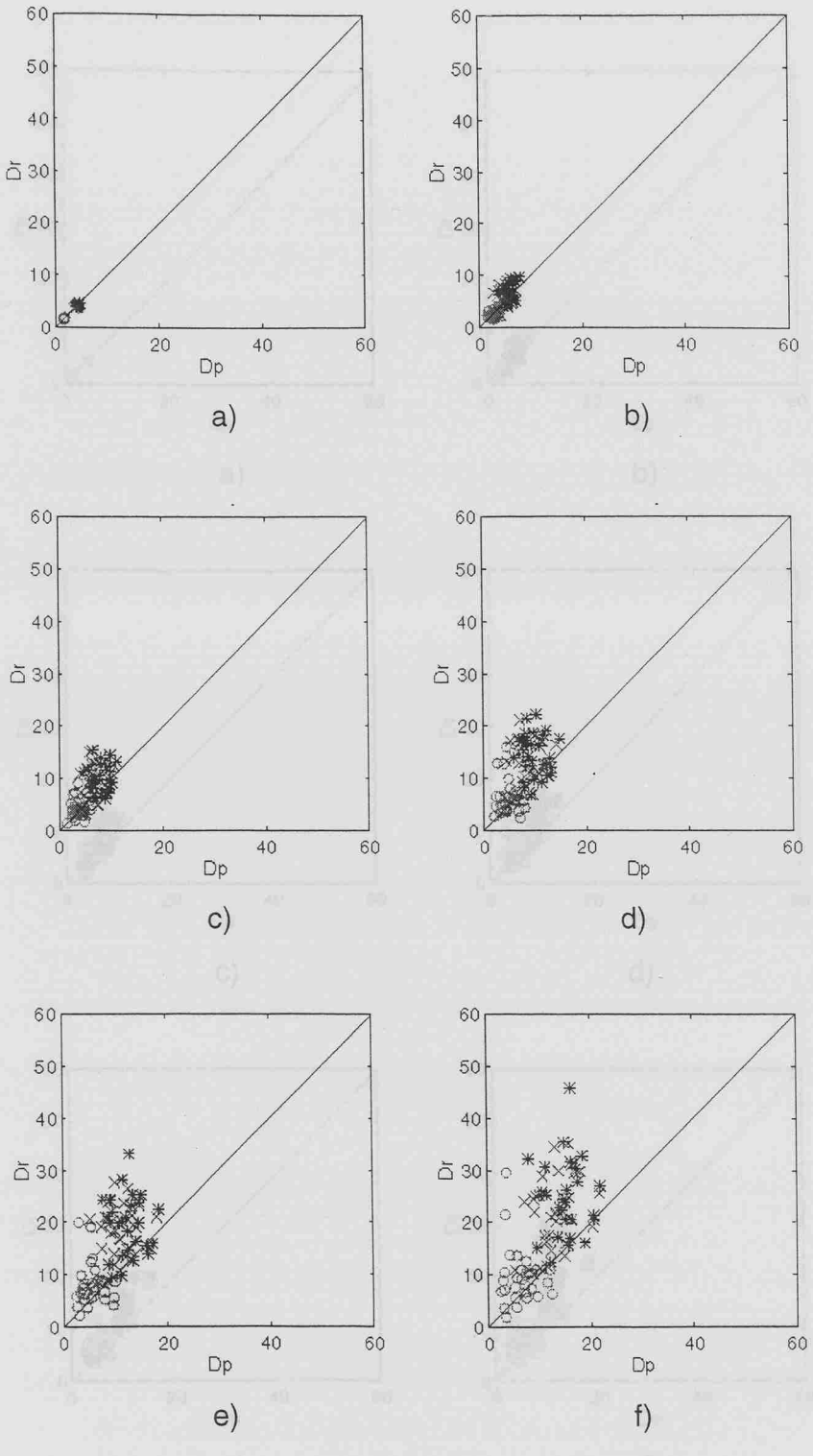

Fig 3.46: Set 3: 15 vortices. Comparison between the two models. Dispersion of vortices. Time evolution of the scatter-plot of $D_{v,t}$ (*), $DX_{v,t}$ (x) and $DY_{v,t}$ (o) from 2-D model (Dp) versus $D_{v,t}$, $DX_{v,t}$ and $DY_{v,t}$, respectively, from 3-D model (Dr). a) t=0; b) $t=0.2 \cdot t_{max}$; c) $t=0.4 \cdot t_{max}$; d) $t=0.6 \cdot t_{max}$; e) $t=0.8 \cdot t_{max}$; f) $t=t_{max}$

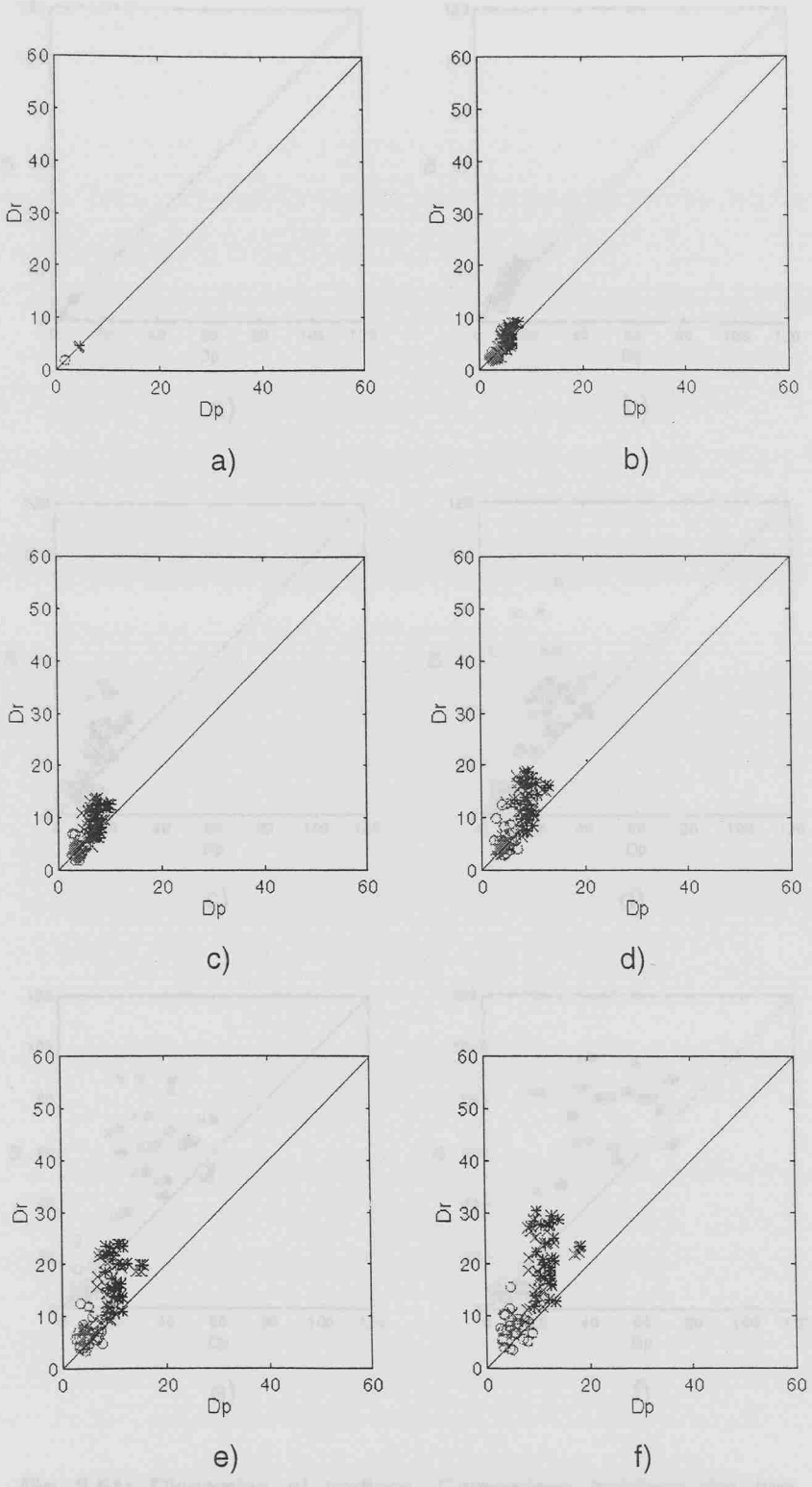

Fig 3.47: Set 3: 15 vortices. Comparison between the two models. Dispersion of particles. Time evolution of the scatter-plot of $D_{m,t}$ (*), $DX_{m,t}$ (x) and $DY_{m,t}$ (o) from 2-D model (Dp) versus $D_{m,t}$, $DX_{m,t}$ and $DY_{m,t}$, respectively, from 3-D model (Dr). a) t=0; b) $t=0.2 \cdot t_{max}$; c) $t=0.4 \cdot t_{max}$; d) $t=0.6 \cdot t_{max}$; e) $t=0.8 \cdot t_{max}$; f) $t=t_{max}$

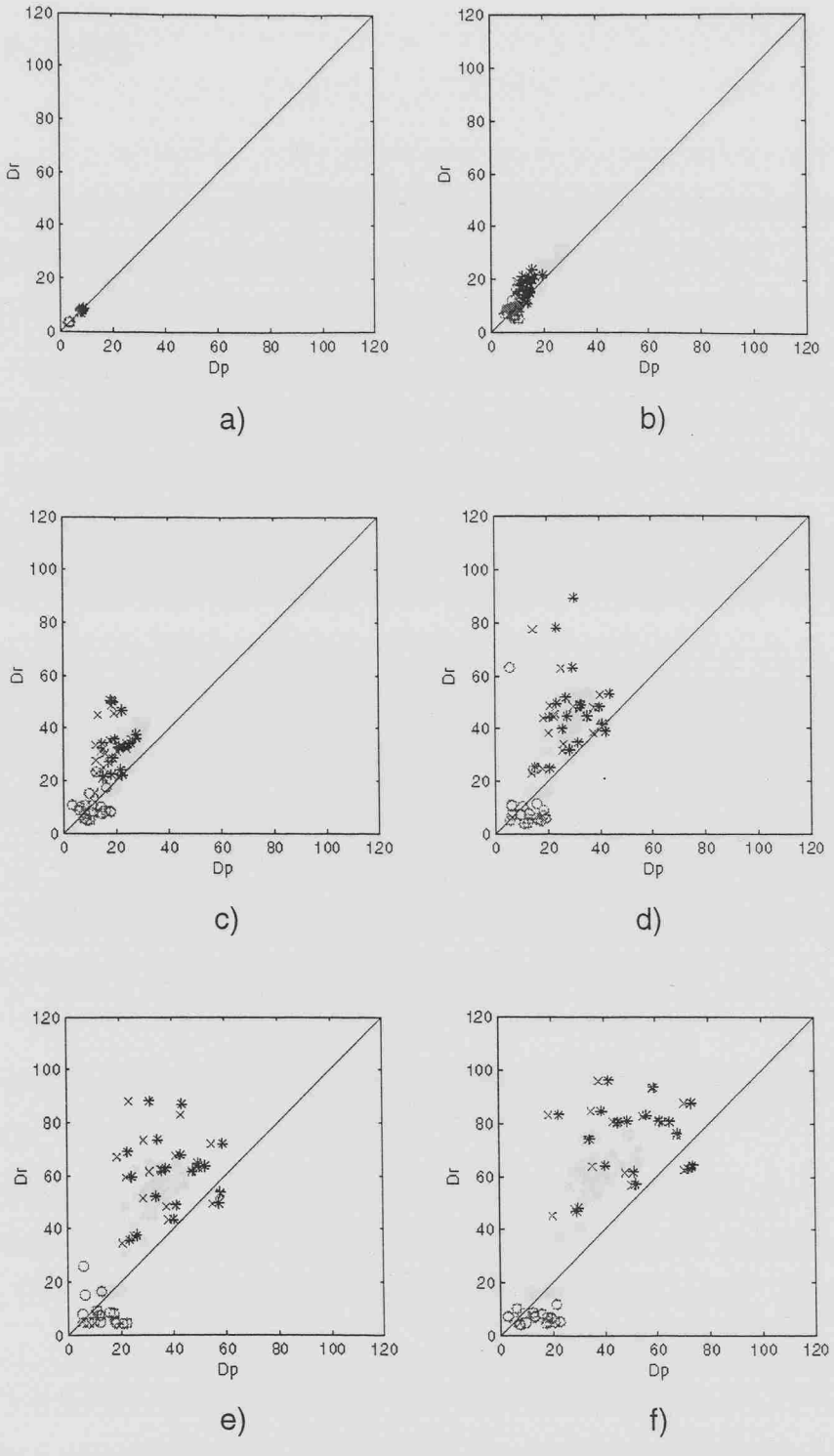

Fig 3.51: Dispersion of vortices. Comparison between the two models. Time evolution of the scatter-plot of $D_{v,t}$ (*), $DX_{v,t}$ (x) and $DY_{v,t}$ (o) from 2-D model (Dp) versus $D_{v,t}$, $DX_{v,t}$ and $DY_{v,t}$, respectively, from 3-D model (Dr). a) t=0; b) $t=0.2 \cdot t_{max}$; c) $t=0.4 \cdot t_{max}$; d) $t=0.6 \cdot t_{max}$; e) $t=0.8 \cdot t_{max}$; f) $t=t_{max}$

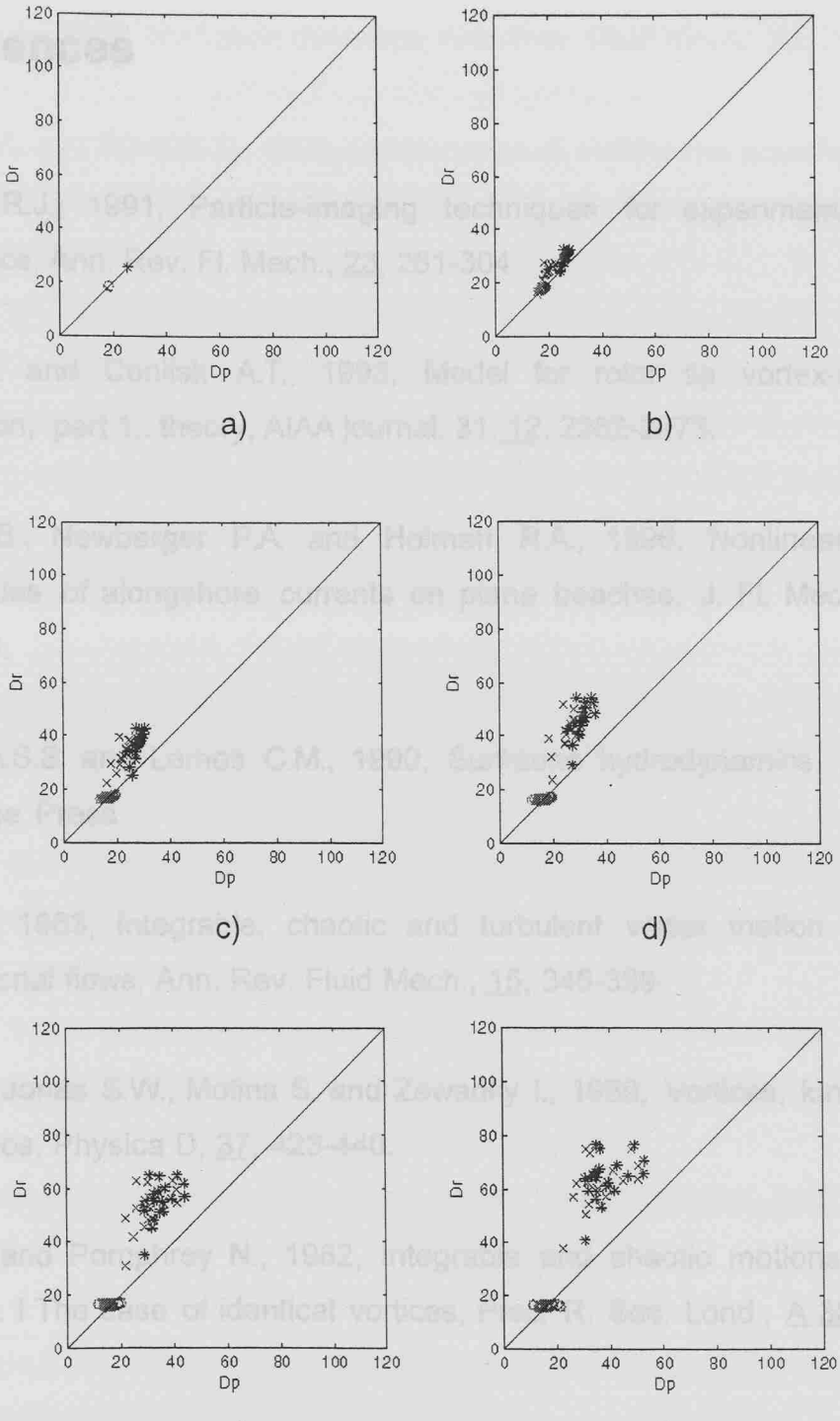

Fig 3.52: Dispersion of particles. Comparison between the two models.Time evolution of the scatter-plot of $D_{m,t}$ (*), $DX_{m,t}$ (x) and $DY_{m,t}$ (o) from 2-D model (Dp) versus $D_{m,t}$, $DX_{m,t}$ and $DY_{m,t}$, respectively, from 3-D model (Dr). a) t=0; b) $t=0.2 \cdot t_{max}$; c) $t=0.4 \cdot t_{max}$; d) $t=0.6 \cdot t_{max}$; e) $t=0.8 \cdot t_{max}$; f) $t=t_{max}$

References

Adrian, R.J., 1991, Particle-imaging techniques for experimental fluid mechanics, Ann. Rev. Fl. Mech., 23, 261-304.

Affes H. and Conlisk A.T., 1993, Model for rotor tip vortex-airframe interaction, part 1,: theory, AIAA journal, 31, 12, 2262-2273.

Allen J.S., Newberger P.A. and Holman R.A., 1996, Nonlinear shear instabilities of alongshore currents on plane beaches, J. Fl. Mech., 310, 181-213.

Arcilla A.S.S. and Lemos C.M., 1990, Surf-zone hydrodynamics, 310 pp, Pineridge Press.

Aref H., 1983, Integrable, chaotic and turbulent vortex motion in two-dimensional flows, Ann. Rev. Fluid Mech., 15, 345-389.

Aref H., Jones S.W., Mofina S. and Zawadky I., 1989, Vortices, kinematics and chaos, Physica D, 37, 423-440.

Aref H. and Pomphrey N., 1982, Integrable and chaotic motions of four vortices. I The case of identical vortices, Proc. R. Soc. Lond., A 380, 359-387.

Barker S.J. and Crow S.C., 1977, The motion of two-dimensional vortex pairs in a ground effect, J. Fluid Mech., 82, 659-671.

Batchelor G.K., 1967, An introduction to fluid dynamics, Cambridge Univ. Press, 615 pp.

Battjes J.A., 1988, Surf-zone dynamics, Ann. Rev. Fluid Mech., 20, 257 -293.

Bidlot J.R. and Stern M.E., 1994, Maintenance of continental boundary-layer shear through counter-gradient vorticity flux in a barotropic model, J. Fluid Mech., 271, 55-85.

Boffetta G., Celani A. and Franzese P., 1996, Trapping of passive tracers in a point vortex system, J. Phys. A: Math. Gen., 29,3749-3759.

Bowen A.J., 1969, Rip currents. 1. Theoretical investigations, J. Geophys. Res., 74,23,5467-5490.

Bowen A.J. and Holman R.A., 1989, Shear instabilities of the mean longshore current. 1. Theory, J. Geophys. Res., 94, C12, 18023-18030.

Chapra S.C. and Canale R.C., 1988, Metodi numerici per l'ingegneria, McGraw-Hill, 658 pp.

Couder Y. and Basdevant C., 1986, Experimental and numerical study of vortex couples in two-dimensional flows, J. Fluid Mech., 173,225-251.

Crow S.C., 1970, Stability theory for a pair of trailing vortices, AIAA Jour., 8, 12, 2172-2179.

Dalrymple R.A., 1975, A mechanism for rip current generation on an open coast, J. Geophys. Res., 80,24,3485-3487.

Dalziel S., 1993, Digimage, image processing for fluid dynamics. Installation guide, system overview & particle tracking, Cambridge Environmental Research Consultants ltd.

Dette H.H., Peters K. and Spingat F., 1996, About rip currents at a mesotidal coast, pp. 477-478 in, Coastal Dynamics 95, (ed. W.R.Dally &R.B.Zeidler), New York, American Society of Civil Engineers.

Dhanak, M.R., 1981, Interaction between a vortex filament and an approaching rigid sphere, J. Fluid Mech., 110, 129-147.

Dodd N., Oltman-Shay J. and Thornton E.B., 1992, Shear instability in the longshore current: a comparison of observation and theory, J. Phys. Oc., 22, 62-80.

Doligaski T.L., Smith C.R. and Walker J.D.A., 1994, Vortex interactions with walls, Ann. Rev. Fluid Mech., 26, 573-616.

Donnelly R.J., 1993, Quantized vortices and turbulence in Helium II, Ann. Rev. Fluid. Mech., 25, 325-371.

Fedorov K.N., Ginsburg A.I. and Kostianoy A.G., 1989, Modelling of "mushroom-like" currents (vortex dipoles) in a laboratory tank with rotating homogeneous and stratrified fluids, pp. 15-23 in, Mesoscale/Synoptic Coherent Structures in Geophysical Turbulence, ed. Nihoul J.C.J, Jamart B.M., Amsterdam.

Feynman R.P., Leighton R.B. and Sands M., 1963, The Feynman lectures on physics, mainly electromagnetism and matter, Vol. II-Part I, Addison-Wesley Pub. co.

Fincham A.M., Maxworthy T. and Spedding G.R., 1996, Energy dissipation and vortex structure in freely decaying stratified grid turbulence, Dyn. Atm. Oceans, 23,155-169.

Fraenkel L.E., 1972, Examples of steady vortex rings of small cross-section in an ideal fluid, J, Fluid Mech., 51,119-135.

Frish U., 1995, Turbulence. The legacy of A.N. Kolmogorov, Cambridge Univ. Press, 296 pp.

Garten J.F., Arendt S., Fritts D.C. and Werne J., 1998, Dynamics of counter-rotating vortex pairs in stratified and sheared environments, J. Fl. Mech., 361, 189-236.

Gill, A.E., 1982, Atmosphere-ocean Dynamics, Academic Press, 662 pp.

Greenspan H.P., Howard L.N., 1963, On a time dependent motion of a rotating fluid, J. Fl. Mech., 17, 385-404.

Greenspan, H.P., 1969, The theory of rotating fluids, Cambridge University Press, 328 pp.

Halliday D. and Resnick R., 1981, Physics-part two, 3rd edition, J. Wiley and Sons.

Hammack J., Scheffner N. and Segur H., 1991, A note on the generation and narrowness of periodic rip currents, J. Geophys. Res., 96, C3,4909-4914.

Inman, D.L., Tait R.J. and Nordstrom C.E., 1971, Mixing in the surf zone, J. Geophys. Res., 76,15, 3493-3514.

Jimenez J. and Orlandi P., 1993, The rollup of a vortex layer near a wall, J. Fluid Mech., 248, 297-313.

Karweit M., 1975, Motion of a vortex pair approaching an opening in a boundary, Phys. Fluids, 18, 12, 1604-1606.

Komar P.D. and Oltman-Shay J., 1991, Nearshore currents, pp 651-680 in, Handbook of coastal and ocean engineering, Vol. 2: Offshore structures, marine foundations, sediment processes and modelling.

Korn G.A. and Korn T.M., 1961, Mathematical handbook for scientists and engineers: definitions, theorems, and formulas for reference and review, New York: McGraw-Hill Book Co. Inc., 943pp.

Kuwahara K. and Takami H., 1973, Numerical studies of two-dimensional vortex motion by a system of point vortices, J. Phys. Soc. Japan, 34, 247-253.

Lamb H., 1932, Hydrodynamics, 6 ed., Cambridge Univ. Press, 738 pp.

Ledwell, J., Watson, A., Law, C., 1993, Evidence for slow mixing across the pycnocline from an open-ocean tracer-release experiment, Nature, 364, 701-703.

Linden P.F., Boubnov B.M. and Dalziel S.B., 1995, Source-sink turbulence in a rotating stratified fluid, J. Fl. Mech., 298, 81-112.

Longuet-Higgins M.S., 1981, Oscillating flow over steep sand ripples, J. Fluid Mech., 107, 1-35.

Lugt H.J. and Ohring S., 1992, The oblique ascent of a viscous vortex pair toward a free surface, J. Fluid Mech., 236,461-476.

Lugt, H.J.,1983, Vortex flow in nature and technology, John Wiley and Sons, 297 pp.

Maxworthy T., 1974, Turbulent vortex rings, J. Fluid Mech., 64, part 2, 227-239.

Maxworthy T., 1977, Some experimental studies of vortex rings, J. Fluid Mech., 81, part 3,227-239.

Meleshko V.V. and Gurzhi A.A., 1994, Stirring of an inviscid fluid by interacting point vortices, Modelling of oceanic vortices, 271-281, G.J.F. van Heijst ed.

Milinazzo F., Saffman P.G., 1977, The calculation of large Reynolds number two-dimensional flow using discrete vortices with random walk, J. Comput. Phys., 23,4,380-392.

Milne-Thomson L.M., 1949, Theoretical Hydrodynamics, 2nd ed., Macmillan and co. Ed., London.

Monin A.S. and Ozmidov R.V., 1985, Turbulence in the ocean, Dordrecht Reidel, 247 pp.

Munk, W., 1966, Abyssal recipes, Deep-sea res., 13, 707.

Murty G.S. and Sankara Rao K., 1970, Numerical study of the behaviour of a system of parallel line vortices, J. Fluid Mech., 40,595-602.

Norbury J., 1973, A family of steady vortex rings, J. Fluid Mech., 57, 417-431.

Novikov E.A., 1975, Dynamics and statistics of a system of vortices, Sov. Phys.-JETP, 41, 5, 937-943.

Novikov E.A. and Sedov Yu.B., 1978, Stochastic properties of a four vortex system, Sov. Phys.-JETP, 48, 3, 440-444.

Oh T. and Dean R.G., 1996, Three-dimensional hydrodynamics on a barred beach, pp 3680-3693 in, Coastal Engineering 1996, Vol. 3, B.L.Edge ed., American Society of Civil Engineers.

Ohring S. and Lugt H.J., 1991, Interaction of a viscous vortex pair with a free surface, J. Fluid Mech., 227,47-70.

Oltman-Shay J., Howd P.A. and Birkemeier W.A., 1989, Shear instabilities of the mean longshore currents. 2. Field observations, J. Geophys. Res., 94, C12, 18031-18042.

Orlandi P., 1990, Vortex dipole rebound from a wall, Phys. Fluids, A2, 8, 1429-1436.

Özkan-Haller T.H. and Kirby J.T., 1996, Numerical study of low frequency surf zone motions, pp 1361-1374 in, Coastal Engineering 1996, Vol. 1, B.L.Edge ed., American Society of Civil Engineers.

Peace A. J. and Riley N., 1983, A viscous vortex pair in ground effect, J. Fluid Mech., 129, 409-426.

Pedlosky, J., 1987, Geophysical fluid dynamics, 2nd edition, Springer-Verlag, New York.

Peregrine H.D., 1996, Vorticity and eddies in the surf-zone, pp. 460-464 in, Coastal Dynamics 95, (ed. W.R.Dally &R.B.Zeidler), New York, American Society of Civil Engineers.

Peregrine H.D., 1998, Surf zone currents, Theoret. Comput. Fluid Dynamics, 10, 295-309.

Peridier V.J., Smith F.T. and Walker J.D.A., 1991a, Vortex-induced boundary-layer separation. Part 1. The unsteady limit problem $Re \rightarrow \infty$, J. Fluid Mech., 232,99-131.

Peridier V.J., Smith F.T. and Walker J.D.A., 1991b, Vortex-induced boundary-layer separation. Part 2. Unsteady interacting boundary layer theory, J. Fluid Mech., 232,133-165.

Polzin, K., Speer K.G., Toole, J.M. and Schmitt, R.W., 1996, Intense mixing of Antarctic Bottom Water in the equatorial Atlantic Ocean, Nature, 380, 54-56.

Polzin, K., Toole J., Ledwell, J. and Schmitt, R., 1997, Spatial variabilty of turbulent mixing in the abyssal ocean, Science, 276, 93-96.

Press W.H., Teukolsky S.A., Vetterling W.T. and Flannery B.P., 1992, Numerical recipes in C, 2nd Ed., Cambridge Univ. Press, 994 pp.

Pullin D.I. and Saffmann P.G., 1998, Vortex dynamics in turbulence, Ann. Rev. Fluid Mech., 30, 31-51.

Robert R. and Sommeria J., 1991, Statistical equilibrium states for two-dimensional flows, J. Fluid Mech., 229, 291-310.

Saffman P.G., 1979, The approach of a vortex pair to a plane surface in inviscid fluid, J. Fluid Mech., 92, 497-503.

Saffman P.G., 1992, Vortex dynamics, Cambridge Univ. Press, 311 pp.

Saffman P.G. and Baker G.R., 1979, Vortex interactions, Ann. Rev. Fluid Mech., 11, 95-122.

Sasaki M., 1985, Velocity profiles in nearshore circulation current, Coastal Eng. in Japan, 28, 125-136.

Shariff K. and Leonard A., 1992, Vortex rings, Ann. Rev. Fluid Mech., 24, 235-279.

Sheffield S.J., 1977, Trajectories of an ideal vortex pair near an orifice, Phys. Fluids, 20,4,543-545.

Siggia E.D. and Aref H., 1981, Point-vortex simulation of the inverse energy cascade in two-dimensional turbulence, Phys. Fluids, 24, 1, 171-173.

Slinn D.N., Allen J.S., Newberger P.A. and Holman R.A., 1998, Nonlinear shear instabilities of alongshore currents over barred beaches, J. Geophys. Res., 103, 18357-18379.

Smith J.A. and Largier J.L., 1995, Observations of nearshore circulation: rip currents, J. Geophys. Res., 100,C6,10967-10975.

Spiegel M.R., 1975, Probability and statistics, 1975, New York: McGraw-Hill book Co.

Svendsen I.A. and Putrevu U., 1996, Surf-zone hydrodynamics, 1-78 in, Advances in coastal and ocean engineering, Vol. 2, P.L.-F. Liu.

Tang E.C.-S.. and Dalrymple R.A., 1989a, Nearshore circulation. B. Rip currents and wave groups , 205-230, in Nearshore sediment Transport, Seymour R.J. ed, Plenum Press.

Tang E.C.-S. and Dalrymple R.A., 1989b, Measuring surf-zone dynamics. B. Field measurements of rip currents, 61-65, in Nearshore sediment Transport, Seymour R.J. ed, Plenum Press.

Telste J.G., 1989, Potential flow about two counter-rotating vortices approaching a free surface, J. Fluid Mech., 201, 259-278.

Tennekes H. and Lumley J.L., 1973, A first course in turbulence, The MIT Press, 300 pp.

Thorpe S.A., 1995, Dynamical processes of transfer at the sea surface, Prog. Oceanog., 35, 315-152.

Thorpe S.A. and Centurioni L.R., 2000, On the use of the method of images to investigate near-shore dynamical processes, J. Mar. Res., 58,779-788.

Thorpe, S.A., 1998, Turbulence in the stratified and rotating world ocean, Theor. Comp. Fluid Dyn.,11 (3/4), 171-181.

Toole, J.M., Polzin K.L. and Schmitt R.W., 1994, Estimates of the diapycnal mixing in the abyssal ocean, Science, 264,1120-1123.

Tritton D.J., 1988, Physical Fluid Dynamics, 2nd. ed., Clarendon Press, Oxford, 519 pp.

Tyvand P.A., 1991, Motion of a vortex near a free surface, J. Fluid Mech., 225,673-689.

van Dyke M., 1982, An album of fluid motion, The Parabolic Press, Stanford, California, 176 pp.

van Heijst G.J.F. and Flor J.B., 1989 a, Dipole formation and collisions in a stratified fluid, Nature, 340, 212-215.

van Heijst G.J.F. and Flor J.B., 1989 b, Laboratory experiments on dipole structures in a stratified fluid, pp. 591-608 in, Mesoscale/Synoptic Coherent Structures in Geophysical Turbulence, ed. Nihoul J.C.J, Jamart B.M., Amsterdam.

Viecelli J.A., 1993, Statistical mechanics and correlation properties of a rotating two-dimensional flow of like-sign vortices, Phys. Fluids A,5, 2484-2501.

Voropayev S.I., 1989, Flat vortex structures in a stratified fluid, In Mesoscale/Synoptic Coherent Structures in Geophysical Turbulence, ed Nihoul J.C.J., Jamart B.M., Amsterdam, 671-689.

Voropayev S.I. and Afanasyev D.Ya., 1992, Two-dimensional vortex-dipole interaction in a stratified fluid, J. Fl. Mech., 236, 665-689.

Wang X., 1992, Interaction of an eddy with a continental slope, PhD Thesis, WHOI-92-40, 216 pp.

Weidman P.D. and Riley N., 1993, Vortex ring pairs: numerical simulation and experiments, J. Fluid Mech., 257, 311-337.

Whitehead J.A., 1989, Laboratory studies of isolated eddies in a rotating fluid, pp. 627-637, in, Mesoscale/Synoptic Coherent Structures in Geophysical Turbulence, ed. Nihoul J.C.J, Jamart B.M., Amsterdam.

Yu D. and Tryggvason G., 1990, The free-surface signature of unsteady, two-dimensional vortex flows, J. Fluid Mech., 218,547-572.

SOUTHAMPTON UNIVERSITY LIBRARY

USER'S DECLARATION

AUTHOR: CENTURIONI, LUCA R TITLE: DYNAMICS OF NEAR-SHORE VORTICES

DATE:

I undertake not to reproduce this thesis, or any substantial portion of it, or to quote extensively from it without first obtaining the permission, in writing, of the Librarian of the University of Southampton.

To be signed by each user of this thesis

DATE	SIGNATURE	ADDRESS